Non-linear scalar field dynamics in particle physics motivated models of the early universe

Inauguraldissertation
zur
Erlangung der Würde eines Doktors der Philosophie
vorgelegt der Philosophisch-Naturwissenschaftlichen Fakultät
der Universität Basel

von

Francesco Cefalà

aus Italien

Basel, 2018

Genehmigt von der Philosophisch-Naturwissenschaftlichen Fakultät auf Antrag von

Prof. Dr. Stefan Antusch, Prof. Dr. Mar Bastero-Gil

Basel, den 18.09.2018

Prof. Dr. Martin Spiess
Dekan

Abstract

In particle physics motivated models of the early universe, non-linear preheating dynamics of scalar fields can give rise to rich phenomenology. An example phenomenon is e.g. the formation of oscillons: quasi-stable, localised, and non-linear scalar field configurations. In the first of three main parts of this thesis we study the gravitational wave (GW) production of asymmetric (ellipsoidal) oscillons in an expanding universe. Based on model-independent, simplifying assumptions on the properties of oscillons, we derive an analytical expression for the anisotropic stress tensor. The latter is subsequently used to numerically compute the stochastic GW background of different "oscillon cosmologies". In particular, we investigate and discuss how different properties of an oscillon cosmology, such as the background expansion or the size, and amplitude of oscillons, manifest themselves in the stochastic background of GWs.

The second and third part of this thesis are devoted to lattice studies in which the non-linear scalar field dynamics, as well as the associated production of GWs is explored in different models. In the second part we consider different realisations of a supersymmetric model of hilltop inflation in which an additional scalar field χ couples to the inflaton. We find that during preheating χ can get resonantly amplified due to a non-standard parametric resonance that is driven by the dynamics of inhomogeneous inflaton fluctuations. Moreover, we show that qualitative differences in the dynamics of the fields are manifested in the resulting GW background.

In the third part we consider the non-linear dynamics of Kähler moduli in two scenarios of moduli stabilisation in type IIB string theory. More explicitly we study the dynamics of the overall volume modulus in the Kachru-Kallosh-Linde-Trivedi (KKLT) scenario, as well as the dynamics of a single blow-up modulus in the Large Volume Scenario (LVS). More specifically, we consider the dynamics of preheating of moduli that get displaced from their post-inflationary minimum through the "vacuum misalignment" mechanism. In both models we show that preheating can be very efficient and lead to the non-linear fragmentation of the moduli and, ultimately, to the formation of oscillons. Interestingly, we find that the dynamics are qualitatively different in the KKLT scenario compared to the dynamics of the blow-up modulus in the LVS. The corresponding differences are also imprinted in the resulting GW background.

Acknowledgements

First of all, my special gratitude goes to my advisor Prof. Dr. Stefan Antusch for his continuous support, guidance, and his faith in my abilities. Secondly, my sincere thanks also go to Prof. Dr. Mar Bastero-Gil for agreeing to be the co-referee of my thesis.

Special thanks are also extended to Dr. Sven Krippendorf, Dr. Francesco Muia, Dr. David Nolde, Dr. Stefano Orani, and Prof. Dr. Fernando Quevedo for numerous fruitful discussions and the pleasant collaboration and excellent teamwork.

I would also like to express my sincere thanks to Dr. Rubén M. Cabezón and Eros Cazzato for valuable discussions and enjoyable breaks. My gratitude also goes to Christian Hohl, Max Homberger, Dr. Sven Krippendorf, Kenneth Marschall, Dr. Francesco Muia, Dr. Stefano Orani, Johannes Rosskopp, Christiane Scherb, Märta Tschudin, and Nora Vocat for taking time to proofread parts of this thesis. I am especially indebted to Prof. Dr. Fernando Quevedo for his kind invitation to the ICTP Trieste.

My thanks also go out to all the former and present members of the Particles and Cosmology group, to all my former and present office mates, and all my other colleagues at the department for the great time we spent together. Thank you!

Last but not least, my deepest love and appreciation goes to my dear friends and my parents Carmelina and Giovanni for their continuous support and encouragement.

Publications

This thesis is based on the author's work conducted from November 2014 until August 2018, at the Department of Physics of the University of Basel, under the supervision of Prof. Dr. Stefan Antusch. Partial results of the presented work have been published in published in [1–4]:

[1] S. Antusch, F. Cefala, D. Nolde, and S. Orani, *Parametric resonance after hilltop inflation caused by an inhomogeneous inflaton field*, *JCAP* **1602** (2016), no. 02 044, [arXiv:1510.0485].

[2] S. Antusch, F. Cefala, and S. Orani, *Gravitational waves from oscillons after inflation*, *Phys. Rev. Lett.* **118** (2017), no. 1 011303, [arXiv:1607.0131]. [Erratum: *Phys. Rev. Lett.* **120**, no. 21, 219901 (2018)].

[3] S. Antusch, F. Cefala, S. Krippendorf, F. Muia, S. Orani, and F. Quevedo, *Oscillons from String Moduli*, *JHEP* **01** (2018) 083, [arXiv:1708.0892].

[4] S. Antusch, F. Cefala, and S. Orani, *What can we learn from the stochastic gravitational wave background produced by oscillons?*, *JCAP* **1803** (2018), no. 03 032, [arXiv:1712.0323].

Contents

Part I

Introduction

Chapter 1

Introduction

Currently, the most popular and successful framework for describing the evolution of our universe is built upon two main pillars. The first is the Standard Model (SM) of Particle Physics. It provides a quantum field theoretical description of the microscopic interactions among the known elementary particles. In particular, it accounts for describing the physics associated with three out of the four known fundamental forces of nature: the electromagnetic, the weak, and the strong force. The SM is complemented by Einstein's theory of General Relativity (GR). It provides a field theoretical description of gravity at a classical level and constitutes the second pillar of modern cosmology.

Together these theories provide a fairly good and reasonable description of how the universe evolved to its present state, at least since the formation of light nuclei. The latter is well captured by the theory of Big Bang Nucleosynthesis (BBN) which, based on the SM particle interactions, correctly predicts the abundances of the lightest elements[1].

The leading model for describing the universe's evolution on large cosmological scales is currently the ΛCDM model. Its simplest version, which is based on only six independent parameters, is in remarkable agreement with cosmological observations [5, 59]. Moreover, in line with the predictions of an early period of single-field slow-roll inflation, recent observational constraints on the primordial seeds of structure are found to be consistent with Gaussian distributed, adiabatic fluctuations characterised by a nearly scale-invariant, slightly red-tilted spectrum.

Ironically, the same cosmological observations that confirm the validity of the model also imply that most of our universe's present energy and matter content is subject to unknown physics. It is clear, however, that some essential building blocks are missing in the SM. Apart from the fact that none of the SM particles has the right properties to be identified as Dark Matter (DM), if the latter is made up of elementary particles, it also lacks any explanation of how neutrinos acquire their mass.

In principle, there are different approaches to how the SM could be extended in order to address the above mentioned issues. A possible solution would be to simply add the missing building blocks "by hand". Alternatively, one may consider

[1] Up to a discrepancy in the abundance of Lithium.

an embedding of the SM into a more fundamental (and possibly more predictive) theory of particle physics e.g. within the framework of Supersymmetry (SUSY) or string theory. Both approaches are legitimate, though the latter is certainly the more elegant one and may, moreover, bring additional benefits depending on how a model is constructed. Some of the additional scalar fields that are naturally present in supersymmetric extensions of the SM could, for example, be associated with a particle physics phase transition. Possible examples would be the spontaneous breaking of a more fundamental gauge group of some Grand Unified Theory (GUT), or the breaking of a family symmetry. The latter could offer a natural explanation for the hierarchical structure of the Yukawa couplings in the SM. String theory, in turn, could allow to successfully describe gravity within the framework of a quantum theory (see e.g. [6]). Moreover, a link between the inflationary sector and the SM can naturally be established if one of the scalar fields present in the theory exhibits the right properties to successfully drive an early period of cosmic inflation. At least in models of slow-roll inflation, such a connection is crucial in order to provide a decay channel through which the energy stored in inflationary degrees of freedom can ultimately be transferred to a thermal bath of relativistic SM particles.

The epoch during which the universe evolves towards thermal equilibrium is referred to as reheating. The latter strongly depends on the details of the underlying theory. So far, we have no experimental guidance whatsoever of how this process happened in detail. What we do know, however, is that it must be certainly terminated before the onset of BBN, in order to guarantee its success. Additional model-dependent bounds arise from requiring that the cosmological evolution is all in all consistent i.e. that the DM abundance and the production of the baryon asymmetry are in agreement with observational bounds, and that BBN can be completed successfully.

In order to reliably test a theory against cosmological inconsistencies, it is essential to study the epoch of reheating in detail. The dynamics during this regime can, indeed, be very diverse. Immediately after inflation, for example, the universe may undergo a non-perturbative stage, referred to as preheating. As the inflaton starts oscillating around the minimum of its potential after inflation, its coherent nature can lead to the resonant amplification of inflaton perturbations and perturbations of other fields that couple to it. In certain cases, the growth of perturbations can be so efficient that the inflaton quickly decays into inhomogeneous fluctuations and the dynamics become non-linear. Depending on the model, this can for example lead to the development of long-lived, non-linear structures such as oscillons [7–14].

In string inspired models of inflation, similar effects may not only occur during preheating after inflation, but potentially also at later stages. String moduli with masses below the Hubble scale after inflation, can get displaced from their post-inflationary minimum and become dynamical at later times [15–17]. In such a case, the universe would undergo a repeated period of (p)reheating [18].

The details of preheating, can be very sensitive to the parameters that characterise a specific model realisation. Already slight changes in certain model parameters can, in principle, lead to qualitatively different cosmological evolutions and thus to different predictions for quantities that are sensitive to the reheating dynamics.

With the first direct observation of Graviational Waves (GW) announced in

February 2016 [19], we have entered a new era of observational cosmology. A possible and fascinating effect that is associated with a stage of preheating is, indeed, the production of a stochastic background of GWs. Being directly related to the cosmological dynamics, the latter could contain precious information about the underlying theory. The observation of such a cosmological GW background could therefore offer an invaluable insight into the physics of the very early universe and allow to explore new physics at energy scales beyond the reach of particle accelerators.

The aim of this thesis is to investigate the non-linear scalar field dynamics during preheating in different realisations of hilltop inflation, as well as in two string inspired scenarios of post-inflationary modular cosmology. Motivated by the fact that a generic feature of the models studied in this thesis turns out to be the natural formation of oscillons, we explore the production of GWs related to their dynamics in a model-independent way.

This thesis is organised as follows: In chapter 2 we briefly review the standard model of cosmology. In chapter 3 we introduce the inflationary paradigm and explain the mechanism for generating the primordial seeds of structure through inflationary quantum fluctuations. Finally, at the end of the chapter, we explicitly discuss the inflationary dynamics for two example models and calculate the inflationary observables. We then turn to chapter 4 where we review the post-inflationary physics of reheating. Particular focus is thereby devoted to the non-perturbative stage of preheating and the associated consequences.

The main part of this thesis is presented in parts III - V. In chapter 5 we investigate the production of GWs from asymmetric oscillons. On the basis of simplifying and model-independent assumptions we derive an analytic expression for the anisotropic stress sourced by asymmetric oscillons in section 5.2. This result is further used in section 5.3 to study how the characterising properties of an oscillon cosmology are manifested in the stochastic background of GWs.

In chapter 6 we study different aspects of preheating after hilltop inflation in scenarios in which the inflaton is coupled to an additional matter field χ. We begin by briefly motivating the model from a particle physics point of view in section 6.1. The preheating dynamics are then discussed in section 6.2. On the basis of two-dimensional lattice simulations we demonstrate and argue that fluctuations of χ can get resonantly produced via a non-standard parametric resonance which can be triggered well after the inflaton has decayed into inhomogeneous fluctuations. Furthermore, we present results of simulations carried out in $3+1$ dimensions. The latter are on one hand found to be in good agreement with our two-dimensional results and on the other hand confirm the results of Ref. [20] that were based on lattice simulations in $2+1$ dimensions. Finally, in section 6.3 we discuss the production of GWs during preheating after hilltop inflation. We thereby compare different results originating from lattice simulations of different model realisations.

In chapter 7 we explore the dynamics of moduli preheating in two scenarios of moduli stabilisation in type IIB string theory. More explicitly, we investigate the dynamics of a Kähler modulus in the Kachru-Kallosh-Linde-Trivedi (KKLT) scenario [21], as well as that of a single, displaced blow-up modulus in the Large Volume Scenario (LVS) [22, 23]. Through a numerical lattice study we find that in both scenarios the dynamics become non-linear and, in particular, that oscillons

naturally form. The corresponding results are discussed in sections 7.1 for the KKLT scenario and in section 7.2 for the blow-up modulus in the LVS, respectively. Interestingly, we find that the underlying mechanisms that lead to growth of fluctuations are qualitatively different in both scenarios. These differences are also manifested in the stochastic background of GWs as discussed in section 7.3.

Part II

Theoretical framework

Chapter 2

A brief introduction into the foundations of cosmology

In this chapter we give a short overview of the fundamentals of modern cosmology and briefly discuss its current status. For a more detailed introduction to cosmology see e.g. Refs. [24, 25]. In section 2.1 we introduce Einstein's theory of General Relativity as the basic framework and point out the fundamental assumptions on which the standard model of cosmology is based. In section 2.2 we give a brief outline how parameter constraints are extracted from cosmological observations and present recent constraints on the baseline ΛCDM model.

2.1 The shape of the universe

The framework for the currently most popular description of our universe is provided by Einstein's theory of GR[1]. Within this beautiful formulation of gravity, the evolution of spacetime is dictated by the Einstein Field Equations (EFEs)

$$R_{\mu\nu} - \frac{1}{2} g_{\mu\nu} R - g_{\mu\nu}\Lambda \;=\; T_{\mu\nu}\,. \tag{2.1}$$

The Ricci tensor $R_{\mu\nu}$ can be expressed solely as a function of the (symmetric) metric $g_{\mu\nu}$ (and its first and second order partial derivatives) as

$$R_{\mu\nu} \;=\; \partial_\rho \Gamma^\rho{}_{\mu\nu} - \partial_\nu \Gamma^\rho{}_{\mu\rho} + \Gamma^\rho{}_{\sigma\rho}\Gamma^\sigma{}_{\mu\nu} - \Gamma^\rho{}_{\sigma\nu}\Gamma^\sigma{}_{\rho\mu}\,, \tag{2.2}$$

where

$$\Gamma^\mu{}_{\nu\rho} \;=\; \frac{1}{2} g^{\mu\alpha}(\partial_\rho g_{\alpha\nu} + \partial_\nu g_{\alpha\rho} - \partial_\alpha g_{\nu\rho})\,, \tag{2.3}$$

are the Christoffel symbols. The quantity R, which is sometimes referred to as the scalar curvature, is defined as the trace of the Ricci tensor

$$R \equiv g^{\mu\nu} R_{\mu\nu}\,. \tag{2.4}$$

On the right-hand side of the EFEs (2.1) we have the stress–energy tensor $T_{\mu\nu}$. Within the context of cosmology it essentially comprises the properties of the matter

[1] See e.g. [26] for an introduction or [27] for a nice reference book.

the universe is "filled" with. The scalar Λ appearing on the left-hand side of eq. (2.1) is referred to as the cosmological constant. Its physical interpretation is that of a constant contribution to the vacuum energy density and it may therefore be absorbed into the stress-energy tensor.

Eq. (2.1) represents a system of ten non-linear partial differential equations that describe the dynamics of the components of the metric tensor. Unfortunately, it is often not possible to find solutions without the use of numerical techniques[2]. In certain cases, however, the complexity of the problem may be reduced so that an exact solution to the EFEs can be obtained [29]. These solutions are generally based on simplifying assumptions that are typically related to the symmetries of the physical problem. As will be discussed shortly, a striking example for such a physical situation is the large scale behavior of the observable universe.

Beside the general framework that is provided by GR, the ΛCDM model relies on the *Cosmological Principle*, i.e. on the assumption that the universe is spatially *homogeneous* and *isotropic* on average. There are various empirical observations that confirm isotropy on scales $\sim 100\,h^{-1}$ Mpc. Examples of such observations are, for instance, the distribution of galaxies [30–33], the diffuse X-ray background [34, 35] or the distribution of supernovae [36, 37]. Nevertheless, the clearest evidence is provided by the nearly isotropic temperature of the cosmic microwave background (CMB) [38]. Spatial homogeneity, on the other hand, follows immediately from isotropy, if the *Copernican Principle*[3] is assumed. It should be noted that direct observational tests of homogeneity are, unfortunately, not feasible. However, one may search for violations of homogeneity (or rather of the Copernican Principle) which would, in turn, disprove this assumption (see e.g. Ref. [39]).

The Cosmological Principle, once adopted, imposes strong constraints on the geometry of spacetime, i.e. on the mathematical form of the metric $g_{\mu\nu}$. Indeed, it can be shown[4] that for any homogeneous and isotropic space there always exists a coordinate system $x^\mu = (t, r, \theta, \varphi)$ in which the line element takes the Friedmann-Lemaître-Robertson-Walker (FLRW) form

$$\begin{aligned} ds^2 &\equiv g_{\mu\nu}(x^\alpha) dx^\mu dx^\nu \\ &= -dt^2 + a^2(t) \left[\frac{dr^2}{1 - \mathcal{K} r^2} + r^2 \left(d\theta^2 + \sin^2\theta d\varphi^2 \right) \right] . \end{aligned} \tag{2.5}$$

The time-dependent function $a(t)$ is referred to as the *scale factor*. It is dimensionless and describes the expansion (or contraction) of the universe. The constant parameter $\mathcal{K}$ describes the curvature of space. In order to be consistent with the Cosmological Principle, the only values that $\mathcal{K}$ can take on are $\mathcal{K} = 0$ or ± 1. They correspond to a flat euclidean space ($\mathcal{K} = 0$), a spherical space ($\mathcal{K} = +1$), or a hyperbolic space ($\mathcal{K} = -1$), respectively. The spatial coordinates (r, θ and φ) used in eq. (2.5) are spherical *comoving coordinates*. This essentially means that the relative distance between points on a coordinate grid remains constant, while their *physical* distance increases (or decreases) proportional to $a(t)$ as the universe expands (or contracts).

[2] For a review on numerical relativity see e.g [28].
[3] In essence, the statement that we are not located at any privileged position in the universe.
[4] For a proof see e.g. section 13.5 in [40].

The matter content of the universe is typically modeled by *perfect fluids*, i.e. by fluids that are spatially isotropic in their rest frame. The stress-energy tensor of a perfect fluid can be expressed as

$$T_{\mu\nu} \;=\; (\rho + p) u_\mu u_\nu + p\, g_{\mu\nu}\,, \tag{2.6}$$

where ρ is the fluid energy density and p is the fluid pressure, both measured in the rest frame of the fluid. The vector u^μ denotes the four-velocity of the fluid. In the rest frame, where $u^\mu = (1, 0, 0, 0)$ and with one index raised, the stress-energy tensor reduces to the diagonal form

$$T^\mu{}_\nu \;=\; \begin{pmatrix} -\rho & 0 & 0 & 0 \\ 0 & p & 0 & 0 \\ 0 & 0 & p & 0 \\ 0 & 0 & 0 & p \end{pmatrix}\,. \tag{2.7}$$

What now remains to be specified is the relationship between the energy density and the pressure. The latter determines the properties of the fluid and is expressed in form of an *Equation Of State* (EOS): $p = p(\rho)$. For the cosmologically relevant fluids, the EOS is usually assumed to be of the form

$$p \;=\; w\rho\,. \tag{2.8}$$

The characteristics of the fluid are therefore exclusively determined by the proportionality factor w, which in general may be time-dependent and is referred to as the Equation Of State parameter (EOSp).

In cosmology we distinguishes between three main types of fluids: non-relativistic matter, relativistic matter and vacuum energy. All of these fluids can be modeled by a constant EOSp with corresponding values presented below:

$$w \;=\; \begin{cases} 0 & \text{pressureless dust (non-relativistic matter)} \\ 1/3 & \text{radiation (relativistic matter)} \\ -1 & \text{cosmological constant (vacuum energy)} \end{cases} \tag{2.9}$$

In general, one may have different types of matter contributing to the total energy density. For the case that different fluids do not interact with each other, as often assumed, one can write the total energy density and the total pressure as

$$\rho \;=\; \sum_i \rho_i, \qquad p \;=\; \sum_i p_i\,, \quad \text{with} \quad p_i \;=\; w_i \rho_i\,, \tag{2.10}$$

where the index i runs over the different matter species.

Once the stress-energy tensor $T_{\mu\nu}$ is specified, the time evolution of the scale factor for a homogeneous and isotropic universe is obtained by solving the EFEs. Essentially, two independent equations, also known as the Friedmann equations, can be deduced from eq. (2.1). The first can be obtained from the 00-component of the EFEs and reads

$$H^2 \;\equiv\; \left(\frac{\dot{a}}{a}\right)^2 \;=\; \frac{\sum_i \rho_i}{3\, m_{\mathrm{Pl}}^2} - \frac{\mathcal{K}}{a^2}\,. \tag{2.11}$$

The quantity $H \equiv \dot{a}/a$, which is known as the *Hubble parameter*, describes the expansion rate of the universe. Since the scale factor is dimensionless, H^{-1} has units of time. The remaining, non-vanishing components (i.e. the ii-components) of (2.1) give

$$\frac{\ddot{a}}{a} + \frac{1}{2}\left(\frac{\dot{a}}{a}\right)^2 = -\frac{\sum_i p_i}{2\,m_{\rm Pl}^2} - \frac{\mathcal{K}}{2\,a^2}\,. \tag{2.12}$$

Notice that in eqs. (2.11) and (2.12) we have absorbed the cosmological constant Λ into the definition of the energy momentum tensor by defining

$$\rho_\Lambda = m_{\rm Pl}^2\,\Lambda\,, \quad \text{and} \quad p_\Lambda = -m_{\rm Pl}^2\,\Lambda\,. \tag{2.13}$$

Other equations such as the continuity equation[5]

$$\dot{\rho} = -3H(\rho + p)\,, \tag{2.14}$$

or the acceleration equation (cf. eq. (1.66) in [24] for example) may be derived from eqs. (2.11) and (2.12) and are therefore not independent.

Assuming $\mathcal{K} = +1$, the Friedmann equations (2.11) and (2.12) were first derived by A. Friedmann in 1922 for a universe filled with pressureless dust and a cosmological constant [41]. Two years later, in 1924, he extended this study to include the case of a hyperbolic space ($\mathcal{K} = -1$) [42]. The Friedmann equations have been studied independently by G. Lemaître in 1928 [43]. Explicitly, he considered the effect of a radiation component contributing to the total energy density [43]. In the 1930s, H.P. Robertson [44–46] and A.G. Walker [47] independently showed that the most general line element complying with the Cosmological Principle has the form of (2.5).

A quantity which is often used to measure the energy density in units of the Hubble parameter H is the *density parameter* $\Omega_{\rm tot}$. It is defined as

$$\Omega_{\rm tot} \equiv \frac{\sum_i \rho_i}{\rho_c} \equiv \sum_i \Omega_i\,, \tag{2.15}$$

where the index i runs over the different matter species (here including the cosmological constant). The critical density ρ_c introduced in eq. (2.15) is defined as

$$\rho_{\rm c} \equiv 3\,m_{\rm Pl}^2\,H^2\,, \tag{2.16}$$

and represents the total energy density that is required for the universe to be spatially flat ($\mathcal{K} = 0$). An alternative expression which is sometimes used to specify the present day value of the energy density for a given species is

$$\Omega_i h^2\,, \tag{2.17}$$

where h is dimensionless and referred to as the *reduced Hubble parameter*. It is defined in terms of the present day value of the Hubble parameter H_0 as

$$h \equiv H_0/(100\ \text{km s}^{-1}\ \text{Mpc}^{-1})\,. \tag{2.18}$$

[5]Which follows from the conservation of energy and momentum $\partial_\mu T^{\mu\nu} = 0$.

It is not difficult to see from eq. (2.15) that the density parameter provides a measure for the spatial curvature of the universe. In fact, if $\Omega_{\text{tot}} = 1$ the universe is spatially flat, while $\Omega_{\text{tot}} > 1$ and $\Omega_{\text{tot}} < 1$ imply a positive or negative curvature, respectively.

Henceforth, we restrict ourselves to a flat euclidean universe and assume $\mathcal{K} = 0$. We shall justify this assumption shortly in section 2.2. From eq. (2.14) together with (2.10) we can find an exact solution for the evolution of the energy density as a function of the scale factor a which reads

$$\rho(a) \;=\; \sum_i \rho_{\text{i},i} \left(\frac{a_\text{i}}{a}\right)^{3(1+w_i)} , \tag{2.19}$$

where $\rho_{\text{i},i} > 0$ is the initial energy density of the species "i" and $a_\text{i} > 0$ is the initial value of the scale factor. Eq. (2.19) tells us, that the energy density is diluted or *redshifted*, as the universe expands. We shall often use this term throughout this thesis to refer to a wavelength (or frequency) shift that is caused by the expansion of the universe. Formally, the redshift z experienced by the universe between some time t_{past} in the past and today is given by (see e.g. [24, p. 58])

$$\frac{a_0}{a_{\text{past}}} \;=\; 1 + z \,. \tag{2.20}$$

Here a_0 refers the present value of the scale factor (conventionally normalised to $a(t_0) \;=\; a_0 = 1$) and a_{past} is the value at $t = t_{\text{past}} \leq t_0$.

The continuity equation (2.14) can be used to obtain the evolution of the scale factor as a function of cosmic time t from eq. (2.11) which gives

$$a(t) \;=\; \begin{cases} a_\text{i} \left[1 + \frac{3}{2}\, H_\text{i}\, (t - t_\text{i})\right]^{3/2} & \text{matter dominated} \quad (w = 0) \\ a_\text{i} \left[1 + 2\, H_\text{i}\, (t - t_\text{i})\right]^{1/2} & \text{radiation dominated} \quad (w = 1/3) \\ a_\text{i}\, e^{H_\text{i}\,(t - t_\text{i})} & \Lambda \text{ dominated} \quad (w = -1) \end{cases} \tag{2.21}$$

where t_i is the initial time, $a_\text{i} \equiv a(t_\text{i})$ is the initial value of the scale factor, and $H_\text{i} \equiv H(t_\text{i}) = \sqrt{\rho(t_\text{i})/(3m_{\text{Pl}}^2)}$ denotes the initial Hubble parameter.

In certain cases, it may be more convenient to use a different time coordinate. Throughout this thesis, we will sometimes work in terms of *conformal time* η which is defined as

$$\eta(t) \;\equiv\; \int_{t_\text{i}}^{t} \frac{dt'}{a(t')} \,. \tag{2.22}$$

Finally, before closing this section, let us introduce the notion of the *Hubble horizon*. The latter is defined as the inverse Hubble parameter $H^{-1}(t)$ and represents a characteristic distance in an expanding universe. More precisely, it corresponds to the distance above which objects recede at a speed larger than the speed of light at time t. Within this thesis we will sometimes use the terms *sub-horizon* and *super-horizon* to refer to length scales $\lambda < H^{-1}$ and $\lambda > H^{-1}$, respectively.

We have now discussed the basic framework on which the ΛCDM model is built and are ready to proceed with the, currently, most successful model of cosmology.

2.2 The ΛCDM model at a glance

Within the context of the ΛCDM model, the background dynamics are described by a FLRW universe, i.e. a homogeneous and isotropic cosmology with matter content given by some composition of perfect fluids. As discussed in the previous section, the fraction of energy that is attributable to a specific type of matter can, for instance, be expressed in terms of the density parameters Ω_i.

The universe is, of course, not perfectly homogeneous. In fact, it is commonly believed that tiny fluctuations of the energy density have been generated during the universe's very early stages, giving rise to the small CMB anisotropies and ultimately to the formation of the Large Scale Structure (LSS). Provided that these primordial fluctuations are Gaussian, their statistical properties are fully described by their power spectrum. In addition to the parameters that are required to describe the background cosmology, further parameters must be introduced to describe the spectrum of primordial fluctuations.

In order to test the viability of a given model and in particular to estimate the ranges of possible parameter values which are most consistent with observations, one has to calculate the cosmological evolution of the model and compare the outcome with observational data. This procedure may essentially be subdivided into two main tasks: (i) The exploration of the parameter space and (ii) the computation of the cosmological evolution for a given set of parameters. The former is typically mastered using Monte Carlo methods. Example codes that are publicly available are, for example, CosmoMC [48,49] and MontePython [50,51]. These codes are complemented by so-called "Boltzmann codes" such as CAMB [52,53] or CLASS [54], that account for simulating the cosmological evolution (including the evolution of perturbations) and computing CMB and LSS observables. For the calculation of the CMB observables, the evolution of the fluctuations is tracked using linear perturbation theory, i.e. by solving a perturbed version of the EFEs. The formation of structure, however, exhibits a highly non-linear behavior. Therefore, more sophisticated methods comprising semi-analytical techniques, and ultimately a combination of non-linear perturbation theory and Newtonian N-body simulations are required[6].

The most popular version of the ΛCDM model, sometimes referred to as the "base ΛCDM", assumes a flat FLRW cosmology and has only six free parameters. The name "ΛCDM" essentially refers to the components of the energy density that, according to the model, dominate the universe today and whose precise origins are as yet unknown: a cosmological constant Λ which today makes up roughly 70% of the energy budget of the universe, and cold dark matter (CDM) accounting for about 25%. The remaining $\sim 5\%$ mostly consist of cold visible matter, i.e. baryons, and a tiny fraction of radiation.

Recent parameter constraints for the base ΛCDM model are presented in table 2.1. The six parameters above the horizontal line represent a possible set of

[6] For pedagogical introductions to cosmological perturbation theory see e.g. [55,56]. For a review on non-linear perturbation theory see [57], or Ref. [58] for a comparison of different approaches.

Parameter	TT+lowP+lensing+ext
$\Omega_b\, h^2$	0.02227 ± 0.00020
$\Omega_{\mathrm{CDM}}\, h^2$	0.1184 ± 0.0012
$100\theta_{\mathrm{MC}}$	1.04106 ± 0.00041
τ	0.067 ± 0.013
$\ln(10^{10} A_{\mathrm{s}})$	3.064 ± 0.024
n_{s}	0.9681 ± 0.0044
H_0	67.90 ± 0.55
Ω_Λ	0.6935 ± 0.0072
Ω_m	0.3065 ± 0.0072

Table 2.1: Parameter constraints for the base ΛCDM model from the *Planck 2015* analysis (cf. table 4 in [5]). The parameters above the horizontal line comprise a set of six independent parameters that were fitted to the data and their value correspond to the 68% confidence limits. The analysis includes the *Planck* measurements of the CMB temperature, polarization, and lensing as well as other external ("ext") data. For more details we refer to the original paper where these results have been published [5].

independent parameters that have actually been fitted to observational data[7] [5]. The datasets that were used include for instance the *Planck 2015* CMB temperature and polarization data, data from Baryon Acoustic Oscillations (BAO) as well as other datasets (for more details cf. [5]). A selection of derived parameters are listed below the horizontal line. The parameters $\Omega_b\, h^2$ and $\Omega_{\mathrm{CDM}}\, h^2$ correspond to the present day baryon and CDM density, respectively. The parameter θ_{MC} denotes the angular size of the sound horizon at the surface of last-scattering (or essentially an approximation of it [5]). Notice that the first three parameters in table 2.1 are sufficient to uniquely determine the background dynamics, since $\Omega_{\mathrm{tot}} = 1$ is assumed. The parameters H_0, Ω_Λ and Ω_m are derived parameters and denote the present Hubble parameter, the density parameter associated with the cosmological constant and to non-relativistic matter, respectively.

The power spectrum of the *primordial curvature perturbations* is assumed to be described by the simple power law

$$\mathcal{P}_{\mathcal{R}}(k) = A_{\mathrm{s}} \left(\frac{k}{k_\star}\right)^{n_{\mathrm{s}}-1} , \tag{2.23}$$

where A_{s} is the amplitude of the fluctuations at a given pivot scale $k_\star$ [5], while the spectral index n_{s} parametrises the tilt of the spectrum. The estimated value of n_{s} (cf. table 2.1) implies that the primordial spectrum is nearly scale invariant, i.e. that the amplitude of fluctuations is almost the same throughout the whole range of observed scales.

[7] At the time of writing this part of the thesis, the *Planck 2018* results [59] were not yet released. We note that no significant deviations were found compared to the parameter estimates present in table 2.1 [59].

The parameter τ denotes the optical depth to reionization. During the reionization epoch [60], free electrons are released which may subsequently rescatter with CMB photons. This rescattering has an impact on the CMB anisotropies and essentially leads to an amplitude of fluctuations that is exponentially suppressed with τ at small scales.

Despite some measurements seem to be in tension with the baseline model[8], various independent probes exist which are in very good agreement. These include, among others, the CMB temperature, polarization and lensing measurements [5], measurements of BAO [66–69] as well as data from Type Ia supernovae [70–73]. The abundances of light nuclei predicted from BBN [74,75] are also in excellent agreement with the ones observed (apart from a discrepancy in the Lithium abundance) [76,77].

Before closing this section, we shall at least provide a brief overview of the history of the universe[9]. A simple way to get a first, though rough, insight into the past of our universe is to extrapolate its expansion history back in time. According to the standard cosmological expansion (and without exceeding the scope of validity of GR[10]), the primordial universe consisted of a hot and dense bath of thermal radiation. From this primordial state the universe expanded and gradually cooled. The theory of BBN, states that the lightest nuclei are formed during the radiation dominated epoch at temperatures $T \sim$ 1-2 MeV. As we have seen in section 2.1, radiation is diluted faster than matter. Consequently the universe gradually becomes dominated by matter which eventually decouples from the radiation. The photons emitted at the time of decoupling ($\sim 10^5$ years after BBN) get redshifted and are today observed as the CMB. During the subsequent period of matter domination, the initially tiny primordial fluctuations ultimately lead to the formation of the LSS.

[8]The amplitude of the spectrum of fluctuations inferred from CMB measurements, for instance, is found to be higher than when estimated from weak gravitational lensing [5, 61, 62] as well as from some analyses of galaxy cluster counts [63–65].

[9]For a more complete discussion see e.g. section 3 in [24].

[10]GR is not expected to provide a viable description of gravity for energies close to and above the Planck scale. So far, however, there is no widely accepted fundamental theory of gravity that manages to describe the physics under such extreme conditions as they possibly were prevalent at very early times.

Chapter 3

Cosmological inflation

In this chapter we introduce the inflationary paradigm [78–80]. We begin our discussion by briefly outlining the physical motivation of inflation. In section 3.2 we discuss how inflation can be realised with a classical and homogeneous scalar field which dominates the energy of universe at very early times. We thereby focus on the simplest class of single-field slow-roll inflation models which comprise the scenarios studied in the main part of this thesis. In section 3.3 we discuss the formalism which explains how quantum fluctuations of the inflationary scalar field naturally generate the seed for the formation of cosmic structure. We further explain how models of inflation can be constrained by comparing the stochastic properties of the fluctuations predicted by the model to those deduced from CMB measurements. Finally, in section 3.4 we explicitly discuss some example models. For a more detailed discussion of inflation and the quantum theory of cosmological perturbations we refer the reader to [55, 81–83, 110].

3.1 Motivation: why inflation?

On closer inspection, it turns out that the standard cosmological model suffers from a couple of considerable shortcomings. Although the ΛCDM model provides a very good description of how the universe evolves, it does not provide a natural explanation for its origins, at least not without inflation.

In this section we outline the issues related to the standard cosmological scenario. Further, we explain how they can be resolved all at once by supplementing the model with an early period of accelerated expansion referred to as inflation.

Monopoles and other unwanted relics

Particle physics motivated models of the early universe often predict the existence of potentially dangerous relics that could spoil the standard cosmological picture. Models that are formulated within the context of Supergravity (SUGRA), for example, predict the existence of elementary particles such as the "gravitino" – the supersymmetric partner of the "graviton" (see e.g. [84]). Unstable gravitinos produced in the early universe can ruin the success of BBN if their decay happens after the formation of the light nuclei [85–87]. Another type of cosmological relics are topological defects

which can be produced during symmetry breaking phase transitions [88]. In fact, one of the motivations for inflation was related to the relic abundances of magnetic monopoles predicted by GUTs [89,90]. Typically, the latter are too high to be compatible with observational bounds [91,92]. Moreover, dynamical and relatively light scalar fields that are generically present in scenarios SUSY breaking, as well as in string theory, can also give rise to cosmological problems [15–17,93]. In scenarios of string compactification, for example, these so-called *moduli* fields basically describe the properties of compactified extra dimensions. Similarly to the gravitino they can spoil the successful completion of BBN [94–96], unless they decay sufficiently before its onset.

Horizon problem

In the absence of an inflationary period, the ΛCDM model does not provide a satisfactory and natural explanation for the smoothness of the CMB. The latter is observed across the entire sky suggesting that the universe has reached a state of thermal equilibrium by the time of decoupling i.e. when the CMB photons were emitted. At that time, however, the universe seemingly consisted of several causally disconnected regions. According to the standard cosmological expansion, these regions have never been in causal contact before, thus rendering it impossible to complete the process of thermalisation. A possible, though unsatisfactory explanation for the smoothness of the CMB would be that these causally disconnected patches somehow, inexplicably, shared the same initial conditions. This fine-tuning problem is known as the *horizon problem* [81].

Flatness problem

Another prominent fine-tuning issue is the so-called *flatness problem*. In section 2.2 we pointed out that the derivation of the cosmological parameters for the baseline ΛCDM model was performed under the assumption that the universe is perfectly flat. If this assumption is relaxed and $\Omega_{\rm tot}$ is treated as a free parameter, the resulting constraints are still consistent with unity. However, a small deviation from flatness $|\Omega_{\rm tot} - 1| \lesssim \mathcal{O}(10^{-2})$ cannot fully be excluded (cf. table 5 in [5]). Even such a tiny "beauty flaw" implies that for a matter or radiation dominated universe, the initial energy density must have been many orders of magnitude closer to the critical density than we observe today [83].

Inflationary solution

An early period of inflation that precedes the standard cosmological regime has the potential to resolve all these issues at once [78]. We note, however, that the problem regarding the production of unwanted relics is effectively model-dependent. In fact, in order to resolve this problem, inflation is required to take place after or, at the earliest, during the relic production mechanism. If this is not the case, a sufficient dilution of the relic density is not guaranteed.

The horizon problem, on the other hand, can smoothly be resolved, provided that inflation lasts long enough [78, 81]. Inflation simply bypasses the horizon problem

by allowing regions that were causally disconnected in the past, say at decoupling, to have been causally connected at very early times[1]. The observable universe could therefore easily have reached a state of thermal equilibrium already during inflation (or even before).

Due to the quasi exponential expansion experienced by the universe during inflation, the energy density is naturally driven close to the critical density. This can be easily understood as follows: the deviation from a perfectly flat universe can be expressed in terms of the density parameter as $|\Omega_{\text{tot}} - 1| = (a\,H)^{-2}$. Since the Hubble parameter is approximately constant during inflation and consequently $a \sim e^{Ht}$, $(a\,H)^{-2}$ is quickly driven towards zero.

The most remarkable aspect of the inflationary paradigm is that, once adopted, it provides a natural mechanism for producing the small inhomogeneities which ultimately led to the formation of structures in the universe. Therefore, inflation constitutes an ideal supplement to the standard cosmological picture and has nowadays become an integral part of modern cosmology.

3.2 Realising inflation with a single, slowly rolling scalar field

As mentioned earlier in this chapter, inflation is defined as a an early period of accelerated expansion. As can easily be shown from the Friedmann equations (2.11) and (2.12), requiring $\ddot{a} > 0$ implies

$$p < -\frac{\rho}{3} \quad \Leftrightarrow \quad w < -\frac{1}{3}\,. \tag{3.1}$$

This condition is automatically fulfilled if the universe is dominated by a cosmological constant. A cosmological constant is, however, rather unsuitable, since inflation would basically last forever. In fact, it is necessary to have a scenario in which inflation happens as an intermediate stage which ends dynamically.

The simplest way to realise inflation is through the dynamics of a single scalar field, henceforth referred to as the *inflaton*. Within this thesis we shall restrict ourselves to the simplest scenarios belonging to the class of so-called *single-field slow-roll (SFSR) inflation models*. The latter turn out to be very promising from the observational point of view [97].

If the universe is dominated by the potential energy of the inflaton, the condition 3.1 is fulfilled and the universe inflates. Eventually, the inflaton's potential energy is slowly converted into kinetic energy, the inflaton accelerates and inflation ends. Notice that after inflation, the energy density remains initially dominated by the inflaton. The subsequent process during which the energy carried by the inflaton is converted into a thermal bath of relativistic particles is called *reheating* and will be discussed in the next chapter.

[1]For an illustrative explanation see e.g. figure 7 in [83].

Let us now concentrate on the dynamics of single field models of inflation with minimal coupling to gravity in a flat FLRW universe

$$ds^2 = g_{\mu\nu}dx^\mu dx^\nu \;=\; -dt^2 + a^2(t)\delta_{ij}dx^i dx^j\,. \tag{3.2}$$

The dynamics of such a system are governed by the action

$$S \;=\; \int d^4x\sqrt{-g}\left(\frac{m_{\rm Pl}^2\,R}{2} + \mathcal{L}_\phi\right)\,, \tag{3.3}$$

where $g \equiv \det(g_{\mu\nu})$. The Lagrangian $\mathcal{L}_\phi$ of the canonically normalised inflaton ϕ with scalar potential $V(\phi)$ is

$$\mathcal{L}_\phi \;=\; -\frac{1}{2}\partial_\mu\phi\,\partial^\mu\phi - V(\phi)\,. \tag{3.4}$$

The relevant equations of motion can be derived from the principle of least action. By varying the action (3.3) with respect to $g_{\mu\nu}$ one obtains the EFEs with the energy-momentum tensor $T_{\mu\nu}$ that is given by the field-dependent part of the action (see e.g. [55, p. 221])

$$\begin{aligned} T_{\mu\nu} \;&=\; -\frac{2}{\sqrt{-g}}\,\frac{\delta(\sqrt{-g}\mathcal{L}_\phi)}{\delta g^{\mu\nu}} \\ &=\; -g_{\mu\nu}\left(\frac{1}{2}\,\partial^\alpha\phi\partial_\alpha\phi + V(\phi)\right) + \partial_\mu\phi\partial_\nu\phi\,. \end{aligned} \tag{3.5}$$

The inflaton is practically homogeneous during inflation and we may neglect the spatial derivatives in (3.5). Assuming $\phi(t,\mathbf{x}) = \phi(t)$, the only non-vanishing components of $T^\mu{}_\nu = g^{\mu\alpha}T_{\alpha\nu}$ are the ones on the diagonal

$$-T^0{}_0 \;=\; \frac{1}{2}\dot\phi^2 + V(\phi) \;\equiv\; \rho_\phi\,, \tag{3.6}$$

$$T^i{}_i \;=\; \frac{1}{2}\dot\phi^2 - V(\phi) \;\equiv\; p_\phi\,, \tag{3.7}$$

where we have identified the respective components with the inflaton's energy density ρ_ϕ and its pressure p_ϕ in accordance with eq. (2.7). Hence, for a universe that is dominated by a homogeneous scalar field, the evolution of the scale factor is dictated by the Friedmann equation (2.11)

$$H^2 \;=\; \frac{\rho_\phi}{3\,m_{\rm Pl}^2} \;=\; \frac{1}{3\,m_{\rm Pl}^2}\left[\frac{1}{2}\dot\phi^2 + V(\phi)\right]\,. \tag{3.8}$$

The equation of motion for the inflaton itself can be obtained by varying the action with respect to ϕ

$$\frac{\delta(\sqrt{-g}\mathcal{L}_\phi)}{\delta\phi} \;=\; \frac{1}{\sqrt{-g}}\,\partial_\mu(\sqrt{-g}\partial^\mu\phi) + \frac{\partial V}{\partial\phi} \;=\; 0\,. \tag{3.9}$$

For a homogeneous inflaton we can again neglect the spatial derivatives and the field equation of motion reduces to

$$\ddot\phi + 3H\dot\phi + \frac{\partial V}{\partial\phi} \;=\; 0\,. \tag{3.10}$$

Notice that eqs. (3.8) and (3.10) are sufficient to uniquely describe the dynamics during inflation. Furthermore, one can see that the expansion of the universe effectively induces a damping (or friction) term ($\propto H$) in the equation of motion of the field. Within this thesis we will sometimes use the term "Hubble friction" or "Hubble damping" to refer to the damping effect that is caused by the expansion.

It is not difficult to see from eqs. (3.6) and (3.7) that the condition (3.1) is indeed fulfilled, provided that the energy density is dominated by the potential energy of the inflaton. In fact, if $\dot{\phi}^2/2 \ll V(\phi)$ we have

$$\frac{p_\phi}{\rho_\phi} = \frac{\frac{1}{2}\dot{\phi}^2 - V(\phi)}{\frac{1}{2}\dot{\phi}^2 + V(\phi)} \simeq -1\,, \tag{3.11}$$

which is (approximately) the EOS of a cosmological constant. Consequently, the universe experiences quasi-exponential expansion at a rate $H \sim V^{1/2}$. This means that within a Hubble time $\Delta t = H^{-1}$, the universe expands by a factor $\Delta a = e^{H\Delta t} = e$ during inflation. It is therefore convenient to quantify the amount of inflationary expansion in terms of powers of e, or in other words, in terms of "e-folds". Formally, the number of e-folds of expansion between a time t_i and a time t_f is defined as

$$N \equiv \ln\left[\frac{a(t_\mathrm{f})}{a(t_\mathrm{i})}\right]. \tag{3.12}$$

As already mentioned, inflation has to last for a certain period of time, or equivalently, the universe has to expand by a certain factor in order to solve the flatness and horizon problems. In terms of e-folds, the minimum amount of expansion required to solve these issues is $N \sim 60$ [83].

3.2.1 Slow-roll approximation

As we have seen above, inflation occurs as long as the potential energy dominates over the kinetic energy

$$\dot{\phi}^2/2 \ll V(\phi)\,. \tag{3.13}$$

We may go one step further and assume that

$$|\ddot{\phi}| \ll 3H|\dot{\phi}|\,, \left|\frac{\partial V}{\partial \phi}\right|. \tag{3.14}$$

Requiring the second condition (3.14) basically means that $|\dot{\phi}|$ does not grow significantly on time scales of the order of H^{-1} [55], thus ensuring that (3.13) is not immediately violated.

The two conditions above can be formulated in terms of the Friedmann equation (3.8) and the field equation of motion (3.10) as follows [55]

$$3H^2 \simeq V(\phi) \quad \Leftrightarrow \quad \frac{|\dot{H}|}{H^2} \ll 1 \tag{3.15}$$

and

$$\dot{\phi} \simeq -\frac{1}{3H}\frac{\partial V}{\partial \phi}\,. \tag{3.16}$$

Eqs. (3.15) and (3.16) are referred to as the (first order) *slow-roll approximation* [98, 99].

The slow-roll approximation effectively implies that the scalar potential $V(\phi)$ must be sufficiently flat in order to allow for an inflationary period. Thus, one may reformulate the slow-roll approximation in terms of a set of dimensionless parameters which are exclusively defined in terms of the inflaton potential and its derivatives. From eqs. (3.15) and (3.16), for example, one can define the following quantity [98,99]

$$\varepsilon_V \equiv \frac{m_{\mathrm{Pl}}^2}{2}\frac{1}{V^2}\left(\frac{\partial V}{\partial \phi}\right)^2 . \tag{3.17}$$

Another parameter that follows from the slow-roll approximation is[2] [98, 99]

$$\eta_V \equiv \frac{m_{\mathrm{Pl}}^2}{V}\frac{\partial^2 V}{\partial \phi^2} . \tag{3.18}$$

The parameters ε_V and η_V are called *slow-roll parameters*. They are essentially a measure for the flatness of the scalar potential and are therefore sometimes referred to as *flatness* or *potential slow-roll parameters* [55, 98]. In terms of ε_V and η_V, the necessary conditions for inflation to occur can be formulated as

$$\varepsilon_V \ll 1 , \quad \text{and} \quad |\eta_V| \ll 1 . \tag{3.19}$$

In principle, an infinite series of hierarchal parameters can be defined in similar way than ε_V and η_V. This allows, for instance, to express the right-hand side of eq. (3.8) solely as a function of the inflaton ϕ [99]. For the purpose of this thesis, however, the first-order slow-roll parameters ε_V and η_V will be perfectly adequate.

We note that the conditions (3.19) are necessary but not sufficient for eqs. (3.15) and (3.16) to be satisfied [99]. In order to uniquely determine the field trajectory, one has to specify an initial field value and an initial field velocity. If $\dot{\phi}$ is initially large, it could violate eq. (3.16) while not being in conflict with the slow-roll conditions (3.19). On the other hand, if the initial field value lies in a sufficiently flat region and the initial field velocity is not too large, the field trajectory will tend to quickly approach the so-called attractor solution described by (3.16) [55].

From the slow-roll conditions (3.19) we can define the end of inflation as the moment at which either ε_V or η_V becomes of order unity[3]. Depending on which of the two conditions is violated first, we can calculate the inflaton field value at the end of inflation ϕ_{end} by solving either for

$$\varepsilon_V(\phi_{\mathrm{end}}) = 1 \quad \text{or} \quad \eta_V(\phi_{\mathrm{end}}) = 1 . \tag{3.20}$$

At this point it is worth mentioning that the slow-roll approximation can be used to determine the number of e-folds of inflation between a time t_{inf} during inflation

[2] In addition to (3.15) and (3.16), the derivation of η_V assumes that eq. (3.16) holds after differentiating it with respect to time.

[3] The violation of the slow-roll conditions does, strictly speaking, not necessarily coincide with the end of inflation but rather indicates the breakdown of the slow-roll approximation. In fact, the universe may still inflate for $N \lesssim \mathcal{O}(1)$ e-fold.

and the end of inflation $t_{\rm end}$. We can rewrite our previous definition of N (cf. eq. (3.12)) as follows

$$N(\phi_\star) \equiv N_\star = \ln \frac{a(t_{\rm end})}{a(t_\star)} = \int_{t_\star}^{t_{\rm end}} dt\, H = \int_{\phi_\star}^{\phi_{\rm end}} d\phi\, \frac{H}{\dot{\phi}}\,. \tag{3.21}$$

Using the slow-roll approximation eqs. (3.15) and (3.16) we can express the right-hand side of the last equality in (3.21) as

$$N_\star \simeq \frac{1}{m_{\rm Pl}^2} \int_{\phi_{\rm end}}^{\phi_\star} d\phi\, \frac{V}{\partial V/\partial \phi}\,. \tag{3.22}$$

The reason we have introduced the slow-roll expression for $N_\star$ eq. (3.22) will become clear towards the end of this chapter. The main idea, however, is the following: the primordial perturbations on scales that are today accessible in CMB measurements were produced $N_\star \sim 60$ e-folds before the end of inflation. Their statistical properties can, in turn, be related to the shape of the inflaton potential around the inflaton field value $\phi_\star$ at the time of their production.

3.3 Quantum fluctuations in the inflationary universe

Within the context of Starobinsky's model [100] it was first[4] shown in 1981 by V. Mukhanov and G. Chibisov [102] that quantum fluctuations, generated during a stage of de Sitter expansion, could provide the seed for the formation of cosmic structures. The mechanism for generating the primordial inhomogeneities via initially small quantum fluctuations became quickly popular and was applied to other models of inflation [103–106]. This mechanism was further developed in [107, 108] (see [109] for a review) and is nowadays well-established within the community.

In this section we provide an overview of how quantum vacuum fluctuations of the inflaton can ultimately explain the presence of inhomogeneities observed in the CMB and the LSS. We begin our discussion by considering the simplified case of a generic, massless scalar field in a pure de Sitter background and explain how the obtained results can be generalised to the case of a curved potential.

Quantum fluctuations of the field are introduced as quantised perturbations about a classical, homogeneous background. We adopt the most common prescription for defining the vacuum state in an expanding de Sitter background and calculate the power spectrum of quantum vacuum fluctuations produced during inflation.

We then proceed by introducing a gauge-invariant quantity called the *comoving curvature perturbation*. The latter is defined in terms of the inflaton fluctuations and its primordial spectrum can be directly constrained by cosmological measurements of the CMB fluctuations and LSS. Furthermore, we explain how this allows us to

[4]We note that the possibility that quantum fluctuations could give rise to primordial inhomogeneities was already considered in 1965 by A. Sakharov in [101], however not within the context of inflation.

constrain models of inflation with observational data. Finally, we briefly discuss the production of primordial gravitational waves during inflation and introduce the primordial spectrum of tensor perturbations.

The following discussion is based on a series of pedagogical introductions into the quantum theory of cosmological perturbations [55, 82, 83, 110, 111], to which we refer for a more extensive overview.

3.3.1 Quantum fluctuations of a massless scalar field in de Sitter spacetime

During inflation, the inflaton is generally very light and the universe expands almost exponentially. In this section we derive an expression for the power spectrum of quantum fluctuations by considering the simplified case of a (generic) massless scalar field in an expanding de Sitter spacetime. On the basis of logical considerations we will use the corresponding result in section 3.3.2 to derive a more general expression for the primordial spectrum of curvature perturbations originating from inflation.

If we give up the assumption of perfect homogeneity, eq. (3.10) is no longer adequate to properly describe the dynamics of the inflaton. Instead, one we may consider the full equation of motion (3.9) which becomes

$$\ddot{\phi} + 3H\dot{\phi} - \frac{\nabla^2}{a^2}\phi + \frac{\partial V}{\partial \phi} = 0\,, \tag{3.23}$$

where $\phi = \phi(t, \mathbf{x})$ is now a function of spacetime and the spatial derivatives are taken with respect to comoving coordinates $\mathbf{x}$.

Assuming that the universe has been smoothed out during inflation, we may expand the field into a homogeneous component $\overline{\phi}$ plus small perturbations $\delta\phi(t, \mathbf{x})$

$$\phi(t, \mathbf{x}) \;=\; \overline{\phi}(t) + \delta\phi(t, \mathbf{x})\,. \tag{3.24}$$

As long as the fluctuations are small compared to the homogeneous background motion, the evolution of the fluctuations can be followed by solving the linearised equations. Plugging eq. (3.24) into eq. (3.23) and expanding to linear order in $\delta\phi$ one obtains

$$\delta\ddot{\phi}(t, \mathbf{x}) + 3H\delta\dot{\phi}(t, \mathbf{x}) + \left(\frac{\partial^2 V(\overline{\phi})}{\partial \overline{\phi}^2} - \frac{\nabla^2}{a^2}\right)\delta\phi(t, \mathbf{x}) \;=\; 0\,, \tag{3.25}$$

with the dynamics of $\overline{\phi}$ being described by eq. (3.10). If we further expand the perturbation $\delta\phi(t, \mathbf{x})$ into Fourier modes $\delta\phi_{\mathbf{k}}(t)$ as

$$\delta\phi(t, \mathbf{x}) \;=\; \int \frac{d^3\mathbf{k}}{(2\pi)^3}\, \delta\phi_{\mathbf{k}}(t)\, e^{i\,\mathbf{k}\cdot\mathbf{x}}\,, \tag{3.26}$$

we obtain the following equation for the Fourier modes

$$\delta\ddot{\phi}_{\mathbf{k}}(t) + 3H\delta\dot{\phi}_{\mathbf{k}}(t) + \left(\frac{k^2}{a^2} + \frac{\partial^2 V(\overline{\phi})}{\partial \overline{\phi}^2}\right)\delta\phi_{\mathbf{k}}(t) \;=\; 0\,, \tag{3.27}$$

where $k \equiv |\mathbf{k}|$ denotes the magnitude of a comoving wavenumber. By assuming that during inflation $H^2 \gg \partial^2 V/\partial\phi^2$ (or equivalently $\eta_V \ll 1$) we can drop the second derivative of the potential in (3.27) and we are left with

$$\delta\ddot{\phi}_{\mathbf{k}}(t) + 3H\delta\dot{\phi}_{\mathbf{k}}(t) + \frac{k^2}{a^2}\delta\phi_{\mathbf{k}}(t) \;=\; 0\,. \tag{3.28}$$

At this point it is convenient to switch to conformal time $d\eta = a^{-1}dt$. Furthermore, we define a new variable

$$v_{\mathbf{k}} \;\equiv\; a\,\delta\phi_{\mathbf{k}}\,. \tag{3.29}$$

In terms of conformal time eq. (3.28) can be translated into the following equation for $v_{\mathbf{k}}$:

$$v''_{\mathbf{k}}(\eta) + \left(k^2 - \frac{a''}{a}\right) v_{\mathbf{k}}(\eta) \;=\; 0\,. \tag{3.30}$$

Assuming exponential expansion, as it is approximately the case during inflation, we have $a''/a \;=\; 2\,(aH)^2 \;=\; 2/\eta^2$, and therefore

$$v''_{\mathbf{k}}(\eta) + \left(k^2 - \frac{2}{\eta^2}\right) v_{\mathbf{k}}(\eta) \;=\; 0\,. \tag{3.31}$$

The general solution to the above equation can be written as [111]

$$v_{\mathbf{k}}(\eta) \;=\; \alpha\,\frac{e^{-i\,k\eta}}{\sqrt{2k}}\left(1 - \frac{i}{k\eta}\right) + \beta\,\frac{e^{i\,k\eta}}{\sqrt{2k}}\left(1 + \frac{i}{k\eta}\right)\,. \tag{3.32}$$

Effectively, eq. (3.31) tells us that for each wavenumber k the modes will behave like a harmonic oscillator with a time-dependent frequency

$$\omega_k^2(\eta) \;=\; k^2 - \frac{2}{\eta^2}\,. \tag{3.33}$$

Let us now proceed with the canonical quantisation of the physical system in the Heisenberg picture. To this end we promote the Fourier modes to quantum operators

$$v_{\mathbf{k}}(\eta) \;\to\; \hat{v}_{\mathbf{k}}(\eta) \;=\; v_k(\eta)\,\hat{a}_{\mathbf{k}} + v_k^*(\eta)\,\hat{a}^\dagger_{-\mathbf{k}}\,, \tag{3.34}$$

with the creation and annihilation operators $\hat{a}^\dagger_{\mathbf{k}}$ and $\hat{a}_{\mathbf{k}}$ satisfying the commutation relations [111]

$$[\hat{a}_{\mathbf{k}}, \hat{a}^\dagger_{\mathbf{q}}] \;=\; \delta^{(3)}(\mathbf{k} - \mathbf{q})\,, \quad [\hat{a}^\dagger_{\mathbf{k}}, \hat{a}^\dagger_{\mathbf{q}}] \;=\; [\hat{a}_{\mathbf{k}}, \hat{a}_{\mathbf{q}}] \;=\; 0. \tag{3.35}$$

The mode functions $v_{\rm k}(\eta)$ obey the equation of motion (3.31) and satisfy the following normalisation relation

$$v^*_{\rm k}\,v'_{\rm k} - (v^*_{\rm k})'v_{\rm k} \;=\; -i\,. \tag{3.36}$$

The relation (3.36) is required in order to be consistent with the equal time commutation relations imposed on $\hat{v}(\eta, \mathbf{x})$ and its conjugate momentum in the Heisenberg picture. Given the general solution (3.41), eq. (3.36) can be rewritten as follows

$$|\alpha|^2 - |\beta|^2 \,=\, 1\,. \tag{3.37}$$

In order to define physical quantum states and in particular the vacuum state

$$\hat{a}_{\mathbf{k}}|0\rangle = 0\,, \tag{3.38}$$

we have to specify the mode functions $v_k(\eta)$. In the case of flat Minkowski spacetime (corresponding to $2/\eta^2 = 0$ in (3.31)), the vacuum state is defined as the lowest-energy state with the solutions

$$v_k(\eta) \,=\, \frac{e^{-ik\eta}}{\sqrt{2k}}\,, \tag{3.39}$$

being uniquely determined. If spacetime is curved, however, this is in general not the case (see e.g. [112,113]). In fact, one may define a different set of mode functions

$$u_k(\eta) \,=\, \alpha_k v_k(\eta) + \beta_k v_k^*(\eta)\,, \quad \text{with} \quad |\alpha_k|^2 - |\beta_k|^2 \,=\, 1\,, \tag{3.40}$$

with α_k and β_k being generally complex valued and time-independent. Just as the v_k, the new mode functions u_k satisfy eqs. (3.31) and (3.36). Yet they are associated with a different set of creation and annihilation operators and therefore represent a different vacuum state[5].

For the case of de Sitter expansion, this ambiguity is typically eliminated by assuming that at very early times ($\eta \to -\infty$) all the cosmologically relevant scales were well inside the Hubble horizon, i.e. $k|\eta| \ll 1$. In this limit, the modes do not feel the expansion and it is then natural to require that the Minkowski vacuum solution eq. (3.39) is recovered. For the general solution (3.41) this implies $\alpha = 1$ and $\beta = 0$ which gives

$$v_k(\eta) \,=\, \frac{e^{-i\,k\eta}}{\sqrt{2k}}\left(1 - \frac{i}{k\eta}\right)\,. \tag{3.41}$$

This solution is commonly referred to as the *Bunch-Davies vacuum solution* [114]. In terms of the mode function of the fluctuations $\delta\phi_{\mathbf{k}} = a^{-1}v_{\mathbf{k}}$ the solution (3.41) in terms of cosmic time t reads

$$\delta\phi_k(t) \,=\, \frac{e^{i\,k/(aH)}H}{\sqrt{2k^3}}\left(i + \frac{k}{aH}\right)\,. \tag{3.42}$$

We have seen that in the sub-horizon limit ($k \gg aH$) the mode functions approach the Minkowski vacuum solution (3.39). Given the general de Sitter space solution (3.41), it is also worth considering the super-horizon limit $k \ll aH$ (or equivalently $k\eta \to 0$), where we have

$$v_k(\eta) \,\simeq\, -\frac{i}{\sqrt{2k^3}\,\eta} \,=\, \frac{i\,aH}{\sqrt{2k^3}} \,\propto\, a\,. \tag{3.43}$$

[5]For further details on the vacuum state ambiguity in curved spacetimes see e.g. [112, 113].

Interestingly, this means that on super-horizon scales, the perturbation $\delta\phi_{\mathbf{k}} = a^{-1}v_{\mathbf{k}}$ is constant or "frozen". Moreover, it turns out that the fluctuations can be regarded as classical fluctuations once they exit the Hubble horizon[6] [104].

In order to characterise the statistical properties of the fluctuations we introduce the *power spectrum* $\mathcal{P}_{\delta\phi}(k)$ of the scalar field fluctuations $\delta\phi_{\mathbf{k}}$. It is defined via the two-point correlation function in Fourier space as[7] [55]

$$\langle \delta\phi^2(\eta, \mathbf{x}) \rangle \;=\; \int d\ln k \; \mathcal{P}_{\delta\phi}(k)\,, \tag{3.44}$$

where the power spectrum is given by

$$\mathcal{P}_{\delta\phi}(k) \;=\; \frac{k^3}{2\pi^2} |\delta\phi_{\mathbf{k}}|^2\,. \tag{3.45}$$

Let us finally make a few remarks on what we have discussed so far in this section. For the derivation of eq. (3.31) (and thus for the derivation of the power spectrum) we have neglected the effective mass squared as well as the time dependence of the Hubble parameter. An exact result to the mode equation can be found if a small constant mass $\partial^2 V/\partial\phi^2 = m_\phi^2$ is included. The resulting spectrum then essentially exhibits a small time dependency. The situation is similar when a slowly varying Hubble parameter is considered [110].

Another effect that we have not taken into account is that of the metric perturbation. When perturbing the metric to first order in perturbation theory, the kinetic term in eq. (3.9) gives rise to an additional contribution which can typically be neglected if the homogeneous inflaton component rolls sufficiently slow[8].

3.3.2 Primordial spectrum of comoving curvature perturbations

In this part of the section we want to introduce a new quantity refferred to as the *comoving curvature perturbation* $\mathcal{R}$. It allows to test models of inflation by comparing their predictions for the power spectrum of $\mathcal{R}$ to observational data obtained from CMB and the LSS measurements.

As indicated by its name, $\mathcal{R}$ is related to the perturbations of the spatial curvature. To be more precise, it measures the spatial curvature on comoving hypersurfaces [55, 110], i.e. it includes effects induced by gravity. These effects have to be included in order to properly follow the evolution of the fluctuations for the following reason: during inflation the energy density is dominated by the potential energy of the inflaton field. According to the EFEs, small fluctuations of the field will inevitably give rise to fluctuations of the metric which, in turn, can backreact on

[6] For a pedagogical and comprehensive explanation see [55, p. 386].

[7] We note that when dealing with quantum fluctuations $\langle \ldots \rangle$ essentially refers to the vacuum expectation value (i.e. $\langle \ldots \rangle \to \langle 0| \ldots |0\rangle$), with the $\delta\phi(\eta, \mathbf{x})$ being quantum operators, i.e. $\delta\phi^2(\eta, \mathbf{x}) \to \delta\hat{\phi}^2(\eta, \mathbf{x})$. On the other hand, for classical fluctuations it simply denotes an ensemble average.

[8] See e.g. [55, pp. 389 f.]

the inflaton itself via the field equation of motion. Consequently, it is not sufficient to only perturb the inflaton. For the purpose of this thesis it shall be sufficient to know that after including the effects of GR up to linear order in cosmological perturbation theory[9] [117–120], one can express the *comoving curvature perturbation during inflation* as follows [110]

$$\mathcal{R} \;=\; \psi + H\frac{\delta\phi}{\dot{\phi}}\,. \tag{3.46}$$

The scalar quantity ψ belongs to the perturbations of the metric and is typically referred to as the curvature perturbation. To first order in perturbation theory, $\mathcal{R}$ is gauge-invariant by construction and its spectrum constitutes an observable quantity. Notice that this is not the case for e.g. the perturbations of the inflaton or the curvature perturbation ψ which both depend on the choice of coordinates [110].

If the perturbations are adiabatic[10] (i.e. purely curvature), which is generally the case in SFSR models of inflation [110], $\mathcal{R}$ has the remarkable property to be conserved on super-horizon scales[11] $k \ll aH$. In essence, this means that the amplitude of any given mode that exits the horizon during inflation, will "freeze" until it reenters. In particular, this implies that those modes which eventually evolve into the CMB fluctuations and the LSS, will "unfreeze" at a much later stage when their sub-horizon evolution is captured by standard cosmology. This is crucial since it means that these fluctuations are insensitive to the unknown physics during reheating right after inflation.

Let us finally introduce the primordial spectrum of the curvature perturbations. During inflation and in the spatially flat gauge ($\psi = 0$), $\mathcal{R}$ can be directly expressed in terms of the inflaton fluctuations $\delta\phi$

$$\mathcal{R}|_{\psi=0} \;=\; H\frac{\delta\phi}{\dot{\phi}}\,. \tag{3.47}$$

The primordial spectrum of $\mathcal{R}$ is defined in the same way as the inflaton power spectrum, i.e. via its two-point correlation function. In accordance with (3.47), we may directly express it in terms of the inflaton power spectrum as follows

$$\mathcal{P}_{\mathcal{R}}(k) \;=\; \left(\frac{H^2}{\dot{\phi}^2}\right)\mathcal{P}_{\delta\phi}(k)\,. \tag{3.48}$$

Using eqs. (3.43) and (3.59) we can easily compute the primordial spectrum of curvature perturbations at horizon exit

$$\mathcal{P}_{\mathcal{R}}(k) \;=\; \left(\frac{H^2}{2\pi\dot{\phi}}\right)^2\Bigg|_{k=aH} \;\equiv\; A_{\rm s}\left(\frac{k}{k_\star}\right)^{n_{\rm s}-1}\,, \tag{3.49}$$

where the subscript denotes that the quantities on the right-hand side of (3.49) are to be evaluated at $k = aH$. In the last definition of (3.49) we have introduced

[9] For pedagogical introductions we refer to the following lecture notes and textbooks [56,115,116].

[10] Perturbations are said to be adiabatic if they satisfy $\delta\rho/\dot{\rho} = \delta p/\dot{p}$ [110], where $\delta\rho$ and δp are the perturbations of the energy density and the pressure, respectively.

[11] For a proof see e.g. [110, pp. 65 f.].

the power-law parametrisation which is commonly assumed to model the primordial spectrum. The *scalar amplitude* A_s denotes the amplitude of the spectrum at the pivot scale $k = k_\star$ and the *scalar spectral index* n_s is used to parametrise the deviation from scale-invariance.

In section 2.2 we briefly mentioned that the power spectrum contains the entire statistical information, if the fluctuations are Gaussian. This is, in fact, consistent with the predictions of SFSR inflation [121,122]. On the other hand, in models where inflation is driven by more than one field, the dynamics may give rise to a significant amount of non-Gaussianities which, if observed, would rule out single-field inflation models [110].

Using the slow-roll approximations (3.15) and (3.16) we can express the spectrum in terms of the inflaton potential

$$\mathcal{P}_\mathcal{R}(k) \simeq \left.\frac{V}{24\pi^2\,\varepsilon_V\,m_\mathrm{Pl}^4}\right|_{k=aH} . \tag{3.50}$$

For a massless scalar field in pure de Sitter spacetime ($\dot{H} = 0$) the spectrum is perfectly scale-invariant (i.e. its amplitude does not depend on any given super-horizon scale $k \geq aH$). During inflation, however, H only approximately constant. This implies that different modes $k = aH$, which exit the horizon at slightly different times, exhibit a slightly different amplitude.

In accordance with the parametrisation of the spectrum introduced in eq. (3.49), we can express A_s and $n_\mathrm{s}(k_\star) \equiv n_\mathrm{s}$ in terms of the slow-roll [123, 124] parameters as follows (see e.g. [83, 111])

$$A_\mathrm{s} \equiv \mathcal{P}_\mathcal{R}(k)|_{k=k_\star} \simeq \frac{V_\star}{24\pi^2\,\varepsilon_{V_\star}\,m_\mathrm{Pl}^4} , \tag{3.51}$$

$$n_\mathrm{s} - 1 \equiv \left.\frac{d\ln\mathcal{P}_\mathcal{R}(k)}{d\ln k}\right|_{k=k_\star} \simeq 2\eta_{V_\star} - 6\varepsilon_{V_\star} . \tag{3.52}$$

Here the subscript $\star$ denotes that the corresponding quantity is to be evaluated when the pivot scale $k_\star$ exits the horizon. Hence, by evaluating the right-hand side of (3.52) $N_\star \approx 60$ e-folds before the end of inflation, we can directly test a given model of SFSR inflation by comparing the predicted value of n_s with the one observed. On the other hand, the observed value of A_s is often used to set the overall normalisation of the potential, i.e. to fix the value of $V_\star$.

We note that, one may introduce additional parameters to describe e.g. the scale-dependence of the spectral index by expanding n_s as a power series in $\ln\left(\frac{k}{k_\star}\right)$

$$n_\mathrm{s}(k) \equiv n_\mathrm{s}(k_\star) + \sum_j \frac{\alpha_{s,j}}{j!}\left[\ln\left(\frac{k}{k_\star}\right)\right]^j . \tag{3.53}$$

The coefficients which we here defined as $\alpha_{s,j}$ are then referred to as *runnings of the spectral index*. Similar to n_s, they can be expressed in terms of higher-order slow-roll parameters [123, 124].

3.3.3 Gravitational waves during inflation

Beside predicting the existence of nearly scale-invariant Gaussian and adiabatic density perturbations, SFSR inflation predicts a stochastic background of *primordial GWs*. The latter are effectively produced in the same way as the inflaton fluctuations, but are rather associated to quantum vacuum fluctuations of the metric degrees of freedom. To be more precise, they are associated with the gauge-invariant *tensor perturbation* ($\equiv h_{ij}$) which can be described by [110]

$$ds^2 \;=\; a^2(\eta)\left[-d\eta^2 + \{\delta_{ij} + h_{ij}(\eta,\mathbf{x})\}dx^i dx^j\right] . \tag{3.54}$$

Up to linear order in perturbation theory, the action that governs the dynamics of the tensor perturbation can be derived by perturbing the Einstein-Hilbert action[12] to second order in h_{ij} [110]

$$S_h^{(2)} \;=\; \frac{m_{\rm Pl}^2}{8}\int d\eta\, d^3x\, a^2(\eta)\left[(h'_{ij})^2 - (\nabla h_{ij})^2\right] . \tag{3.55}$$

Notice that for each degree of freedom this is precisely the action of a massless scalar field in a flat FLRW universe (apart from a factor of 1/4), implying that the derivation of the power spectrum can essentially be carried in the same way.

The tensor perturbations satisfy the transversality ($\partial^i h_{ij} \;=\; 0$, for $i = 1,2,3$), and traceless ($h_i^i \;=\; 0$) conditions. Consequently, there are only $6-4=2$ physical degrees of freedom left, corresponding to the polarization states [27]

$$h_{ij}(\eta,\mathbf{x}) \;=\; \sum_{\lambda=+,\times} h^{(\lambda)}(\eta)\,\epsilon_{ij}^{(\lambda)}(\mathbf{x}) , \tag{3.56}$$

where $\epsilon_{ij}(\mathbf{x},\lambda)$ satisfies the transversality and traceless conditions and is called the polarization tensor, and $\lambda = +,\times$ denotes the polarization state.

The Euler-Lagrange equation describing the evolution of h_{ij} can be derived from the second order action (3.55). In terms of the rescaled (and canonically normalised) tensor field

$$v_{ij}(\eta,\mathbf{x}) \;\equiv\; \frac{m_{\rm Pl}\,a(\eta)}{2}h_{ij}(\eta,\mathbf{x}) \;=\; \frac{1}{2}\sum_{\lambda=+,\times}\int \frac{d^3\mathbf{k}}{(2\pi)^3}\, v_{\mathbf{k}}^{(\lambda)}(\eta)\epsilon_{ij}^{(\lambda)}(\mathbf{k})\, e^{i\,\mathbf{k}\cdot\mathbf{x}} . \tag{3.57}$$

one obtains the following equation of motion for the Fourier modes [110]

$$v_{\mathbf{k}}^{(\lambda)''}(\eta) + \left(k^2 + \frac{a''}{a}\right) v_{\mathbf{k}}^{(\lambda)}(\eta) \;=\; 0 . \tag{3.58}$$

Indeed, the modes $v_{\mathbf{k}}^{(\lambda)}$ satisfy exactly the same equation of motion as a massless scalar field eq. (3.30), with the only difference that we have to account for the two different polarization states. The quantisation of the tensor modes can therefore be reduced to that of a massless scalar field [109] and we may use the results obtained in section 3.3.1 to deduce the primordial spectrum of GWs.

[12] Corresponding to the field-independent part in (3.3).

By making use of eqs. (3.43) and (3.59) we can infer the power spectrum at horizon exit in a pure de Sitter spacetime to be

$$\begin{aligned}\mathcal{P}_h(k) &= \sum_{\lambda=+,\times} \frac{k^3}{2\pi^2}|h_{\mathbf{k}}^{(\lambda)}|^2 = \frac{k^3}{2\pi^2}\left|\frac{2\,v_{\mathbf{k}}^{(\lambda)}}{a\,m_{\rm Pl}}\right|^2 \\ &= \frac{8}{m_{\rm Pl}^2}\left(\frac{H}{2\,\pi^2}\right)^2 \equiv A_{\rm t}\left(\frac{k}{k_\star}\right)^{n_{\rm t}}, \end{aligned} \tag{3.59}$$

where in the last definition we have introduced the common power-law parametrisation of the primordial tensor spectrum. The parameters $A_{\rm t}$ and $n_{\rm t}$ are referred to as the *amplitude of primordial tensor perturbations* and the *tensor spectral index*, respectively.

Again, we can make use of the slow-roll approximation to express the amplitude $A_{\rm t}$ and the spectral tilt $n_{\rm t}$ in terms of the potential [83, 111]

$$A_{\rm t} \equiv \mathcal{P}_h(k_\star) \simeq \frac{2\,V_\star}{3\,\pi^2\,m_{\rm Pl}^4}, \tag{3.60}$$

$$n_{\rm t} \equiv \left.\frac{d\ln\mathcal{P}_h(k)}{d\ln k}\right|_{k=k_\star} \simeq -2\,\varepsilon_{V_\star}. \tag{3.61}$$

where a subscript $\star$ denotes the corresponding quantity to be evaluated at $k = k_\star$.

For SFSR inflation models, the number of independent parameters that is used to model the power spectra of both, primordial curvature perturbations and tensor perturbations, can be reduced by one parameter due to the following consistency-relation

$$r \equiv \frac{A_{\rm t}}{A_{\rm s}} = 16\,\varepsilon_{V_\star} = -8\,n_{\rm t}. \tag{3.62}$$

The parameter r is called the *tensor-to-scalar ratio* and it is directly related to the energy scale during inflation via

$$V_\star^{1/4} = \left(r\,A_{\rm s}\,\frac{3}{2}\,\pi^2\,m_{\rm Pl}^4\right)^{1/4}. \tag{3.63}$$

Furthermore, it can be related to the field-distance travelled by the inflaton during the last e-folds of inflation. In fact, by assuming that ε_V remains constant during inflation, we can use the slow-roll expression for the number of e-folds eq. (3.22) to derive

$$N_{\Delta\phi} \simeq \frac{\Delta\phi}{\sqrt{2\,\varepsilon_V}} = \frac{\Delta\phi}{\sqrt{r/8}}, \tag{3.64}$$

where $N_{\Delta\phi}$ denotes the number of e-folds of expansion experienced by the universe during a distance $\Delta\phi$ travelled by the inflaton. In general, ε_V is rather expected to grow monotonously during inflation (although not much). Therefore, eq. (3.64) may more realistically be formulated as [125]

$$N_{\Delta\phi} \lesssim \frac{1}{m_{\rm Pl}}\frac{\Delta\phi}{\sqrt{r/8}}, \quad \text{or} \quad \frac{\Delta\phi}{m_{\rm Pl}} \gtrsim N_{\Delta\phi}\sqrt{r/8}. \tag{3.65}$$

The current upper limit on the value of r is provided by the *Keck Array and BICEP2 Collaborations* and is [126]

$$r \,<\, 0.09 \quad (95\,\%\,\mathrm{CL})\,. \tag{3.66}$$

According to eq. (3.63) this can be translated into an upper limit on the energy scale of inflation

$$V_\star^{1/4} \lesssim \mathcal{O}(10^{-2})\, m_{\mathrm{Pl}}\,, \tag{3.67}$$

where we have used $A_\mathrm{s} = 2.2 \times 10^{-9}$ which is consistent with the value in table 2.1.

We note that even if one allows for a non-trivial evolution of ε_V after CMB scales exit the horizon, the Lyth bound (3.65) cannot be evaded (or significantly weakened) for SFSR inflation models [127]. This implies that a tensor-to-scalar ratio which is not too far from the current upper limit (3.66) would strongly disfavor small-field models of SFSR inflation, in which $\Delta\phi \ll m_{\mathrm{Pl}}$.

3.4 Example models of inflation

Since 1981, when inflation was introduced, a large number inflationary models have been proposed[13]. Amongst these, the most promising models seem to be those of SFSR type with a concave potential [97].

Typically, SFSR models of inflation are classified according to the variation of the inflaton $\Delta\phi$, during the last $N_\star \sim 60$ e-folds of inflation. In general, one distinguishes between large-field ($\Delta\phi \gg m_{\mathrm{Pl}}$), medium-field ($\Delta\phi \sim m_{\mathrm{Pl}}$), and small-field models ($\Delta\phi \ll m_{\mathrm{Pl}}$) [128].

To gain a better understanding of how inflation can be realised in practice, we want to consider two explicit example models. One will be a classical example of chaotic inflation [131]. It is characterised by a convex potential and belongs to the class of large-field models. The second model that we want to consider is a small-field hilltop inflation model [79, 132–135]. The corresponding potential is symmetric and very flat around the origin where it features a local maximum and has a non-zero Vacuum Expectation Value (VEV). These kind of models are also referred to as "new inflation models" [79, 80].

3.4.1 Large-field chaotic vs. small-field hilltop

Large-field chaotic inflation with monomial potential

We begin our discussion by considering a model of chaotic inflation with a potential given by a simple monomial

$$V(\phi) \,=\, \lambda\, \phi^p\,, \tag{3.68}$$

where we assume $p \geq 1$, and the coupling λ has dimensions of m_{Pl}^{4-p}. For the case of a quadratic potential, the schematic form of the potential (3.68) is depicted in figure 3.1.

[13] For some reviews see e.g. [128–130]

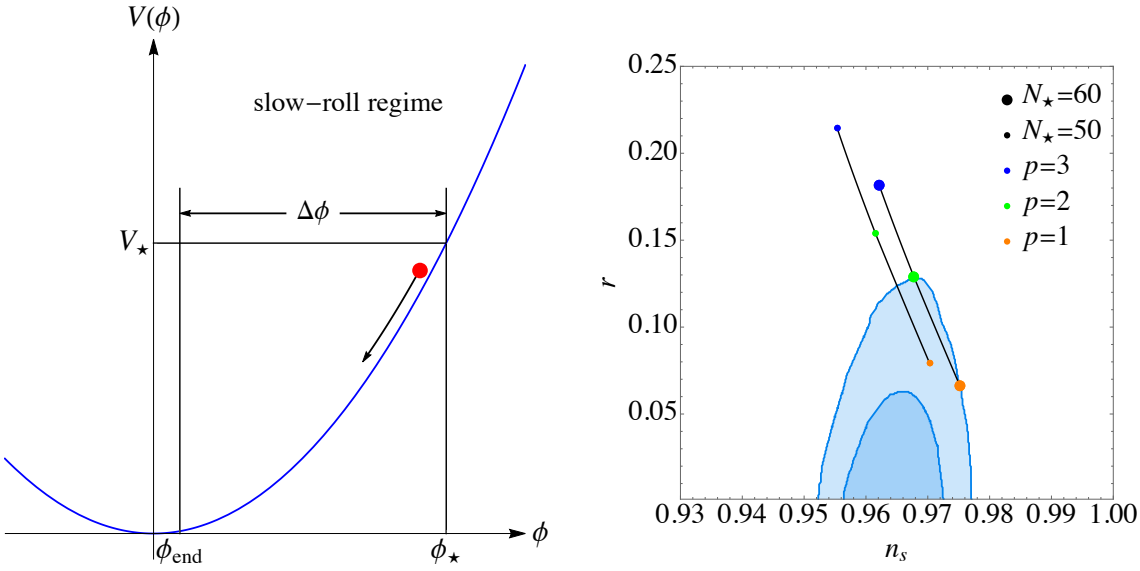

Figure 3.1: *Left:* Schematic form of the chaotic inflation potential. The plot is shown for a quadratic potential $V \sim \phi^2$. Inflation occurs for $|\phi| > |\phi_{\rm end}|$ while the inflaton slowly rolls down its potential towards the minimum $\phi = 0$. In these scenarios, the field distance travelled by the inflaton during the last $N_\star \sim 60$ e-folds of inflation is found to be $\Delta\phi \gtrsim 10 m_{\rm Pl}$.
Right: Predictions for the primordial spectra for the model $V(\phi) = \lambda\phi^p$. The predictions are presented for $N_\star = 60$ (large dots) and $N_\star = 50$ (small dots) and for three different values of p: $p = 1$ (orange dots), $p = 2$ (green dots) and $p = 3$ (blue dots). The solid black lines correspond to continuous values $1 \leq p \leq 3$. The predictions are compared to the 68% and 95% CL regions for $n_{\rm s}$ and r (cf. figure 12 in [97] for further details). Notice that these bounds clearly exclude the model for $p = 3$, and highly disfavour $p = 2$ at 95% CL.

Using the expressions (3.17) and (3.18), we can easily calculate the slow-roll parameters for the potential (3.68)

$$\varepsilon_V = m_{\rm Pl}^2 \frac{p^2}{2\phi^2}\,, \tag{3.69}$$

$$\eta_V = m_{\rm Pl}^2 \frac{p\,(p-1)}{\phi^2}\,. \tag{3.70}$$

Notice that the slow-roll parameters do not depend of the coupling λ. This implies that the inflaton field value at the end of inflation is independent of λ and consequently the inflaton field value $\phi_\star$ at horizon exit. The latter can be deduced from (3.22) and depends therefore only on $N_\star$ and $\phi_{\rm end}$. Furthermore, this implies that the predictions for the spectral index $n_{\rm s}$ and the tensor-to-scalar ratio r are independent of λ. In essence, the value λ is chosen to be consistent with the observational bounds on the scalar amplitude $A_{\rm s}$.

As discussed in section 3.2.1, inflation ends as soon as one of the slow-roll conditions (3.19) is violated. For the model (3.68) this essentially depends on the specific value of p. For $1 \leq p \leq 2$ inflation ends when $\eta_V \simeq 1$, while for $p \geq 2$ the relevant condition is $\varepsilon_V \simeq 1$. Based on this consideration, we can calculate the inflaton field

value, $\phi_{\rm end}$, at the end of inflation finding

$$\phi_{\rm end}/m_{\rm Pl} = \begin{cases} p/\sqrt{2} & \text{for} \quad 1 \leq p \leq 2 \\ \sqrt{p\,(p-1)} & \text{for} \quad p \geq 2 \end{cases} \tag{3.71}$$

In order to calculate the predictions for the primordial spectrum of curvature perturbations, we have to evaluate the slow-roll parameters when the relevant CMB scales exit the horizon, $N_\star \sim$ 50-60 e-folds before the end of inflation. Given $\phi_{\rm end}$, we can use eq. (3.22) to express $N_\star$ as a function of the inflaton field value at horizon exit $\phi_\star$, finding

$$N_\star \simeq \frac{1}{m_{\rm Pl}^2} \int_{\phi_{\rm end}}^{\phi_\star} d\phi \, \frac{V}{\partial V/\partial \phi} = \frac{\phi_\star^2 - \phi_{\rm end}^2}{m_{\rm Pl}^2\, 2p}. \tag{3.72}$$

By solving (3.72) for $\phi_\star$ and plugging in the corresponding value of $\phi_{\rm end}$ for the respective case we find

$$\phi_\star/m_{\rm Pl} = \begin{cases} \sqrt{p\,(2N_\star + p^2)} & \text{for} \quad 1 \leq p \leq 2 \\ \sqrt{2p\,[N_\star + (p-1)\,p]} & \text{for} \quad p \geq 2 \end{cases} \tag{3.73}$$

To calculate the model predictions for the spectral index $n_{\rm s}$ and the tensor-to-scalar ratio r, we simply evaluate the right-hand side of eqs. (3.52) and (3.62) at $\phi = \phi_\star$. For the spectral index we find

$$n_{\rm s} = 1 + 2\eta_{V_\star} - 6\varepsilon_{V_\star} = \begin{cases} 1 - \frac{p+2}{2N_\star + p^2} & \text{for} \quad 1 \leq p \leq 2 \\ 1 - \frac{p+2}{2(N_\star + (p-1)p)} & \text{for} \quad p \geq 2 \end{cases}. \tag{3.74}$$

On the other hand, the calculation for r gives

$$r = 16\varepsilon_{V_\star} = \begin{cases} 8p/(2N_\star + p^2) & \text{for} \quad 1 \leq p \leq 2 \\ 4p/[N_\star + (p-1)p] & \text{for} \quad p \geq 2 \end{cases}. \tag{3.75}$$

In figure 3.1 we compare the model predictions to the *Planck 2015* constraints[14] on $n_{\rm s}$ and r. The theoretical results are shown for $p = 1, 2, 3$ (orange, green, blue), and for $N_\star = 60, 70$ (small dots, large dots). The solid black lines correspond to continuous values of p: $1 \leq p \leq 3$. The predictions are compared to the 68% and 95% CL (bluish) regions for $n_{\rm s}$ and r (cf. figure 12 in [97] for further details). One can see, that the model is disfavoured at 68% CL.

We have already argued above that the predictions are independent of the coupling λ. The only observable quantity in which the coupling appears, is the scalar amplitude $A_{\rm s}$. Unless there is some physically motivated reason which fixes the value of λ from the beginning, we can simply set its value to be consistent with the observational bounds on $A_{\rm s}$. In principle one would have to solve eq. (3.51) for λ. At this point we skip the calculation since it is not particularly insightful and the result will not be relevant for this thesis.

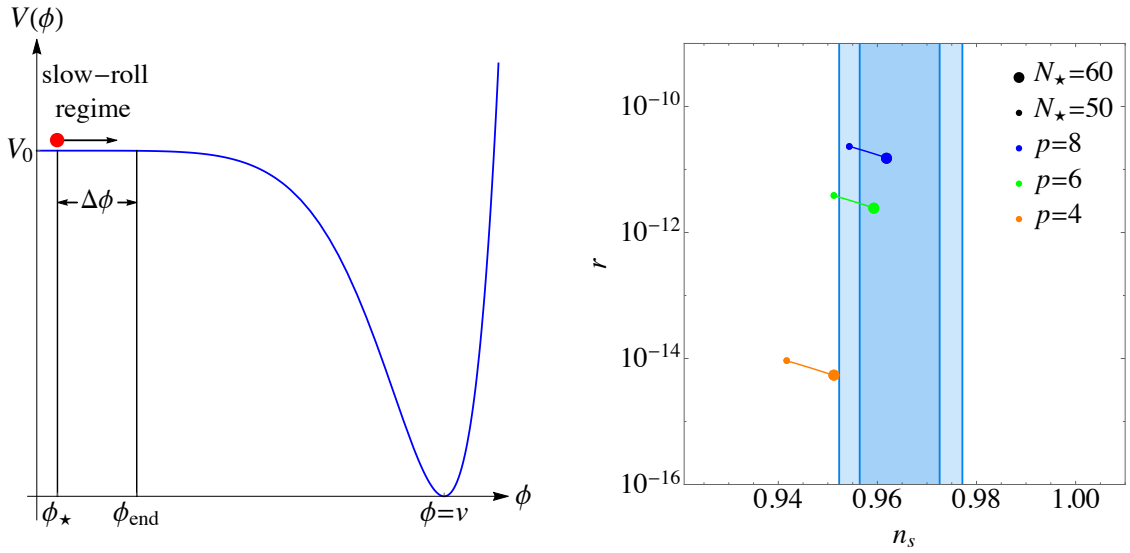

Figure 3.2: *Left:* Schematic form of the hilltop potential. Slow-roll inflation occurs close to the origin ($\phi \simeq 0$) while the inflaton rolls down its potential towards one of its VEV $\phi \pm v$. In units of $m_{\rm Pl}$, the field varies only very little ($\Delta\phi \ll v \ll m_{\rm Pl}$), over the last $N_\star \sim 60$ e-folds of slow-roll inflation where $V(\phi) \simeq V_0 \simeq V_\star$. *Right:* Theoretical predictions for the primordial spectra. The predictions are presented for $N_\star = 50, 60$ (small dots, large dots) and for $p = 4, 6, 8$, corresponding to the orange, green, and blue dots, respectively. The solid black lines correspond to continuous values $50 \leq N_\star \leq 60$. Again, the predictions are compared to the 68% and 95% CL regions for $n_{\rm s}$ and r (see Ref. [97] for further details). Realisations of the model with $p = 6$ and $p = 8$ are consistent with the bounds, while the realisation with $p = 4$ is disfavoured by the bound on $n_{\rm s}$ at 95% CL.

Small-field hilltop inflation

Let us now consider a model of small-field hilltop inflation with a scalar potential given by

$$V(\phi) = V_0 \left(1 - \frac{\phi^p}{v^p}\right)^2 . \tag{3.76}$$

The overall normalisation of the potential V_0 has units of $m_{\rm Pl}^4$ and $p \geq 4$ will be considered to be an even integer. The potential features two minima at $\phi = \pm v \ll m_{\rm Pl}$. The schematic form of the hilltop potential is shown in figure 3.2.

In these kind of scenarios, inflation happens close to $\phi = 0$ while the inflaton slowly rolls away from the origin towards one of its VEVs at $\phi = \pm v$. In what follows, we will assume that inflation ends in the positive vacuum $\phi = v$.

According to eqs. (3.17) and (3.18) the slow-roll parameters for the hilltop

[14] For the more recent *Planck 2018* constraints see [136].

p	$V_0/m_{\rm Pl}^4$	$n_{\rm s}$	r
4	1.750×10^{-22}	0.951	5.374×10^{-15}
6	8.006×10^{-20}	0.959	2.458×10^{-12}
8	4.977×10^{-19}	0.962	1.528×10^{-11}

Table 3.1: Selected parameter choices for the hilltop inflation model obtained assuming $v = 10^{-2} m_{\rm Pl}$ and $N_\star = 60$. The results are presented together with the corresponding predictions for the scalar spectral index $n_{\rm s}$ and the tensor-to-scalar ratio r.

model (3.76) can be approximated by

$$\varepsilon_V \simeq m_{\rm Pl}^2 \frac{2\,p^2 \phi^{2p-2}}{v^{2p}}\,, \tag{3.77}$$

$$\eta_V \simeq -m_{\rm Pl}^2 \frac{2\,p\,(p-1)\phi^{p-2}}{v^p}\,, \tag{3.78}$$

where we have used that during inflation $V \simeq V_0$ and $\phi \ll v$.

Eqs. (3.77) and (3.78) make it obvious that during inflation we have[15] $\varepsilon_V \ll |\eta_V|$. Hence, we can determine the end of inflation from the slow-roll condition for $|\eta_V|$ which gives

$$\phi_{\rm end}^{p-2} \simeq \frac{v^p}{m_{\rm Pl}^2\, 2\,p\,(p-1)}\,. \tag{3.79}$$

The inflaton field value at horizon crossing can again be calculated from

$$N_\star \simeq \frac{1}{m_{\rm Pl}^2} \int_{\phi_{\rm end}}^{\phi_\star} d\phi\, \frac{V}{\partial V/\partial\phi} \simeq \frac{v^p\,(\phi_\star^{2-p} - \phi_{\rm end}^{2-p})}{m_{\rm Pl}^2\, 2\,p\,(p-2)}. \tag{3.80}$$

By rearranging eq. (3.80) we can write $\phi_\star$ in terms of $N_\star$ and $\phi_{\rm end}$

$$\phi_\star^{2-p} \simeq \phi_{\rm end}^{2-p} + \frac{m_{\rm Pl}^2\, 2\,p\,(p-2)\,N_\star}{v^p} \simeq m_{\rm Pl}^2\, \frac{2\,p\,[N_\star\,(p-2) + p - 1]}{v^p}\,, \tag{3.81}$$

where in the last approximation we have replaced $\phi_{\rm end}$ according to eq. (3.79).

Finally, we can calculate the predictions for the primordial spectra of curvature and tensor perturbations. Using eqs. (3.52) and (3.62) together with the previously derived results we obtain the following expressions for the spectral index $n_{\rm s}$ and the tensor-to-scalar ratio r

$$n_{\rm s} = 1 + 2\eta_{V_\star} - 6\varepsilon_{V_\star} \simeq 1 + 2\eta_{V_\star} = 1 - \frac{2(p-1)}{N_\star(p-2) + p - 1}\,, \tag{3.82}$$

$$r = 16\varepsilon_{V_\star} \simeq 32\,p^2 \left[\frac{2p[N_\star(p-2) + (p-1)]}{m_{\rm Pl}^{p/(1-p)}\, v^{p/(p-1)}}\right]^{\frac{2p-2}{2-p}}\,. \tag{3.83}$$

[15] During inflation we have that $\eta_V^2/\varepsilon_V \sim \phi^{-2} \gg 1$. Since $|\eta_V| < 1$ it follows that $\varepsilon_V \ll \eta_V^2 \ll |\eta_V|$.

For $4 \leq p \leq 8$ and $N_\star \sim 60$ eq. (3.83) we can estimate the value of r to be

$$r \sim \mathcal{O}(10^{-6})\, v^{\frac{2p}{p-2}} \ll 1\,. \tag{3.84}$$

Notice that given the bound (3.65), the prediction for r is not very surprising since the hilltop model is a small-field model by construction ($v \ll m_{\rm Pl}$). Moreover, the predicted value is far too small to be detected (see e.g. [137]). On the other hand, if a large $r \gtrsim 10^{-3}$ should be detected at some point in the future, the model will immediately be ruled out.

So far we have not specified the constant vacuum energy V_0 appearing as an overall rescaling of the potential (3.76). In fact, just as the coupling λ in the chaotic inflation model discussed above, we can chose V_0 such that the model is consistent with the observational bounds on $A_{\rm s}$

$$V_0 \simeq V_\star \stackrel{!}{=} 24\pi^2\, A_{\rm s}\, \varepsilon_{V_\star}\, m_{\rm Pl}^4\,. \tag{3.85}$$

In figure 3.2 the predictions for $n_{\rm s}$ and r are compared to the *Planck 2015* constraints. Results are presented for $p = 4, 6, 8$ (orange, green, blue), and for $N_\star = 50$ and $N_\star = 60$ denoted by small and large dots, respectively. All the predictions have been computed by assuming $v/m_{\rm Pl} = 10^{-2}$. For $p = 6$ and $p = 8$ the model is consistent with the bounds. On the other hand, for $p = 4$ the model turns out to be disfavoured at 95% CL.

In the main part of this thesis, we will continue working on these realisations of the hilltop model. The relevant information is therefore summarised in table 3.1 including the value of V_0 that follows from eq. (3.85).

Chapter 4

Post-inflationary dynamics: (P)reheating

At the end of inflation the entire energy is still dominated by the inflationary degrees of freedom. By the onset of BBN, at temperatures $T \gtrsim 1$ MeV, this energy must have been transferred into a thermal bath of relativistic SM particles. This process, known as *reheating*[1], is necessary in order to guarantee the success of the primordial nucleosynthesis.

After giving an overview of the different stages of reheating we will focus on the non-perturbative stage referred to as *preheating*. We outline of how this stage can be studied in practice and discuss some explicit examples of preheating mechanisms that can lead to rapid growth of scalar field fluctuations. We shall thereby focus on those mechanisms that will be relevant in the models considered in the main part of this thesis.

After having gained a first understanding of the preheating process we conclude this chapter by emphasising why it is important to study preheating in detail and what it can teach us about the physics of the very early universe.

4.1 Reheating: an overview

Let us now turn to a brief discussion of the post-inflationary physics by providing an overview of the qualitative stages that the universe may experience between the end of inflation and the onset of BBN. We begin our discussion with the perturbative decay of the inflaton which, however, does often not provide an appropriate description of the dynamics, at least not from the very beginning of reheating after inflation.

Perturbative inflaton decay

At the end of inflation the inflaton ϕ starts oscillating around the minimum of its potential. Assuming that ϕ remains homogeneous, the oscillating inflaton might be interpreted as a condensate of massive particles, say with mass m_ϕ, and vanishing

[1] For some reviews see e.g. [138, 139].

momenta [24]. Let us now introduce an additional scalar field χ that couples to the inflaton according to the following interaction Lagrangian

$$\mathcal{L}_{\rm int} \;=\; -\sigma\,\phi\chi^2\,, \tag{4.1}$$

where the coupling σ has dimensions of $m_{\rm Pl}$. The tree-level decay rate of $\phi \to \chi\chi$ is given by [140]

$$\Gamma \;=\; \frac{\sigma^2}{8\pi m_\phi}\,. \tag{4.2}$$

The evolution of the inflaton energy is then described by a Boltzmann equation[2], and the decay of inflaton particles manifests itself in an exponential dilution of the comoving energy density $a^3\rho_\phi \sim e^{-\Gamma t}$. Note that according to the continuity equation (2.14), $a^3\rho_\phi$ would simply be conserved, in the absence of any interactions.

Alternatively, one may also consider the effect of Γ on the field itself by re-expressing the energy density ρ_ϕ in terms of ϕ in the respective Boltzmann equation. Indeed, one can find the following approximate and modified Klein-Gordon equation [24]

$$\ddot{\phi} + (3H + \Gamma)\,\dot{\phi} + \frac{\partial V}{\partial \phi} \;=\; 0\,. \tag{4.3}$$

Hence, the energy loss in ϕ caused by single-particle decays into two χ particles has simply the effect of an additional damping on the amplitude of ϕ.

For a small coupling constant σ, the decay rate is typically much smaller than the Hubble rate at the end of inflation. The inflaton energy is therefore initially diluted due to the expansion of the universe. Once the Hubble parameter becomes comparable to Γ, the inflaton decay becomes efficient and the energy loss due to the expansion eventually becomes negligible. Hence, the energy that is transferred to χ particles can be estimated to be $\rho_\chi = 3m_{\rm Pl}^2 H^2 \sim 3m_{\rm Pl}^2\Gamma^2$.

If we further assume that the decay products are light and behave like radiation, we can estimate the temperature of the thermal bath of χ particles to be [139]

$$T_{\rm reh} \;\sim\; \left(\frac{90}{g_*\pi^2}\right)^{1/4} \sqrt{m_{\rm Pl}\Gamma}\,, \tag{4.4}$$

where g_* is the total number of relativistic degrees of freedom and we have used that $\rho = \pi^2\, g_*/30\, T^4$, in thermal equilibrium. The temperature $T_{\rm reh}$ at which thermal equilibrium is established is referred to as the *reheating temperature*. A successful onset of BBN requires $T_{\rm reh} \gtrsim 1$ MeV. On the other hand, in order to prevent the thermal production of dangerous relics, $T_{\rm reh}$ cannot be arbitrarily high. For example, in models of SUGRA where the gravitino mass is of the order of 100 GeV, the reheating temperature should not be higher than $T_{\rm reh} \sim 10^5$-10^7 GeV [141].

In practice, however, the perturbative description of the inflaton decay is often not justified. Dissipative effects associated with quantum fluctuations [138], for

[2]See e.g. [24, pp. 244 f.].

example, are not captured by the perturbative approach. Although corrections to (4.3) may be included (see e.g. [142]), their implementation turns out to be very complicated.

Another effect the perturbative description does not take into account is the non-perturbative growth of scalar field fluctuations, immediately after inflation. This mechanism is often interpreted as a non-perturbative production of scalar particles with non-vanishing momenta and is commonly referred to as *preheating* (see below).

Nevertheless, once fluctuations have been sufficiently redshifted, such that condensates of remaining non-relativistic species may be interpreted as a collection of particles, the perturbative approach can be applied to describe their decay into relativistic particle species at late times [139].

Non-perturbative preheating

The process of reheating often starts with a non-perturbative stage commonly referred to as preheating[3] [143–147]. At the end of inflation, when the inflaton starts oscillating about the minimum of its potential the dynamics can lead to a strong and rapid growth of both, inflaton fluctuations and fluctuations of other fields that couple to it.

The growth of fluctuations can happen via different mechanisms such as *tachyonic preheating* [148,149], *tachyonic oscillations* [150] or *parametric resonances* [143, 147, 151, 152]. Later in this chapter we will explicitly discuss some examples.

The dynamics during preheating may initially be followed using linear perturbation theory. Depending on the considered model, however, the growth of fluctuations may be very efficient. In particular, non-linear effects such as the backreaction of fluctuations on the homogeneous component, as well as mode-mode interactions, also referred to as *rescattering* [153] eventually become important and the growth of fluctuations is terminated. The subsequent evolution must then be followed by solving the full non-linear equations.

The duration of preheating and in particular of the linear regime generally depends on the underlying mechanism. For example, if the growth of fluctuations happens via tachyonic preheating, the linear stage may end within less than a single oscillation [148]. If tachyonic oscillations is the driving mechanism, linear preheating may last a couple of oscillations until non-linear effects terminate the rapid growth [150, 154]. Amongst the mentioned mechanisms, parametric resonance is generally the most "inefficient", particularly if it happens in the *narrow resonance regime* as we will explicitly see in section 4.2.2. In this case, the linear regime can last for dozens of oscillations [143, 147].

Depending on the model, the dynamics during the non-linear regime can give rise to various interesting phenomena. An example is e.g. the fragmentation of real scalar fields into non-topological, soliton-like field configurations referred to as oscillons [7]. Similar configurations can also appear in models with complex fields in form of so-called Q-balls [155, 156]. Another example is the formation of topological defects such as domain walls [157]. Certain models give rise to the production of

[3] We note that the term "preheating" was first proposed in Ref. [143].

large inhomogeneities which can lead to the production of Primordial Black Holes (PBHs)[4] [161]. For example, this can happen during hybrid inflation due to the amplification of large wavelength fluctuations that exit the horizon during inflation and eventually re-enter at a later stage, where they can collapse and lead to a copious production of PBHs [158]. As will be discussed in greater detail in section 4.4.3, the violent dynamics of preheating can also give rise to the production of a stochastic background of GWs [162].

Thermalisation

The last stage required for the completion of reheating is the thermalisation of the decay products of the inflaton [152, 163–166]. The thermalisation process is said to be completed when the following two conditions are satisfied [138, 167]:

1. The energy density of the universe is dominated by radiation ($w \simeq 1/3$).

2. The universe has reached a state of local thermal equilibrium, i.e. kinetic and chemical equilibrium are established[5].

The first condition can often be reached comparatively quickly [167]. On the other hand, for the second condition to be satisfied it generally requires that both, particle number-conserving and particle number-violating interactions are involved in the process of thermalisation [138].

Perturbative limit

If non-perturbative effects are absent and the inflaton decays in the perturbative limit as discussed above, the number density of the decay products is found to be far too small to be compatible with thermal equilibrium [138]. In order to reach thermal equilibrium the number of particles must increase and their energy must be re-distributed. As mentioned above, this requires the presence of both, particle number-conserving and number-violating interactions [138].

Thermalisation after preheating

During the non-linear stage of preheating the fields may fragment and become very inhomogeneous. The system will then typically follow a stage of *turbulence* [168, 169], during which the energy is steadily transferred to modes with higher momenta, i.e. towards the ultraviolet (UV).

The turbulent regime typically happens on much longer time scales than the preceding phase of preheating [168, 169] and can be subdivided into two, qualitatively different regimes: (i) if the energy of the system is dominated by the homogeneous

[4] See for example Refs. [158–160].

[5] If interactions between particles are weak, kinetic equilibrium implies that occupation numbers approach either a Bose-Einstein distribution in case of bosons or a Fermi-Dirac distribution for fermions [139]. Chemical equilibrium means that the sum of the chemical potentials of the reactants is equal to that of the reaction products.

component (the "zero-mode"), the latter continues to decay into inhomogeneous fluctuations [169]. This regime is referred to as *driven turbulence*. The duration of the driven turbulence regime is typically longer than the preceding phase of preheating but nevertheless shorter than the subsequent process of (ii) *free turbulence* [169]. During this regime the energy density is dominated by fluctuations and is re-distributed, or cascades, towards modes with higher comoving momenta. Both phases are characterised by a self-similar evolution and result in a smoothening of the fluctuation spectra [169].

As the occupation numbers in the increasing UV cut-off become of order unity, the classical description breaks down and the thermalisation process gets dominated by quantum effects. During this final (and longest) stage, the system slowly evolves towards thermal equilibrium and the spectra of the occupation numbers eventually approach an equilibrium distribution.

4.2 More on preheating

A substantial part of this thesis is devoted to the study of the non-perturbative and non-linear dynamics of preheating after inflation, as well as scenarios in which qualitatively similar effects may be present (cf. section 4.3). We shall therefore discuss briefly the most common tools and techniques for studying these dynamics.

So far we have been only considering a single scalar field ϕ. In most of the scenarios studied within this thesis we will, indeed, mainly focus on the dynamics of a single scalar field, while assuming that other fields are dynamically irrelevant during preheating. In some cases, however, we shall consider the presence of additional fields that couple to the inflaton.

In the more generic case of N_f scalar fields, $\phi^1, \ldots, \phi^{N_f}$, the action that governs the dynamics can be written as

$$S = \int d^4x\sqrt{-g}\left(\frac{m_{\rm Pl}^2 R}{2} - \frac{1}{2}\sum_\ell \partial^\mu\phi^\ell\,\partial_\mu\phi^\ell - V(\phi^1,\ldots,\phi^{N_f})\right) . \tag{4.5}$$

In flat FLRW spacetime, the full set of coupled Euler-Lagrange equations that describe the evolution of the system is

$$\ddot{\phi}^\ell + 3H\dot{\phi}^\ell - \frac{\nabla^2}{a^2}\phi^\ell + \frac{\partial V}{\partial\phi^\ell} = 0\,, \quad \ell = 1,\ldots,N_f\,, \tag{4.6}$$

$$H^2 \;=\; \frac{1}{3\,m_{\rm Pl}^2}\left[\frac{1}{2}\sum_\ell\left((\dot{\phi}^\ell)^2 + \frac{|\nabla\phi^\ell|^2}{a^2}\right) + V(\phi^1,\ldots,\phi^{N_f})\right] . \tag{4.7}$$

By the end of inflation, the universe has been smoothed and the only present inhomogeneities are assumed to be small quantum vacuum fluctuations. Given some initial conditions for the fields, the dynamics can in principle be studied by integrating the classical equations (4.6) - (4.7). Typically, the calculations have to be performed numerically, although in some simple cases one may even find approximate solutions (at least during the linear regime). Some of these cases will be discussed below in this section.

There are different common approaches to study the dynamics of scalar fields in scenarios in which the initially small vacuum fluctuations get dynamically amplified. Initially, when the fluctuations are small one may decompose the respective fields into a homogeneous background $\overline{\phi}^{\ell}$ and a small perturbation $\delta\phi^{\ell}(t, \mathbf{x})$, i.e. in analogy to the procedure in section 3.23. The evolution of the perturbations can then be followed by simultaneously solving the homogeneous background evolution and the linearised equation for the perturbations in Fourier space.

The linear approach eventually breaks down once different modes start interacting with each other, or the backreaction of the fluctuations on the homogeneous component becomes important. In such cases, one has to solve the fully non-linear equations (4.6) - (4.7). This, in turn, is typically performed by means of lattice simulations in which the evolution is followed on a discretised version of spacetime.

Lattice simulations are a powerful tool to study the non-linear dynamics during preheating but are often computationally very expensive. Another issue related to the lattice approach is that due to the expansion of the universe, the resolution decreases over time. Therefore, one has to be very careful when interpreting results of simulations for which the system has experienced a considerable amount of expansion throughout a simulation.

A common way to study the growth of fluctuations related e.g. to parametric resonances is by the application of *Floquet theory* [170]. Although it is not well suited to study the dynamics of preheating in detail, it allows to get a first understanding of the dynamics during the oscillatory regime, immediately after inflation. The basic idea is to get an estimate of both the growth rate, as well as the range of wave lengths of those fluctuations that are resonantly enhanced.

Within this thesis we will at some point make use of the techniques mentioned above. They are discussed in greater detail in appendix C.

Comment on the semiclassical limit

In the discussion above we have briefly mentioned how preheating is typically studied, namely by solving classical equations of motion but with fluctuations initialised in their quantum vacuum state.

In section 3.3.1 we pointed out that the fluctuations become classical once they exit the horizon during inflation. Within this thesis we will mainly be interested in the dynamics during preheating on scales well inside the horizon. Is it then really justified to follow the dynamics in classical manner? At least for those fluctuations which experience exponential growth, the answer is yes. In that case one can show that up to small quantum corrections[6], the mode functions eventually become real-valued [171]. Neglecting these corrections implies that the fluctuations can be treated as classical random variables, which justifies the (semi)classical approach.

Quantifying preheating

In order to quantify the effects of preheating, different quantities can be considered. A useful quantity to measure the behavior of the fluctuations of some field ϕ is the

[6] And up to a (time-independent) phase shift [171].

variance of the fluctuations

$$\langle \delta\phi^2(t) \rangle \;=\; \int \frac{d^3\mathbf{k}}{(2\pi)^3} \, |\delta\phi_{\mathbf{k}}|^2 \;=\; \int d\ln k \, \frac{k^3 \, |\delta\phi_{\mathbf{k}}|^2}{2\pi^2} \,. \tag{4.8}$$

The latter may be considered together with the spectrum of fluctuations

$$\mathcal{P}_{\delta\phi}(k) \;=\; \frac{k^3 \, |\delta\phi_{\mathbf{k}}|^2}{2\pi^2} \,. \tag{4.9}$$

In particular, for a sharply peaked spectrum, the variance is a good measure for the amplitude of the largest fluctuation

$$\delta\phi^2_{\text{largest}} \;\sim\; \langle \delta\phi^2 \rangle \,. \tag{4.10}$$

Another set of quantities which is often used is the comoving number density of particles n_ϕ together with the comoving occupation number $n_k(t)$. The former is defined as

$$n_\phi(t) \;\equiv\; \int \frac{d^3\mathbf{k}}{(2\pi)^3} \, n_k(t) \,. \tag{4.11}$$

The comoving occupation number is defined in terms of the rescaled fluctuations $\delta\tilde{\phi}_{\mathbf{k}} = a(t)^{3/2}\delta\phi_{\mathbf{k}}(t)$ and their velocity (see e.g. [147])

$$n_k(t) \;\equiv\; \frac{1}{2\omega_k} \left(|\delta\dot{\tilde{\phi}}_{\mathbf{k}}|^2 + \omega_k^2 |\delta\tilde{\phi}_{\mathbf{k}}|^2 \right) - \frac{1}{2} \,, \tag{4.12}$$

where the frequencies ω_k are given by

$$\omega_k^2 \;\equiv\; \frac{k^2}{a^2} + \frac{\partial^2 V}{\partial \overline{\phi}^2} \,. \tag{4.13}$$

Throughout this thesis we will work with the variance and the spectrum of fluctuations, respectively. Notice that whether one considers the variance and the spectrum of fluctuations or the number density and the occupation numbers does typically not make a big difference. Both sets of quantities will usually exhibit a similar qualitative behaviour.

Notice that the quantities introduced above are all non-local. In certain cases it is insightful to consider local quantities, in particular in the presence of non-linear phenomena such as oscillons. Examples of such quantities are e.g. the spatial field distribution or energy density distribution $\rho(\mathbf{x}, t)$. The latter can be computed numerically within the scope of lattice simulations.

4.2.1 Tachyonic Preheating

Tachyonic preheating can occur in concave potentials $V(\phi)$, during the first roll down of the field towards the minimum of its potential. In other words, the necessary condition for the tachyonic amplification of scalar field fluctuations is a negative effective mass squared $\partial^2 V/\partial\phi^2 < 0$. As the field rolls through such a tachyonic region, all the IR modes $\delta\phi_k$, for which $k^2/a^2 + \partial^2 V/\partial\phi^2 < 0$, will experience exponential growth.

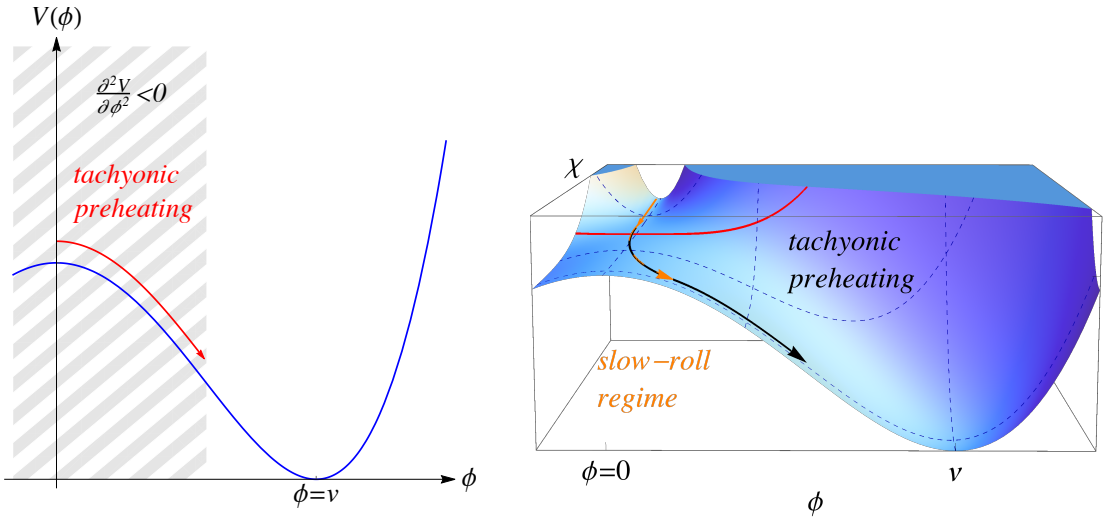

Figure 4.1: *Left:* Illustration of the potential (4.14). Tachyonic preheating happens in the gray shaded area where $\partial^2 V/\partial\phi^2 < 0$, while ϕ rolls away from the origin towards one of its VEVs $\phi \pm v$.
Right: Schematic illustration of hybrid inflation. During inflation, the waterfall ϕ is stabilised at $\phi = 0$ and inflation happens while the inflaton (here named χ) slowly rolls along a flat valley. As the inflaton approaches a critical value (solid red line) the waterfall acquires a tachyonic mass squared and becomes destabilised. Inflation is then ended by the dynamics of the waterfall and the system enters into the tachyonic preheating regime.

In order to get a better understanding of the process, consider a model described by the following scalar potential

$$V(\phi) = \frac{\lambda}{4}\left(\phi^2 - v^2\right)^2 , \tag{4.14}$$

where $\lambda \ll m_{\rm Pl}$ is some dimensionless parameter. The potential has two minima at $\phi = \pm v$ and is symmetric around the origin. A schematic illustration of the potential (4.14) is shown in figure 4.1.

The above potential is the classical example of a waterfall field potential in hybrid inflation [172]. There inflation is not ended by the dynamics of the inflaton field itself, but rather through a symmetry breaking phase transition, triggered by a tachyonic (or spinodal) instability in ϕ. In the single-field limit inflation happens while a second field (i.e. the inflaton) slowly rolls along a flat valley, orthogonal to the ϕ direction. During inflation ϕ is stabilised at $\phi = 0$. Eventually, the inflaton reaches a critical field value at which the effective mass squared of ϕ becomes tachyonic. The waterfall ϕ then becomes dynamical, violates the slow-roll conditions, and inflation ends. This mechanism is illustrated in figure 4.1.

In the following we shall focus on the dynamics of tachyonic preheating of the field ϕ in a potential given by (4.14) which we may alternatively write as

$$V(\phi) = \frac{m^4}{4\lambda} - \frac{m^2}{2}\phi^2 + \frac{\lambda}{4}\phi^4 , \tag{4.15}$$

where $m \equiv v\sqrt{\lambda}$.

The field has a negative effective mass squared for $0 \leq \phi \leq m/\sqrt{3\lambda} = v/\sqrt{3}$ (cf. figure 4.1). While ϕ rolls away from the origin towards the minimum $\phi = \pm v$, it passes through the tachyonic region and all modes with $\omega_k^2 \sim k^2/a^2 - m^2 < 0$ will experience exponential growth. To see this, let us go one step further and consider the linearised equations for the perturbations of ϕ. If we further assume that $H \ll m$, during the first roll-down, we may ignore the expansion of the universe and consider the linearised equation in Minkowski spacetime, which reads

$$\delta\ddot{\phi}_{\mathbf{k}} + \omega_k^2 \delta\phi_{\mathbf{k}} \,=\, 0\,, \quad \text{where} \quad \omega_k^2 \,=\, k^2 - m^2\,. \tag{4.16}$$

For simplicity we have neglected a field-dependent contribution to the effective mass squared coming from the quartic term in the potential (4.15).

The mode equation (4.16) has the solution

$$\delta\phi_{\mathbf{k}}(t) \,=\, (\delta\phi_{\mathbf{k}})_{\text{vac}} \cosh(\omega_k\, t) + \frac{(\delta\dot{\phi}_{\mathbf{k}})_{\text{vac}}}{\omega_k} \sinh(\omega_k\, t)\ , \tag{4.17}$$

where $(\delta\phi_{\mathbf{k}})_{\text{vac}} \sim 1/\sqrt{2k}$ is the Minkowski vacuum solution. Exponential growth will therefore occur for all modes with $m^2 > k^2$, whereas modes with $m^2 \leq k^2$ will have (harmonically) oscillating solutions.

4.2.2 Parametric Resonance

As briefly mentioned above, parametric resonance occurs in the oscillatory regime. Depending on the scalar potential, fluctuations of both, the oscillating field, as well as fields that couple to it can get resonantly amplified.

As an example in which parametric resonance can occur we consider a simple model with two massive scalar fields ϕ and χ that couple to each other via a dimensionless coupling constant $g^2 > 0$

$$V(\phi, \chi) \,=\, \frac{m_\phi^2}{2}\phi^2 + \frac{m_\chi^2}{2}\chi^2 + \frac{g^2}{2}\phi^2\chi^2\,. \tag{4.18}$$

In the following we assume that the matter field χ is stabilised at the minimum of its potential $\overline{\chi} = \dot{\overline{\chi}} = 0$, during and immediately after inflation. Inflation then effectively happens in form of SFSR inflation along the ϕ direction, while the inflaton slowly rolls down its parabolic potential.

Notice that the potential corresponds to the chaotic model (3.68), with $p = 2$ and $\lambda = m_\phi^2/2$, for which we discussed the inflationary dynamics in section 3.4. Although the model is strongly disfavoured by CMB observations, it suites ideally for illustrating the dynamics of parametric resonance due to its simplicity.

Equations of motion in Minkowski spacetime and Floquet analysis

In the following we assume that inflation has already happened and that the inflaton just entered the oscillatory regime. In order to gain a first understanding on how the fluctuations of χ evolve in an oscillating homogeneous inflaton background $\overline{\phi}(t)$

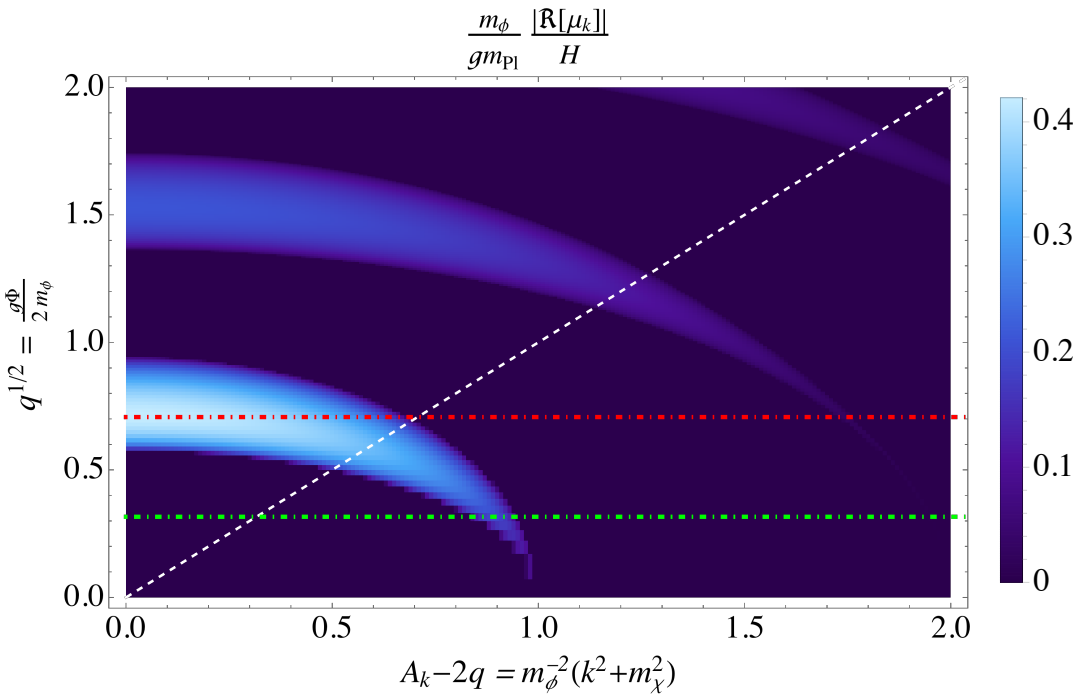

Figure 4.2: Floquet chart of the solutions to the Mathieu equation (4.24). The white dashed line denotes $A_k - 2q = q^{1/2}$. The Floquet exponents are shown in dependence of A_k and $2q$, and in units of $gHm_{\rm Pl}/m_\phi$. The Foquet chart exhibits a characteristic band structure where the exponentially growing solutions appear in form of bands that become narrower for $A_k - 2q \gg q^{1/2}$.

we may perform a Floquet analysis. To this end we ignore the expansion of the universe and the homogeneous inflaton equation of motion becomes

$$\ddot{\overline{\phi}}(t) + m_\phi^2 \overline{\phi}(t) \;=\; 0\,. \tag{4.19}$$

Assuming $\overline{\phi}_{\rm i} \;=\; \Phi$, and $\dot{\overline{\phi}}_{\rm i} = 0$ for the initial conditions, eq. (4.19) has the solution

$$\overline{\phi}(t) \;=\; \Phi \cos(m_\phi\, t)\,. \tag{4.20}$$

For $\overline{\chi}(t) = \dot{\overline{\chi}}(t) = 0$, the linearised equations for the perturbations in Minkowski space read

$$\delta\ddot{\phi}_{\mathbf{k}}(t) + \left(\omega_k^\phi\right)^2 \delta\phi_{\mathbf{k}}(t) \;=\; 0\,, \tag{4.21}$$

$$\delta\ddot{\chi}_{\mathbf{k}}(t) + \left(\omega_k^\chi(t)\right)^2 \delta\chi_{\mathbf{k}}(t) \;=\; 0\,, \tag{4.22}$$

where

$$\omega_k^\phi \;=\; \sqrt{k^2 + m_\phi^2}\,, \quad \text{and} \quad \omega_k^\chi(t) \;=\; \sqrt{k^2 + m_\chi^2 + g^2\Phi^2\cos^2(m_\phi\, t)}\,. \tag{4.23}$$

The inflaton fluctuations have oscillatory solutions that can be described by (4.17), where $(\omega_k^\phi) > 0$. The fluctuations of χ, in turn, have a time-dependent frequency squared which is not just periodic, but also harmonic.

Indeed, we may bring eq. (4.22) into the form of the Mathieu equation (cf. eq. (C.2.11) in appendix C.2 The)

$$\frac{d^2\delta\chi_{\mathbf{k}}(\tau)}{d\tau^2} + [A_k + 2q\cos(2\tau)]\,\delta\chi_{\mathbf{k}}(\tau) \;=\; 0\,, \tag{4.24}$$

by identifying

$$A_k \;=\; \frac{k^2+m_\chi^2}{m_\phi^2} + 2q\,, \quad q \;=\; \frac{g^2\Phi^2}{4\,m_\phi^2}\,, \quad \text{and} \quad \tau = m_\phi t \tag{4.25}$$

The Floquet exponents of the solutions to eq. (4.24), can be computed by solving eq. (4.24) from $\tau = \tau_0 = 0$ to $\tau = T$, where the period of the system is simply given by the period of the frequency squared in (4.24), hence

$$T \;=\; \pi\,. \tag{4.26}$$

Eq. (4.24) is then solved for the following sets of initial conditions corresponding to (see appendix C.2)

$$\{\delta\chi_{\mathbf{k},1}(0) = 1, \delta\dot\chi_{\mathbf{k},1}(0) = 0\}\,, \quad \text{and} \quad \{\delta\chi_{\mathbf{k},2}(0) = 0, \delta\dot\chi_{\mathbf{k},2}(0) = 1\}\,. \tag{4.27}$$

Finally, the Floquet exponents are given by

$$\Re[\mu_k^\pm] \;=\; \frac{1}{T}\ln|\sigma_k^\pm|\,, \tag{4.28}$$

where

$$\sigma_k^\pm \;=\; \frac{1}{2}\left(\delta\chi_{\mathbf{k},1} + \delta\dot\chi_{\mathbf{k},2} \pm \sqrt{[\delta\chi_{\mathbf{k},1} - \delta\dot\chi_{\mathbf{k},2}]^2 + 4\,\delta\chi_{\mathbf{k},2}\delta\dot\chi_{\mathbf{k},1}}\right)\Bigg|_{\tau=T}\,. \tag{4.29}$$

Notice that this procedure is effectively equivalent to the procedure described in appendix C.2 for the multi field case.

Figure 4.2 shows the stability/instability chart of the Floquet solutions to the Mathieu equation (4.24). The Floquet exponents are shown in units of $gHm_{\rm Pl}/m_\phi$, and as a function of the parameters $A_k - 2q = m_\phi^{-1}\sqrt{k^2+m_\chi^2}$ and $q^{1/2} = g\Phi/(2m_\phi)$. The exponentially growing solutions ($|\Re[\mu_k]| > 0$) form a band structure on the Floquet chart. Bands in which the solutions are unstable are separated by stable regions where $|\Re[\mu_k]| = 0$.

Note that for the fastest growing modes we have $\frac{m_\phi}{gm_{\rm Pl}}\frac{|\Re[\mu_k]|}{H} \sim \mathcal{O}(0.1)$. In order to have efficient growth of fluctuations in an expanding universe we need $\frac{|\Re[\mu_k]|}{H} \gg 1$ [139], which we can translate into the following condition on the coupling g and the inflaton mass m_ϕ

$$\frac{gm_{\rm Pl}}{m_\phi} \gg \mathcal{O}(10) \quad \Leftrightarrow \quad \frac{\Re[\mu_k]}{H} \gg 1\,, \tag{4.30}$$

where $\sqrt{6}H \;\simeq m_\phi\Phi$.

Broad and narrow parametric resonance

Depending on the Floquet parameters A_k and q (or equivalently on the model parameters g, m_ϕ,...), parametric resonance can happen in two qualitatively different ways, which are referred to as *narrow* and *broad parametric resonance* [147]. The former happens for modes which lie in the thin region of a given band where $A_k - 2q \gg q^{1/2}$. Broad parametric resonance, on the other hand leads to growth of low-momentum modes $A_k - 2q \ll q^{1/2}$ and is in general much more efficient. Resonant amplification of fluctuations happens over a much broader range of wavenumbers, with growth rates much larger compared to the narrow resonance regime.

Figure 4.3 shows an example of narrow parametric resonance with $q = 0.1$ (upper/green plots) as well as an example of broad parametric resonance with $q = 0.5$ (lower/red plots). These two values of q are also denoted in the Floquet chart in figure 4.2 by the green ($q = 0.1$), and red ($q = 0.5$) dotted-dashed lines. On the left we show the evolution of a selected mode, over several homogeneous oscillations of the background field. The figures on the right show the spectrum of χ fluctuations $(A_k - 2q)^3/2|\delta\chi_{\mathbf{k}}|^2$, at different moments in time. In these plots, the dashed black line denotes the corresponding mode for which the evolution is explicitly shown. The results have been obtained by solving eq. (4.24) numerically, with initial conditions for the fluctuations given by the Minkowski vacuum

$$(\delta\chi_{\mathbf{k}})_{\rm vac} \sim \frac{1}{\sqrt{2k}}\,. \tag{4.31}$$

By comparing the results of the two scenarios one can clearly see that the resonance is much more efficient in the broad resonance regime $q = 0.5$. For $q = 0.1$, in fact, only modes within a narrow band get amplified, corresponding to the thin peak in the spectrum (upper right plot in figure 4.3).

A characteristic of broad parametric resonance is that adiabaticity is violated during this process, i.e. that the adiabatic condition

$$\left|\frac{\dot\omega_k(t)}{\omega_k^2(t)}\right| \ll 1\,, \tag{4.32}$$

is not satisfied. For the case of Mathiueu's equation (4.24), where $\omega_k^2 = A_k + 2q\cos(2\tau)$, the adiabatic condition becomes

$$\left|\frac{\dot\omega_k(t)}{\omega_k^2(t)}\right| = \left|\frac{2q\sin(2\tau)}{(A_k + 2q\cos(2\tau))^{3/2}}\right| \ll 1. \tag{4.33}$$

When $2q \ll A_k$, for example, we have $|\dot\omega_k(t)/\omega_k^2(t)| \simeq 2q\sin(2\tau)/A_k$, and eq. (4.32) is always satisfied. On the other hand, for $2q \gg A_k$, the adiabatic condition may be approximated as

$$\left|\frac{\dot\omega_k(t)}{\omega_k^2(t)}\right| \approx \left|\frac{2q\sin(2\tau)}{(2q\cos(2\tau))^{3/2}}\right|\,. \tag{4.34}$$

In this case, the adiabatic condition is violated twice per period of oscillation $T = \pi$, namely whenever τ takes on values around uneven multiples of $\pi/4$.

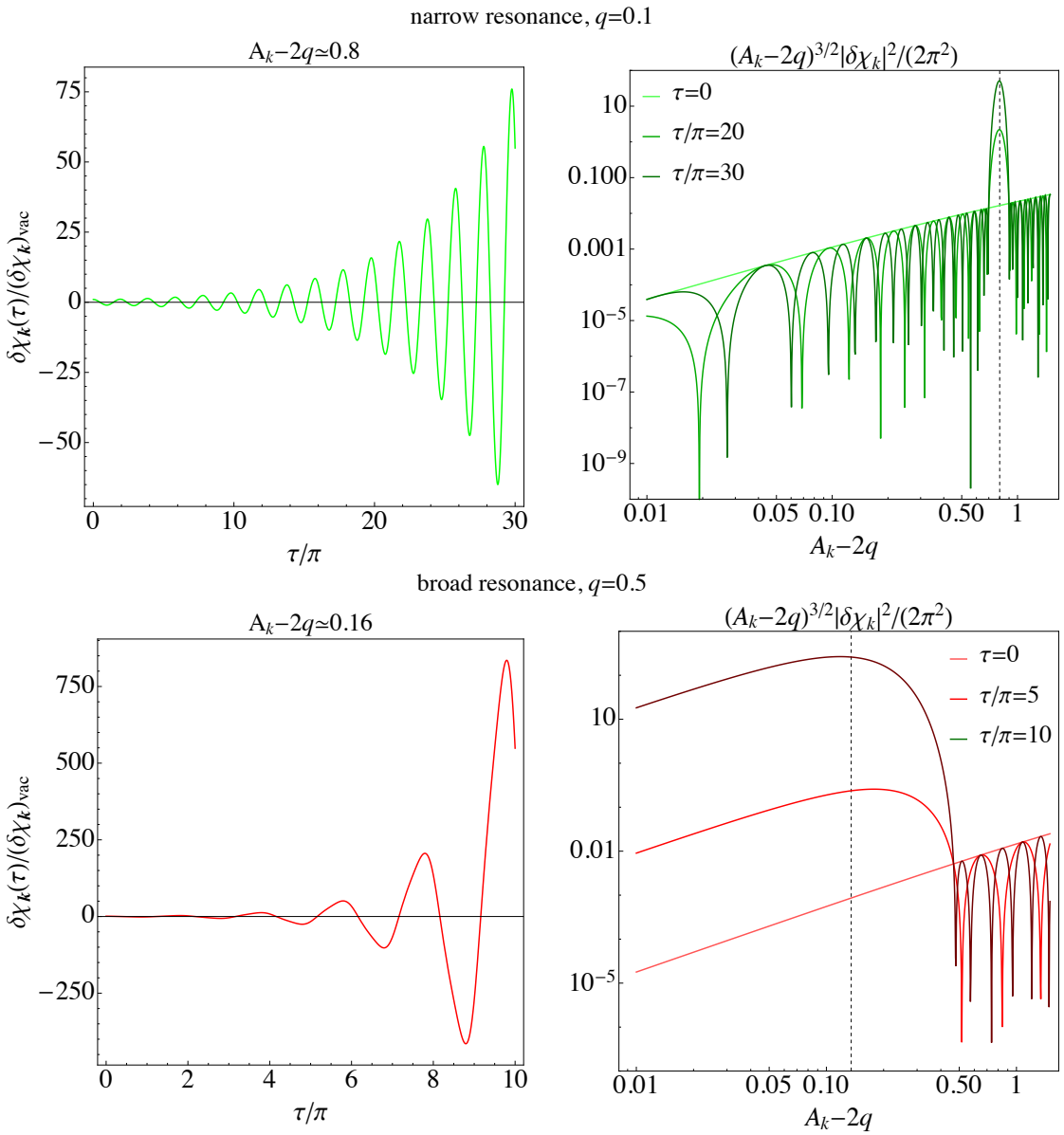

Figure 4.3: *Upper plots:* example of narrow parametric resonance with $q = 0.1$. The left plot shows the evolution of the mode with $A_k - 2q \simeq 0.8$ over 30 oscillations of the homogeneous background in Minkowski space. The right part of the plot shows the spectrum of χ fluctuations at three different moments in time: the initial (vacuum) spectrum and after 15 and 30 oscillations of ϕ.
Lower plots: example of broad parametric resonance with $q = 0.5$. Again, the left plot shows the evolution of a selected mode $A_k - 2q \simeq 0.16$. The evolution is shown over 10 homogeneous ϕ oscillations. The spectrum of χ fluctuations is shown on the right at $\tau = 0$, $\tau = 5\pi$, and $\tau = 10\pi$, respectively. In this case, the growth is significantly enhanced compared to the case where $q = 0.1$.

Notice that for the model discussed above we always have $A_k \geq 2q$. As mentioned above, in this case broad parametric resonance can also happen for modes with low momenta $A_k - 2q \ll q^{1/2}$. In fact, for wavenumbers that are negligibly small

compared to q we can approximate (4.33) as

$$\left|\frac{\dot{\omega}_k(t)}{\omega_k^2(t)}\right| \approx \left|\frac{2q\sin(2\tau)}{(2q+2q\cos(2\tau))^{3/2}}\right| . \tag{4.35}$$

In this case, adiabaticity is violated only once when τ has values around uneven multiples of $\pi/2$.

On the other hand, for modes for which the frequency varies slowly enough such that eq. (4.32) is satisfied, the solution to the mode equation (4.22) can be approximated by a so-called WKB solution (see for instance [24, pp. 249 ff.])

$$\delta\chi_{\mathbf{k}}(t) \simeq \frac{\alpha_k}{\sqrt{2\omega_k^\chi(t)}} e^{-i\int dt'\omega_k^\chi(t')} + \frac{\beta_k}{\sqrt{2\omega_k^\chi(t)}} e^{i\int dt'\omega_k^\chi(t')} , \tag{4.36}$$

where the constant and k-dependent coefficients α_k and β_k are called Bogolyubov coefficients. The solution eq. (4.36) is oscillating and only valid as long as $\omega_k^2 > 0$. For example, if we had considered a trilinear interaction term ($\sim \phi\chi^2$) instead of the quartic considered in (4.18) there would have been modes for which the frequency squared periodically becomes tachyonic. The resonant growth of such modes is then sometimes also referred to as *tachyonic resonance* [173]. For modes which satisfy the adiabaticity condition, but exhibit a negative frequency squared there exists an approximate WKB solution which reads [173]

$$\delta\chi_{\mathbf{k}}(t) \simeq \frac{\alpha_k}{\sqrt{2\Omega_k^\chi(t)}} e^{-\int dt'\Omega_k^\chi(t')} + \frac{\beta_k}{\sqrt{2\Omega_k^\chi(t)}} e^{\int dt'\Omega_k^\chi(t')} , \tag{4.37}$$

with $(\Omega_k^\chi)^2 \equiv -(\omega_k^\chi)^2$. In contrast to the solution (4.36), this solution is exponentially evolving, rather than oscillatory.

Parametric resonance in an expanding universe

When the expansion of the universe is taken into account, both the amplitude of the field Φ and the comoving wavenumbers get redshifted. This, in turn, implies that comoving modes will travel towards the lower left corner in the Floquet chart. Depending on the efficiency of the resonance, certain modes might get amplified over multiple periods of time, while crossing several distinct resonance bands.

Due to the decay of the zero-mode in an expanding universe, the system may even "jump" over several instability band, within a single oscillation. If that is the case, the resonant growth of fluctuations happens in a more "irregular" manner [7]. The process is then referred to as stochastic resonance [147]. For the Mathieu equation (4.24) the number of the resonance band n_{band} is given by $n_{\text{band}} = A_k^{1/2}$ which, according to (4.25), is proportional to $\sqrt{2q}$. In an expanding universe q is not constant since it depends on the amplitude of the oscillating field which, in turn, is redshifted. If q is extremely large, even a small decrease per oscillation can change the number of the resonance band by orders of magnitude [147].

[7] See e.g. figure 5 and figure 6 in Ref. [147].

4.2.3 Tachyonic oscillations

Another preheating mechanism that we will encounter in the main part of this thesis are tachyonic oscillations [150, 154]. This mechanism is generic in small-field inflation models in which the potential features a negative effective mass squared in some region of the potential. An example model in which tachyonic oscillations can be the driving mechanism for the growth of fluctuations is, for instance, the hilltop inflation model (3.76) introduced in section 3.4.1.

Compared to parametric resonances, the process of tachyonic oscillations can be much more violent and efficient. The fluctuations can, indeed, grow very quickly such that non-linear effects become important, already after a couple of homogeneous background oscillations [150].

We begin our discussion by providing an explanation of this process and a recap of the essential findings of [150]. For illustrative purposes we show numerical results of linear preheating for a realisation of the small-field hilltop inflation model.

Tachyonic oscillations are generally preceded by a phase of tachyonic preheating. The latter may be so efficient that the growth of fluctuations is terminated in less than a single homogeneous oscillation of the inflaton ϕ [150]. On the other hand, if tachyonic preheating is too mild for non-linear effects to become important the field will eventually start performing coherent oscillations around the minimum of its potential. Unless the damping caused by the expansion of the universe is too strong, the inflaton may thereby periodically re-enter into the tachyonic region.

Tachyonic amplification will be experienced by all modes which acquire a negative frequency squared $\omega_k^2 < 0$ inside the tachyonic region of the potential ($\frac{\partial^2 V}{\partial \phi^2} < 0$), i.e. for modes

$$\frac{k}{a} < \frac{k_{\max}}{a} \equiv \max\left[\sqrt{-\frac{\partial^2 V}{\partial \phi^2}}\right] = \sqrt{-\frac{\partial^2 V}{\partial \phi^2}}\bigg|_{\phi \equiv \phi_{\max}} , \tag{4.38}$$

where $\phi_{\max}$ is the inflaton field value at which $-\frac{\partial^2 V}{\partial \phi^2}$ has its local minimum. Considering the hilltop inflation potential (3.76), we have [150]

$$k_{\max} = \frac{p\sqrt{V_0}}{v}\left(\frac{p-2}{2(2p-1)}\right)^{\frac{p-2}{2p}} , \quad \text{and} \quad \phi_{\max} = v\left(\frac{p-2}{2(2p-1)}\right)^{\frac{1}{p}} . \tag{4.39}$$

Conditions for tachyonic oscillations

Tachyonic oscillations will generally occur when the following three conditions are satisfied:

1. The scalar potential must feature a negative curvature in some field region, such that

$$\frac{k^2}{a^2} < -\frac{\partial^2 V}{\partial \phi^2} ,$$

for wavenumbers $k/a < k_{\max}/a \equiv \max[|\partial^2 V/\partial \phi^2|^{1/2}]$.

2. Tachyonic preheating must be sub-dominant in the sense that the backreaction of the fluctuations should not become important during the first descent of the inflaton towards its VEV.

3. Hubble damping should not be too strong in order to allow the field to repeatedly re-enter into the tachyonic region.

For the hilltop inflation model (3.76) these conditions can be formulated more concretely in terms of the model parameters, as was done in [150]. The backreaction of the fluctuations becomes important when the variance $\langle \delta\phi^2 \rangle$ grows to values comparable to v^2 [150]. Hence, if $\langle \delta\phi_{\mathbf{k}}^2 \rangle < v^2$ after the first roll down of the inflaton, preheating does not immediately end. The value of the variance after the first stage of tachyonic preheating can be estimated analytically [150]. In essence, the second condition is satisfied if the following inequality holds:

$$\left(\frac{v}{m_{\rm Pl}}\right)^{1/(p-2)} > \frac{V_0^{1/4}}{v}\left[2p(p-1)^{p-1}\right]^{1/(2p-4)} . \tag{4.40}$$

The energy loss ΔV, during the first oscillation of the background can be estimated as [150, 154]

$$\Delta V = V(\phi_{\rm end}) - V(\phi_1) \approx 3H\dot{\phi}\Delta\phi\,, \tag{4.41}$$

where $0 \simeq \phi_{\rm end} \ll v$ is the inflaton field value at the end of inflation, and $\phi_{\rm end} < \phi_1 \ll v$ is the minimum field value after one complete oscillation of ϕ. During the first oscillation one can approximate the quantities on the right-hand side of (4.41) as $H \simeq \sqrt{V_0/3}/m_{\rm Pl}$, $\Delta\phi \approx 2v$, and $\dot{\phi} \approx \sqrt{V_0}$. Since the potential energy at the end of the slow-roll regime is still approximately constant we have $V(\phi_{\rm end}) \simeq V_0$. In order to evluate $V(\phi_1)$ we can neglect the term proportional to $(\phi/v)^{2p}$ in the potential (3.76), since $\phi_1 \ll v$. Then, resolving eq. (4.41) for ϕ_1 gives [150]

$$\frac{\phi_1}{v} \approx \left(\frac{\sqrt{3}}{m_{\rm Pl}}v\right)^{1/p} . \tag{4.42}$$

If ϕ_1 is smaller than the inflaton field value $\phi_{\rm inf}$ at the inflection point

$$\partial^2 V/\partial\phi^2\big|_{\phi=\phi_{\rm inf}} = 0\,, \tag{4.43}$$

the inflaton re-enters into the tachyonic region and the third condition is satisfied, at least after the first complete oscillation of the homogeneous background. The field value at the inflection point can be calculated by solving eq. (4.43) for $\phi_{\rm inf}$. This gives

$$\phi_{\rm inf} = \left(\frac{p-1}{2p-1}\right)^{1/p} v\,. \tag{4.44}$$

By comparing this expression with (4.42) we obtain an upper bound on v:

$$\phi_1 < \phi_{\rm inf} \quad \Leftrightarrow \quad v < \frac{m_{\rm Pl}}{\sqrt{3}}\left(\frac{p-1}{2p-1}\right) \sim \mathcal{O}(0.1)\, m_{\rm Pl}\,. \tag{4.45}$$

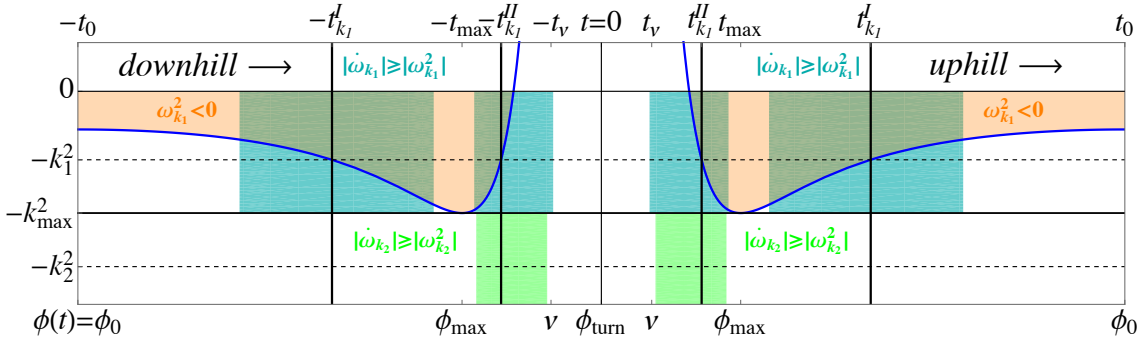

Figure 4.4: Schematic illustration of the different evolutionary phases of inflaton fluctuations during one homogeneous oscillation in Minkowski spacetime. The solid blue line represents the evolution of the curvature of the hilltop inflation potential. The time variable is rescaled such that $t = 0$ after half a period of oscillation. Here we qualitatively show the different evolutionary regimes experienced by two different modes $k_1 < k_{\max}$ and $k_2 > k_{\max}$ denoted by the dashed lines. For a detailed discussion we refer to the main text below.

Tachyonic oscillations in Minkowski spacetime

In order to get an understanding of tachyonic oscillations, it is instructive to first consider the behaviour of different modes during one period of oscillation of the homogeneous inflaton ϕ in Minkowski spacetime. Notice that in this case the background evolution is periodic. Subsequently, we comment on effects induced by the expansion of the universe.

Evolution of modes with $k \gg k_{\max}$ and $k \gtrsim k_{\max}$:

We begin our discussion with the simplest case which is the linear evolution of short-wavelength modes for which $k \gg k_{\max}$. For these modes, the frequency squared is always positive, though time-dependent. If the frequency varies slowly enough ($|\dot\omega_k| \ll \omega_k^2$), however, an oscillatory WKB approximation (cf. (4.36)) can be used to describe the evolution of the short-wavelength fluctuations.

On the other hand, modes with wavenumbers k that are only slightly larger than $k_{\max}$ can experience non-adiabatic growth in form of a self-resonance [150]. The WKB approximation is no more applicable in such a case and the mode evolution must be followed differently, e.g. by numerically solving the mode equation, though it is not impossible to find analytical estimates as demonstrated in Ref. [150].

The approach used by the authors in [150] is based on subdividing the evolution of the modes into qualitatively different regimes during one oscillation of the inflaton background. Within each of these regimes the evolution has been solved independently and matched at the interfaces between two different regimes.

The different regimes are illustrated in figure 4.4 for a mode $k_2 > k_{\max}$ as well as for a tachyonic mode with $k_1 < k_{\max}$. Moreover, note that $t = 0$ denotes the time after half a period of oscillation. The solid blue line denotes the curvature of the potential during one homogeneous background oscillation. The inflaton is assumed to start oscillating at $\phi(t = -t_0) \equiv \phi_0$ with $\dot\phi(-t_0) = 0$. Let us now consider

the former case for which the frequency squared is always positive ($\omega_{k_2}^2 > 0$ for $t \in [-t_0, t_0]$).

As the inflaton rolls downhill towards $\phi = v$, the evolution of the mode $k_2 > k_{\max}$ is adiabatic between $t = -t_0$ and $t \gtrsim -t_{\max}$ where the mode enters into the non-adiabatic regime ($-t_{\max} \lesssim t \lesssim -t_v$). The evolution becomes again adiabatic around the turning point ($t = 0$ and $\phi_{\text{turn}} > v$) and the field starts rolling back. On the way back, the inflaton re-enters into the non-adiabatic region ($t_v \lesssim t \lesssim t_{\max}$) and eventually climbs up the potential. Thereby, it crosses $\phi = v$ and $\phi = \phi_{\max}$ for the second time, after which the mode evolution becomes again adiabatic. Once the field reaches $\phi = \phi(t_0) = \phi_0$ (i.e. after one complete oscillation), the process repeats.

Within the adiabatic regions (uncolored regions along the dashed horizontal line where $\partial^2 V/\partial\phi^2 = -k_2^2$), in particular for $t \leq -t_{\max}$ and $t \geq t_{\max}$ the evolution of the mode with $k_2 > k_{\max}$ can be described by an oscillatory WKB approximation. For the time interval $-t_{\max} \leq t \leq t_{\max}$, where the frequency departs from adiabaticity, the authors of [150] derived an exact solution to an approximate version of the mode equation. In essence, the solution was obtained by replacing the curvature of the potential in the mode equation by an approximate function, for which the equation has an exact solution (see [150] for details). The WKB approximation and the exact solution were then matched at the interfaces $t = \pm t_{\max}$.

In Minkowski space this process repeats periodically and is therefore sufficient to have the solution of the modes throughout one period of oscillation. The only thing which changes from oscillation to oscillation are the initial conditions of the modes at $\phi(t) = \phi_0$. Analytical estimates for e.g. the behaviour of the occupation numbers n_k obtained through this approach are presented in [150] to which we refer for further details.

Evolution of modes with $k < k_{\max}$:

Let us now consider the behaviour of tachyonic modes $k < k_{\max}$. While the field rolls down its potential towards its VEV it eventually passages through the tachyonic region (orange region in figure 4.4), these modes get exponentially amplified due to a tachyonic instability. Notice that the amount of amplification depends on the wavenumber k. Long wavelength modes with $k \gg k_{\max}$ enter earlier into the region where $\omega_k^2 < 0$, while modes $k \lesssim k_{\max}$ enter later.

The mode with wavenumber k_1 as depicted in figure 4.4, for example, experiences exponential growth for $-t_{k_1}^I \leq t \leq -t_{k_1}^{II}$, and as well for $t_{k_1}^{II} \leq t \leq t_{k_1}^I$. The cyan regions denotes periods in which the frequency ω_{k_1} varies non-adiabatically. As one can see, the mode with $k = k_1$ does not only become tachyonic, but also evolves non-adiabatically within certain periods. Outside these non-adiabatic regions, but still within the tachyonic region, the mode evolution can be described with an epxponentially evolving WKB approximation[8] [150] (cf. eq. (4.37)).

The evolution of these tachyonic modes has been studied analytically in Ref. [150]. The approach taken by the authors is thereby formally equivalent to that described above for modes $k > k_{\max}$. In essence, the evolution of a given mode was subdivided

[8] See also Refs. [173, 174].

into regions in which the evolution is qualitatively different. The authors of [150] differentiated between purely adiabatic and purely tachyonic regions for $t \leq -t_{\max}$ and $t \geq t_{\max}$, and assumed non-adiabatic evolution for $-t_{\max} \leq t \leq t_{\max}$.

We note that this assumption is, strictly speaking, not justified as demonstrated explicitly in figure 4.4 for the mode $k_1 < k_{\max}$. For that mode we have computed $\dot{\omega}_{k_1}$ and, as can be seen in figure 4.4, it turns out that within certain periods the corresponding mode exhibits non-adiabatic tachyonic growth. Nevertheless, the results presented in [150] are in excellent agreement[9] with those obtained from numerical computations. This, in turn, may indicate that the effect related to the non-adiabatic change of ω_k, inside the tachyonic region, might be sub-dominant.

In [150] the authors assumed adiabaticity outside the tachyonic regions for $t < -t^I_{\rm tach}$ and $t > t^{\rm I}_{\rm tach}$. The evolution of the modes within these two regimes was described by assuming two different[10] oscillating WKB solutions. The latter were then matched at the interfaces $t = -t^{\rm I}_{\rm tach}$ and $t = t^{\rm I}_{\rm tach}$ with two different, exponentially evolving WKB solutions. Around the turning point, where the mode frequency varies non-adiabatically (cf. figure 4.4) the authors proceeded as in the case where $k > k_{\max}$ discussed above, i.e. by replacing $\partial^2 V/\partial\phi^2$ in the mode equation with an approximate function for which an exact solution can be found. The corresponding solution obtained for $-t_{\max} \leq t \leq t_{\max}$ was then matched at the interfaces with the WKB solutions that describe the mode evolution inside the tachyonic region. The matching of solutions essentially fixes the (constant) Bogolyubov coefficients[11] within the respective adiabatic regions.

As mentioned above, the tachyonic modes grow exponentially while the field rolls downhill towards its VEV. The opposite is the case as the field rolls back uphill, towards its initial value $\phi = \phi_0$. There the modes *decrease* exponentially. Naively, one may expect that the overall growth of modes is cancelled by this effect, since the evolution of ϕ is symmetric around $t = 0$. From the matching of solutions at $t = t_{\max}$, however, it turns out that the decrease of modes, experienced while ϕ rolls uphill inside the tachyonic region, is essentially k dependent [150]. The duration of the period during which the tachyonic modes decrease was found to last less than the time spent inside the tachyonic region [150]. Contrary to the scenario of tachyonic preheating where the growth is maximised for modes in the IR, tachyonic oscillations are found to be most efficient more towards the UV around a characteristic peak scale $H \ll k_{\rm p}$ that we shall further specify in the following.

Effect of the expansion

So far we have discussed how tachyonic oscillations lead to growth of fluctuations in Minkowski spacetime. Let us now briefly comment on the effect of the universe's expansion which has been studied analytically in [150].

In an expanding universe the amplitude of the homogeneous background does not remain constant throughout each oscillations, but gets rather continuously damped. For fluctuations with very small wavenumbers this can cause a net growth that is

[9] See figure 7 in [150].

[10] Basically corresponding to different Bogolyubov coefficients for $t < -t^{\rm in}_{\rm tach}$ and $t > t^{\rm in}_{\rm tach}$.

[11] In other words, the coefficients α_k and β_k in eqs. (4.36) and (4.37).

slightly enhanced compared to the situation in Minkowski spacetime. This is due to the fact that as the inflaton rolls back up its potential (i.e. towards small field values) at the end of an entire oscillation, it eventually does not reach the same field value from where it started rolling down towards its minimum at the beginning of the oscillation. This, in turn, means that the fluctuations spend less time per oscillation inside the region in which the fluctuations exponentially decrease.

Another effect is that the comoving modes get redshifted as the universe expands. In essence, both the redshifting of the homogeneous amplitude and of the mode effectively lead to time-dependent rates of growth.

As mentioned above, the growth of fluctuations caused by tachyonic oscillations is most efficient around a characteristic scale $k_{\rm p}$. For the hilltop inflation model (3.76) it was shown in [150] that at the end of preheating, when $\langle \delta\phi^2 \rangle \sim v^2$, this peak scale is approximately given by

$$\frac{k_{\rm p}}{a} \simeq \left(\frac{v}{m_{\rm Pl}}\right)^{\frac{p-2}{2p}} m_\phi \,, \tag{4.46}$$

where $m_\phi = \sqrt{\frac{2p^2 V_0}{v^2}}$ is the inflaton's mass evaluated at the minimum of the potential $\phi = v$.

Example: numerical results of linear preheating after hilltop inflation

For an illustrative purpose and to conclude this section we would like to present some numerical results of linear preheating after hilltop inflation. We have simulated the evolution of the homogeneous inflaton and the linear perturbations for the hilltop inflation potential (3.76) with $p = 6$ and $v = 10^{-2} m_{\rm Pl}$ and $V_0 = 8.006 \times 10^{-20} m_{\rm Pl}^4$ as in table 3.1. To this end we have simultaneously solved the homogeneous field equation of motion (3.10) and the linearised equation for the perturbations

$$\delta\ddot{\phi}_{\mathbf{k}} + \left(\frac{k^2}{a^2} + \frac{\partial^2 V}{\partial \overline{\phi}^2}\right) \delta\phi_{\mathbf{k}} = 0 \,. \tag{4.47}$$

The initial value of the homogeneous field $\overline{\phi}_{\rm i}$ and its derivative $\dot{\overline{\phi}}_{\rm i}$ were chosen shortly after the end of the slow-roll regime when the Hubble parameter is still approximately constant and $\eta_V \simeq 25$:

$$\overline{\phi}_{\rm i} = 8.03 \times 10^{-2} v \quad \text{and} \quad \dot{\overline{\phi}}_{\rm i} = 2.21 \times 10^{-9} v^2 \,, \tag{4.48}$$

with the initial Hubble parameter set to $H_i = \sqrt{V_0/(3m_{\rm Pl}^2)}$. For the initial value of the field fluctuations $\delta\phi_{\mathbf{k}}$ we used Bunch-Davies vacuum initial conditions, given by eq. (C.1.8).

Figure 4.5 shows results of the numerical simulations. The upper plot shows the evolution of the homogeneous inflaton $\overline{\phi}$ in units of v (blue curve) and the evolution of the variance (4.8) (orange), over approximately six background oscillations. One can see that the variance of the fluctuations progressively increases after each oscillation. Moreover, notice that although the growth is most efficient when the inflaton

rolls down (i.e. when $\overline{\phi}/v < 1$ increases) one can clearly see that the variance eventually starts growing while $\overline{\phi}$ rolls uphill (i.e. when $\overline{\phi}/v$ decreases). As the fluctuations grow, the variance becomes comparable to v^2 within less than five background oscillations. The backreaction of the fluctuations on the zero-momentum mode then quickly becomes important and the linearised treatment is no more applicable [150].

The lower plot shows the spectrum of inflaton fluctuations (blue curves) at different moments in time. The spectra are shown in terms of comoving wavenumbers k/m_ϕ. Lighter blue tones correspond to earlier times, where the lightest blue curve corresponds to the initial vacuum spectrum. All other spectra are shown after consecutive oscillations of $\overline{\phi}$, when the field reaches its turning point for $\phi < v$ (i.e. its minimum value when $\dot{\overline{\phi}} = 0$ and $\overline{\phi} < v$). The darkest blue line shows the spectrum after five oscillations.

After five complete oscillations we can estimate the peak scale k_p according to (4.46) which gives

$$k_\mathrm{p} \simeq 0.31 m_\phi \,. \tag{4.49}$$

As can be seen from figure (4.5), this estimate is in good agreement with the numerical results.

For smaller scales $k > k_\mathrm{p}$, tachyonic oscillations become less and less efficient. As we explained above, the growth of these modes happens mainly due to self-resonant growth caused by the non-adiabatic variation of the frequency squared, i.e. essentially through broad parametric resonance [150].

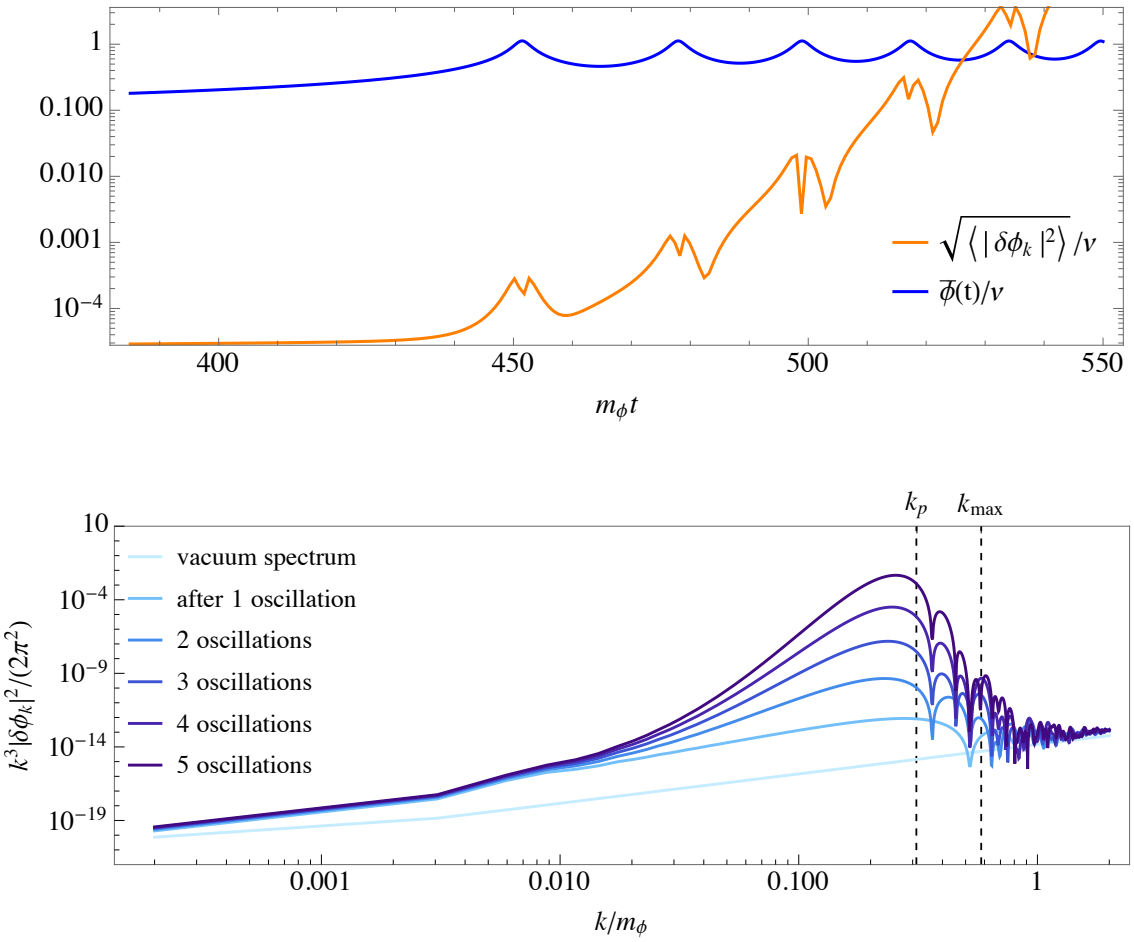

Figure 4.5: *Upper:* Evolution of $\overline{\phi}/v$ (blue curve) and $\langle|\delta\phi^2_{\mathbf{k}}|\rangle^{1/2}/v$ (orange), shown over ~ 6 oscillations of $\overline{\phi}$. The fluctuations grow mainly due to tachyonic amplification as can be seen from the behaviour of the variance. Indeed, the growth is the strongest while $\overline{\phi}$ rolls down (i.e. when $\overline{\phi} < v$ increases towards $\overline{\phi} = v$). After $\lesssim 5$ oscillations of $\overline{\phi}$ we have $(\langle|\delta\phi^2_{\mathbf{k}}|\rangle)^{1/2}/v \sim 1$, and the linearised description breaks down.
Lower: Spectra of inflaton fluctuations (blue curves) plotted as a function of the comoving wavenumbers k/m_ϕ shown at different moments in time, corresponding to different blue tones. The spectrum is shown after 1, 2,..., 5 complete oscillations of $\overline{\phi}$, at moments at which $\dot{\overline{\phi}} = 0$. The lightest blue curve shows the initial vacuum spectrum for comparison. The dashed lines denote the analytical estimate of characteristic peak scale $k_{\rm p}$, and the value $k_{\rm max}$ at the interface between tachyonic and non-tachyonic modes.

4.3 Non-standard preheating from the decay of string moduli

A generic feature of effective field theories of inflation that are formulated within the framework of SUGRA or string theory is the presence of (many) moduli fields[12]. As already mentioned in section 3.1, in scenarios of string compactification these fields parametrise the spacetime-dependent properties of compactified dimensions [177].

The presence of these moduli may not remain without consequence for the post-inflationary cosmological evolution. Indeed, moduli fields are often associated with a non-standard cosmological evolution after inflation which is sometimes referred to as *Modular Cosmology* [15–17]. The latter corresponds to an intermediate period of matter domination between reheating and the onset of BBN.

The reason for such an intermediate stage is the following: The moduli scalar potential usually depends on the VEV of the inflaton, which itself might be identified with one of the moduli of the theory. Moduli which acquire masses below the Hubble scale ($m < H$) get shifted from their post-inflationary VEV. This mechanism is often referred to as *Vacuum Misalignment*. In turn, this displacement ($\equiv \Delta\phi_{\rm i}$) from the post-inflationary minimum is typically [178–182]

$$\Delta\phi_{\rm i} \lesssim m_{\rm Pl}\,. \tag{4.50}$$

In such scenarios, the standard view of the post-inflationary evolution is the following: after inflation, moduli fields with masses $m < H$ are "frozen" at a distance $\Delta\phi_{\rm i} \lesssim m_{\rm Pl}$ from their post-inflationary minimum. The universe reheats and becomes radiation dominated until the Hubble parameter eventually drops below the modulus mass m. When this is the case the corresponding modulus becomes dynamical and starts oscillating around its post-inflationary VEV. Thereby, the universe gradually becomes dominated by the energy density of the modulus leading to late-time epoch of matter domination.

It is usually assumed that the moduli then decay into a thermal bath of radiation, after a characteristic time scale (see e.g. [183])

$$\tau_{\rm char} \simeq \frac{16\pi^2 m_{\rm Pl}^2}{m^3}\,, \tag{4.51}$$

thus leading to an additional stage of reheating. In the presence of many moduli with masses below the inflationary Hubble parameter, this process eventually repeats for several times. Moreover, requiring that the cosmological moduli problem is avoided puts the following constraint on the mass of the moduli (see e.g. [183])

$$m \gtrsim 30\,\text{TeV}\,. \tag{4.52}$$

Just as the inflaton, moduli fields are scalar fields and their dynamics are determined by their scalar potential. Depending on the potential, as well as on the transition into a modulus dominated epoch one may ask the question whether the

[12] See e.g. Refs. [18, 175–177].

dynamics of moduli could lead to non-perturbative and non-linear effects as in scenarios of preheating after inflation. Such a situation was considered in Ref. [3] within the context the KKLT scenario [21] as well as for a blow-up Kähler modulus in the LVS[13] [22, 23] and will be discussed in greater detail in chapter 7.

4.4 What can preheating teach us?

So far we have discussed some of the mechanisms that can drive the growth of scalar perturbations during preheating. In section 4.1 we have briefly mentioned that the dynamics during this stage can potentially give rise to various, model-dependent physical effects. Inevitably, the question arises what we can actually learn from this complicated and often dynamically rich process.

In this section we outline some of the physical consequences of preheating and how a complete understanding of this process can help to constrain models of the very early universe. We will mainly focus on those implications of preheating that are relevant to those models considered in the main part of this thesis. For a more complete outline we refer to [139].

4.4.1 Production of oscillons and related consequences

All the models considered within the main part of this thesis in which the dynamics are found to become non-linear have one feature in common: the production of oscillons [7–14].

Oscillons are localised, quasi-spherical, and non-linear configurations of real scalar fields. As their name suggests these configurations are oscillatory and are characterside by the fact that the amplitude of oscillations within these localised regions is generically much larger than that of their environment. Oscillons were found to naturally form in models of inflation [13, 14, 192–196] and also in other field theoretical scenarios [7, 8, 197–200]. Despite the fact that they continuously radiate[14] energy in form of scalar waves [186, 187], they were found to be extremely long-lived compared to their period of oscillation [11, 188–191].

In figure 4.6 we show successive snapshots of the spatial field distribution showing the field profile of an oscillon, represented by a two-dimensional slice through a three-dimensional oscillon. The snapshots are taken at different moments in time throughout half a period of oscillation. One can see that the oscillon clearly stands out among the background which exhibits only tiny fluctuations compared to the relatively large-amplitude of the oscillon.

Conditions for oscillon formation

In order for quasi-stable oscillons to be formed, three necessary conditions must be satisfied (see for instance [7, 201]):

[13] For an earlier study of the non-linear dynamics during preheating after Kähler Moduli Inflation see [184].

[14] For a work in which the quantum radiation of oscillons has been studied see Ref. [185].

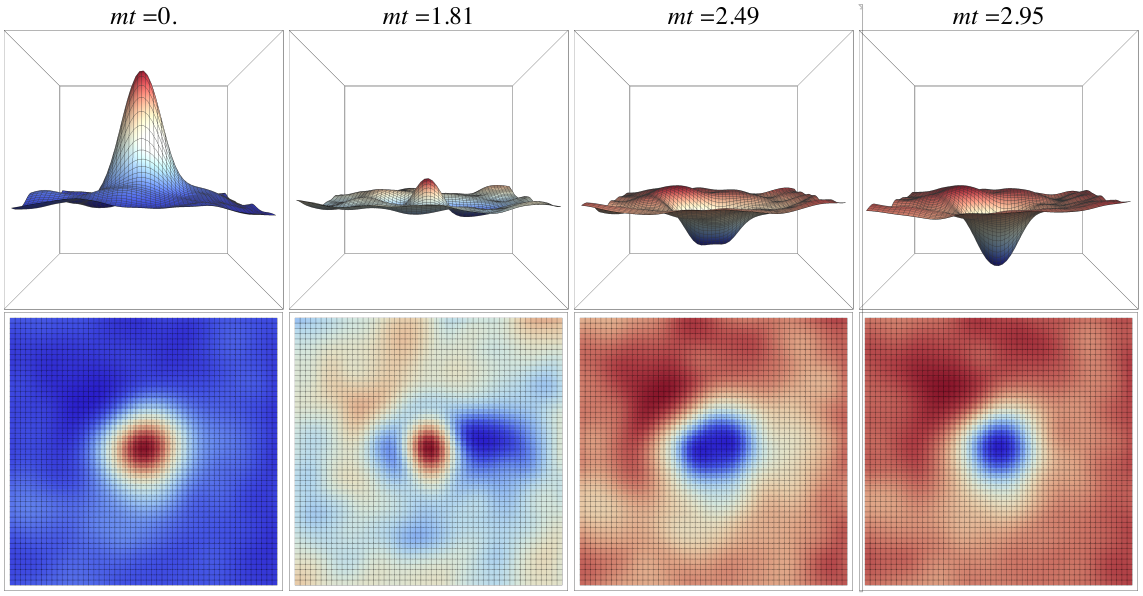

Figure 4.6: Successive snapshots of the spatial field distribution showing the field profile of an oscillon, here represented by a two-dimensional slice through a three-dimensional oscillon. The figure was obtained from the results of lattice simulations of the hilltop inflation model (3.76) with $p = 6$ and $v = 10^{-2} m_{\rm Pl}$. The field distribution is shown at different moments in time throughout about half a period of oscillation. The time is shown relative to the first slice (where we set $t = 0$) and in units of the inflaton mass m at the minimum of its potential. As one can see, the oscillon performs half an oscillation in a time $m\Delta t \simeq 3$.

1. There must be an efficient (preheating) mechanism that allows for the growth of scalar fluctuations.

2. The growth of the field fluctuations must be sufficiently strong for non-linear interactions to become important.

3. The scalar potential must be shallower than quadratic within some region around the minimum of the potential[15].

The first and second conditions are, strictly speaking, only required to provide suitable "initial conditions" for the formation of oscillons. The third condition is, in turn, necessary for the potential to support stable and localised scalar field configurations. Notice, that it may well be that all three conditions are satisfied, but that no oscillons are formed. In fact, an arbitrary fluctuation will not necessarily relax into an oscillon, unless its wavelength and amplitude lies within a certain range that favours the formation.

[15]For a more precise condition which is, however, only applicable to small amplitude oscillons see [202].

Possible implications for oscillon-featuring cosmological environments

The existence of oscillons in a cosmological environment can have different implications. Due to their non-linear nature and their longevity, oscillons could give rise to an extended period of matter domination unless they behave as relativistic matter. This, in turn, can extend the duration of the entire reheating process [139]. In certain models oscillons were found to have an impact on the outcome of baryogenesis [203, 204].

As we can clearly see from figure 4.6 oscillons are not perfectly symmetric. This is due to the fact that they interact with their environment and also among themselves. Since these objects are not perfectly symmetric, their dynamics could lead to the production of GWs. The latter has first been studied in [205] within the context of axion-monodromy inflation [206, 207], but also in Refs. [2] for the hilltop inflation model (3.76) with $p = 6$ and $v = 10^{-2} m_{\rm Pl}$. GWs from oscillons have also been investigated for "cuspy" potentials where the scalar potential is of the form $V(\phi) \sim |\phi|^p$ [208].

If GWs from oscillons would be observed at some point in the future, this could in principle provide us valuable information about the underlying theory. Later, in the main part of this thesis, we shall discuss which kind of information might be extracted from the oscillation of a GW signal generated by oscillons.

4.4.2 Precise predictions for the primordial spectra

When we were discussing the inflationary dynamics of chaotic and hilltop inflation in section 3.4.1, we compared the model predictions for the primordial spectra with observational constraints (cf. figures 3.1 and 3.2). Thereby we showed different predictions corresponding to different assumptions for the time of horizon exit of the pivot scale $k_\star$, i.e. different values of the number of e-folds of inflation $N_\star$ experienced by the universe between the time of horizon exit and the end of inflation.

The reason for assuming a certain range for $N_\star$ rather than one precise value is due to the lack of knowledge about the post-inflationary evolution. In fact, for a given scale $k = a_k H_k$, the number of e-folds N_k at which k leaves the horizon is constrained by the following expression [209]

$$\frac{k}{a_0 H_0} = \frac{a_k H_k}{a_0 H_0} = e^{-N_k} \frac{a_{\rm end}}{a_{\rm reh}} \frac{a_{\rm reh}}{a_{\rm eq}} \frac{H_k}{H_{\rm eq}} \frac{a_{\rm eq} H_{\rm eq}}{a_0 H_0}\,, \tag{4.53}$$

where the subscripts "end", "reh", "eq", and "0" denote quantities evaluated at the end of inflation, at the end of reheating, at matter-radiation equality, and today.

For the Hubble parameter H_k at the time at which the scale k exits the horizon, we can use the slow-roll approximation

$$H_k = \sqrt{\frac{V_k}{3\, m_{\rm Pl}^2}}\,. \tag{4.54}$$

Moreover, the factor $a_{\rm eq}/a_0$ is simply given by the redshift at matter-radiation equality, i.e.

$$\frac{a_{\rm eq}}{a_0} = (1 + z_{\rm eq})^{-1} = 1/3366\,, \tag{4.55}$$

where in the last equality we have inserted $z_{\rm eq} = 3365$ (cf. table 4 in [5]).

Between the end of reheating and matter-radiation equality, the universe is dominated by radiation, thus implying (cf. eq. (2.19))

$$\frac{a_{\rm reh}}{a_{\rm eq}} \;=\; \left(\frac{\rho_{\rm reh}}{\rho_{\rm eq}}\right)^{-1/4} . \tag{4.56}$$

The energy density at matter-radiation equality can be calculated as follows

$$\rho_{\rm eq} \;=\; 2\,\rho_{\rm m,eq} \;=\; 2\,\rho_{\rm m,0}\left(\frac{a_0}{a_{\rm eq}}\right)^3 \;=\; 6\,\Omega_{\rm m,0} m_{\rm Pl}^2\,H_0^2\,(1+z_{\rm eq})^3 \;, \tag{4.57}$$

with $\rho_{\rm m,0}$ and $\rho_{\rm m,eq}$ denoting the present energy density of non-relativistic matter and at matter-radiation equality.

Resolving eq. (4.53) for N_k and replacing the corresponding quantities gives

$$N_k \;=\; \frac{1}{4}\ln\left[\frac{2\,m_{\rm Pl}^2\,\Omega_{\rm m,0}\,H_0^2\,V_k}{3\,m_{\rm Pl}^4\,(1+z_{\rm eq})}\frac{a_0^4}{k^4}\right] + \frac{1}{4}\ln\left[\frac{V_k}{\rho_{\rm reh}}\right] + \ln\left[\frac{a_{\rm end}}{a_{\rm reh}}\right] . \tag{4.58}$$

Taking [5]

$$\Omega_{\rm m,0} \;=\; 0.308 \quad \text{and} \quad H_0 \;=\; 67.81\,\mathrm{km\,s^{-1}Mpc^{-1}} \,, \tag{4.59}$$

for the present day matter density parameter and the present Hubble parameter, and $z_{\rm eq}$ as in eq. (4.55), we can evaluate (4.58) for $k_\star = k/a_0$ which yields

$$N_\star \;\approx\; 61.8 + \ln\left[\frac{a_{\rm end}}{a_{\rm reh}}\right] + \frac{1}{4}\ln\left[\frac{V_k}{\rho_{\rm reh}}\frac{V_k}{m_{\rm Pl}^4}\right] . \tag{4.60}$$

Assuming that the background evolution can be described by an effective EOSp $w_{\rm eff}$ during the reheating process, we may write[16] (see e.g. [5, 210])

$$\begin{aligned} N_\star \;&\approx\; 61.8 + \frac{1}{3(1+w_{\rm eff})}\ln\left[\frac{\rho_{\rm reh}}{\rho_{\rm end}}\right] + \frac{1}{4}\ln\left[\frac{V_k}{\rho_{\rm reh}}\frac{V_k}{m_{\rm Pl}^4}\right] \\ &=\; 61.8 + \frac{1-3w_{\rm eff}}{12(1+w_{\rm eff})}\ln\left[\frac{\rho_{\rm reh}}{\rho_{\rm end}}\right] + \frac{1}{4}\ln\left[\frac{V_k}{\rho_{\rm end}}\frac{V_k}{m_{\rm Pl}^4}\right] . \end{aligned} \tag{4.61}$$

We can see that the precise value of $N_\star$ depends on how the universe evolves between the end of inflation and the end of reheating. This, in turn, may crucially depend on the dynamics during preheating. Consequently, for a precise estimate of $N_\star$, a careful study of (p)reheating is indispensable.

4.4.3 Production of GWs – The early universe's fingerprint?

As emphasised above, preheating after inflation as well as other preheating-like scenarios in which other scalar fields (e.g. moduli fields) are involved may have

[16] Where we have omitted an additional term of $\lesssim \mathcal{O}(1)$ depending on the number of effective bosonic degrees of freedom (cf. [5]).

taken place at very early times, before the synthesis of the light nuclei. The potentially violent dynamics during such regimes can give rise to an inhomogeneous fragmentation of the involved scalar degrees of freedom and thus to the production of GWs [2, 3, 162, 205, 208, 211–218]. Whether and how such a fragmentation occurs is essentially model-dependent. Consequently, also the resulting stochastic GW background, if produced, will exhibit features that are characteristic to the model at hand. Examples of such features are e.g. the bandwidth of frequencies at which GWs are produced, but also the characteristic amplitude of the energy spectrum, and more interestingly its shape (i.e. the frequency-dependence of the amplitude).

While CMB observations provide constrains on the shape of the inflaton potential *during* inflation, GWs produced during the reheating process could be a promising candidate for filling the observational gap between the time of horizon exit and recombination. This is essentially due to the fact that, unlike the CMB photons, GWs can propagate almost freely since the time of their production.

Unfortunately, GWs which are associated with the dynamics of preheating are often produced at frequencies too high to be observable with current and planned GW detectors [219–223]. Nevertheless, models predicting GWs with frequencies in the observational range do exist [208, 224, 225].

GW production from inhomogeneous scalar fields

In the following we discuss the production of GWs when sourced by inhomogeneities of scalar fields. We will thereby follow the discussions presented in section 2 and 3 of Ref. [214] and summarise the main results.

Consider a system of N_f scalar fields in an expanding FLRW background whose dynamics are governed by the action (4.5). Including perturbations of the metric in synchronous coordinates we may write the perturbed FLRW line-element as

$$ds^2 \;=\; g_{\mu\nu}dx^\mu dx^\nu \;=\; -dt^2 + a^2(t)(\delta_{ij} + \tilde{h}_{ij})dx^i dx^j \,. \tag{4.62}$$

GWs are then represented by the Transverse-Traceless (TT) part ($\equiv h_{ij}$) of the metric perturbation $\tilde{h}_{ij}$. In the following, we will only consider the evolution of the GWs and neglect[17] the vector and scalar modes that are comprised within $\tilde{h}_{ij}$. In turn, the GWs obey the equation of motion

$$\ddot{h}_{ij} \;+\; 3H\dot{h}_{ij} \;-\; \frac{1}{a^2}\nabla^2 h_{ij} \;=\; \frac{2}{m_{\rm Pl}^2}\Pi_{ij}^{\rm TT} \,. \tag{4.63}$$

The quantity $\Pi_{ij}^{\rm TT}$ which provides the source of the GWs denotes the TT part of the anisotropic stress

$$a^2\Pi_{ij} = \left(T_{ij} - a^2\, p\,(\delta_{ij} + h_{ij})\right) \,, \tag{4.64}$$

with p denoting the homogeneous background pressure, and T_{ij} represents the (i,j) component of the energy-momentum tensor which is given as in eq. (3.5) but with

[17] We note that scalar metric fluctuations can have an impact on the evolution of the GWs and can in particular lead to an enhanced GW energy density, even if the backreaction on the scalar fields is negligible [226].

the only difference that we now sum over all the contributing fields $\phi^1, \ldots, \phi^{N_f}$

$$T_{\mu\nu} = \sum_\ell \left[\partial_\mu \phi^\ell \partial_\nu \phi^\ell - g_{\mu\nu} \left(\frac{1}{2} g^{\rho\sigma} \partial_\rho \phi^\ell \partial_\sigma \phi^\ell + V \right) \right] . \tag{4.65}$$

After extracting the TT part of eq. (4.64) and keeping only terms which are first order in the gravitational coupling, the source term of the GWs reduces to[18] [214]

$$\Pi_{ij}^{\mathrm{TT}} = \frac{1}{a^2} T_{ij}^{\mathrm{TT}} = \frac{1}{a^2} \sum_\ell \left[\partial_i \phi^\ell \partial_j \phi^\ell \right]^{\mathrm{TT}} . \tag{4.66}$$

In order to solve the evolution equation (4.63) one may use different approaches (see e.g. Refs. [162, 211, 214]). One possibility is to solve both, the field evolution as well as (4.63) numerically on a discrete spacetime lattice. Later in the main part of this thesis we shall, indeed, present results that were obtained by means of this method.

Here we concentrate on a different approach that is also used in this thesis and that was first proposed in [214]. It is based on solving eq. 4.63 in Fourier space, which adopting the Fourier convention eq. (A.0.5), reads

$$\ddot{h}_{ij}(\mathbf{k}, t) + 3H \dot{h}_{ij}(\mathbf{k}, t) + \frac{k^2}{a^2} h_{ij}(\mathbf{k}, t) = \frac{2}{m_{\mathrm{Pl}}^2} \Pi_{ij}^{\mathrm{TT}}(\mathbf{k}, t) , \tag{4.67}$$

where again $k = |\mathbf{k}|$ denotes the magnitude of *comoving* momentum. The TT part of the anisotropic stress Π_{ij} can now be extracted as follows

$$\begin{aligned} \Pi_{ij}^{\mathrm{TT}}(\mathbf{k}, t) &= \Lambda_{ij,lm}(\hat{\mathbf{k}}) \, \Pi_{ij}(\mathbf{k}, t) \\ &= \left(P_{il}(\hat{\mathbf{k}}) P_{jm}(\hat{\mathbf{k}}) - \frac{1}{2} P_{ij}(\hat{\mathbf{k}}) P_{lm}(\hat{\mathbf{k}}) \right) \Pi_{ij}(\mathbf{k}, t) , \end{aligned} \tag{4.68}$$

where $P_{ij}(\hat{\mathbf{k}})$ is called projection tensor and is defined as [27]

$$P_{ij}(\hat{\mathbf{k}}) \equiv \delta_{ij} - \hat{k}_i \hat{k}_j , \quad \text{and} \quad \hat{k}_i \equiv k_i / |\mathbf{k}| . \tag{4.69}$$

To solve eq. (4.67) it is convenient to rewrite it in terms of conformal time $d\eta = a^{-1} dt$ and in terms of the rescaled perturbation

$$\bar{h}_{ij} \equiv a h_{ij} . \tag{4.70}$$

Eq. (4.67) then becomes

$$\bar{h}_{ij}''(\mathbf{k}, \eta) + \left(k^2 - \frac{a''}{a} \right) \bar{h}_{ij}(\mathbf{k}, \eta) = \frac{2}{m_{\mathrm{Pl}}^2} \, a \, T_{ij}^{\mathrm{TT}}(\mathbf{k}, \eta) . \tag{4.71}$$

Within this thesis we focus on GWs sourced by sub-horizon sized inhomogeneities corresponding to scales $k \gg aH$. In this limit we can drop the term proportional to a'' in eq. (4.71) and eq. (4.71) reduces to

$$\bar{h}_{ij}''(\mathbf{k}, \eta) + k^2 \bar{h}_{ij}(\mathbf{k}, \eta) = \frac{2}{m_{\mathrm{Pl}}^2} \, a \, T_{ij}^{\mathrm{TT}}(\mathbf{k}, \eta) . \tag{4.72}$$

[18] The term $\propto p \delta_{ij}$ is a pure trace and vanishes after extracting the TT part, while the term $\propto p h_{ij}$ gives rise to a term that is second order in the gravitational coupling.

Notice, that in the case of a radiation dominated cosmological background we have in any case $a''/a = 0$. If the universe evolves as matter $a''/a \sim a^2 H^2 \ll k^2$ and the term can be neglected on scales well inside the horizon.

Assuming that the source is inactive for $\eta \leq \eta_{\rm i}$, (and thus $\bar{h}_{ij}(\mathbf{k},\eta) = \bar{h}'_{ij}(\mathbf{k},\eta) = 0$), the solution to eq. (4.72) may be written as [214]

$$\bar{h}_{ij}(\mathbf{k},\eta) = \frac{2}{m_{\rm Pl}^2\, k} \int_{\eta_{\rm i}}^{\eta} d\eta' \sin\left[k(\eta-\eta')\right]\, a(\eta')\, T_{ij}^{\rm TT}(\mathbf{k},\eta')\,. \tag{4.73}$$

The above solution is valid as long as GWs are actively produced. Once the source becomes inactive, say at $\eta = \eta_f$, the GWs will eventually start propagating freely, obeying the wave equation

$$\bar{h}''_{ij}(\mathbf{k},\eta) + k^2 \bar{h}_{ij}(\mathbf{k},\eta) = 0\,, \quad \text{for} \quad \eta \geq \eta_{\rm f}\,. \tag{4.74}$$

Eq. (4.74) has an oscillating solution which can be expressed as

$$\bar{h}_{ij}(\mathbf{k},\eta) = A_{ij}(\mathbf{k})\, \sin[k\,(\eta_{\rm f}-\eta)] + B_{ij}(\mathbf{k})\, \cos[k\,(\eta_{\rm f}-\eta)]\,, \tag{4.75}$$

with the $\mathbf{k}$-dependent coefficients A_{ij} and B_{ij} yet to be determined. Requiring that the solution (4.73) coincides with (4.75) at $\eta = \eta_{\rm f}$ (and requiring the same for $\bar{h}'_{ij}$) one finds

$$B_{ij}(\mathbf{k}) = \bar{h}_{ij}(\mathbf{k},\eta_{\rm f}) = \frac{2}{m_{\rm Pl}^2\, k} \int_{\eta_{\rm i}}^{\eta_{\rm f}} d\eta' \sin\left[k(\eta_{\rm f}-\eta')\right]\, a(\eta')\, T_{ij}^{\rm TT}(\mathbf{k},\eta')\,, \tag{4.76}$$

$$A_{ij}(\mathbf{k}) = k^{-1}\, \bar{h}'_{ij}(\mathbf{k},\eta_{\rm f}) = \frac{2}{m_{\rm Pl}^2\, k} \int_{\eta_{\rm i}}^{\eta_{\rm f}} d\eta' \cos\left[k(\eta_{\rm f}-\eta')\right]\, a(\eta')\, T_{ij}^{\rm TT}(\mathbf{k},\eta')\,. \tag{4.77}$$

Energy density and energy spectrum of GW

Let us now introduce the energy density of GWs which is formally given by the 00-component of the effective stress-energy tensor of GWs (see e.g. [27, 227])

$$T_{\mu\nu}^{\rm GW} \;=\; \frac{m_{\rm Pl}^2}{4} \langle \partial_\mu h_{ij} \partial_\nu h^{ij} \rangle_{\mathcal{V}}\,, \tag{4.78}$$

where the angle brackets denote an average over a portion of (comoving) volume $\mathcal{V}$ encompassing length scales that are large compared to the characteristic wavelength of the GWs. The expression on the right-hand side of (4.78) was first derived by R. Isaacson in the 1960s [228, 229]. It is therefore sometimes referred to as Isaacson stress-energy tensor (see e.g. [227]).

The energy density carried by the GWs is given by

$$\begin{aligned}
\rho_{\rm GW} \;\equiv\; T_{00}^{\rm GW} \;&=\; \frac{m_{\rm Pl}^2}{4} \langle \dot{h}_{ij}(\mathbf{x},t) \dot{h}_{ij}(\mathbf{x},t) \rangle_{\mathcal{V}} \\
&\simeq \frac{m_{\rm Pl}^2}{4a^4} \langle \bar{h}'_{ij}(\mathbf{x},\eta) \bar{h}'_{ij}(\mathbf{x},\eta) \rangle_{\mathcal{V}} \\
&= \frac{m_{\rm Pl}^2}{4a^4} \frac{1}{\mathcal{V}} \int_{\mathcal{V}} d^3\mathbf{x} \bar{h}'_{ij}(\mathbf{x},\eta) \bar{h}'_{ij}(\mathbf{x},\eta) \\
&= \frac{m_{\rm Pl}^2}{4a^4} \frac{1}{\mathcal{V}} \int \frac{d^3\mathbf{k} d^3\mathbf{k}'}{(2\,\pi)^6} \int_{\mathcal{V}} d^3\mathbf{x}\, e^{i(\mathbf{k}+\mathbf{k}')\mathbf{x}}\, \bar{h}'_{ij}(\mathbf{k},\eta) \bar{h}'_{ij}(\mathbf{k}',\eta) \\
&= \frac{m_{\rm Pl}^2}{4a^4} \frac{1}{\mathcal{V}} \int \frac{d^3\mathbf{k}}{(2\,\pi)^3}\, \bar{h}'_{ij}(\mathbf{k},\eta) \bar{h}'^{*}_{ij}(\mathbf{k},\eta)
\end{aligned} \tag{4.79}$$

where we dropped terms $\propto a\,H$ and $\propto a^2\,H^2$, respectively. These terms are negligible on sub-horizon scales $k \gg aH$.

The spectrum of GWs is defined as the energy density per logarithmic momentum interval and is typically normalised to the value of the critical density ρ_c (cf. eq. (2.16) in section 2.1)

$$\Omega_\mathrm{GW}(k,\eta) = \frac{1}{\rho_\mathrm{c}}\frac{d\rho_\mathrm{GW}}{d\ln\,k} = \frac{m_\mathrm{Pl}^2\,k^3}{\rho_\mathrm{c}\,4a^4}\frac{1}{\mathcal{V}}\int\frac{d\Omega}{(2\,\pi)^3}\,\bar{h}'_{ij}(\mathbf{k},\eta)\bar{h}'^{*}_{ij}(\mathbf{k},\eta)\,, \tag{4.80}$$

where $d\Omega$ here denotes a solid angle in momentum space. By replacing $\bar{h}'_{ij}$ in eq. (4.80) with the solution (4.75) one finds

$$\begin{aligned}\Omega_\mathrm{GW}(k,\eta) &= \frac{m_\mathrm{Pl}^2\,k^3}{\rho_\mathrm{c}\,4a^4}\frac{1}{\mathcal{V}}\int\frac{d\Omega}{(2\,\pi)^3}\,\langle\bar{h}'_{ij}(\mathbf{k},\eta)\bar{h}'^{*}_{ij}(\mathbf{k},\eta)\rangle_T \\ &= \frac{m_\mathrm{Pl}^2\,k^3}{\rho_\mathrm{c}\,4a^4}\frac{1}{\mathcal{V}}\int\frac{d\Omega}{(2\,\pi)^3}\frac{k^2}{2}\sum_{i,j}(|A_{ij}(\mathbf{k})|^2 + |B_{ij}(\mathbf{k})|^2)\,,\end{aligned} \tag{4.81}$$

where $\langle\ldots\rangle_T$ denotes an average over one period of oscillation $T = 2\pi/k$ for GWs with wavenumber k. Using eqs. (4.76) and (4.77) to replace the coefficients A_{ij} and B_{ij} the spectrum takes the form [214]

$$\begin{aligned}\Omega_\mathrm{GW}(k,\eta) = \frac{k^3}{2\,a^4\,\rho_\mathrm{c}\,m_\mathrm{Pl}^2}\frac{1}{\mathcal{V}}\int\frac{d\Omega}{(2\,\pi)^3}\sum_{i,j}\Bigg[&\left|\int_{\eta_\mathrm{i}}^{\eta_\mathrm{f}} d\eta'\cos(k\eta')\,a(\eta')\,T_{ij}^{\mathrm{TT}}(\mathbf{k},\eta')\right|^2 \\ &+ \left|\int_{\eta_\mathrm{i}}^{\eta_\mathrm{f}} d\eta'\sin(k\eta')\,a(\eta')\,T_{ij}^{\mathrm{TT}}(\mathbf{k},\eta')\right|^2\Bigg]\,.\end{aligned} \tag{4.82}$$

In cases where the spatial part of the stress-energy tensor can be estimated analytically one may either obtain analytical estimates or solve the integral eq. (4.82) numerically. In Ref. [214], for example, it was shown that superpositions of scalar perturbations which do not (or only weakly) interact with each other and for which the evolution can be approximated by a WKB solution do not emit gravitational waves. In order to compare the spectrum emitted at time $\eta = \eta_\mathrm{f}$, when the source becomes inactive, with present constraints from present (and future) GW observatories we have to account the expansion history between the time of emission η_f and today. Assuming that the universe evolves with an effective EOSp w between the moment at which the source becomes inactive ("f") and the end of reheating ("reh"), we may account for the relative expansion as follows

$$\begin{aligned}\frac{a_\mathrm{f}}{a_0} &= \frac{a_\mathrm{f}}{a_\mathrm{reh}}\frac{a_\mathrm{reh}}{a_0} \\ &= \frac{1}{\rho_\mathrm{f}^{1/4}}\left(\frac{a_\mathrm{f}}{a_\mathrm{reh}}\right)^{1-\frac{3}{4}(1+w)}\left(\frac{g_0}{g_\mathrm{reh}}\right)^{1/12}\rho_{\gamma,0}^{1/4}\,,\end{aligned} \tag{4.83}$$

where the subscript "0" denotes a quantity evaluated today, g is the number of relativistic degrees of freedom at the corresponding time, and $\rho_{\gamma,0}$ is the present

day radiation energy density. Moreover, we have used that entropy conservation[19] is satisfied for the thermal bath of radiation.

The energy density of GWs redshifts like radiation i.e. $\rho_{\rm GW} \sim a^{-4}$. Thus for the relation between the present day spectrum $\Omega_{\rm GW,\,0}$ and that at the time of emission is (see e.g. [214])

$$\begin{aligned}\Omega_{\rm GW,\,0} &= \Omega_{\rm GW,\,f}\left(\frac{a_{\rm f}}{a_{\rm reh}}\right)^{1-3w}\left(\frac{g_0}{g_{\rm reh}}\right)^{1/3}\rho_{\gamma,0}\\ &= 4.3\times10^{-5}\,\Omega_{\rm GW,\,f}\left(\frac{a_{\rm f}}{a_{\rm reh}}\right)^{1-3w}\left(\frac{g_0}{g_{\rm reh}}\right)^{1/3}\rho_{c,0}\,,\end{aligned} \tag{4.84}$$

where we have used that $\rho_{\gamma,0}h^2 \simeq 4.3\times10^{-5}\rho_{c,0}$, with the present day critical energy density $\rho_{c,0} \sim 10\,{\rm GeV/m^3}$, and $h \simeq 0.67$ is the reduced Hubble parameter (cf. (2.18)). The corresponding frequencies of the GWs as they would be observable today are given by [214]

$$f = \frac{k_0}{2\pi} = \frac{k}{a_{\rm f}\,\rho_{\rm f}^{1/4}}\left(\frac{a_{\rm f}}{a_{\rm reh}}\right)^{\frac{1-3w}{4}} 4\times10^{10}\,{\rm Hz}\,. \tag{4.85}$$

where k_0 is the physical wavenumber today and $k/a_{\rm f}$ is the physical wavenumber at the moment of emission. Throughout this thesis we assume

$$\frac{g_0}{g_{\rm reh}} = \frac{1}{100}\,, \tag{4.86}$$

as in Ref. [214].

[19] In essence that $ga^3T^3 \sim$ const., where T is the temperature of the thermal bath.

Part III

Gravitational wave production from oscillons

Chapter 5

GWs from asymmetric oscillons with Gaussian spatial profile

Birkhoff's theorem [27, 230] implies that spherically symmetric configurations of matter do not emit GWs. The non-linear nature of oscillons, however, gives rise to interactions among oscillons and their environment, as well as among oscillons themselves. These interactions can induce deformations and distortions of the oscillon's field profile which could lead to the production of GWs. Hence, the question arises whether and to which extent oscillons can produce a stochastic background of GWs. More importantly, if GWs are produced, what would be the implications in case of observation of a GW signal which originates from an oscillon featuring cosmological phase?

Mainly on the basis of numerical lattice simulations, the GW production from oscillons was studied in [2,3,205,208]. Analytical estimates for the emitted power in GWs originating from (spherically symmetric) adjacent oscillons have been derived in [205]. The authors also considered the case of ellipsoidal oscillons and came to the conclution that GW production from oscillons is highly suppressed.

In this chapter we investigate the GW production from asymmetric (ellipsoidal) oscillons which are characterised by a three-dimensional Gaussian field profile. In section 5.1 we motivate and summarise our main assumptions on the oscillon dynamics. In section 5.2 we derive an analytical expression for the TT-projected GW source originating from asymmetric Gaussian oscillons. We first derive an expression for the case of a single oscillon. Subsequently we turn to the more generic case of N asymmetric oscillons, (randomly) distributed throughout a portion of comoving volume $\mathcal{V}$. The respective results are further used in section 5.3 to numerically infer the spectrum of GWs. We thereby adopt an approach that was proposed in [214]. Finally, we discuss how the qualitative features of different oscillon cosmologies manifest themselves in the stochastic background of GWs. The results presented in this chapter are based on work that was partly published in Ref. [4].

5.1 GWs from Gaussian oscillons: preliminaries and assumptions

Numerical lattice simulations have shown that a common feature of the stochastic GW background produced in the presence of oscillons, is a characteristic peak structure which can exhibit multiple, distinct peaks [3,205]. A schematic illustration of a typical GW background resulting from the dynamics experienced within oscillon favouring models is shown in figure 5.1. Usually, the spectrum has a dominant peak at some physical scale $k^{\rm peak}_{\rm phys} = k^{\rm peak}/a$ and possibly also other peaks at multiples of $k^{\rm peak}_{\rm phys}$. The latter typically become less and less pronounced as the physical wavenumber increases. This peak structure originates from the oscillon dynamics. As we shall argue later, the positions of the peaks effectively correspond to the fundamental oscillation frequency of the source and its higher harmonics. For scales below $k^{\rm peak}_{\rm phys}$, the spectrum typically exhibits a relatively flat plateau which slowly falls off towards the IR. Of course, the precise shape of the spectrum depends on dynamics of the system which are dictated by the model. The IR plateau, for example, can be more ore less pronounced and may not even be related to the oscillon dynamics.

In what follows, we shall concentrate on infering the dominant part of the GW spectrum that purely originates from the oscillon dynamics. In order to derive an approximate expression for the source of GWs induced by asymmetric oscillons we make the following simplifying assumptions:

1. We assume that the oscillon's field profile can be approximated by a three-dimensional Gaussian with constant *physical* width (see below). More explicitly, for the field configuration of a single oscillon sitting at a position $\mathbf{x}^0 = (x^0, y^0, z^0)^T$ and time t we assume

$$\phi_{\rm oscillon}(\mathbf{x}, t) = \Phi(t)\mathcal{F}(\mathbf{x}, t) \tag{5.1}$$

where we have used *comoving* spatial coordinates. The time-dependent function $\Phi(t)$ represents the oscillon's field value at its center and $\mathcal{F}(\mathbf{x}, t)$ is the spatial profile given by

$$\mathcal{F}(\mathbf{x}, t) = e^{\frac{-a^2(t)}{2}\frac{(\mathbf{x}-\mathbf{x}^0)^2}{\mathbf{R}^2}} = e^{\frac{-a^2(t)}{2}\left(\frac{(x-x^0)^2}{R_x^2}+\frac{(y-y^0)^2}{R_y^2}+\frac{(z-z^0)^2}{R_z^2}\right)}\,. \tag{5.2}$$

Notice that the *comoving* oscillon widths in x, y, and z directions were expressed in terms of the (constant) *physical* widths R_x, R_y and R_z. The time dependence in the spatial profile $\mathcal{F}$ is only due to the time dependence of *comoving* widths in an expanding background.

2. The asymmetry of an oscillon is implemented by assuming that one of the widths, say e.g. R_y, differs from R_x and R_z. This, in turn, allows to eliminate one of the widths:

$$R_x = R_z \equiv R, \quad \text{and} \quad R_y = R\,(1+\Delta)\,, \tag{5.3}$$

where Δ parametrises the asymmetry of the oscillon.

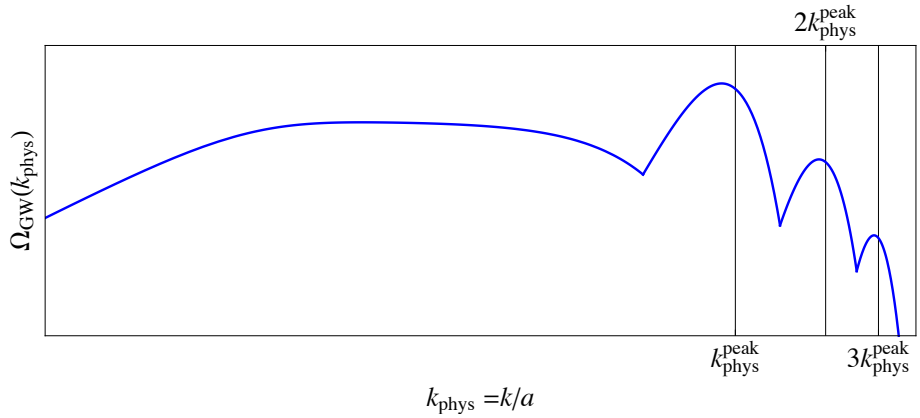

Figure 5.1: Schematic illustration of a typical GW spectrum produced in the presence of oscillons. The spectrum features a peak structure that may consist of multiple, distinct peaks. Usually, the spectrum exhibits one dominant peak at a characteristic *physical* wavenumber $k^{\rm peak}_{\rm phys}$ corresponding to the fundamental frequency of the source, (or equivalently to the fundamental frequency of the square of the time-dependent oscillon amplitude). Depending on the harmonicity of the oscillon's oscillations, other peaks may appear at multiples of $k^{\rm peak}_{\rm phys}$. Peaks at higher wavenumbers are, however, typically less and less pronounced due to an exponential suppression of the source as $k_{\rm phys}$ increases. Another typical feature of the spectrum is a relatively flat plateau for wavenumbers $k_{\rm phys} \ll k^{\rm peak}_{\rm phys}$. The latter might not necessarily be related to the oscillon dynamics and can, in principle, originate from the dynamics preceding the formation of oscillons.

5.2 The GW source of asymmetric, Gaussian oscillons

5.2.1 Single oscillon source

Before discussing the general case of multiple oscillons, we would like to consider the simplified case of a single oscillon sitting at position x^0. Without loss of generality, the latter is assumed to be the origin, i.e. $\mathbf{x}^0 = (0,0,0)^T$. Based on our previous assumptions we can compute the TT part of the energy-momentum tensor $T^{\rm TT}_{ij}$ according to (4.68)

$$T^{\rm TT}_{ij}(\mathbf{k},t) \;=\; \Lambda_{ij,lm}(\hat{\mathbf{k}})\, T_{lm}(\mathbf{k},t) = \Phi^2(t)\, \Lambda_{ij,lm}(\hat{\mathbf{k}}) \mathcal{T}_{lm}(\mathbf{k},t)\,, \tag{5.4}$$

where $\mathcal{T}_{ij}(\mathbf{k},t) \equiv \Phi^{-2}(t) T_{ij}(\mathbf{k},t)$ is given by

$$\begin{aligned}
\mathcal{T}_{ij}(\mathbf{k},t) &= \int d^3\mathbf{x}\, e^{-i\mathbf{k}\mathbf{x}} \partial_i \mathcal{F}(\mathbf{x},t) \partial_j \mathcal{F}(\mathbf{x},t) \\
&= a^2(t) \int d^3\mathbf{x}\, e^{-i\mathbf{k}\mathbf{x}}\, e^{-a^2(t)\sum_s x_s^2 R_s^{-2}}\, \frac{x_i\, x_j}{R_i^2\, R_j^2} \\
&= -\frac{\pi^{3/2}}{4\, a^3(t)}\, e^{-\frac{k_x^2 R_x^2 + k_y^2 R_y^2 + k_z^2 R_z^2}{4\, a^2(t)}}\, R_x\, R_y\, R_z \left(k_i k_j - \delta_{ij} \frac{2\, a^2(t)}{R_i\, R_j} \right) \\
&= e^{-\frac{R^2\left(k_x^2 + k_z^2 + k_y^2 (1+\Delta)^2\right)}{4\, a^2(t)}}\, \mathcal{S}_{ij}\,.
\end{aligned} \tag{5.5}$$

The quantity $\mathcal{S}_{ij}$ appearing in the last equality of (5.5) is defined as follows

$$\mathcal{S}_{ij} \equiv -\frac{\pi^{3/2} R^3 \,(1+\Delta)}{4\,a^3(t)} \left[k_i k_j - \frac{2\,a^2(t)}{R^2} \left(\delta_{ij} + \delta_{is}\delta_{jr} \frac{\delta_{s2}\delta_{r2}\Delta(2+\Delta)}{(1+\Delta)^2} \right) \right] . \tag{5.6}$$

Furthermore we chose

$$R_x = R_z \equiv R, \quad \text{and} \quad R_y = R\,(1+\Delta)\,. \tag{5.7}$$

Finally, for the TT part of $\mathcal{T}_{ij}(\mathbf{k},t)$ we find

$$\begin{aligned} \mathcal{T}_{ij}^{TT}(\mathbf{k},t) &= \Lambda_{ij,lm}(\hat{\mathbf{k}})\mathcal{T}_{lm}(\mathbf{k},t) \\ &= e^{-\frac{R^2\left(k_x^2+k_z^2+k_y^2(1+\Delta)^2\right)}{4\,a^2(t)}} \frac{\pi^{3/2}\Delta(\Delta+2)R}{4a(t)(\Delta+1)}\, f_{ij}(\mathbf{k})\,, \end{aligned} \tag{5.8}$$

with the $\mathbf{k}$-dependent tensor $f_{ij}(\mathbf{k})$ given by

$$(f_{ij}) = \frac{1}{|\mathbf{k}|^4} \begin{pmatrix} -k_x^2k_y^2 + (k_x^2+k_y^2)k_z^2 + k_z^4 & k_xk_y(k_x^2+k_z^2) & -k_xk_z(k_x^2+2k_y^2+k_z^2) \\ k_xk_y(k_x^2+k_z^2) & -(k_x^2+k_z^2)^2 & k_yk_z(k_x^2+k_z^2) \\ -k_xk_z(k_x^2+2k_y^2+k_z^2) & k_yk_z(k_x^2+k_z^2) & k_x^4 - k_y^2k_z^2 + k_x^2(k_y^2+k_z^2) \end{pmatrix}$$

Notice that eq. (5.8) implies that spherically symmetric field configurations do not emit gravitational waves:

$$\mathcal{T}_{ij}^{TT}(\mathbf{k},t) = 0\,, \qquad \text{for} \qquad \Delta = 0\,. \tag{5.9}$$

5.2.2 Multiple oscillons

We now turn to the more generic case of multiple oscillons. Assuming a system of N oscillons sitting at different positions $\mathbf{x}^q$, but with identical spatial field profile, we can write the field as

$$\phi_{\rm multi}(\mathbf{x},t) = \sum_{q=1}^{N} \Phi_q(t) e^{\frac{-a^2(t)}{2}\frac{(\mathbf{x}-\mathbf{x}^q)^2}{\mathbf{R}^2}} \equiv \sum_{q=1}^{N} \Phi_q(t)\,\mathcal{F}_q(\mathbf{x},t)\,, \tag{5.10}$$

with

$$\mathcal{F}_q(\mathbf{x},t) \equiv e^{\frac{-a^2(t)}{2}\frac{(\mathbf{x}-\mathbf{x}^q)^2}{\mathbf{R}^2}}\,, \tag{5.11}$$

as in (5.2). In the following we assume that the time-dependent functions $\Phi_q(t)$, describing the field evolution at the center of the oscillons at positions $\mathbf{x}^q$, have all the same periodicity and the same amplitude. For the multi-oscillon system described by eq. (5.10) we can write down the TT part of the energy-momentum tensor in position space

$$\begin{aligned} T_{ij}^{\rm TT,\,multi} &= \left[\partial_i\phi_{\rm multi}\partial_j\phi_{\rm multi}\right]^{\rm TT} \\ &= \left[\partial_i\left(\sum_q \Phi_q(t)\,\mathcal{F}_q(\mathbf{x},t)\right)\partial_j\left(\sum_q \Phi_q(t)\,\mathcal{F}_q(\mathbf{x},t)\right)\right]^{\rm TT} \\ &= \left[\sum_q \Phi_q^2(t)\,\partial_i\mathcal{F}_q(\mathbf{x},t)\partial_j\mathcal{F}_q(\mathbf{x},t) + \sum_{q\neq r}\Phi_q(t)\Phi_r(t)\,\partial_i\mathcal{F}_q(\mathbf{x},t)\partial_j\mathcal{F}_r(\mathbf{x},t)\right]^{\rm TT}. \end{aligned} \tag{5.12}$$

The second sum in the last equality of eq. (5.13) arises from contributions induced by interferences between two adjacent oscillons, sitting at positions $\mathbf{x}^q$ and $\mathbf{x}^r$. These contributions are exponentially suppressed with the square distance between the different oscillons. If we further assume that the oscillons are sufficiently separated from each other, we can neglect the interference term and eq. (5.13) reduces to

$$T_{ij}^{\rm TT,\,multi} \simeq \left[\sum_q \Phi_q^2(t)\,\partial_i\mathcal{F}_q(\mathbf{x},t)\partial_j\mathcal{F}_q(\mathbf{x},t)\right]^{\rm TT} . \tag{5.13}$$

In order to perform the TT projection we have to switch to Fourier space, where we have

$$\begin{aligned} T_{ij}^{\rm TT,\,multi}(\mathbf{k},t) &\simeq \Lambda_{ij,lm}(\hat{\mathbf{k}})\sum_q \Phi_q^2(t)\int d^3\mathbf{x}\, e^{-i\mathbf{k}\mathbf{x}}\partial_l\mathcal{F}_q(\mathbf{x},t)\partial_m\mathcal{F}_q(\mathbf{x},t) \\ &= \Lambda_{ij,lm}(\hat{\mathbf{k}})\,\mathcal{T}_{lm}(\mathbf{k},t)\sum_q \Phi_q^2(t)\,e^{-i\,\mathbf{k}\,\mathbf{x}^q} . \end{aligned} \tag{5.14}$$

Finally, the GW spectrum arising from the dynamics in the multi-oscillon system can be computed by plugging eq. (5.14) into (4.82), which gives

$$\begin{aligned} \Omega_{\rm GW}(k,\eta) = \frac{k^3}{2\,a^4\,\rho_{\rm c}\,m_{\rm Pl}^2}\frac{1}{\mathcal{V}}\int\frac{d\Omega}{(2\,\pi)^3}\sum_{i,j}\Bigg[\left|\int_{\eta_i}^{\eta_f} d\eta'\cos(k\eta')\,a(\eta')\,T_{ij}^{\rm TT,\,multi}(\mathbf{k},\eta')\right|^2 \\ + \left|\int_{\eta_i}^{\eta_f} d\eta'\sin(k\eta')\,a(\eta')\,T_{ij}^{\rm TT,\,multi}(\mathbf{k},\eta')\right|^2\Bigg] . \end{aligned} \tag{5.15}$$

To evaluate the integral over the solid angle in k-space, we transform to spherical coordinates and approximate the integral by a discrete sum as

$$\int d\Omega \to \sum_{i,j=0}^{N_{\rm angles}} \sin\theta_i\,\Delta\theta\,\Delta\phi\,, \tag{5.16}$$

where

$$\theta_j = j\,\Delta\theta = j\,\frac{\pi}{N_{\rm angles}}, \qquad \text{and} \qquad \phi_j = j\,\Delta\phi = j\,\frac{2\pi}{N_{\rm angles}}\,. \tag{5.17}$$

Once the background cosmology, as well as all other free parameters, such as the oscillon amplitude, the oscillon positions, etc. are fixed, eq. (5.15) is evaluated numerically for discrete values of θ_j, ϕ_j and k.

5.3 Which information does $\Omega_{\rm GW}$ contain?

In this section we discuss how the physical properties that characterise an oscillon featuring cosmological environment, may leave their imprint in the stochastic background of GWs. To this end we, evaluate eq. (5.15) for different oscillon systems (i.e. different realisations of (5.14)), and assuming different background cosmologies.

Parametrisation and initial conditions for "artificial" oscillon systems

For the case of N oscillons sitting at positions $\mathbf{x}^q$ we assume that the functions $\Phi_q(t)$, describing the field evolution at the oscillon's center, have all the same maximum amplitude A as well as the same oscillation frequency ω_{osc}. Explicitly, we assume that the $\Phi_q(t)$ are described by a simple cosine, i.e.

$$\Phi_q(t) = A\,\cos(\omega_{\text{osc}} t + \varphi_q)\,. \tag{5.18}$$

Hence, the only difference between different $\Phi_q(t)$ will be a (randomly chosen) phase φ_q.

As mentioned above, the spectrum of GWs may exhibit multiple distinct peaks, with the positions of the peaks in (physical) k-space corresponding to the fundamental frequency of the source and its higher harmonics (cf. figure 5.1). We note that assuming a simple cosine will automatically result in a GW spectrum that exhibits only a single peak. In principle, one could use a different and more complicated periodic function (e.g. a series of different cosines). For simplicity, however, and due to the fact that the source is suppressed for large values of k, we restrict to the case described by (5.18).

Note that the frequency of the source does not coincide with the oscillation frequency of the field amplitude if the latter is given by (5.18). In fact, since $T_{ij}^{\text{TT}} \sim \Phi_q^2$, the source will oscillate with a frequency, that is twice that of (5.18). As demonstrated in figure 5.2, this can change if the scalar potential is anharmonic.

The evolution of the scale factor is dictated by the evolution of the energy density or equivalently by the evolution of the Hubble parameter (cf. eq. (2.21)). To this end we have to choose the value of the initial Hubble parameter H_{i} by making use of the fact that eq. (5.18) is precisely the solution to the homogeneous Klein-Gordon equation in Minkowski spacetime for a quadratic scalar potential

$$V(\Phi) = \frac{m^2}{2}\Phi^2\,, \tag{5.19}$$

with $m = \omega_{\text{osc}}$. Based on our experience (i.e. based on what we have observed in numerical lattice simulations), we assume that the initial (average) energy density ρ_{i}, at the time when oscillons are formed, is significantly smaller than at the center of the oscillons

$$\rho_{\text{i}} = 3m_{\text{Pl}}^2\,H_{\text{i}}^2 \ll V(A)\,. \tag{5.20}$$

In terms of the energy density, oscillons correspond to local overdensities which are surrounded by an environment consisting of very small amplitude fluctuations of the field around the minimum of the potential. In these regions, typically covering a much larger portion of volume than that covered by the oscillons, the energy can be orders of magnitude smaller than the energy at the center of an oscillon. Correspondingly, the size of the comoving volume $\mathcal{V}$ should initially (at $a = a_{\text{i}} = 1$) be much larger than the volume covered by a sphere with a radius corresponding to the width of the oscillons R:

$$\mathcal{V} \gg R^3\,. \tag{5.21}$$

Moreover, in order to be consistent with neglecting the interference terms in eq. (5.13), we assume that the minimum separation between two oscillons $d_{\rm min}$ is not smaller than four times the width of an oscillon

$$d_{\rm min} \geq 4R\,, \tag{5.22}$$

if the presence of multiple oscillons is considered.

In what follows we are going to discuss the impact of various parameters on the spectrum of GWs. While for certain parameters, the effect on the energy spectrum $\Omega_{\rm GW}$ might be estimated analytically, it will in other cases be useful to explicitly compute the spectrum according to eq. (5.15). If not otherwise stated, we fix the amplitude of the oscillons A, the width of the oscillons R, the oscillation frequency $\omega_{\rm osc}$, the initial Hubble parameter $H_{\rm i}$ and the comoving volume $\mathcal{V}$ to the following values:

$$A = 0.05\, m_{\rm Pl}\,, \qquad \omega_{\rm osc}/m_{\rm Pl} = m_{\rm Pl}R = 1\,, \tag{5.23}$$

$$H_{\rm i} = \frac{1}{10}\sqrt{\frac{\frac{\omega_{\rm osc}^2}{2}A^2}{3\,m_{\rm Pl}^2}} \simeq 0.002 m_{\rm Pl}\,, \quad \text{and} \quad \mathcal{V} = (100\,R)^3 \sim \mathcal{O}\left(\frac{H_{\rm i}^{-3}}{100}\right)\,. \tag{5.24}$$

For the evolution of the scale factor we assume a matter dominated universe, with the initial scale factor at $t = t_{\rm i} = 0$ being normalised to unity

$$a_{\rm i} \equiv a(0) = 1, \quad \text{and} \quad \left.\frac{\dot{a}(t)}{a(t)}\right|_{t=0} = H_{\rm i}\,, \tag{5.25}$$

which gives (cf. eq. 2.21)

$$a(t) = \left(1 + \frac{3H_{\rm i}t}{2}\right)^{2/3}\,. \tag{5.26}$$

5.3.1 Effect of the (constant) oscillon amplitude A

In order to understand how the amplitude of the oscillons affects the GW spectrum we can simply insert expression (5.18) for Φ_q in eq. (5.14). Then the amplitude A can be factored out in eq. (5.15) and we find

$$\Omega_{\rm GW} \propto A^4\,. \tag{5.27}$$

Hence, a change in the oscillon amplitude A simply results in an overall rescaling of the GW spectrum. Notice, however, that such a change can have a potentially strong impact on the magnitude of the spectrum since $\Omega_{\rm GW}$ scales with the fourth power of A. For example, an increase in amplitude by $\sim 10\%$ would result in an increase in $\Omega_{\rm GW}$ of about $\sim 50\%$.

5.3.2 Effect of the asymmetry parameter Δ

We now consider the effect of the asymmetry parameter Δ. If we recall eq. (5.8) and assume (without loss of generality) that the asymmetry is manifested in the y-direction we find

$$\mathcal{T}_{ij}^{TT} \propto e^{-\frac{R^2\, k_y^2 (2\Delta+\Delta^2)}{4\, a^2(\eta)}}\, \frac{\Delta(\Delta+2)}{(\Delta+1)}\,. \tag{5.28}$$

Assuming that $\Delta \ll 1$ eq. (5.28) together with (5.15) implies

$$\Omega_{\mathrm{GW}} \propto \Delta^2 + \mathcal{O}(\Delta^4)\,. \tag{5.29}$$

Notice, that due to the exponential in eq. (5.28), the $\mathcal{O}(\Delta^4)$-term exhibits a (potentially small) time dependence.

In addition to this simple analytic estimate we have numerically computed the spectrum Ω_{GW} using (5.15) for different values of Δ. The corresponding results are presented in figure 5.3. The latter shows the spectrum as a function of the physical wavenumber $k_{\mathrm{phys}} = a^{-1}k$ arising from a single oscillon in a matter dominated universe. The spectrum evaluated at $a(\eta_{\mathrm{f}}) \equiv a_{\mathrm{f}} = 3$, is shown for different values of Δ, represented by differently coloured curves. One can clearly see that the shape of the spectrum remains practically unaffected when changing Δ. Just as for the amplitude A, a change in Δ simply results in an overall rescaling of Ω_{GW}.

5.3.3 On the imprint of the background cosmology

Let us now discuss how the background evolution, i.e. effective EOSp w, is imprinted in the spectrum of GW. To investigate how the background cosmology affects the GW signal, we have numerically computed Ω_{GW} by evaluating eq. (5.15) for a single, centered oscillon. In our numerical calculation the background evolution is modeled by

$$a(t) = \left(\frac{9}{4}\right)^{\frac{1}{3\,(1+w)}} \left(\frac{2}{3} + H_{\mathrm{i}}\,(1+w)\,t\right)^{\frac{2}{3\,(1+w)}}\,, \tag{5.30}$$

which implies

$$a(0) = 1\,, \qquad \text{and} \qquad \left.\frac{\dot{a}(t)}{a(t)}\right|_{t=0} = H_{\mathrm{i}}\,. \tag{5.31}$$

In order to estimate the dependence of the spectrum on the effective EOSp, we have varied w between $w = 0$ (matter dominated) and $w = 1/3$ (radiation dominated) in steps of $\Delta w = 1/12$. Our results are presented in figures 5.4 and 5.5. In figure 5.4 we show the spectra computed at $a(\eta_{\mathrm{f}}) \equiv a_{\mathrm{f}} = 10$. While changes of the parameters discussed in the previous sections (i.e. A and Δ) resulted all in an overall rescaling of Ω_{GW}, here the situation turns out to be different. Interestingly, we find that the background cosmology manifests itself in the slope of the GW spectrum (on a log-log scale). Indeed, one can clearly see that the slope of the peak increases with the value of w.

In order to determine the w-dependence of the peak we assumed the following power-law ansatz to fit the numerical data

$$\Omega_{\rm GW}(k_{\rm phys}) = A_{\rm GW} \left(\frac{k_{\rm phys}}{\omega_{\rm osc}}\right)^{n_{\rm GW}} , \tag{5.32}$$

where $A_{\rm GW}$ refers to the amplitude of the peak in the GW spectrum at

$$k_{\rm phys} = \omega_{\rm osc} , \tag{5.33}$$

and

$$n_{\rm GW} \equiv \frac{d \log \Omega_{GW}}{d \log k_{\rm phys}} , \tag{5.34}$$

is the spectral tilt.

The solid lines shown in figure 5.4 correspond to the results obtained from our fitting analysis. The details of the analysis are listed in table 5.1. In figure 5.5 we show the amplitude $A_{\rm GW}$ (left) and the spectral tilt $n_{\rm GW}$ (right), both as a function of the EOSp w. In both figures the red dots correspond to data points obtained from numerically evaluating[1] eq. (5.15) and the error bars denote the standard error obtained from our fitting analysis (cf. table 5.1).

Within the scope of our fitting analysis we found that the w-dependence of the amplitude $A_{\rm GW}$ may be described with an exponential ansatz

$$A_{\rm GW} = \alpha \, e^{\kappa \, w} , \tag{5.35}$$

with

$$\alpha = 5.68 \cdot 10^{-7} \pm 1.1 \cdot 10^{-8} , \quad \text{and} \quad \kappa = 9.46 \pm 0.06 . \tag{5.36}$$

On the other hand, to fit the data related to the spectral tilt we assumed a linear ansatz

$$n_{\rm GW} = \beta + \gamma \cdot w , \tag{5.37}$$

finding that the data is most accurately described for

$$\beta = 2.49 \pm 0.03 \quad \text{and} \quad \gamma = 1.55 \pm 0.14 . \tag{5.38}$$

5.3.4 Consequences of a dynamical number of oscillons $N = N(\eta)$

Considering a time-dependent number of oscillons might initially seem somewhat arbitrary. However, later in chapter 7 we shall see that models in which the production of oscillons can happen over an extended period of time indeed exist. In principle, one could consider an infinite number of possibilities of how N might depend on η. In the following we restrict ourselves to the comparison of the following three cases:

[1] However, using the single-oscillon stress-energy tensor.

w	$A_{\rm GW} \pm {\rm SE}$	$n_{\rm GW} \pm {\rm SE}$
0	$5.956 \cdot 10^{-7} \pm 7.2 \cdot 10^{-9}$	2.48 ± 0.02
1/12	$1.292 \cdot 10^{-6} \pm 1.3 \cdot 10^{-8}$	2.58 ± 0.02
1/6	$2.762 \cdot 10^{-6} \pm 1.8 \cdot 10^{-8}$	2.78 ± 0.01
1/4	$5.996 \cdot 10^{-7} \pm 4.8 \cdot 10^{-8}$	2.90 ± 0.02
1/3	$1.332 \cdot 10^{-5} \pm 1.0 \cdot 10^{-7}$	2.97 ± 0.02

Table 5.1: Estimated values of the amplitude $A_{\rm GW}$ and the spectral index $n_{\rm GW}$ together with their standard error (SE) resulting from our fitting analysis.

1. Constant number of oscillons: $N = {\rm cst.}$
2. Linearly increasing number of oscillons: $N \propto \eta$.
3. The number of oscillons increases with the physical volume of the universe: $N \propto a^3$.

In order to model the time dependence of the number of oscillons we use a Heaviside step function $\Theta(\eta - \eta_q)$. The latter is implemented in the expression for the stress-energy tensor eq. (5.14). To give a practical example, if N scales linearly with η we have

$$T_{ij}^{\rm TT,\,multi}(\mathbf{k},\eta) \;=\; \Lambda_{ij,lm}(\hat{\mathbf{k}})\,\mathcal{T}_{lm}(\mathbf{k},\eta)\sum_q \Theta(\eta-\eta_q)\,\Phi_q^2(\eta)\,e^{-i\,\mathbf{k}\,\mathbf{x}^q}\,, \qquad (5.39)$$

where

$$\eta_q = \eta_{\rm i} + (q-1)\Delta\eta\,, \quad \text{and} \quad \Delta\eta = \frac{\eta_{\rm f}-\eta_{\rm i}}{N(\eta_{\rm f})}\,, \qquad (5.40)$$

with $\eta_{\rm i}$ and $\eta_{\rm f}$ denoting the initial and final conformal times, respectively.

Using eq. (5.15) we have evaluated the energy spectrum of GWs, $\Omega_{\rm GW}$, at $a(\eta_{\rm f}) \equiv a_{\rm f} = 3$ for the three different scenarios mentioned above. For the final number of oscillons $N(\eta_f)$ we assumed $N(\eta_f) = 10$. Moreover, in all three cases we assumed the same, matter dominated background cosmology ($w = 0$). The positions of the oscillons $\mathbf{x}^q$, as well as the phases φ_q appearing in the functions Φ_q (cf. eq. (5.18)) have been chosen randomly[2]. We note that in any of the three scenarios we have used the same positions, the same phases, and also the same asymmetry parameter $\Delta = 0.1$. The resulting effects are therefore exclusively attributable to the time-dependence of N.

The results of our numerical computation are presented in figure 5.6. The red curve shows the spectrum obtained with a constant number of oscillons ($N = 10 = {\rm cst.}$). The blue and green curves correspond to spectra obtained assuming $N \propto \eta$ and $N \propto a^3$, respectively. Clearly, these three scenarios result in different spectra. In particular, one can see that for scenarios in which the number of oscillons

[2]In essence, the phases have been chosen between 0 and 2π.

per comoving volume varies, the spectral tilt eventually becomes scale-dependent. Moreover, notice that the peaks at $k_{\rm phys} = 2\omega_{\rm osc}$ lie almost perfectly on top of each other. This, in turn, implies that the amplitude of the GW spectrum at a given time does not depend on the previous evolution of N, but rather on the number of sources at the time of emission. Oscillons continuously produce GWs at the characteristic peak scale $k_{\rm phys}^{\rm peak} = 2\omega_{\rm osc}$ which eventually get redshifted. The strength of the signal emitted at a certain time, depends on one hand on the strength of the source (i.e. on the amplitude A and the asymmetry Δ), and on the other hand on the number of sources. The time period during which the sources are actively producing GWs is imprinted in the width of the spectrum. Recall that we have evaluated the spectrum after a time period during which the universe has expanded by a factor $a_{\rm f} = 3$. This implies that the wavenumbers of the GWs produced at the very beginning became redshifted to $k_{\rm phys}^{\rm peak} = 2/3\omega_{\rm osc}$ which is exactly what we can observe in figure 5.6.

5.3.5 Comments on other effects

Another effect that has explicitly been considered is the scaling of the amplitude of the GW spectrum $\Omega_{\rm GW}$ with the number of oscillons N per comoving volume $\mathcal{V}$. At this point we refuse to show explicit results since they are less exciting than the ones previously showed. In fact, we found that to good approximation, $\Omega_{\rm GW}$ simply scales with the number of oscillons, i.e.

$$\Omega_{\rm GW}^{N} \sim \Omega_{\rm GW}^{\rm single}\,(N \pm \delta) \quad \text{with} \quad \delta \lesssim \mathcal{O}(1)\,. \tag{5.41}$$

Here $\Omega_{\rm GW}^{\rm single}$ denotes the spectrum obtained from a single oscillon within the same comoving volume and δ is a small numerical factor depending on the positions $\mathbf{x}^q$ as well as on the phases φ^q.

Let us now comment on some other effects that have not explicitly been considered within our analysis but can, in principle, have an effect on the resulting GW spectrum. First of all, in more realistic scenarios, the quantities that were assumed to be constant (i.e. the field profile and the amplitude) are generically dynamical. These quantities may vary such that the GW emission is temporarily enhanced. Effects that lead to such enhancement could, for instance, be the collision of and interaction between different oscillons. Over longer periods of time, however, one would rather expect the amplitude of the oscillons to slowly decay. Their shape is expected to evolve towards spherical symmetry. Consequently, the GW emission should gradually be suppressed. In scenarios in which oscillons are produced over an extended period of time, in turn, also the production of GWs may be prolonged. Finally, depending on how the oscillons decay, this could lead to a final burst of GWs.

5.4 Summary

In this chapter we have investigated the production of GWs from asymmetric (ellipsoidal), Gaussian oscillons in an expanding FLRW background. To this end we adopted the approach proposed in Ref. [214] (see the discussion in section 4.4.3). On the basis of model-independent, simplifying assumptions we derived an analytical

expression for the TT part of the anisotropic stress induced by a system that is composed of N identical, randomly distributed and asymmetric oscillons. We then used our analytical results for numerical computations of the GW spectrum.

First of all, we found that asymmetric oscillons generically produce a spectrum of GWs that has a peak at a characteristic wavenumber corresponding to the fundamental oscillation frequency of the source. Under the assumption that H and $\Phi(t)$ are the only dynamical quantities, we found that the spectrum can be described by a simple power law:

$$\Omega_{\mathrm{GW}}(k) \sim k^{n_{\mathrm{GW}}} . \tag{5.42}$$

We investigated how changes of parameters, such as the width or the amplitude of the oscillons, can affect the resulting spectrum of GWs. In particular, we found that both, changes in the amplitude A, as well as changes in the asymmetry parameter Δ, result in an overall rescaling of the amplitude of the GW spectrum.

We also considered the effect of different background cosmologies, due to assuming different EOSps w. We found that both the amplitude of the spectrum and the spectral tilt n_{GW} are sensitive to the value of w. To be more precise, our fitting analysis suggests that the amplitude increases exponentially with w, while the spectral tilt is found to behave as $n_{\mathrm{GW}} \sim w$. The overall shape of the spectrum, however, remains well-described by a simple power law.

Another effect that we considered was an extended period of oscillon production, or in other words, a time-dependent number of oscillons $N = N(\eta)$. In these cases the spectrum is not expected to obey a simple power law relation.

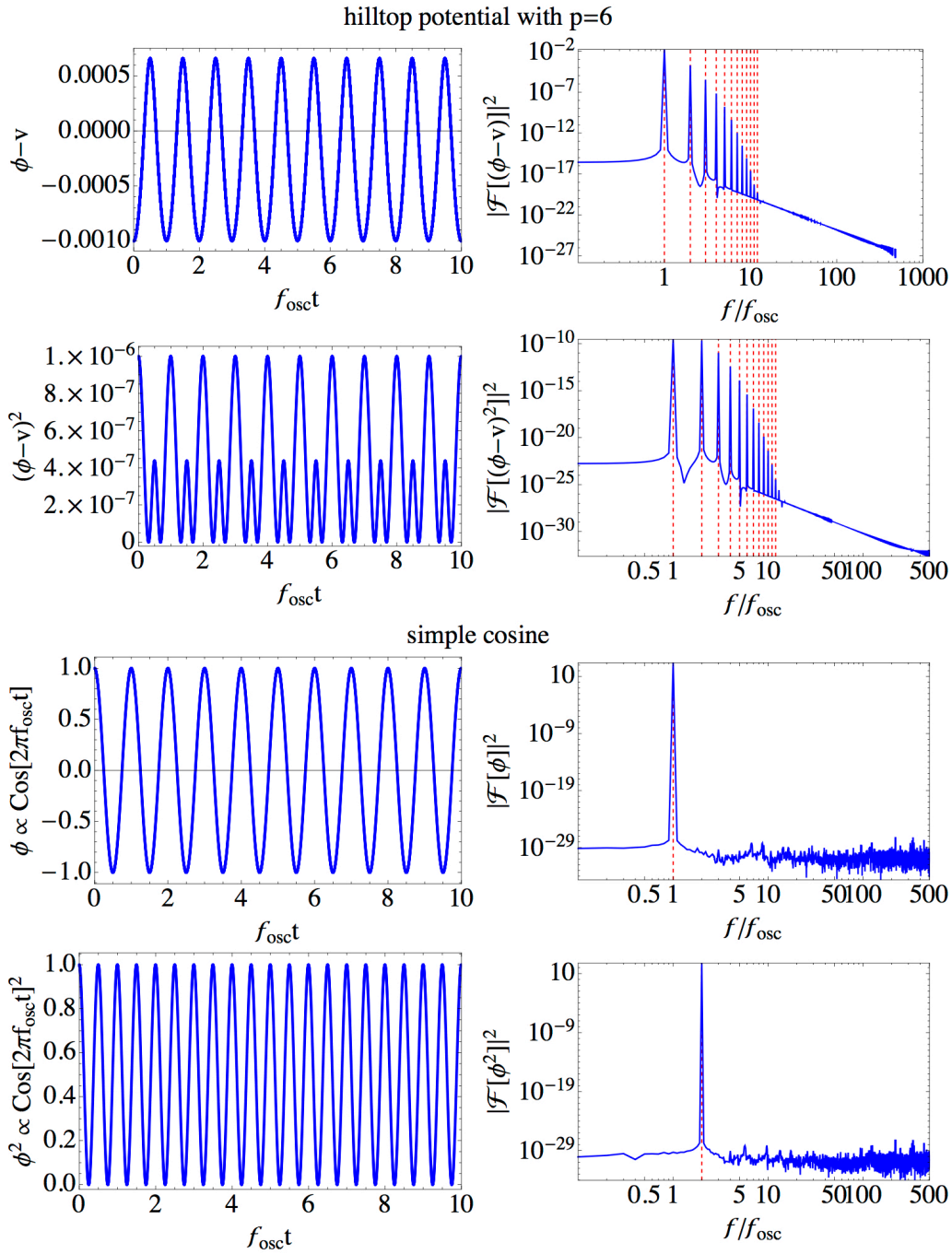

Figure 5.2: *Left:* Homogeneous scalar field evolution in Minkowski spacetime depicted over a time period corresponding to ten oscillations. The upper two plots, show the evolution of $\phi(t) - v$ and $(\phi(t) - v)^2$ in the (anharmonic) hilltop inflation model (3.76) with $p = 6$. The lower two plots show $\phi(t)$ and $\phi(t)^2$ obtained when assuming $\phi \sim \cos(f_{\mathrm{osc}}t)$.
Right: Power spectral density $|\mathcal{F}|^2$, where $\mathcal{F}$ denotes the Fourier transform of the respective signal, depicted on the left side of the plot. The frequency is depicted in units of the fundamental frequency $f_{\mathrm{osc}} = 2\pi\omega_{\mathrm{osc}}$ of ϕ. One can see that in the case of a harmonic potential the source ($\propto \phi^2$) has a fundamental frequency which is twice that of ϕ and, of course, no higher harmonics are present. In the case of the anharmonic hilltop potential, however, $\phi(t)$ can be decomposed into its fundamental frequency and additional higher harmonics. Moreover, notice that the source of GWs, which is proportional to $\phi(t)^2$, exhibits the same fundamental frequency as ϕ and the higher harmonics lie at the same positions.

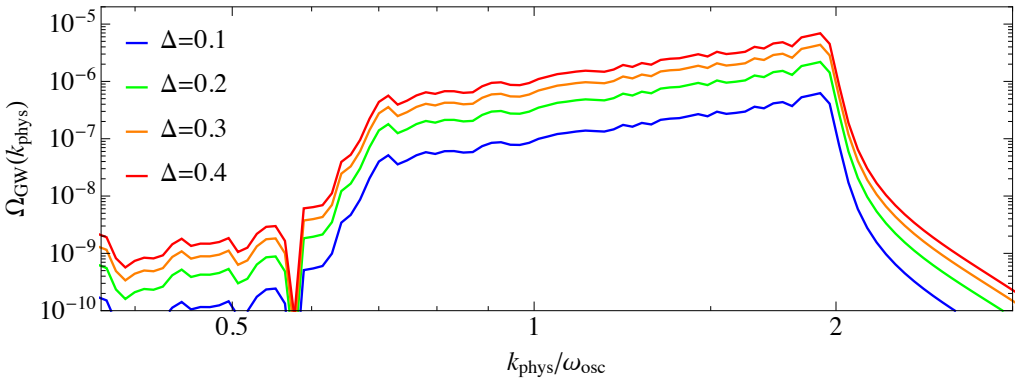

Figure 5.3: The spectrum $\Omega_{\rm GW}$ as function of the physical wavenumber $k_{\rm phys}/\omega_{\rm osc} = (a\omega_{\rm osc})^{-1}k$ and different values of the asymmetry parameter Δ: $\Delta = 0.1$ (blue), $\Delta = 0.2$ (green), $\Delta = 0.3$ (orange) and $\Delta = 0.4$ (red). The results were obtained by assuming a single oscillon with constant asymmetry Δ in a matter dominated cosmology. The spectrum is shown at $a(\eta_{\rm f}) \equiv a_{\rm f} = 3$.

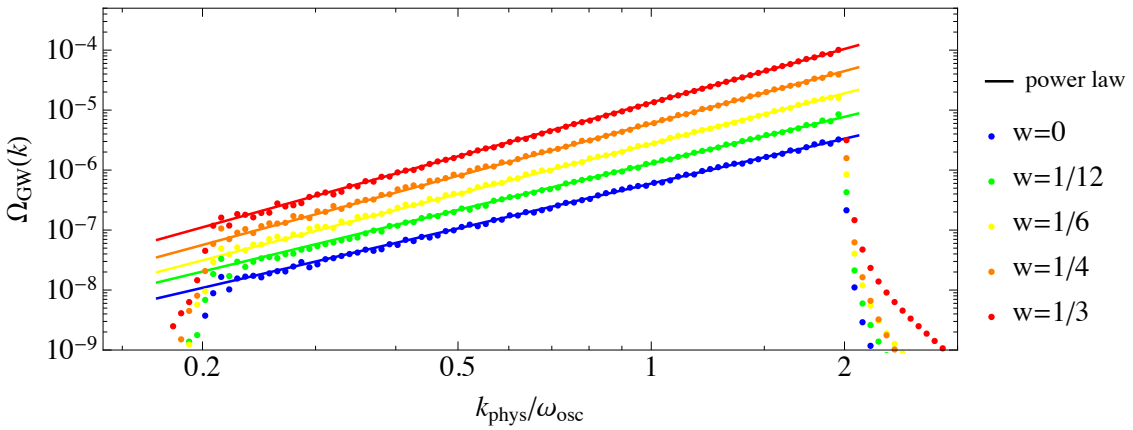

Figure 5.4: GW spectra $\Omega_{\rm GW}(k)$ obtained by assuming different background cosmologies i.e. different EOSps. The different colors correspond to: $w = 0$ (blue), $w = 1/12$ (green), $w = 1/6$ (yellow), $w = 1/4$ (orange), and $w = 1/3$ (red). As one can see, the EOSp is imprinted in the slope of the spectrum (on a double logarithmic scale). The spectra are shown at $a(\eta_f) \equiv a_f = 10$.

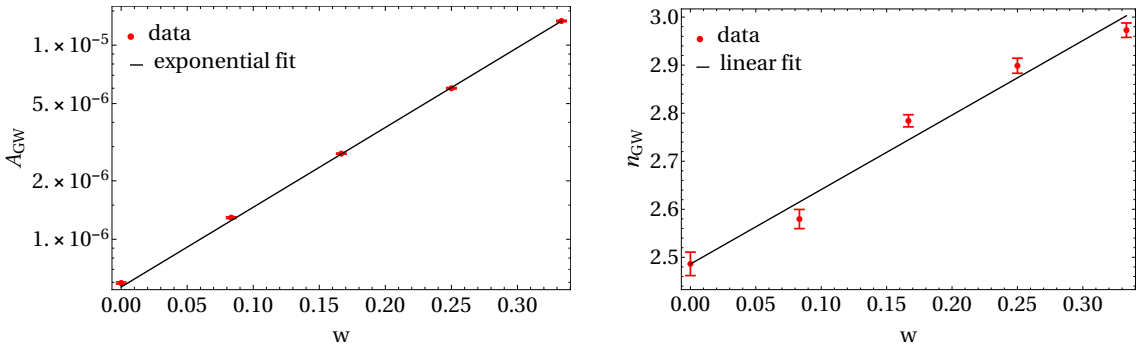

Figure 5.5: *Left:* The amplitude A_{GW} of the GW spectrum at $k_{\mathrm{phys}} = \omega_{\mathrm{osc}}$ assuming a power law for $\Omega_{\mathrm{GW}}(k)$. The amplitude is shown as a function of the EOSp w. The dots and the error bars represent the data points and their standard error (cf. table 5.1) originating from our fitting analysis. The solid black line denotes an exponential function fitted to the data (cf. eq. (5.35)).
Right: The spectral index n_{GW} as a function of the EOSp w (cf. eqs. (5.32) and (5.34)). Data points together with their standard error are again shown in red, while the solid black line denotes a linear fit to the data.

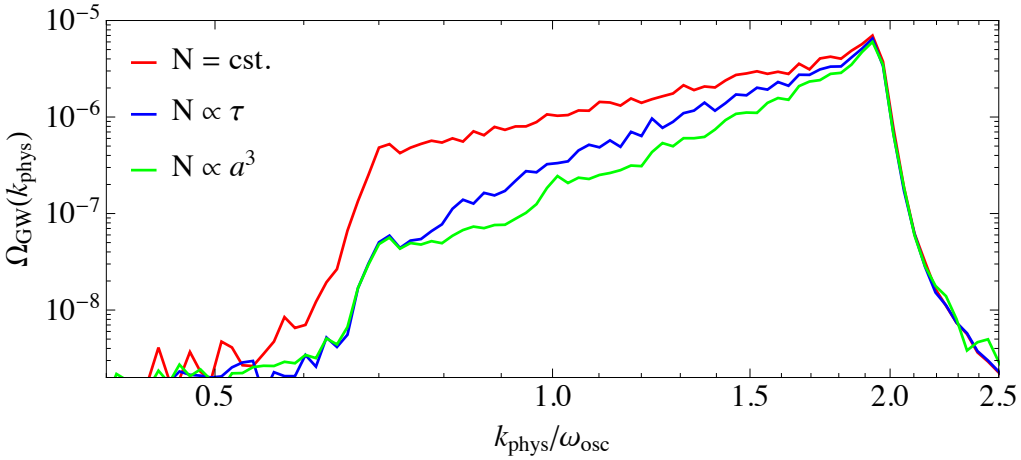

Figure 5.6: GW spectra computed assuming different time dependencies for the number of oscillons N. The red line corresponds to $N = 10 = \mathrm{cst.}$, the blue one was obtained by assuming a linear increase with conformal time ($N \propto \eta$), and for the green curve we assumed that N increases with the physical volume $N \propto a^3$. The spectra are all shown at $a(\eta_{\mathrm{f}}) \equiv a_{\mathrm{f}} = 3$. In all three cases we assumed a matter dominated background and the same final number of oscillons $N(\eta_{\mathrm{f}}) = 10$.

Part IV

Tachyonic oscillations after hilltop inflation and related consequences

Chapter 6

Preheating after hilltop inflation with additional matter field

In order to allow for successful reheating into the SM, the inflationary sector must ultimately be embedded into a realistic model of particle physics. In this chapter we discuss different aspects of preheating after supersymmetric hilltop inflation for realisations in which the inflaton is coupled to an additional matter field χ. In particular, the latter can have two important roles. Firstly, before the onset of hilltop inflation, χ can drive a period of so-called "preinflation" through which the initial conditions for the subsequent period of hilltop inflation can dynamically be generated. Secondly, if one identifies χ with a right-handed sneutrino, the supersymmetric partner of a right-handed neutrino, the observed baryon asymmetry of the universe could be produced via non-thermal leptogenesis [231–234].

This chapter is organised as follows. In section 6.1 we introduce the model within the framework of SUSY and briefly discuss the mechanism of preinflation. In section 6.2.2 we begin with reviewing the dynamics of preheating after hilltop inflation, before we turn to the discussion of preheating in the presence of χ. Finally, in section 6.3 we consider the production of GWs during preheating after hilltop inflation. In particular, we compare different results obtained from lattice simulations of different realisations of the model. This chapter is based on results that have been partly published in Refs. [1, 2].

6.1 Supersymmetric hilltop inflation

Within the framework of SUSY[1], the Pure Hilltop (PH) inflation potential 3.76 introduced in section 3.4.1 can be constructed from the following effective superpotential

$$W_{\rm PH} \,=\, \sqrt{V_0}\, S \left(1 - \frac{2^{p/2}\,\Phi^p}{v^p}\right) , \tag{6.1}$$

[1]For a nice introduction into SUSY see [235].

with S and Φ representing chiral superfields[2]. As in (3.76), the dimensionful parameters V_0 and v have units of $m_{\rm Pl}^4$ and $m_{\rm Pl}$, respectively.

The form of the superpotential (6.1) can be constrained by imposing[3] a $U(1)_{\rm R} \times \mathbb{Z}_p$ symmetry of the superpotential. It then emerges if S carries two units of $U(1)_{\rm R}$ charge while being a singlet under $\mathbb{Z}_p$. The superfield Φ, in turn, carries one unit of $\mathbb{Z}_p$ but remains uncharged under $U(1)_{\rm R}$.

Here, the inflaton superfield Φ, whose scalar component ultimately takes the role of the inflaton, is assumed to be a gauge-singlet. The superfield S, on the other hand, is responsible for generating the hilltop inflation potential via its F-term. It is therefore often referred to as "driving field". In the following we shall assume that S acquires a super-Hubble mass due to Kähler corrections and remains stabilised at its minimum ($S = 0$) during inflation (see e.g. [236]). The F-term scalar potential then reads

$$\begin{aligned} V(\phi) \;=\; V_F \;&=\; \left|\frac{\partial W_{\rm PH}}{\partial S}\right|^2 + \left|\frac{\partial W_{\rm PH}}{\partial \Phi}\right|^2 + V_{\rm SUGRA} \\ &= V_0\left(1 - \frac{\phi^p}{v^p}\right)^2 + V_{\rm SUGRA} + \dots\,, \end{aligned} \tag{6.2}$$

where $\phi = \sqrt{2}\,\Re[\Phi]$. The ellipses stand for terms that contain the imaginary inflaton component $\Im[\Phi]$. The latter can, in principle, have an effect on the inflationary dynamics and thus modify the predictions for the primordial spectra [237]. In this thesis, however, we shall consider only realisations for which the effect of $\Im[\Phi]$ is negligible.

The term $V_{\rm SUGRA}$ in (6.2) accounts for additional Kähler corrections to the inflaton mass. These corrections are generic in SUGRA based F-term inflation models and often spoil the flatness of the inflaton potential thus preventing a successful period of inflation. This issue is commonly referred to as the η-problem[4] [181, 238]. In the following we assume that these Kähler corrections are negligible, so that the scalar potential takes the form of (3.76).

A possible but rather inelegant strategy to circumvent this problem would be fine-tune the Kähler potential. The more appealing alternative, however, is to impose an approximate symmetry of the Kähler potential which protects the inflaton potential from unwanted contributions that spoil its flatness. Examples of such symmetries are e.g. a Heisenberg [239, 240] or a shift symmetry[5] [244]. For the hilltop inflation model studied in this chapter, it was shown in [245] that an approximate Heisenberg symmetry preserves the flatness of the potential.

Compared to a shift symmetry, the Heisenberg symmetry has the advantage that the inflaton is not required to be a gauge-singlet [242]. This opens the possibility to

[2] Notice that we use the same symbols for both, chiral superfields and their scalar components.

[3] Notice that any additional effective operators that respect the imposed symmetries are strongly Planck-suppressed and can therefore be neglected.

[4] We note that the η-problem does not only arise in SUGRA realisations of inflation but is rather a generic problem of effective field theories of inflation which suffer from radiative corrections to the inflaton mass.

[5] See e.g. also Refs. [236, 241–243].

associate inflation with a particle physics phase transition in which the inflaton is a D-flat direction of scalar fields that break some more general symmetry such as a GUT symmetry or a flavour symmetry (see e.g. [134, 246]). This, in turn, might be achieved by replacing Φ^p with a combination of fields that form a singlet under the considered symmetry group.

6.1.1 Preinflation and the initial conditions for hilltop inflation

As discussed in section 3.4.1, inflation occurs while the inflaton rolls slowly away from the origin ($\phi \sim 0$). A question that we have not answered so far is why the inflaton initially acquires such small values, close to the top of the hill. A possible explanation for this is provided if the last $N_\star$ e-folds of inflation were preceded by a phase of "preinflation" [133–135, 247]. Such a phase could be realised if the driving field S, or alternatively some other (D-flat) combination of matter fields acquires a non-vanishing VEV during inflation. This can deform the potential and stabilise the inflaton at the top of the hill. As the respective stabilising field approaches zero, the deformation vanishes and inflation happens along the hill.

In the following we consider an extension of the hilltop inflation model, in which the inflaton couples to an additional matter field X, which takes the role of the preinflaton. Explicitly, we consider a model described by the superpotential

$$W \;=\; \sqrt{V_0}\, S \left(1 - \frac{2^{p/2}\,\Phi^p}{v^p}\right) + \lambda \Phi^2 X^2 \,, \tag{6.3}$$

where the coupling λ has units of $m_{\rm Pl}^{-1}$. Notice that just as $W_{\rm PH}$, the superpotential (6.3) can be fixed by imposing $U(1)_{\rm R} \times \mathbb{Z}_p$ symmetry and distributing one unit of $U(1)_{\rm R}$ charge and $(p-2)/2$ units of $\mathbb{Z}_p$ charge to X, while the charges of Φ and S remain the same as discussed above.

If we again assume that S gets a super-Hubble mass during inflation the F-term scalar potential now reads

$$\begin{aligned} V(\phi,\chi) \;&=\; \left|\frac{\partial W}{\partial S}\right|^2 + \left|\frac{\partial W}{\partial \Phi}\right|^2 + \left|\frac{\partial W}{\partial X}\right|^2 + V_{\rm SUGRA} \\ &=\; V_0 \left(1 - \frac{\phi^p}{v^p}\right)^2 + \frac{\lambda^2}{2}\phi^2\chi^2(\phi^2+\chi^2) + V_{\rm SUGRA} + \dots \,, \end{aligned} \tag{6.4}$$

where $\chi = \sqrt{2}\,\Re[X]$. We note that the scalar potential depends solely on $|X|$. The potential and consequently the dynamics are the same for both $\Im[X]$ and $\Re[X]$. We shall therefore not include $\Im[X]$ in the following discussion.

If $\chi \neq 0$ initially, ϕ acquires a χ-dependent effective mass squared which confines it at the top of the hill ($\phi = 0$). As χ drops below some critical value, the inflaton destabilises due to the growth of quantum fluctuations and it eventually starts rolling towards one of its VEVs $\phi = \pm v$. We note that depending on the coupling λ, as well as on the SUGRA corrections absorbed in $V_{\rm SUGRA}$, inflation may happen along a non-trivial multi-field trajectory (see Ref. [135] for more details). Within this thesis we assume that these corrections are such that the last $N_\star$ e-folds of observable

inflation happen in the single-field limit along the ϕ direction and can be described by the potential (3.76) (cf. the discussion in section 3.4.1).

6.2 Dynamics of preheating

In this section we focus on the dynamics of preheating after hilltop inflation in the model (6.2). Before turning to the discussion of the dynamics in the presence χ, however, let us briefly recap the dynamics of preheating in the pure hilltop inflation model (i.e. for $\lambda = 0$).

6.2.1 Preheating after pure hilltop inflation – a brief review

There are two stages that can lead to efficient growth of fluctuations after hilltop inflation [150, 194]. The first stage is that of *tachyonic preheating* which happens as the inflaton rolls down for the first time from the top of the hill towards $\phi = v$. As discussed in section 4.2.3, this leads to exponential growth of modes $\delta\phi_k$ for which $k/a < \sqrt{-\partial^2 V/\partial\phi^2}$. The growth related to tachyonic preheating is most efficient for small values of v. In particular if (cf. eq. (4.40)) [150]

$$\left(\frac{v}{m_{\rm Pl}}\right)^{1/(p-2)} < \frac{V_0^{1/4}}{v}\left[2p(p-1)^{p-1}\right]^{1/(2p-4)}, \tag{6.5}$$

preheating ends due to non-linear effects, already during this phase.

When (6.5) is not satisfied, the zero-mode starts oscillating about the minimum of the potential $\phi = v$. As argued in section 4.2.3, when [150]

$$v/m_{\rm Pl} < \frac{1}{\sqrt{3}}\left(\frac{p-1}{2p-1}\right) \sim \mathcal{O}(0.1)\, m_{\rm Pl}\,, \tag{6.6}$$

the inflaton eventually re-enters into the tachyonic region and preheating continues via tachyonic oscillations. This mechanism can be very efficient such that preheating ends due to non-linear effects within only a couple of oscillations of the zero mode [194]. The amplification of inflaton fluctuations is most efficient around a characteristic peak scale

$$\frac{k_{\rm p}}{a} \simeq \left(\frac{v}{m_{\rm Pl}}\right)^{\frac{p-2}{2p}} m_\phi\,. \tag{6.7}$$

Indeed, it can be so strong that the inflaton fragments into localised bubbles that *overshoot* over the top of the hill into the wrong vacuum. Typically, these bubbles oscillate a couple of times between the two minima of the potential $\phi = \pm v$, until they eventually relax around the true vacuum. Instead of dissipating away, however, they continue their life as quasi-stable oscillons (cf. section 4.4.1). In Ref. [194] these oscillons were found to be separated by a characteristic distance $\lambda_{\rm p} \sim 2\pi/k_{\rm p}$ coinciding with the characteristic peak scale at which the growth of fluctuations is most efficient.

6.2.2 Parametric resonance of χ driven by inhomogeneous ϕ

The non-linear dynamics of preheating after hilltop inflation have been studied in Ref. [194] for $p = 4$ and different values of v. Throughout this chapter we focus on the dynamics of preheating in realisations of the supersymmetric part of the potential (6.4) (i.e. neglecting V_{SUGRA}) with

$$v \;=\; 10^{-2} m_{\mathrm{Pl}}\,. \tag{6.8}$$

As it turns out, depending on the value of λ, χ can experience resonant amplification of fluctuations which we attribute to a non-standard parametric resonance, triggered by the dynamics of ϕ. We will show that the resonant growth does not occur as usual, due to the coherent oscillations of the homogeneous ϕ, but rather happens well after the inflaton's zero mode has decayed into inhomgeneous fluctuations.

Instead of the coupling λ is closely related to ratio between the preinflaton mass m_χ and the inflaton mass m_ϕ via

$$\frac{m_\chi}{m_\phi} \;=\; \frac{\lambda\, v^3}{\sqrt{2p^2\, V_0}} \;\sim\; \lambda, \tag{6.9}$$

where the masses are defined at the minimum of the potential ($\phi = v$ and $\chi = 0$) as

$$m_\phi^2 \;\equiv\; \left.\frac{\partial^2 V}{\partial \phi^2}\right|_{\mathrm{min}} \;=\; \frac{2p^2 V_0}{v^2}\,, \tag{6.10}$$

$$m_\chi^2 \;\equiv\; \left.\frac{\partial^2 V}{\partial \chi^2}\right|_{\mathrm{min}} \;=\; \lambda^2\, v^4\,. \tag{6.11}$$

In the following section we discuss results of lattice simulations obtained for the model (6.4) with $p = 6$ and in $2 + 1$ dimensions. In section 6.2.4 we present and discuss results carried out in $3 + 1$ dimensions and for different values of the parameter p. We compare the results with those carried out in two spatial dimensions and among themselves.

We note that the results published in [1] (on which this chapter is based) were complemented by a numerical Floquet analysis that was generalised to inhomogeneous background fields (see section 4 in [1] for details). This analysis was carried out by Dr. David Nolde and will not be discussed in detail within this thesis. However, we shall briefly comment on the techniques used, as well as on the results obtained, since the latter essentially confirm our interpretation of the process as a parametric resonance.

6.2.3 Results of lattice simulations in $2 + 1$ dimensions

The results presented in this section originate from numerical lattice simulations of preheating in the model (6.4) with $p = 6$ and $v = 10^{-2} m_{\mathrm{Pl}}$. Here, the value of V_0 was chosen to be

$$V_0 = 1.05 \times 10^{-19} m_{\mathrm{Pl}}^4\,, \tag{6.12}$$

$\langle\phi\rangle_\mathrm{i}/v$	$\langle\dot{\phi}\rangle_\mathrm{i}/v^2$	$\langle\chi\rangle_\mathrm{i}$	$\langle\dot{\chi}\rangle_\mathrm{i}$	$H_\mathrm{i}/m_\mathrm{Pl}$	N	LH_i
8×10^{-2}	2.49×10^{-9}	0	0	1.87×10^{-10}	2048	0.21

Table 6.1: Initial conditions and lattice setup. The initial conditions for the inflaton have been obtained by numerically solving the homogeneous inflaton equation of motion during the slow-roll regime until $|\eta_V| \simeq 25$ and $\varepsilon_V \ll 1$.

which corresponds to $N_\star \simeq 55$ in eq. (3.85) when evaluating $\varepsilon_{V_\star}$. The simulations were performed with a modified version of LatticeEasy (cf. appendix C.3.1 and C.4).

Initialisation and lattice setup

The initial conditions for the field's zero modes were chosen as follows: the inflaton ϕ has been initialised at the end of inflation shortly after the slow-roll regime but before the system has experienced any significant growth of vacuum fluctuations. For the preinflaton χ we assumed zero initial conditions $\chi = \dot{\chi} = 0$. At the end of this chapter, we shall briefly comment on the effect of non-vanishing initial χ. The initial field fluctuations, in turn, have been initialised as quantum vacuum fluctuations (see appendix C.3.1).

The numerical values of the initial fields, their derivatives, and the initial Hubble parameter H_i are summarised in table 6.1, together with the lattice configuration (i.e. box size L, and number of points per spatial dimension N).

Lattice results for different m_χ/m_ϕ in $2+1$ dimensions

Let us now turn to the discussion of our lattice results. We have simulated the non-linear evolution of the inflaton ϕ and the matter field χ in the model (6.4) for different values of the mass ratio m_χ/m_ϕ (or equivalently different values of λ). More explicitly, we considered the three cases $m_\chi/m_\phi \approx 0.364$, $m_\chi/m_\phi = 0.5$, and $m_\chi/m_\phi = 1$, which essentially corresponds to setting $\lambda = 1\times10^{-3}\, m_\mathrm{Pl}^{-1}$, $\lambda \approx 1.375\times10^{-3}\, m_\mathrm{Pl}^{-1}$ and $\lambda \approx 2.750\times10^{-3}\, m_\mathrm{Pl}^{-1}$, respectively.

Our results for the field variances and the field spectra are presented below in figure 6.1 and 6.2. The reason for putting particular attention to the variances is the following: at very late times, when the amplitudes of the fluctuations have been redshifted to small values, such that the potential they feel is approximately quadratic, we may take advantage of the virial theorem to approximate the field's energy densities. The latter may then be used to set the initial conditions for the perturbative decay of the fields.

Figure 6.1 shows the evolution of the variances $\sqrt{\langle\delta\phi^2\rangle}$ and $\sqrt{\langle\delta\chi^2\rangle}$, both in units of v and as a function of the scale factor a. The evolution is depicted for the three different mass ratios $m_\chi/m_\phi \approx 0.364$ (upper left), $m_\chi/m_\phi = 0.5$ (upper right) and $m_\chi/m_\phi = 1$ (lower left). For these three scenarios we also show the evolution of the Hubble parameter (lower right).

We can see that initially, the evolution of ϕ fluctuations is practically identical in all three scenarios. For $a \lesssim 1.4$ the fluctuations grow due to tachyonic oscillations

(cf. section 4.2.3). The growth is so efficient that non-linear interactions become important already after a couple of oscillations and the growth stops. The behavior of $\sqrt{\langle \delta\chi^2 \rangle}$, in turn, differs in any of the considered scenarios. For $m_\chi/m_\phi \approx 0.364$ and $m_\chi/m_\phi = 0.5$ the fluctuations eventually get amplified. On the other hand, for $m_\chi/m_\phi = 1$ we can see that the χ fluctuations are not amplified at all.

Notice that the resonant growth of $\delta\chi$ is different in the two scenarios for which $m_\chi/m_\phi < 1$. For the scenario with $m_\chi/m_\phi \approx 0.364$ efficient growth of fluctuations happens almost immediately after the inflaton has become inhomogeneous. For $m_\chi/m_\phi = 0.5$, in turn, the universe first expands by a factor of ~ 2 before efficient growth comes into effect. In that case, the growth is less efficient and happens over a more extended period of time than compared to the case where $m_\chi/m_\phi \approx 0.364$. In both cases, however, the resonance of χ fluctuations is sufficiently strong for non-linear effects to become important. We also observe, that the evolution of $\sqrt{\langle \delta\phi^2 \rangle}$ is, apparently, affected by the dynamics of χ fluctuations. This is not surprising and is essentially a consequence of energy conservation. The energy sources for the growth of χ fluctuations are, in fact, the fluctuations of ϕ.

Figure 6.2 shows the spectra of χ and ϕ fluctuations[6] for $m_\chi/m_\phi \approx 0.364$ (upper three), $m_\chi/m_\phi = 0.5$ (middle three) and $m_\chi/m_\phi = 1$ (lower three). For each of the scenarios the spectra are shown at three consecutive times: $a \approx 1.4$, shortly after the end of tachyonic oscillations; $a \approx 3$; and at the end of the simulation at $a \approx 10$.

As one would already expect from the behaviour of the variances, there is no growth of χ fluctuations and the spectrum of χ essentially remains that of vacuum fluctuations in the scenario where $m_\chi/m_\phi = 1$. The only fluctuations that grow are those of the inflaton. There a peak develops at $k/a \simeq 300 H_\mathrm{i}$ which eventually broadens towards the UV due to rescattering of modes.

The behaviour of the spectrum for the other two scenarios is qualitatively similar to that of the variance. For $m_\chi/m_\phi \approx 0.364$ the growth of fluctuations starts quickly after the end of the linear regime. In that case both fields acquire a peaked spectrum of fluctuations. Initially, the fluctuations of ϕ dominate over those of χ. However, the spectrum of $\delta\chi$ eventually catches up. The amplitude of the spectrum grows for most of the modes by more than one order of magnitude larger than that of the $\delta\phi$ and spectrum becomes noticeably flatter towards the IR. The situation is similar for $m_\chi/m_\phi = 0.5$ with the difference that the growth of fluctuations starts somewhat later and is less efficient.

On the range of couplings that favour resonant growth of $\delta\chi$

In order to study how the resonant amplification of χ fluctuations in an inhomogeneous ϕ background depends on the mass ratio (or equivalently on the coupling λ) we carried out a more sophisticated analysis consisting of a total of 94 lattice simulations, each of which performed with a different value of m_χ/m_ϕ. Just as for the results discussed above, the simulations were performed in $2+1$ dimensions, however, only with 1024 lattice points per spatial dimension[7]. We carefully checked

[6] See eq. (4.9) in section 4.2 for the definition of the power spectrum.

[7] And with same initial conditions for the homogeneous components as in table 6.1.

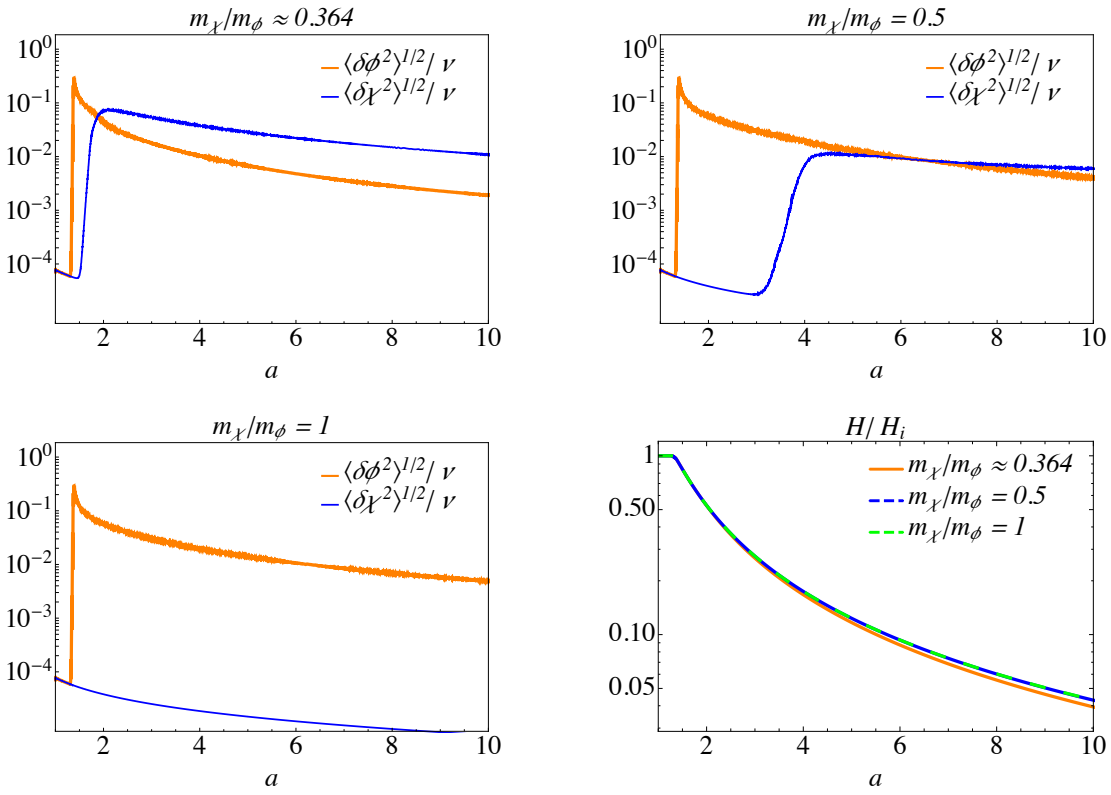

Figure 6.1: Evolution of the variances $\sqrt{\langle\delta\phi^2\rangle}$ and $\sqrt{\langle\delta\chi^2\rangle}$ as a function of the scale factor a. The evolution is depicted for realisations where $m_\chi/m_\phi \approx 0.364$, $m_\chi/m_\phi = 0.5$, and $m_\chi/m_\phi = 1$. Initially, the fluctuations of ϕ behave always the same, regardless of the value of m_χ/m_ϕ: During the linear regime ($a \lesssim 1.4$), the fluctuations grow due to tachyonic oscillations until non-linear effects become important at $a \sim 1.4$. The growth of χ fluctuations, on the other hand always happens after the evolution of ϕ has become non-linear ($a \gtrsim 1.4$). The strength of the growth depends, moreover, strongly on the value of m_χ/m_ϕ (or equivalently on the coupling λ). The lower right plot shows the evolution of the Hubble parameter $H(a)$ for the three considered scenarios.

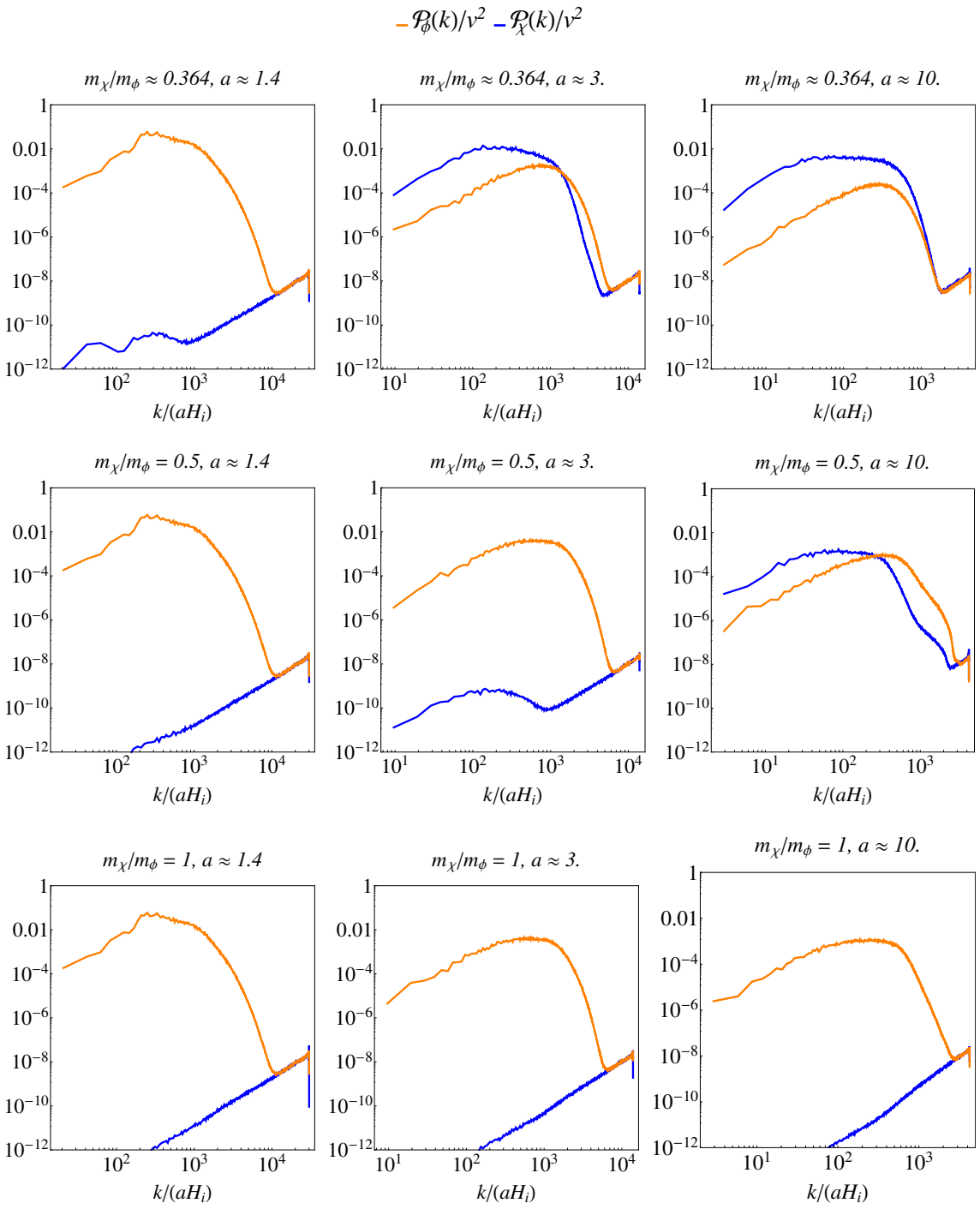

Figure 6.2: Results of field spectra for $m_\chi/m_\phi \approx 0.364$ (upper three), $m_\chi/m_\phi = 0.5$ (middle three), and $m_\chi/m_\phi = 1$ (lower three). The spectra of ϕ (orange) and χ (blue) fluctuations are depicted at three distinct moments in time, corresponding to $a \approx 1.4$ (left), $a \approx 3$ (middle), and $a \approx 10$ (right). Also here one can clearly see that the spectrum of ϕ initially evolves independently of the mass ratio. One can see that the efficiency of the energy transfer from ϕ to χ fluctuations is sensitive to the value of m_χ/m_ϕ. For $m_\chi/m_\phi \approx 0.364$, for example, one can clearly see that at $a \approx 10$ the inflaton fluctuations have lost a considerable amount of power, and the χ fluctuations eventually start dominating.

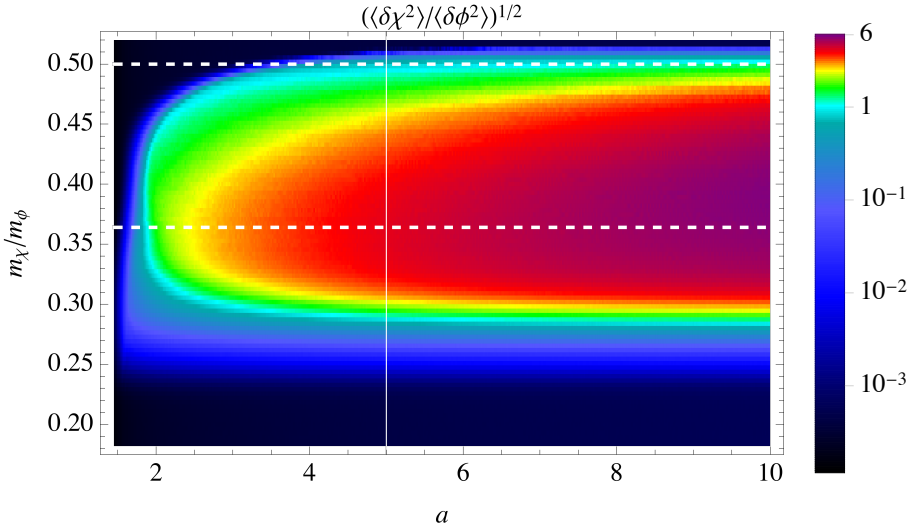

Figure 6.3: Evolution of $\sqrt{\langle\delta\chi^2\rangle/\langle\delta\phi^2\rangle}$ as a function of a and for different values of m_χ/m_ϕ. In total, the evolution is depicted for 94 values of m_χ/m_ϕ. The results were obtained from lattice simulations in 2+1 dimensions with box size $LH_\mathrm{i} = 0.21$ but with 1024 points per spatial dimension. As one can see, the amplification of χ fluctuations happens only within a certain range (or band) of m_χ/m_ϕ, within which the efficiency of the growth can vary strongly, particularly between the middle of the band $m_\chi/m_\phi \sim 0.35$-0.37 and the boundaries.

that reducing the resolution did not significantly change our results[8]. Explicitly, we scanned over $0.18 \lesssim m_\chi/m_\phi \lesssim 0.52$, in steps of $\Delta\frac{m_\chi}{m_\phi} = 0.0036$, which corresponds to scanning over $0.5\, m_\mathrm{Pl}^{-1} \leq 10^3\lambda \leq 1.43\, m_\mathrm{Pl}^{-1}$ in steps of $\Delta\lambda = 10^{-5}\, m_\mathrm{Pl}^{-1}$.

Our results are presented in figure 6.3 showing the relative growth of χ fluctuations over ϕ fluctuations represented by $\sqrt{\langle\delta\chi^2\rangle/\langle\delta\phi^2\rangle}$. The latter is shown as a function of the scale factor a and m_χ/m_ϕ. The results clearly demonstrate that the growth of χ fluctuations is only efficient within a certain band of mass ratios $0.25 \lesssim m_\chi/m_\phi \lesssim 0.5$. We carefully checked for larger values of the mass ratio around $m_\chi/m_\phi \sim 1$, without finding any evidence of resonant χ growth. The same conclusion applies to small $m_\chi/m_\phi \lesssim 0.2$.

Notice that $\sqrt{\langle\delta\chi^2\rangle/\langle\delta\phi^2\rangle}$ did not reach its final value by the end of our simulations. This becomes more clear when looking at figure 6.1 where one can see that, apparently, $\langle\delta\chi^2\rangle$ and $\langle\delta\phi^2\rangle$ redshift differently.

Generalised Floquet analysis for inhomogeneous backgrounds

As already mentioned, the lattice results discussed above were originally complemented by a generalised Floquet analysis that was carried out by Dr. David Nolde. The results are published in Ref. [1] where they are presented in section 4, to which we refer for more details.

[8]Indeed, it can be seen from figure 6.2 that at the end of the simulation $a \simeq 10$, the fluctuations at half the cutoff scale are practically vacuum fluctuations.

In essence, an approximate equation for the initial growth stage of χ fluctuations was derived. The latter reads [1]

$$\delta\ddot{\chi}_{\mathbf{k}} + \left(k^2 + \lambda^2 v^4\right)\delta\chi_{\mathbf{k}} + 2\lambda^2 v^3 \delta\phi_0 \cos(\omega_\phi t)\left(\delta\chi_{\mathbf{k}+\mathbf{k}_\mathrm{p}} + \chi_{\mathbf{k}-\mathbf{k}_\mathrm{p}}\right) = 0, \tag{6.13}$$

where $\omega_\phi = \sqrt{k_\mathrm{p}^2 + m_\phi^2}$, and $\delta\phi_0$ denotes the amplitude of the ϕ mode which dominates the spectrum (i.e. that with wavenumber $k = k_\mathrm{p}$). The derivation of the above equation was based on the following simplifying assumptions [1]:

- The amplitude of the ϕ fluctuations is much smaller than v: $\delta\phi(t, \mathbf{x}) = \phi(t, \mathbf{x}) - v \ll v$. Although this assumption is not justified during the tachyonic oscillations regime, it eventually becomes valid quickly after, i.e. when the fluctuations have been sufficiently redshifted due to Hubble damping.
- The fluctuations $\delta\chi$ are initially much smaller than the inflaton fluctuations.
- We neglect the expansion of the universe. This, in turn, is justified if the period of the oscillations of the fluctuations is much smaller compared to H^{-1}.
- $\delta\phi(t, \mathbf{x})$ is approximated by a standing wave with wavenumber $|\mathbf{k}| = k_p$, i.e.

$$\delta\phi(t, \mathbf{x}) = \delta\phi_0 \cos\left(\mathbf{k}_\mathrm{p} \cdot \mathbf{x}\right)\cos\left(\omega_\phi t\right) . \tag{6.14}$$

Eq. (6.13) then follows from the assumptions stated above, after expanding the full equation of motion for χ (cf. eq (4.6)) to linear order in both, $\delta\phi$ and $\delta\chi$ and transforming to Fourier space.

Notice that eq. (6.13) represents as a system of infinitely many differential equations: for each wavenumber $\mathbf{k}$ one would have to solve eq. (6.13) for each $\delta\chi_{\mathbf{k}+\ell\mathbf{k}_\mathrm{p}}$ for every integer number ℓ. This is, however, unfeasible. In practice, a momentum cutoff was applied and the Floquet analysis was performed for discrete values of $\mathbf{k}_\ell = \mathbf{k} + \ell\mathbf{k}_\mathrm{p}$. The Floquet system then reduces to a system that is mathematically equivalent to the multi-field case (cf. appendix C.2), with the difference that instead of multiple fields χ^ℓ we have different modes $\delta\chi_{\mathbf{k}_\ell}$ (for further details we refer to the discussion in section 4 of Ref. [1]).

Let us finally comment on the main result of this analysis. Similar to what we found in our purely numerical lattice study, the Floquet analysis showed that for mass ratios $0.25 \lesssim m_\chi/m_\phi \lesssim 0.5$ the fluctuations of χ experience exponential growth. In addition, we found indications of a second resonance band at $m_\chi/m_\phi \sim 1$ for which the Floquet exponents were found to be significantly smaller than for the previously mentioned band (cf. figure 2 in [1]). Indeed, this was our main motivation for performing numerical lattice simulations assuming $m_\chi/m_\phi \sim 1$. As discussed above, however, we did not observe any signs of growth in these scenarios.

Indicators for inhomogeneous parametric resonance

The results discussed in the previous part of this section clearly indicate that χ grows due to a parametric resonances that is driven by the dynamics of the inhomogeneous inflaton. The reasons are the following:

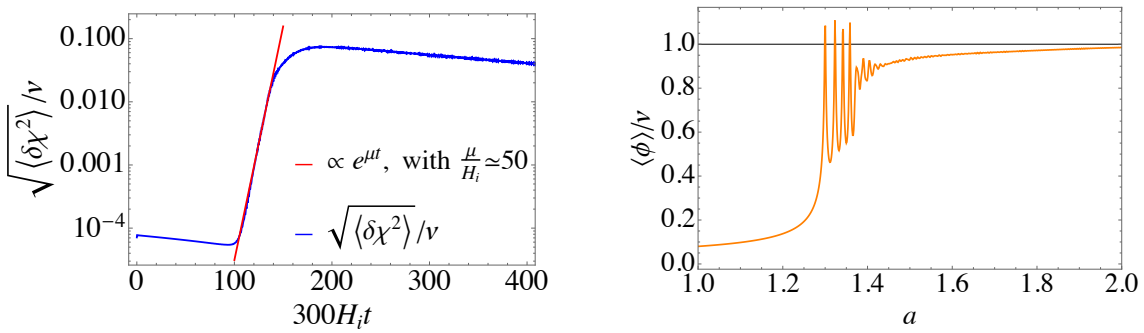

Figure 6.4: *Left:* Evolution of the variance $\sqrt{\langle\delta\chi^2\rangle}$ as a function of cosmic time t (blue). The evolution is shown for the scenario with $m_\chi/m_\phi \simeq 0.364$. The red curve corresponds to an exponential fit to the variance.
Right: Evolution of $\langle\phi\rangle$ as a function of the scale factor a. Initially, the field performs homogeneous oscillations during which the ϕ fluctuations grow due to tachyonic oscillations. After five oscillations, the homogeneous component eventually fragments into inhomogeneous fluctuations at $a \sim 1.4$ and the growth of fluctuations stops. Subsequently, the zero-mode quickly decays (i.e. $\langle\phi\rangle - v$ quickly approaches zero) and most of the energy is transferred to fluctuations.

- The growth of χ fluctuations is rapid and exponential as demonstrated in figure 6.4 by means of the variance $\sqrt{\langle\delta\chi^2\rangle}$. This, in turn, is typical for the process of parametric resonance (see e.g. the discussion in section 4.2.2).

- By the time at which the growth of χ fluctuations starts, the inflaton's zero mode is practically entirely decayed into inhomogeneous fluctuations (cf. figure 6.4). This implies that the energy that is transferred to χ fluctuations must originate from inhomogeneous fluctuations of ϕ. Indeed, the stronger the growth of χ fluctuations, the stronger the drop in $\langle\delta\phi^2\rangle$.

- The efficiency of the growth depends significantly on the interaction term (i.e. on the coupling λ or equivalently on m_χ/m_ϕ). Those realisations that lead to rapid growth of fluctuations are found to lie within a certain range (or band) of values of m_χ/m_ϕ. Outside this band, the χ fluctuations do not grow at all.

Comment on non-zero initial conditions for $\langle\chi\rangle$

Although we assumed $\langle\chi\rangle_\mathrm{i} = \langle\dot{\chi}\rangle_\mathrm{i} = 0$ to initialise χ in our lattice simulations, the precise initial conditions depend on the dynamics during the stage of preinflation[9], which in turn depends on terms arising from SUGRA corrections. If the latter give

[9]To be more precise, the initial conditions for χ depend on the *transition* between the preinflation regime and hilltop inflation. When $\chi \simeq \phi \simeq 0$, i.e. in the flat region of the potential, the dynamics are not dominated by the classical field evolution but rather by that of quantum fluctuations. Within this regime, the fields perform a random walk until their amplitude reaches a value at which the classical evolution starts to dominate. This value essentially depends on the SUGRA corrections.

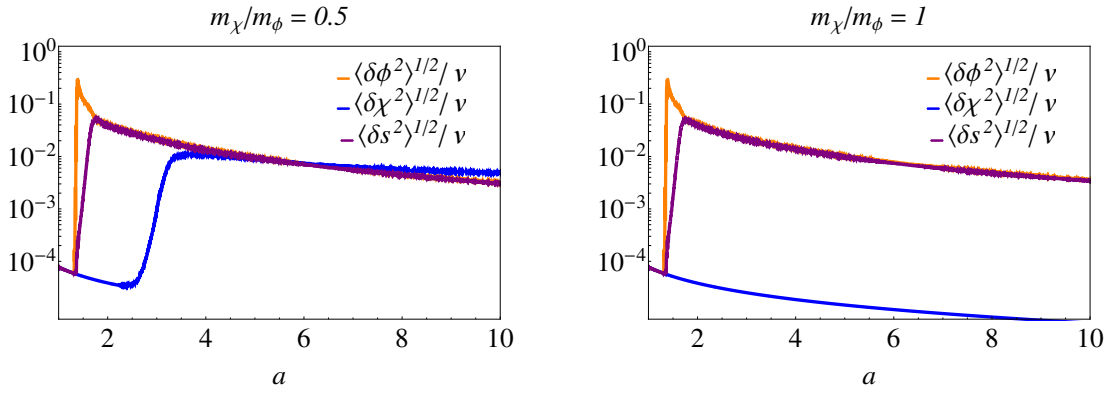

Figure 6.5: Comparison of the evolution of the variances $\sqrt{\langle\delta\phi^2\rangle}/v$, $\sqrt{\langle\delta\chi^2\rangle}/v$ and $\sqrt{\langle\delta s^2\rangle}/v$, where $s = \sqrt{2}\,\Re[S]$ denotes the real part of the driving field. The evolution is again shown as a function of the scale factor a, and for $m_\chi/m_\phi = 0.5$ (left) and $m_\chi/m_\phi = 1$ (right). $\sqrt{\langle\delta\phi^2\rangle}$ and $\sqrt{\langle\delta\chi^2\rangle}$ evolve practically in the same way as in the absence of s. The latter, in turn, is always amplified until $\sqrt{\langle\delta s^2\rangle} \simeq \sqrt{\langle\delta\phi^2\rangle}$ after which $\sqrt{\langle\delta s^2\rangle}$ essentially evolves like $\sqrt{\langle\delta\phi^2\rangle}$. Notice, that unlike the growth of χ fluctuations, the resonant growth of s happens already during the linear regime of tachyonic oscillations, during which the energy is initially dominated be the homogeneous mode of ϕ.

rise to small mass corrections, our initial conditions may, indeed, be justified [135]. However, if such corrections are absent, $\langle\chi\rangle$ can be non-zero initially.

The effect on preheating of a non-vanishing initial χ condensate depends in turn on the mass ratio m_χ/m_ϕ. In particular, the band for which efficient growth χ fluctuations is possible might be extended to smaller values of $m_\chi/m_\phi \lesssim 0.5$ (for details cf. the discussion in appendix A of [1]). The results presented above therefore essentially represent a lower bound on the maximum possible amplification of χ fluctuations.

Parametric resonance of the driving field S

When we introduced the supersymmetric hilltop inflation model in section 6.1 we assumed that the driving field S is stabilised at $S = 0$ during inflation. However, just as the preinflaton χ, S couples to the inflaton and can in principle get amplified during preheating.

Including, the real part of the driving field, $s = \Re[S]/\sqrt{2}$, the scalar potential with $p = 6$ which follows from (6.4) reads

$$V(\phi,\chi,s) = V_0\left(1-\frac{\phi^6}{v^6}\right)^2 + \frac{\lambda^2}{2}\phi^2\chi^2(\phi^2+\chi^2) + \frac{m_\phi^2}{2}s^2\left(\frac{\phi}{v}\right)^{10} - 6\sqrt{2}\,\lambda s\chi^2\left(\frac{\phi}{v}\right)^6 . \tag{6.15}$$

Notice that at the minimum of the potential $\phi = v$, $\chi = s = 0$, s has exactly the same mass as the inflaton and does not depend on λ.

To investigate the dynamics of preheating in the presence of s we performed numerical lattice simulations of the model (6.15) The initial conditions were chosen as in table 6.1 and with $\langle s\rangle_{\mathrm{i}} = \langle \dot{s}\rangle_{\mathrm{i}} = 0$. The results of the simulation are presented in figure 6.5 which shows the evolution of the variances of ϕ, χ, and s assuming $m_\chi/m_\phi = 0.5$ (left), and $m_\chi/m_\phi = 1$ (right). The evolution is again shown as a function of the scale factor a. One can see that regardless of the value of m_ϕ/m_χ (or λ, respectively), the fluctuations of s are always strongly amplified due to parametric resonance. In contrast to the growth of χ fluctuations, the perturbations of s get amplified already during the (linear) tachyonic oscillations regime. When ϕ becomes non-linear, the rate of growth of δs changes, however, until non-linearities terminate the growth. Moreover, notice that in contrast to the χ fluctuations, which eventually start dominating over those of ϕ, $\sqrt{\langle \delta s^2\rangle}$ grows until it becomes comparable to $\sqrt{\langle \delta\phi^2\rangle}$, after which it follows nearly the same evolution. The evolution of the χ fluctuations, however, remains practically the same as in the absence of s (cf. figure 6.1).

6.2.4 Results of lattice simulations in $3+1$ dimensions for $p = 4$, 6 and 8

So far we focused on results obtained from lattice simulations in $2+1$ dimensions. In this section, we present results obtained from more realistic three-dimensional lattice simulations of the hilltop inflation model[10] (6.4), i.e. in the presence of an additional matter field χ that couples to the inflaton ϕ. As in section 6.2.3 we focus on realisations where

$$v = 10^{-2} m_{\rm Pl} \,. \tag{6.16}$$

In addition to the hilltop potential with $p = 6$, we also consider two additional realisations of (6.4), namely $p = 4$, and $p = 8$. Moreover, for each of these three realisations we consider the two where

$$\lambda = 1 \times 10^{-3} m_{\rm Pl}^{-1} \,, \quad \text{and} \quad \lambda \approx 1.375 \times 10^{-3} m_{\rm Pl}^{-1} \,, \tag{6.17}$$

or in terms of the mass ratio eq. (6.9)

$$m_\chi / m_\phi \simeq 0.364 \,, \quad \text{and} \quad m_\chi / m_\phi = 0.5 \,. \tag{6.18}$$

Thus, in total we performed six lattice simulations, one for each realisation of (6.4).

Initialisation and lattice configuration

As mentioned above, the results presented below have been carried out by performing numerical lattice simulations with a modified[11] version of LatticeEasy in $3+1$ dimensions and with 256 points per spatial dimension. Each of the simulations was performed within a comoving box of size $L = 10\pi/m_\phi$, with m_ϕ as in eq. (6.10).

Within our lattice simulations, the inflaton was initialised shortly after the end of inflation when

$$|\eta_V| \simeq 25 \quad \text{and} \quad \varepsilon_V \ll 1 \,. \tag{6.19}$$

In practice, the numerical values for the homogeneous mode $\langle\phi\rangle_{\rm i}$ and its derivative $\langle\dot{\phi}\rangle_{\rm i}$ were obtained by numerically solving the homogeneous inflaton equation of motion (3.10), with slow-roll initial conditions (3.16) (i.e. when $|\eta_V| \ll 1$ and $\varepsilon_V \ll 1$) up to $\eta_V = 25$. As in section 6.2.3, the field χ was initialised with zero initial conditions. The initial field fluctuations of both fields have been initialised according to the prescription used by LatticeEasy (cf. appendix C.3.1).

For each of the three realisations[12] of the hilltop potential (corresponding to different values of p), the numerical values of the initial homogeneous field components are summarised in table 6.2.

[10] We note that SUGRA corrections are, again, assumed to be negligible.

[11] For more details on what has been modified see appendix C.4.

[12] As discussed in section 6.1.1 we restrict to those cases in which inflation happens in the single-field limit, with $\chi = 0$ at the end of inflation. Therefore, the initial conditions for the inflaton are independent of m_χ/m_ϕ.

$V_0/m_{\rm Pl}^4$	$v/m_{\rm Pl}$	p	$\langle\phi\rangle_{\rm i}/v$	$\langle\dot{\phi}\rangle_{\rm i}/v^2$	$\langle\chi\rangle_{\rm i}$	$\langle\dot{\chi}\rangle_{\rm i}$
1.750×10^{-22}	10^{-2}	4	0.0102	2.13×10^{-11}	0	0
8.006×10^{-20}	10^{-2}	6	0.0803	2.21×10^{-9}	0	0
4.977×10^{-19}	10^{-2}	8	0.168	8.32×10^{-9}	0	0

Table 6.2: Numerical values of the model parameters related to the inflaton potential and initial conditions for lattice simulations. Notice that the values of V_0 correspond to those that were already shown in table 3.1 and are only summarised again to improve clarity.

Variances and spectra

Let us now turn to the discussion of our lattice results. We begin with the evolution of the variances $\langle\delta\phi^2\rangle$ and $\langle\delta\chi^2\rangle$. The latter are presented in figure 6.6 as a function of the scale factor a, for $m_\chi/m_\phi \approx 0.364$ (plots on the left) and $m_\chi/m_\phi = 0.5$ (plots on the right). The upper two plots show the evolution of the $\langle\delta\phi^2\rangle$ (orange) and $\langle\delta\chi^2\rangle$ (blue) for the case where $p = 4$. The middle plots correspond to results of simulations with $p = 6$, and the lower two plots with $p = 8$.

The evolution of $\langle\delta\phi^2\rangle$ is qualitatively similar in all realisations. The fluctuations get initially amplified due to tachyonic oscillations (cf. the discussion in section 6.2.1) until non-linear effects terminate the growth. The evolution of $\langle\delta\chi^2\rangle$, on the other hand, clearly depends on the values of both p and m_χ/m_ϕ. As one can see, apart from the simulation where $p = 8$ and $m_\chi/m_\phi = 0.5$, the fluctuations of χ get always amplified due to parametric resonance which is triggered not before ϕ becomes non-linear. Indeed, this is what we already observed in the results of two-dimensional simulations (cf. the discussion in section 6.2.3) of the same model with $p = 6$. In particular, we find that the three-dimensional simulations show the same qualitative dependence in the dynamics of χ fluctuations on the value of m_χ/m_ϕ. In essence, the growth of $\delta\chi$ is significantly more efficient for $m_\chi/m_\phi \approx 0.364$ than for $m_\chi/m_\phi = 0.5$. Moreover, a clear tendency is visible in how the behaviour of the fluctuations depends on p. The growth of χ fluctuations starts later and becomes also less efficient when increasing p.

Another result which we would like to present is the evolution of the ratio of the variances $\langle\delta\chi^2\rangle/\langle\delta\phi^2\rangle$. The latter is shown in figure 6.7 for $m_\chi/m_\phi \approx 0.364$ (left) and $m_\chi/m_\phi = 0.5$ right. Here, we restrict to the case where $p = 6$. By comparing these results to those presented in section 6.2.3, and in particular to figure 6.3 one can see that at $a \approx 5$ and apart from factors $\sim \mathcal{O}(1)$ the results of the two-dimensional simulations are in good agreement with those presented here. In both simulations where $m_\chi/m_\phi \approx 0.364$ we have $1 < \langle\delta\chi^2\rangle/\langle\delta\phi^2\rangle < 6$. On the other hand, for $m_\chi/m_\phi = 0.5$ we find $0.1 < \langle\delta\chi^2\rangle/\langle\delta\phi^2\rangle < 1$ at $a \approx 5$.

Let us now turn to the field spectra which are depicted in figure 6.8 as a function of the physical wavenumber $a^{-1}k$. The orange curves correspond to the inflaton field spectra, while the spectra of χ fluctuations are shown in blue. The solid lines originate from simulations where $m_\chi/m_\phi \approx 0.364$, while results of simulations with $m_\chi/m_\phi = 0.5$ are denoted by dashed lines. The spectra are all shown at the end

of the corresponding simulation ($a \approx 5$). As we have already observed in our two-dimensional simulations (cf. figure 6.2), for those realisations where χ fluctuations experience resonant growth, the corresponding spectra typically peak at values of k/a that are slightly below the peak scale of the ϕ fluctuations. Another similarity is that, particularly for $p = 4$ and $p = 6$ and $m_\chi/m_\phi \approx 0.364$, the spectra of χ fluctuations are less peaked and eventually flatten towards the IR.

Comment on the behaviour of the homogeneous components

Although not shown explicitly, we have also considered the evolution of $\langle\phi\rangle$ and $\langle\chi\rangle$. Regarding the evolution of the homogeneous inflaton component we find that the qualitative behaviour of $\langle\phi\rangle$ is always the same, regardless of the value of p and m_χ/m_ϕ. In essence, the field initially performs homogenous oscillations during which the ϕ fluctuations get amplified due to tachyonic oscillations. As the fluctuations grow, non-linear effects eventually become important after a couple of oscillations. The homogeneous component then quickly decays as demonstrated in figure 6.4 (right part) and the field gets dominated by inhomogeneous fluctuations.

The situation is slightly different for χ, where initially we have $\langle\chi\rangle = 0$. There we find that in those cases, where the fluctuations of χ are efficiently amplified, the homogeneous component is also (simultaneously) produced but rather decays quickly. In particular, for all the considered scenarios we find that χ remains always dominated by its fluctuations. Indeed, although $\langle\chi\rangle/\sqrt{\langle\delta\chi^2\rangle}$ might initially grow, the growth eventually stops and we find that $\langle\chi\rangle/\sqrt{\langle\delta\chi^2\rangle} \ll 1$ throughout the entire evolution. The largest values that we observed for $\langle\chi\rangle/\sqrt{\langle\delta\chi^2\rangle}$ were $\mathcal{O}(0.1)$ for the scenario with $p = 6$ and $m_\chi/m_\phi = 0.5$.

Oscillons in $3 + 1$ dimensions

The production of oscillons during preheating after hilltop inflation was studied within Ref. [194] where the pure hilltop inflation model (6.2) was considered for different values of v and with fixed $p = 4$. The findings presented there were based on numerical lattice simulations of the scalar field evolution in both two and three spatial dimensions.

In [20] the study was extended by considering the effect of resonantly produced χ fluctuations on the formation and evolution of oscillons in the potential (6.4) with $p = 6$. On the basis of numerical lattice simulations in $2 + 1$ dimensions it was found, among others, that the formation of oscillons is sensitive to the efficiency of the parametric resonance of χ. In particular, it was shown that for a coupling $\lambda = 10^{-3} m_{\rm Pl}^{-1}$ (or equivalently for a mass ratio m_χ/m_ϕ) which leads to a fast and strong ampification of χ fluctuations, no oscillons are formed. On the other hand, it was shown that for $m_\chi/m_\phi = 0.5$, where the resonance is weaker and happens later, oscillons are eventually formed in both fields. In particular, it was found that the oscillons of the χ field turn out to be strongly correlated to those of ϕ and are essentially formed at the same spatial positions.

In what follows we discuss results related to the formation of oscillons. The latter were extracted from our three-dimensional lattice simulations and are presented in figure 6.9. The upper row of plots shows results from a simulation with $p = 4$ and

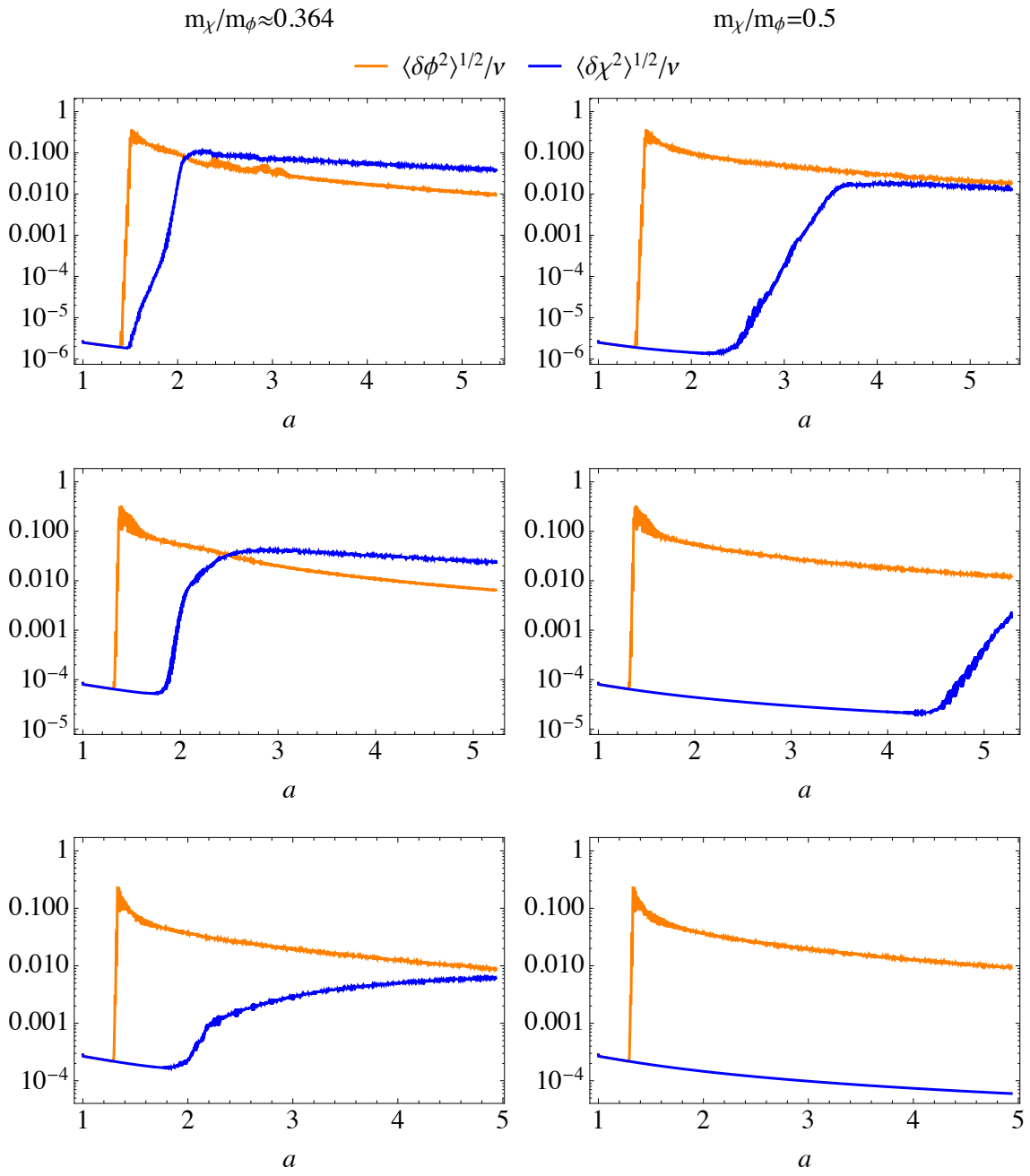

Figure 6.6: Evolution of the variances $\sqrt{\langle\delta\phi^2\rangle}$ and $\sqrt{\langle\delta\chi^2\rangle}$ depicted as a function of the scale factor for $p = 4$ (upper plots), $p = 6$ (middle plots), and $p = 8$ (lower plots). The figures on the left show results of simulations where $m_\chi/m_\phi \approx 0.364$ and those on the right correspond to simulations with $m_\chi/m_\phi = 0.5$ For the case where $p = 6$ (middle) one can see that the variances behave qualitatively very similar as in our two-dimensional lattice simulation. In particular, one can see that the growth starts later and is less efficient for $m_\chi/m_\phi = 0.5$. The same qualitative behaviour is exhibited within the other realisations ($p = 4$, and $p = 8$) with the difference, that increasing p consistently leads to a decrease in the efficiency of resonant χ amplification.

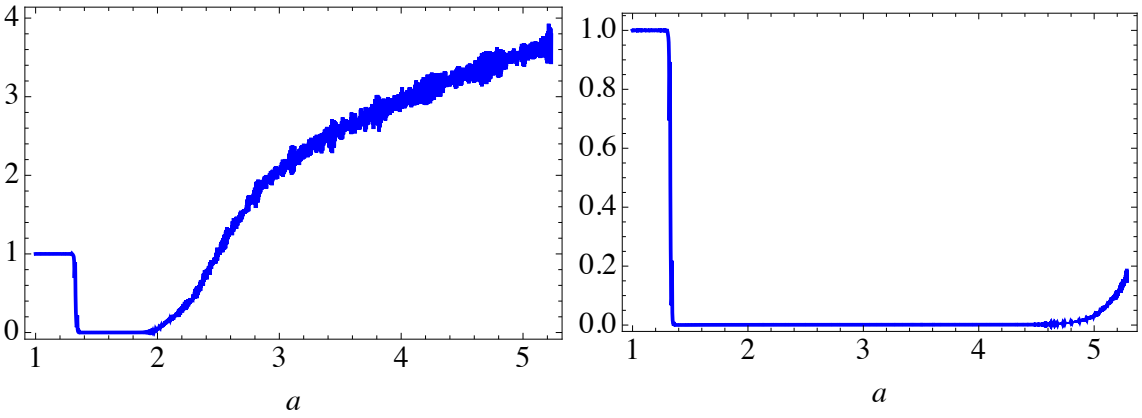

Figure 6.7: Evolution of $\sqrt{\langle\delta\chi^2\rangle}/\sqrt{\langle\delta\phi^2\rangle}$ as a function of the scale factor a for $p = 6$ and $m_\chi/m_\phi \approx 0.364$ (left) and $m_\chi/m_\phi = 0.5$. When comparing these results to those obtained from two-dimensional simulations (cf. the dashed white lines in figure 6.3), we find that the two- and three-dimensional simulations agree very well at $a \simeq 5$.

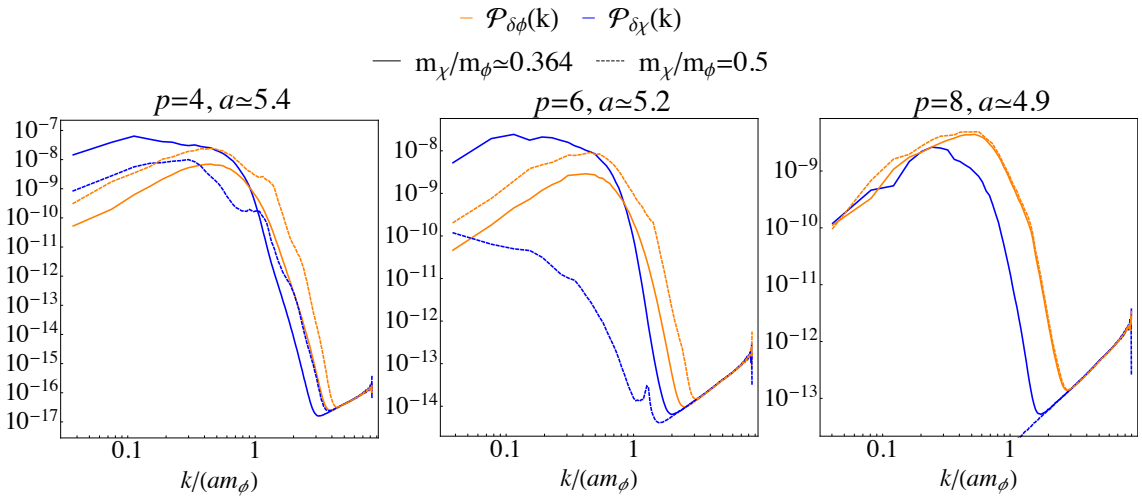

Figure 6.8: Field spectra depicted at the end of the simulation when $a \sim 5$, for $p = 4$ (left), $p = 6$ (middle), and $p = 8$ (right). The inflaton field spectrum is again shown in orange and the spectrum of χ fluctuations in blue. Results are shown for $m_\chi/m_\phi \approx 0.364$ (dashed) and $m_\chi/m_\phi = 0.5$ (solid). One can see that the energy in χ fluctuations indeed comes from the inhomogeneous fluctuations of ϕ. In particular, the stronger the power in χ, the larger the decrease of the amplitude in the ϕ spectrum.

$m_\chi/m_\phi = 0.5$, the middle row for $p = 6$ and $m_\chi/m_\phi = 0.5$, and the lower four plots for $p = 8$ and $m_\chi/m_\phi \approx 0.364$. The plots on the outermost left-hand side always show the spatial energy density distribution represented by surfaces of equal energy density. Green surfaces denote regions with six times the average energy density $\langle\rho\rangle$ and blue corresponds to regions where $\rho = 12\langle\rho\rangle$. The other plots show the distribution of the fields around the minimum of the potential represented by surfaces of equal amplitude and in units of v. The plots on the middle left shows

$(\phi - v)$, the ones on the middle right show χ, and those on the outermost right-hand side show both fields together. For the plots in the middle two columns of the figure different colors correspond to positive/negative values of $(\phi - v)$ (blue/green), and positive/negative values of χ (yellow/red). In the plots on the outermost right-hand side the different colors denote isosurfaces of constant $|\phi - v|$ (yellow), and $|\chi|$ (blue), respectively. All the results have been extracted at the end of the corresponding simulation, i.e. at $a \approx 5$.

In agreement with the two-dimensional results published in [20] we find that in those scenarios where the amplification of χ fluctuations due to parametric resonance is particularly strong (i.e. $p = 4$ and $p = 6$ with $m_\chi/m_\phi \approx 0.364$) no oscillons are formed. On the other hand, in all other scenarios in which χ experiences resonant growth of fluctuations we find that oscillons are formed, at least in ϕ. Notice, that these cases are exactly those depicted in figure 6.9. As one can see from the figure, for $p = 4$ and $p = 6$ and $m_\chi/m_\phi = 0.5$ we find that oscillons are formed in both fields. Moreover, from the figures on the outermost right it is evident that the oscillons in χ (blue areas) form at the same positions as the oscillons in ϕ (yellow areas), thus confirming the findings of Ref. [20].

The situation is less clear for the scenario with $p = 8$, and $m_\chi/m_\phi = 0.5$, at least by the end of our simulation. As can be seen from the energy density distribution and also in the field distribution of ϕ, oscillons are clearly formed. For χ on the other hand, it is less evident whether some of the colored spots are oscillons or unstable fluctuations. Nevertheless, as can be seen from the outermost right figure in the lower row, the fluctuations of χ (blue) and those of ϕ (yellow) seem to be uncorrelated in this case.

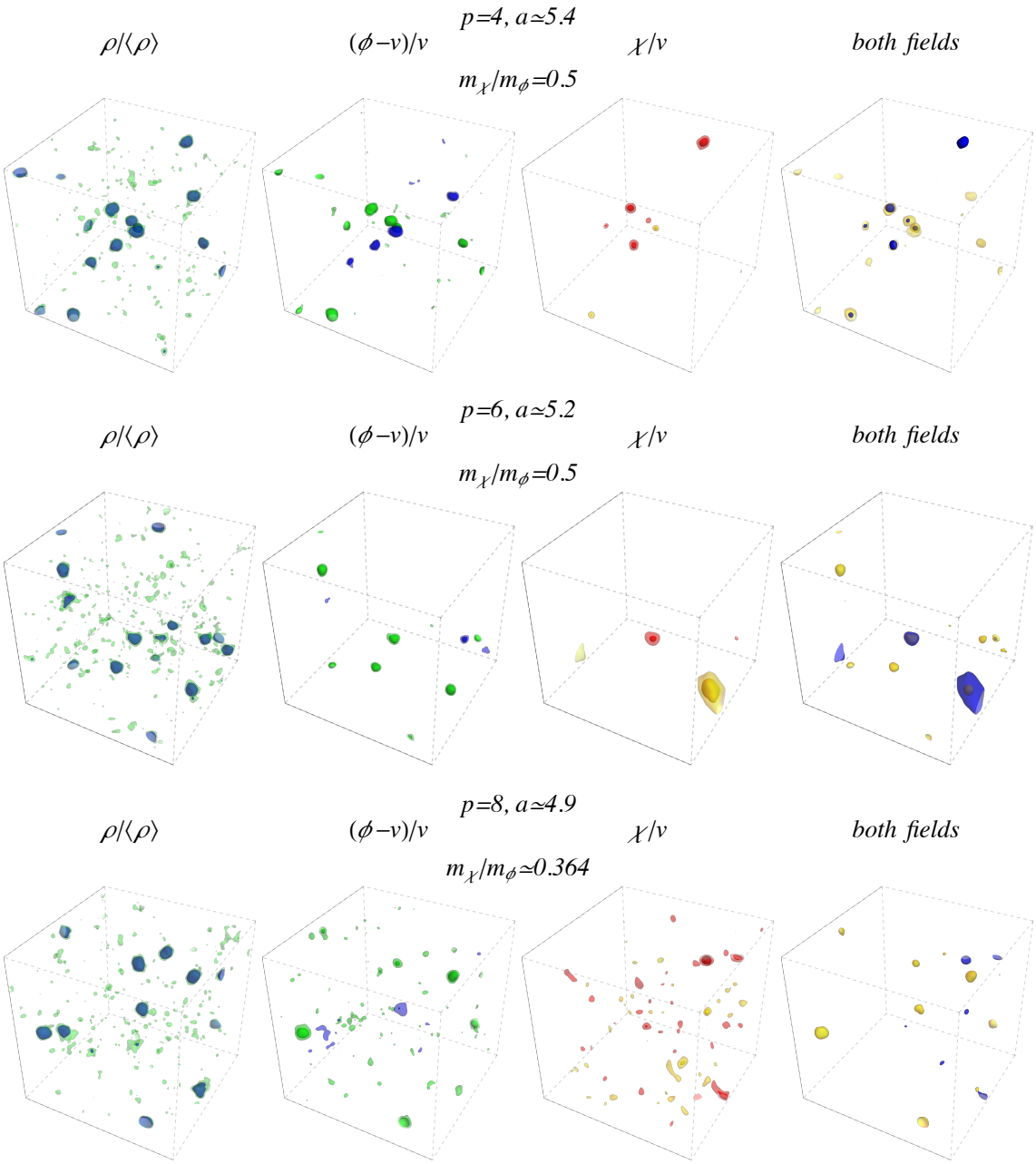

Figure 6.9: Snapshots of the energy density and field distributions from simulations with: $p = 4$ and $m_\chi/m_\phi = 0.5$ (upper four), $p = 6$ and $m_\chi/m_\phi = 0.5$ (middle four), $p = 8$ and $m_\chi/m_\phi = 0.5$ (lower four). For each simulation we show (from left to right): isosurfaces of the energy density in units of the average energy density $\langle\rho\rangle$, corresponding to $\rho = 6\langle\rho\rangle$ (green) and $\rho = 12\langle\rho\rangle$ blue; isosurfaces of $(\phi - v)/v$ with blue and green representing positive and negative values, respectively; isosurfaces of χ/v with positive and negative values denoted by yellow and red; isosurfaces of $|\phi/|/v$ (yellow) and $|\chi|/v$ (blue). All snapshots are taken at the end of the corresponding simulation at $a \approx 5$.

6.3 Gravitational wave production after hilltop inflation

As emphasised in section 4.4.3, GWs could potentially serve as an insightful probe of the early universe. This motivated us to study the production of GWs during preheating after hilltop inflation. To this end we modified the original version of LatticeEasy to simultaneously solve the equations for the (TT) tensor perturbations. A detailed description on how we implemented the relevant equations into LatticeEasy is provided in appendix C.4.1. Moreover, in order to reduce the numerical error related to the spatial discretisation we have replaced the second-order accurate Laplacian used by LatticeEasy, with one that is fourth-order accurate in space (see appendix C.4.2 for details). This led to a considerable improvement of our numerical results (cf. the discussion in section 6.3.1).

The results of our lattice simulations are presented in figure 6.11. The latter shows the spectra of GW $\Omega_{\rm GW}(k)$ as a function of the physical wavenumber $a^{-1}k/m_\phi$ at the end of our simulations. The spectra are shown for $p = 4$ (upper plot), $p = 6$ (middle plot), and $p = 8$ (lower plot). Within each of the figures three distinct spectra are shown corresponding to results of simulations carried out assuming: $m_\chi/m_\phi \approx 0.364$ (orange dotted curves), $m_\chi/m_\phi = 0.5$ (green dashed curves), and $m_\chi/m_\phi = 0$, i.e. the pure hilltop inflation model (solid blue curve).

In all of the considered scenarios the spectra look qualitatively similar. They all feature a broad peak (or a relatively flat plateau) towards the IR which falls off quickly towards the UV for $a^{-1}k \gtrsim m_\phi$. Notice that the spectra do not exhibit a characteristic peak structure as discussed in section 5.1, although asymmetric oscillons are clearly formed as shown in figure 6.9. This does, however, not mean that oscillons do not contribute to the GW spectrum. Indeed, when comparing the results of the different simulations with each other, a difference can be seen between scenarios in which oscillons are formed and those where the production of oscillons is suppressed due to the strong resonance of χ (orange dotted lines in the upper two plots). In particular, one can see that in the presence of oscillons, the spectrum exhibits more power towards the UV for $a^{-1}k \gtrsim m$. For the case where $p = 8$, on the other hand the spectra are practically indistinguishable. As discussed above, in that case the amplification of χ fluctuations is either weak or does not happen at all and the system is mostly dominated by the fluctuations of ϕ (cf. the field power spectrum on the right of figure 6.8).

The reason why no distinctive oscillon features are visible in the GW spectrum is merely due to the violent preheating dynamics during the early non-linear regime. As demonstrated in figure 6.10, the dominant contribution to the GW spectrum is produced in the absence of oscillons are not yet produced. As we shall see shortly, it turns out that the GW spectrum produced subsequently, after oscillons have formed, is simply covered.

In order to obtain an estimate of the present day GW spectrum amplitude $\Omega_{\rm GW,0}$ and the corresponding present day GW frequencies f_0 (in Hz), we can make use of the relations eqs. (4.84) and (4.85) to account for the effect of the expansion between the moment of emission and today. Assuming that immediately after the end of our simulations the universe reheats into a thermal bath of relativistic particles, we

obtain (for all scenarios) the following estimate for the present day amplitude of the GW spectrum (at the plateau)

$$\Omega_{\mathrm{GW},0}(f_0) \sim \mathcal{O}(10^{-11})\,. \tag{6.20}$$

On the other hand, we find that today the plateau (corresponding to wavenumbers $a^{-1}k \lesssim m_\phi$ in figure 6.10) would be observable at frequencies

$$f_0 \lesssim 5 \times 10^8\,\mathrm{Hz}\,, \quad \text{for} \quad p = 4\,, \tag{6.21}$$

and

$$f_0 \lesssim 5 \times 10^9\,\mathrm{Hz}\,, \quad \text{for} \quad p = 6 \quad \text{and} \quad p = 8\,. \tag{6.22}$$

Hence, the spectra are far outside the reach of current and envisaged GW detectors [219–223].

6.3.1 Comment on Phys.Rev.Lett. 118 (2017) no.1, 011303

In this section we would like to briefly comment on results of the GW spectrum produced during preheating after hilltop inflation that were originally published in [2]. There we claimed the dynamics of the oscillons can give rise to a pronounced peak in the GW which develops over an extended period of time around $a^{-1}k \sim m_\phi$. Our claims were based on results of lattice simulations in $3+1$ dimensions and with 128 points per dimension. There we found that over 2-3 e-folds of expansion the peak grew by about two orders of magnitude larger than the IR plateau produced during the early stages of non-linear preheating (cf. figure 6.11 or also figure 1 in [2]).

Unfortunately, it turned out that these results were overestimated due to numerical errors related to an insufficient accuracy in the discrete spatial derivatives. We noticed[13] this issue after having carried out a simulation of the same scenario but with four times the resolution[14] (per spatial dimension) [4]. Since performing a simulation with even higher resolution was simply impractical for us we decided to replace the second-order accurate, centered difference scheme used by LatticeEasy, with a centered difference approximation of the spatial Laplacian that is fourth order accurate in space (see eq. (C.4.35) and the related discussion).

This finally allowed us to perform a successful convergence analysis for the GW spectrum. The corresponding results are presented in figure 6.12. The latter shows results of lattice simulations of the pure hilltop inflation model, that were performed with exactly the same setup as in [2] (i.e. same parameter choices, same box size and same initial conditions). The solid blue curve shows results carried out with 128 lattice points per dimension, while the solid red curve represents results of a simulation with 256^3 lattice points. As one can see, both simulations are in very good agreement up to $a \simeq 9$ and apart from the unphysical UV tail.

As already argued above, the reason why the characteristic and peaky oscillon signal is not explicitly visible in the GW spectrum is not that the oscillons do

[13] We note that this was also recently noted by other researchers in Ref. [248].
[14] Which essentially took us about nine months.

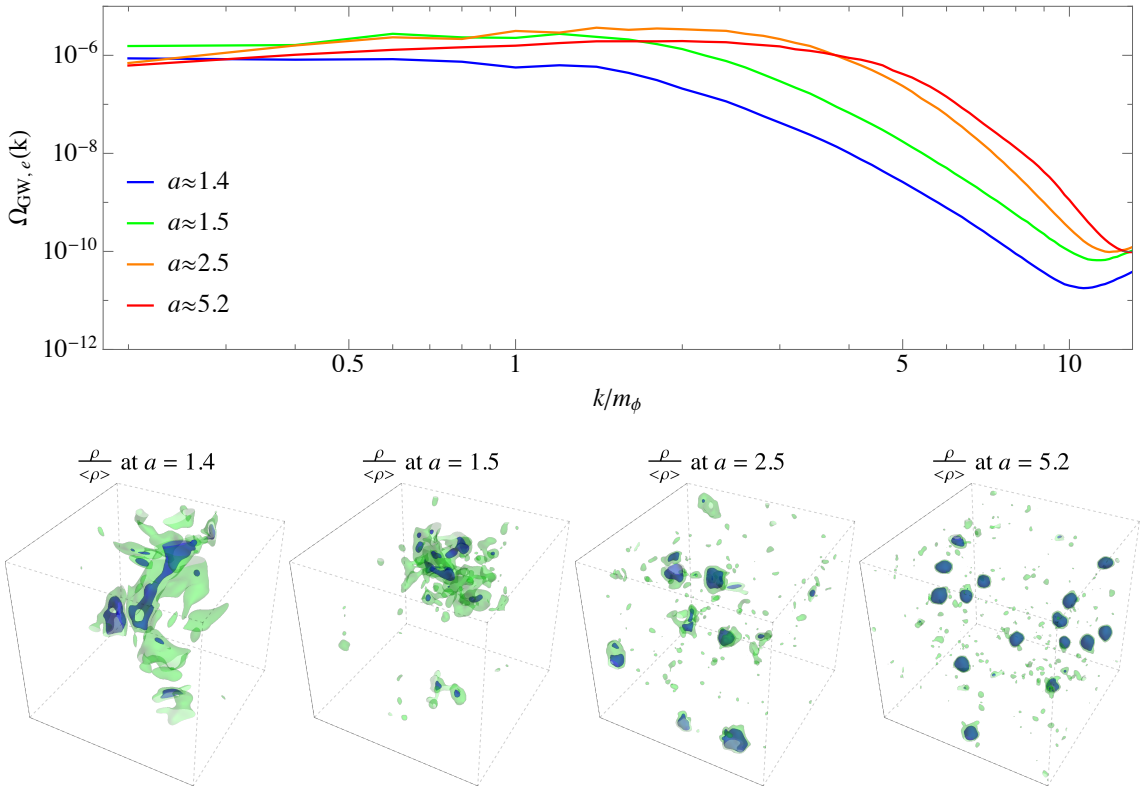

Figure 6.10: *Upper:* GW spectrum produced during preheating after inflation for the pure hilltop inflation model with $p = 6$. The spectrum is shown at different moments of time, corresponding to $a \approx 1.4$ (blue), $a \approx 1.5$ (green), $a \approx 2.5$ (orange), and at the end of the simulation $a \approx 5.2$ (blue). The spectrum is shown as a function of the comoving wavenumbers k/m_ϕ.
Lower: Snapshots of the energy density distribution. The green areas correspond to isosurfaces for which the energy density is six times the average energy density $\langle\rho\rangle$. Blue surfaces, in turn, denote isosurfaces where $\rho = 12\langle\rho\rangle$. By comparing both figures one can clearly see, that a broad peak in the GW spectrum already develops during the early, non-linear stage of preheating, before oscillons start to be formed around $a \sim 2.5$. Notice, however, that oscillon formation has not ended at $a \approx 2.5$. Indeed, one can see that some of the bubbles are still about to fragment further.

not produce GWs, but rather due to the fact that the early non-linear stage of preheating is the dominant source of the spectrum. In order to display the effect of the oscillons explicitly, we have "overleaped" this early regime by manually turning off the GW source until $a \simeq 2.8$. The resulting GW spectrum produced for $a \gtrsim 2.8$ is also shown in figure 6.12 where it is represented by the dashed lines[15]. As can be clearly seen, a peak is produced at a (characteristic) frequency corresponding to the physical mass scale (denoted by the solid black line in figure 6.12). In contrast to our original findings [2], the peak eventually stops growing and gets redshifted (cf.

[15]Again blue and red denote a simulation carried out with 128 points, and 256 points per dimension, respectively.

the plot on the lower right of figure 6.12). Notice, however, that GWs still continue to be produced but with continuously decreasing efficiency. This, in turn, is most likely related to a decrease in amplitude and/or to a decrease in asymmetry. Finally, to conclude this section let us emphasise that our general statement of Ref. [2], i.e. that asymmetric oscillons can produce a characteristic peak in the GW spectrum remains valid, as already confirmed in chapter 5.

6.4 Summary

In this chapter we have studied the scalar field dynamics during preheating after hilltop inflation in the presence of an additional scalar field χ that couples to the inflaton ϕ. We first gave a short motivation of the model and briefly reviewed the preheating dynamics of the inflaton in the absence of χ.

Within our study we considered realisations of the hilltop inflation model for which efficient growth of ϕ fluctuations happens via the process of tachyonic oscillations. Explicitly, we focused on realisations of the hilltop model with $v = 10^{-2} m_{\rm Pl}$.

To study the non-linear preheating dynamics after inflation we performed numerical lattice simulations in $2+1$ and $3+1$ dimensions. Independently, of the dimensionality of the lattice box we found that χ can get resonantly amplified from its initially small vacuum fluctuations up to amplitudes that may even exceed those of the inflaton fluctuations.

From two-dimensional lattice simulations of the hilltop model with $p = 6$ we found that the amplification of χ fluctuations happens only *after* the homogeneous inflaton component has already decayed into inhomogeneous fluctuations and only if the mass ratio takes values within the range

$$0.25 \lesssim m_\chi/m_\phi \lesssim 0.5\,. \tag{6.23}$$

Based on our lattice results we argued that the growth of χ fluctuations can be attributed to a (non-standard) parametric resonance is driven by the dynamics of the *inhomogeneous* inflaton ϕ, rather than by its homogeneous component.

The strength and rapidity of the growth of χ fluctuations, as well as the moment at which the resonant amplification is triggered was found to vary significantly between different values of m_χ/m_ϕ within the above range. For $m_\chi/m_\phi \sim 0.35$, for example, we found that the fluctuations of χ get amplified very strongly and almost immediately after the inflaton's homogeneous component has decayed into inhomogeneous fluctuations. For $m_\chi/m_\phi \sim 0.5$, on the other hand it can take more than half an e-fold until χ fluctuations eventually start growing.

For two selected realisations, characterised by the mass ratios $m_\chi/m_\phi \approx 0.364$ and $m_\chi/m_\phi = 0.5$, we have performed more realistic, three-dimensional lattice simulations and found good qualitative and quantitative agreement with the two-dimensional results. We thereby confirmed some of the findings of Ref. [20] which were based on simulations in $2+1$ dimensions. In particular we found that in those scenarios in which the resonant amplification of χ fluctuations is strong and happens quickly after the decay of the inflaton's zero mode, both fields fragment into inhomogeneous fluctuations but no oscillons are formed until the end of our simulation. On the other hand, for scenarios in which the growth of χ fluctuations is milder

and happens later, non-linearities in form of oscillons can form in both fields. As observed in [20] we find that the oscillons of the χ field are strongly correlated to those of the inflaton, in the sense that they form at the same spatial positions.

The results presented in this chapter clearly highlight the importance of studying preheating well after the non-linear fragmentation of the inflaton, particularly if the presence of additional fields is considered. In order to provide realistic predictions for the outcome of reheating, a full understanding of the preheating dynamics is indispensable. Quantities like the reheat temperature, abundances of non-thermally produced relics, or the baryon asymmetry, when produced through non-thermal leptogenesis may be sensitive to how the energy gets distributed among the different particle species. Indeed, it was only recently shown in [249], that when χ is identified with a right-handed sneutrino, a non-vanishing abundance of χ particles can significantly alter the predictions for the baryon asymmetry.

Finally, we have discussed and compared the GW spectra resulting from the non-linear dynamics of preheating in different realisations of the hilltop inflation model. Although we did not observe the characteristic oscillon-related peak structure (cf. the discussion in chapter 5) we found clear differences in the GW spectra when resulting from realisations that exhibit qualitatively different preheating dynamics. In particular, we found that for those scenarios in which oscillons are formed the GW spectra generically exhibit more power towards the UV (at wavenumbers around and above the mass scale of the inflaton).

Although we found that for all of the considered realisations the present day frequencies of the GWs would be too high to be observable at current and proposed GW detectors, our results again highlight the diversity of information that might be imprinted in the stochastic GW background about the underlying theory.

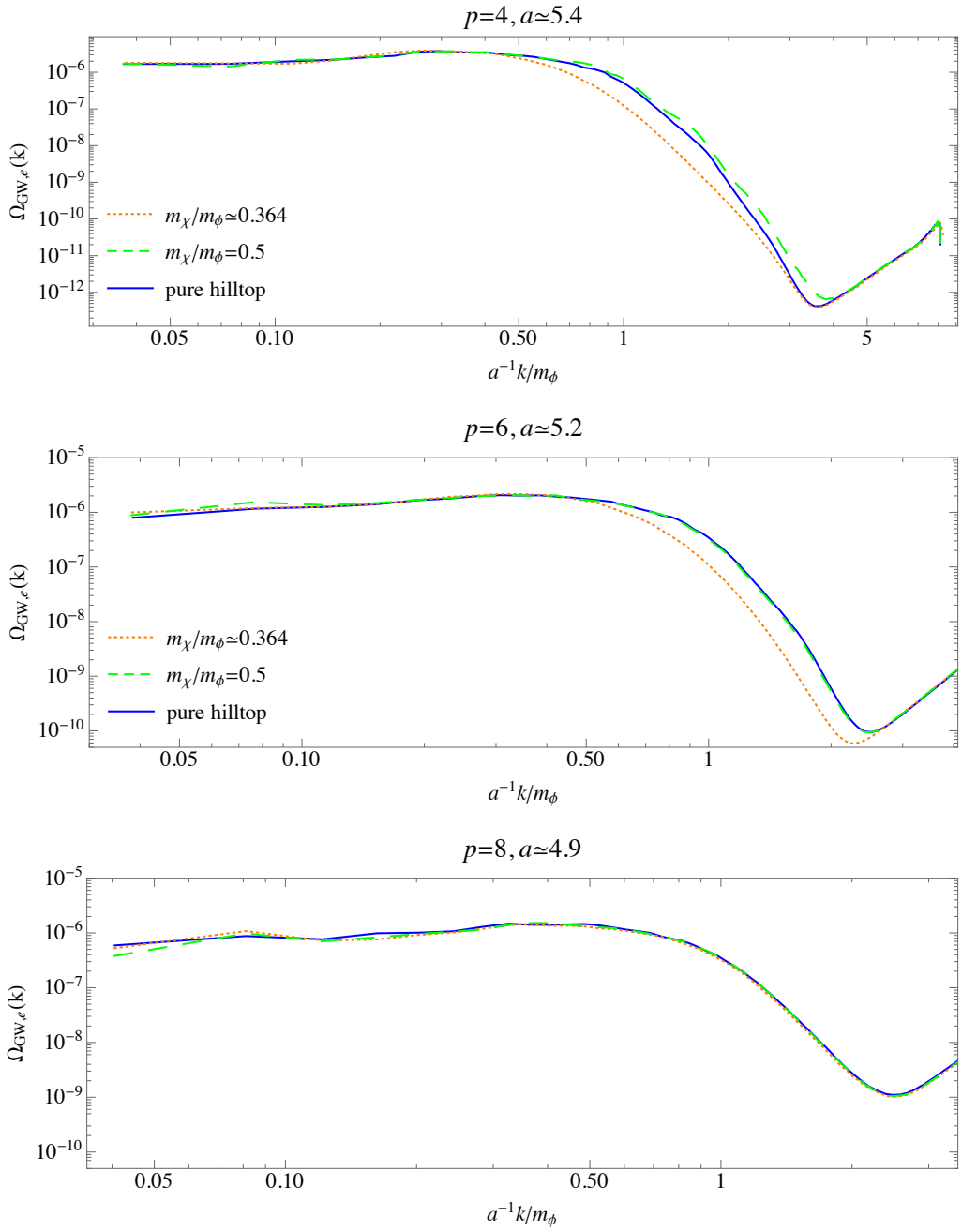

Figure 6.11: GW spectra at the moment of emission and as a function of the physical wavenumber (shown in units of m_ϕ). The results were obtained from lattice simulations of the model (6.4) for $p = 4$ (upper figure), $p = 6$ (middle figure), $p = 8$ (lower figure). Each figure shows results obtained by simulating the scalar field evolution for the three different realisations characterised by assuming: $m_\chi/m_\phi \approx 0.364$ (dotted orange curves), $m_\chi/m_\phi = 0.5$ (dashed green curves), and for the pure hilltop scenario $m_\chi/m_\phi = 0.5$ (solid blue curves). The spectra are shown at the end of the corresponding simulation at $a \approx 5$. The spectrum features a flat plateau in the IR which falls off quickly for $a^{-1}k \gtrsim m_\phi$. Notice that despite the fact that oscillons are present in most of the simulations, a characteristic oscillon-related peak structure is not visible. What one can clearly see, however, is that the presence of oscillons results in an enhanced spectrum on scales $a^{-1}k \gtrsim m_\phi$, compared to those cases where no oscillons are formed (orange dotted curves in the upper two plots).

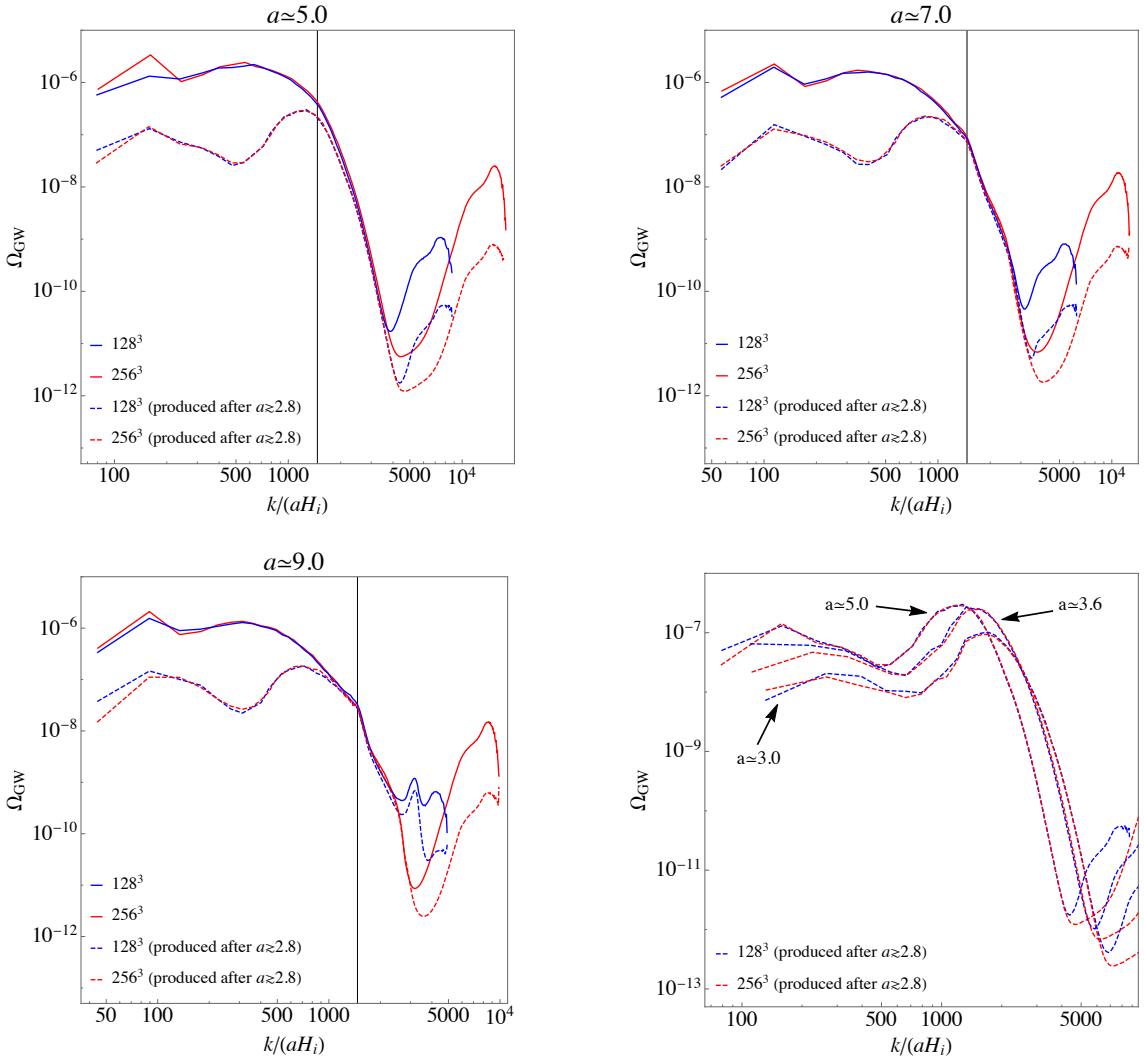

Figure 6.12: GW spectra shown at different moments in time (denoted by the scale factor a) and as a function of the physical wavenumber. The spectra originate from lattice simulations of the (pure) hilltop inflation model that were performed as in [2]. The different colors correspond to simulations carried out with different resolutions, i.e. same box size $LH_{\rm i} = 0.01$ but different number of lattice points: 128^3 (blue), and 256^3 (red). As one can see, up to $a \simeq 9$ the simulations are in very good agreement. In order to distinguish the spectrum originating from the dynamics of oscillons from the foreground produced during the early, non-linear stage of preheating we performed simulations in which the GW source was manually shut off until $a \simeq 2.8$. The corresponding results are denoted by the dashed lines. From those results one can clearly see that a peak forms at the characteristic wavenumber $a^{-1}k \simeq m_\phi$ denoted by the solid black line. In contrast to our earlier claims, however, the growth of the peak eventually stops and the spectrum gets redshifted (cf. the plot on the lower right). On the other hand, one can see that GWs continue to be produced at $a^{-1}k \simeq m_\phi$ but with a gradual decrease in efficiency.

Part V

Non-linear dynamics of moduli in string inspired models

Chapter 7

Non-linear dynamics during moduli preheating

As motivated in section 4.3, moduli fields are a generic feature of scalar field theories that are formulated within the framework of SUGRA or string theory. Moduli with masses below the Hubble parameter during inflation can get displaced from their post-inflationary VEV through the mechanism of vacuum misalignment. Once the Hubble parameter drops below the mass of the moduli, they eventually become dynamical and start oscillating around the minimum of their potential.

It is usually assumed that the intermediate epoch of modular cosmology is terminated through the perturbative decay of the moduli into a thermal bath of radiation (see e.g. [18]). In other words, the universe undergoes an additional period of reheating.

It was already shown in [183,250] that a period of modular cosmology can have a noticeable effect on the predictions of the primordial spectra. However, it is conceivable that the dynamics might lead to similar effects as in scenarios of (p)reheating after inflation. If that would be the case, this could in turn have additional and interesting implications.

Similar to the scenarios discussed in the previous chapter, moduli could experience efficient growth of fluctuations and fragment into inhomogeneous structures. This, in turn, could potentially source GWs. Moreover, if moduli preheating occurs at relatively low energies, the GWs may even lie within the reach of current and planned GW observatories.

In this chapter, we study the dynamics during moduli preheating[1] in scenarios of moduli stabilisation in type IIB string theory. In section 7.1 we consider the example of a displaced Kähler modulus in the KKLT scenario. After a brief introduction of the model we present and discuss results of Floquet analyses and of non-linear lattice simulations. In section 7.2 we discuss results of lattice simulations of the non-linear dynamics of a single blow-up modulus in the LVS. Within the scope of our lattice simulations we also considered the production of GWs for the above mentioned scenarios. The corresponding results are discussed and compared in section 7.3.

[1] For an earlier study in which the non-perturbative decay of moduli via parametric resonance has been considered see [251].

Then, in section 7.4 we briefly comment on the dynamics in other string inspired scenarios, before we summarise in section 7.5. The work presented in this chapter is partly published in Ref. [3].

7.1 Non-linear dynamics in the KKLT scenario

We begin this chapter with a discussion of the dynamics in the KKLT scenario [21] considering the overall Kähler modulus T. The KKLT scenario is an example of moduli stabilasation in type IIB string compactification[2] on a Calabi-Yau orientifold. After carrying out the compactification procedure and integrating out heavy moduli (e.g. the dilaton and complex structure moduli), we are left with a single volume modulus. The KKLT scenario then reduces to a four dimensional effective $\mathcal{N} = 1$ SUGRA described by the following tree-level Kähler potential[3]

$$K/m_{\rm Pl}^2 = -3\log\left(T+\overline{T}\right)\,, \tag{7.1}$$

and the superpotential

$$W/m_{\rm Pl}^3 = W_0 + Ae^{-aT}\,, \tag{7.2}$$

where $T = \tau + i\alpha$ is the overall Kähler modulus. The exponential contribution to the Kähler potential arises from a non-perturbative effect, with A being a function of the dilaton and the complex structure moduli, while a depends on the non-perturbative effect. In order for the effective field theory approach to be valid one has to ensure that $\tau \gg 1$. This, in turn, requires $W_0 \ll 1$ which can, for instance, be achieved by tuning the fluxes [253]. Furthermore, let us note that the effective potential resulting from eq. (7.1) and (7.2) has a negative minimum at $D_T W = 0$. In order to lift up the Anti-de-Sitter vacuum, an additional term $V_{\rm up} = \frac{D}{\tau}$ is added to the potential. The scalar potential is then given by

$$V/m_{\rm Pl}^4 = \frac{1}{6\tau^2}\left(aA^2(3+a\tau)e^{-2a\tau} - 3aAe^{-a\tau}W_0\right) + \frac{D}{\tau}\,. \tag{7.3}$$

In the following discussion we assume that the axion field α remains stabilised at its minimum $\alpha = 0$. Moreover, we concentrate on realisations of the potential (7.3) defined by fixing the remaining parameters in the following ranges:

$$10^{-12} \leq W_0 \leq 10^{-5}\,, \qquad 1 \leq A \leq 10\,, \qquad \text{and} \qquad 1 \leq a \leq 2\pi\,. \tag{7.4}$$

The upper bound on W_0 is chosen in order for the modulus to be stabilised with $\tau \gg 1$, while the lower bound is fixed by demanding that both the gravitino and the moduli are sufficiently heavy to guarantee the success of BBN [3]. The range for a is motivated by the fact that we assume the presence of a to be associated with non-perturbative gaugino condensation from D7 branes [3].

[2] For a review on moduli stabilisation from flux compactification see e.g. [252].

[3] In principle there can be an additional contribution to the Kähler potential from the vacuum expectation value of the complex structure Kähler potential and the dilaton which we omitted here (for more details see Ref. [3]).

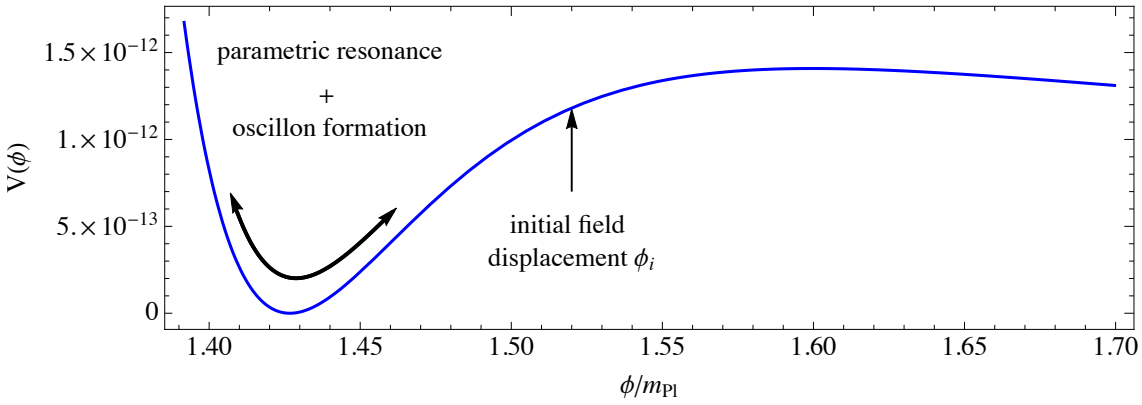

Figure 7.1: The scalar potential of the canonically normalised Kähler modulus $\phi/m_{\rm Pl} = \sqrt{3}\log\tau/2$ in the KKLT scenario. The potential is depicted for $W_0 = 10^{-5}$, $A = 10$, and $a = 2\pi$. The (vertical) thin arrow represents the initial field displacement $\phi_{\rm i}$.

In what follows we will work with the potential for the canonically normalised field Kähler modulus $\phi/m_{\rm Pl} = \frac{\sqrt{3}}{2}\log\tau$, which reads

$$V/m_{\rm Pl}^4 = \frac{2}{3}e^{-\frac{4}{\sqrt{3}}\phi}\left[\frac{aA}{2}e^{-ae^{\frac{2}{\sqrt{3}}\phi}}\left(A\left(ae^{\frac{2}{\sqrt{3}}\phi}+6\right)-6\,W_0\,e^{\frac{1}{2}ae^{\frac{2}{\sqrt{3}}\phi}}\right)+6D\right]. \qquad (7.5)$$

For $W_0 = 10^{-5}$, $A = 10$, and $a = 2\pi$ the potential (7.5) is illustrated in figure 7.1.

In the following we treat the initial displacement ($\phi_{\rm i} > \phi_{\rm min}$) of the modulus with respect to its post-inflationary VEV ($\phi = \phi_{\rm min}$) as a phenomenological parameter. Moreover, we assume that the modulus is "frozen" at $\phi = \phi_{\rm i}$ until it dominates the energy density $H^2 \simeq V(\phi_{\rm i})/(3m_{\rm Pl}^2)$.

7.1.1 Results of Floquet analyses in Minkowski spacetime

In order to get a brief overview of the dynamics of the Kähler modulus and to determine at which scales non-perturbative growth of ϕ fluctuations may be triggered, we first performed numerical Floquet analyses[4] of the KKLT scenario in Minkowski spacetime. Explicitly, we considered two different realisations of the model (7.5) corresponding to $W_0 = 10^{-12}$, and $W_0 = 10^{-5}$. The parameters a and A were kept fixed as follows

$$a = 2\pi \quad \text{and} \quad A = 10\,. \qquad (7.6)$$

For both realisations we have numerically computed the Floquet exponents for modes of different wavenumbers and as a function of the initial field displacement $\phi_{\rm i}$. The latter was assumed to lie within the following range

$$\phi_{\rm min} < \phi_{\rm i} \leq \phi_{\rm min} + \frac{\phi_{\rm max} - \phi_{\rm inf}}{2}\,, \qquad (7.7)$$

[4]See appendix C.2 for an explanation of the procedure.

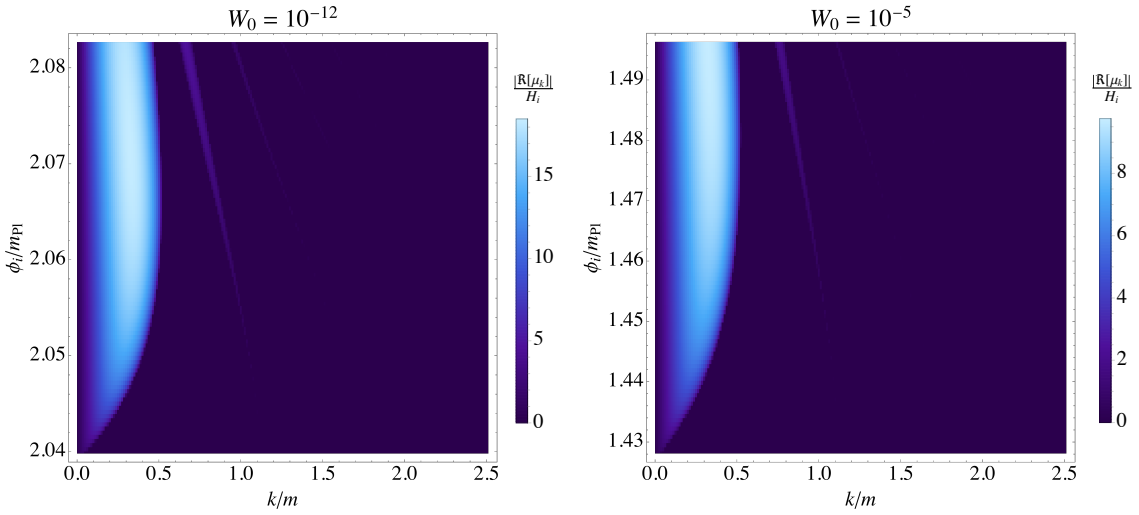

Figure 7.2: Floquet stability/instability chart of the KKLT model with $a = 2\pi$, $A = 10$, and $W_0 = 10^{-12}$ (left) and $W_0 = 10^{-5}$ (right). The Floquet exponents $|\Re[\mu_k]|$ are depicted in units of the Hubble parameter $H_{\rm i} = m_{\rm Pl}^{-1}\sqrt{V(\phi_{\rm i})/3}$ and as a function of the oscillation amplitude $\phi_{\rm i}$ of the homogeneous field. In both cases, the Floquet chart exhibits band structure consisting of a broad and pronounced band for scales $k \lesssim 0.5$ which eventually narrows towards small amplitudes close to $\phi_{\rm min}$. Two other narrower and fainter bands are visible for scales $0.5 < k < 1.5$.

where as above $\phi_{\rm min}$ denotes the field value at the minimum of the potential, $\phi_{\rm inf}$ is the field value at the inflection point of the potential, and $\phi_{\rm max}$ is the field value at the local maximum of the potential (cf. figure 7.1). Explicitly, the numerical values are

$$\begin{aligned} \phi_{\rm min} &= 2.03894\,, \quad \phi_{\rm infl} = 2.0563\,, \\ \phi_{\rm max} &= 2.14378\,, \quad \text{for} \quad W_0 = 10^{-12}\,, \end{aligned} \tag{7.8}$$

and

$$\begin{aligned} \phi_{\rm min} &= 1.42672\,, \quad \phi_{\rm infl} = 1.46044\,, \\ \phi_{\rm max} &= 1.59967\,, \quad \text{for} \quad W_0 = 10^{-5}\,. \end{aligned} \tag{7.9}$$

Our results are presented in figure 7.2. The figure shows the real part of the Floquet exponent $|\Re[\mu_k]|$ in units of the initial Hubble parameter $H_{\rm i} = m_{\rm Pl}^{-1}\sqrt{V(\phi_{\rm i})/3}$ for $W_0 = 10^{-12}$ (left) and $W_0 = 10^{-5}$ (right).

In both cases we obtain qualitatively similar results. The Floquet charts exhibit a broad instability band for modes $k/m \lesssim 0.5$ where

$$m \equiv \sqrt{\frac{\partial^2 V}{\partial \phi^2}}\bigg|_{\phi=\phi_{\rm min}} = \begin{cases} 2.66059 \times 10^{-12} m_{\rm Pl} & \text{for} \quad W_0 = 10^{-12} \\ 3.68875 \times 10^{-5} m_{\rm Pl} & \text{for} \quad W_0 = 10^{-5} \end{cases}, \tag{7.10}$$

is the modulus mass at the minimum of the potential. The band becomes weaker and narrower towards small amplitudes. In addition, we observe two other instability bands at larger $k/m > 0.5$ which are separated by large stability regions where

W_0	D	$\langle\phi\rangle_\mathrm{i}/m_\mathrm{Pl}$	$\langle\dot{\phi}\rangle_\mathrm{i}/m_\mathrm{Pl}^2$	$H_\mathrm{i}/m_\mathrm{Pl}$	N	LH_i
10^{-12}	1.23896×10^{-26}	2.1	0	2.47365×10^{-14}	256	0.7
10^{-5}	4.68242×10^{-12}	1.53	0	6.44852×10^{-7}	512	0.7

Table 7.1: Initial conditions and lattice setup used for numerical lattice simulations. In both scenarios the initial value of the homogeneous background field $\langle\phi\rangle_\mathrm{i}$ was considered as a phenomenological parameter and was chosen half way between the value at the inflection point of the potential and the field value at the local maximum of the potential (cf. figure 7.1). The initial value of the Hubble parameter was calculated by assuming that the energy density is initially purely dominated by the field's potential energy.

$|\Re[\mu_k]| = 0$. Within these bands the instability is considerably weaker. The only difference between the two different scenarios is that for the realisation with $W_0 = 10^{-12}$, the Floquet exponents are found to be about an overall factor of two larger than compared to the case where $W_0 = 10^{-5}$.

Based on these results, we would expect that, in an expanding universe, fluctuations grow for IR modes with comoving wavenumbers $k \lesssim 0.5m$. In order to clarify whether the growth is sufficiently strong to give rise to non-linear effects we performed numerical lattice simulations for both realisations. The corresponding results will be discussed in the next section.

7.1.2 Discussion of lattice simulations in $3+1$ dimensions

Using LatticeEasy we simulated the evolution of the Kähler modulus for two realisations of the potential (7.5) in $3+1$ dimensions. Both simulations were performed with $a = 2\pi$ and $A = 10$, but with different values for W_0: $W_0 = 10^{-12}$ and $W_0 = 10^{-5}$.

The initial conditions for the homogeneous component $\langle\phi\rangle_\mathrm{i}$ (and its velocity $\langle\dot{\phi}\rangle_\mathrm{i}$), as well as the lattice setup (number of points per spatial dimension N, and comoving box size L) are summarised in table 7.1. As mentioned above, the initial field value was considered as a phenomenological parameter. For our simulations we chose $\langle\phi\rangle_\mathrm{i}$ half way between the value at the inflection point and the field value at the local maximum of the potential, i.e.

$$\langle\phi\rangle_\mathrm{i} = \phi_\mathrm{min} + \frac{\phi_\mathrm{max} - \phi_\mathrm{inf}}{2} \,. \tag{7.11}$$

The fluctuations of the modulus have been initialised as quantum vacuum fluctuations[5].

Results of the simulation of the KKLT model with $W_0 = 10^{-12}$ are presented in figures 7.3 and 7.4. Figure 7.3 shows the time evolution of the homogeneous component $\langle\phi\rangle$ (left) with the solid black line denoting the field value ϕ_inf at the

[5]For further details regarding the initialisation of the fluctuations in LatticeEasy see appendix C.3.

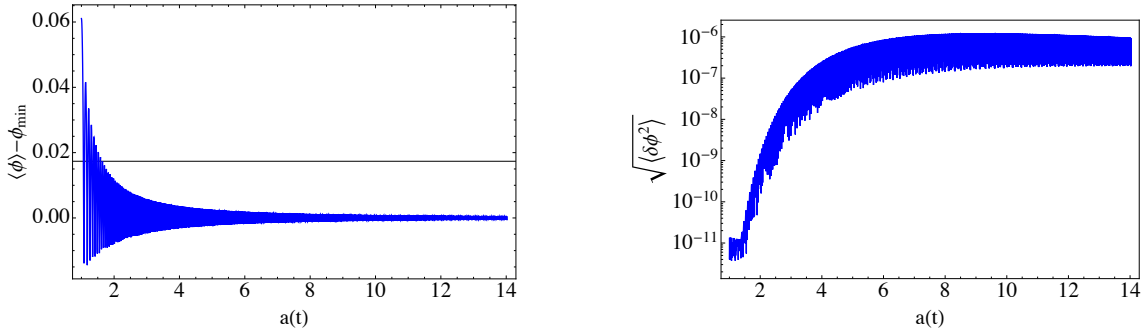

Figure 7.3: Results of a lattice simulation of the KKLT model with $W_0 = 10^{-12}$. The left part of the figure shows the evolution of the homogeneous component $\langle\phi\rangle$ as a function of the scale factor a. The solid black line denotes the field value at the inflection point, or more precisely $\phi_{\rm inf} - \phi_{\rm min} = 0.01736$. The evolution of the variance $\sqrt{\langle\delta\phi^2\rangle}$ is depicted as a function of the scale factor on the right part of the plot.

inflection point. On the left part of the figure we show the evolution of the variance $\sqrt{\langle\delta\phi^2\rangle}$. Both, the evolution of $\langle\phi\rangle$ and $\sqrt{\langle\delta\phi^2\rangle}$ are shown as a function of the scale factor a.

During the first seven oscillations of the homogeneous component the modulus periodically crosses the inflection point and enters into the tachyonic region. In this scenario, however, tachyonic oscillations turn out to be not an efficient mechanism for the growth of fluctuations. Indeed, as can bee seen from the evolution of the variance, no efficient growth of fluctuations takes place for $a \lesssim 1.5$. Hence, neither the initial stage of tachyonic preheating which happens during the first descent of the modulus towards its VEV, nor the subsequent tachyonic oscillations give rise to a noticeable growth of fluctuations. In this scenario, the dominant mechanism is that of a parametric self-resonance. The latter becomes efficient *after* the amplitude of the homogeneous background drops below $\phi_{\rm inf}$. The resonant behaviour extends over many oscillations of $\langle\phi\rangle$ although becoming less and less efficient as the amplitude of the homogeneous component decays due to Hubble friction. This can be understood from our previous Floquet analysis. Indeed, for small amplitudes, the instability band narrows and becomes less pronounced (i.e. on to the lower left part of figure 7.2). Around $a \sim 8$ the growth of fluctuations eventually stops and the excited modes get redshifted. Notice that at that point the amplitude of the homogeneous component is still about a factor $\mathcal{O}(10^3)$ larger than the amplitude of the fluctuations. This implies that the backreaction of the fluctuations on $\langle\phi\rangle$ remains negligible and that the field remains practically homogeneous.

In figure 7.4 we also show the spectrum of the fluctuations $k^3|\delta\phi_k|^2/(2\pi^2)$ as a function of the physical momentum $a^{-1}k/m$. The spectrum is depicted at consecutive moments in time denoted by different colors corresponding to: $a = 2.29$ (blue), $a = 5.76$ (green), $a = 8.36$ (ornage), and at the end of the simulation $a = 14.03$ (red). We can see that eventually a peak develops at $k/a \sim 0.2m$ which initially continues to grow until $a \simeq 6$, while being simultaneously and relatively quickly redshifted towards smaller k/a. The shape of the spectrum remains practically unchanged, as one would expect in the absence of non-linear mode-mode interactions.

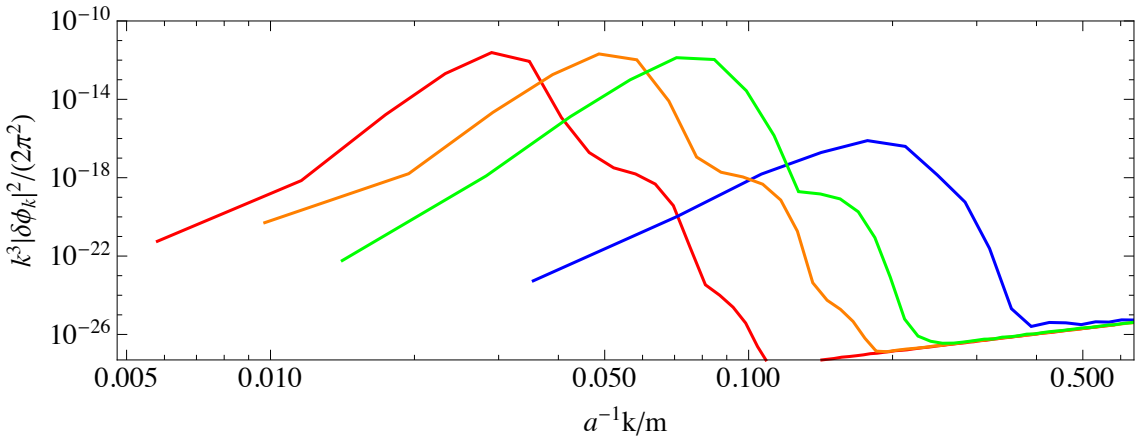

Figure 7.4: Spectrum of ϕ fluctuations as a function of the physical wavenumber $a^{-1}k/m$. The spectrum is shown at different moments in time corresponding to: $a = 2.29$ (blue), $a = 5.76$ (green), $a = 8.36$ (orange), and at the end of the simulation $a = 14.03$ (red). The results originate from a lattice simulation of the KKLT model with $W_0 = 10^{-12}$. Initially, a peak forms at $a^{-1}k/m \sim 0.1$ which eventually stops growing and gets subsequently redshifted ($a \gtrsim 5.76$), without changing its shape.

Let us now turn to the discussion of our lattice results obtained with $W_0 = 10^{-5}$. The results are presented in figures 7.5 - 7.7. The left part of figure 7.5 shows the evolution of the mean $\langle\phi\rangle$ as a function of the scale factor a where the solid black line again denotes the field value at the inflection point of the potential $\phi_{\rm inf}$. Here, the evolution is similar as in the previously discussed case ($W_0 = 10^{-12}$). The first couple of oscillations are tachyonic but the growth of fluctuations is not very efficient during this early stage (and also not during the very first stage of tachyonic preheating). This can be seen by comparing the evolution of $\langle\phi\rangle$ with that of the variance $\sqrt{\langle\delta\phi^2\rangle}$ which is shown on the right part of figure 7.5. Indeed, efficient growth of fluctuations starts not before the amplitude of the zero-mode has fallen below the inflection point at $a \simeq 1.6$. Notice that over a certain period of expansion, the fluctuations grow much less (compared to their initial vacuum amplitude) than in the scenario with $W_0 = 10^{-12}$. This is what one would expect on the basis of our Floquet analysis (cf. figure 7.2). Interestingly, in this case non-linear effects eventually show up already at $a \simeq 5$, even though the growth of fluctuations is much less efficient than in the previously discussed scenario ($W_0 = 10^{-12}$), where non-linear effects are completely absent. How can this be? The reason is the following: the initial amplitude of the vacuum fluctuations is sensitive to the value of W_0 and can change by many orders of magnitude as one can see by comparing the spectra (cf. figures 7.4 and 7.6). The amplitude of the homogeneous mode, however, remains of the same order. This, in turn, means that in the presently considered scenario where $W_0 = 10^{-5}$, the necessary amount of growth for the backreaction of the fluctuations to become important is significantly smaller.

Figure 7.6 shows the spectrum of Kähler modulus fluctuations. The spectrum is again shown as a function of the physical wavenumber $a^{-1}k/m$ and at different moments in time corresponding to differently coloured curves: $a = 4.98$ (blue),

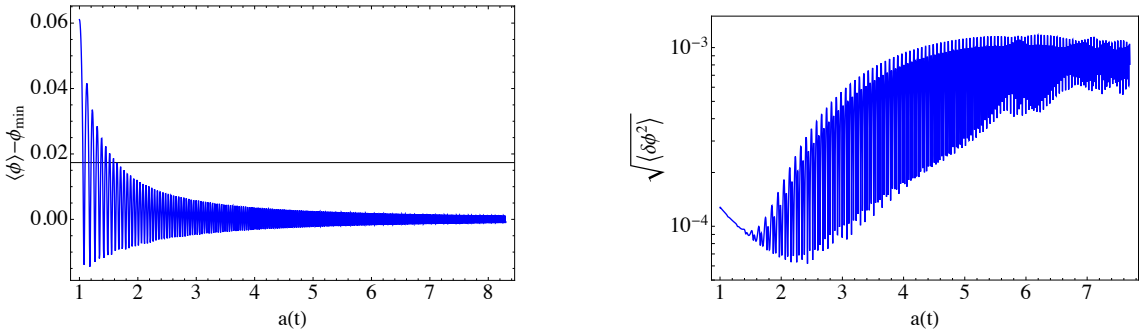

Figure 7.5: Results of a lattice simulation of the KKLT model with $W_0 = 10^{-5}$. The left part of the figure shows the evolution of the homogeneous component $\langle\phi\rangle$ as a function of the scale factor a. The solid black line again denotes $\phi_{\text{inf}} - \phi_{\text{min}} = 0.03372$. The right part of the figure shows the evolution of the variance $\sqrt{\langle\delta\phi^2\rangle}$ (as a function of a). Notice that in this case the amplitude of the vacuum fluctuations is about seven orders of magnitude larger than for the realisation with $W_0 = 10^{-12}$, while in both scenarios the amplitude of the homogeneous component is of the same order. Here, non-linear effects eventually show up at $a \sim 5$ when $\sqrt{\langle\delta\phi^2\rangle}$ becomes comparable to the amplitude of the homogeneous mode $\langle\phi\rangle - \phi_{\text{min}}$.

$a = 6.41$ (green), $a = 7.07$ (orange), and $a = 8.3$ (red) at the end of the simulation. In this case, the evolution clearly differs from that in the case where $W_0 = 10^{-12}$. Initially, a peak develops at $a^{-1}k/m$ which eventually broadens towards the UV due to non-linear interactions between different modes. In addition, a second (but considerably less dominant) peak forms at $a^{-1}k \lesssim 2m$.

Another interesting result we want to show is the spatial distribution of the energy density. The latter is shown in figure 7.7 at different moments in time: $a = 6.41$ (upper left), $a = 7.07$ (upper right), $a = 7.7$ (lower left), and $a = 8.3$ (lower right). The green surfaces correspond to isosurfaces of constant energy density with six times the mean energy density $\langle\rho\rangle$. The blue surfaces represent surfaces where $\rho = 12\langle\rho\rangle$. We can see that large, localised overdensities form. The latter essentially correspond to oscillons, i.e. localised, large amplitude oscillations in field space. Interestingly, the number of oscillons per comoving volume L^3 seems to be increasing over time. Moreover, notice that the dynamics apparently seem to be very complex: we can see oscillons interacting with each other, giving rise to non-spherical and non-ellipsoidal structures that emerge and eventually disappear.

In our discussion of preheating after hilltop inflation in section 6.2 of chapter 6 we mentioned that the fluctuations eventually develop very large amplitudes which can lead to local overshootings of the field into the wrong vacuum[6]. It is conceivable that a similar effect might also occur in the KKLT scenario i.e. that the field overshoots the barrier at ϕ_{max}. If such an overshooting would indeed happen, this would lead to "decompactification" of the vacuum which effectively means that the four dimensional effective field theory description breaks down. Within our simulations we checked for such effects without finding any signs of overshootings.

[6]See Ref. [194].

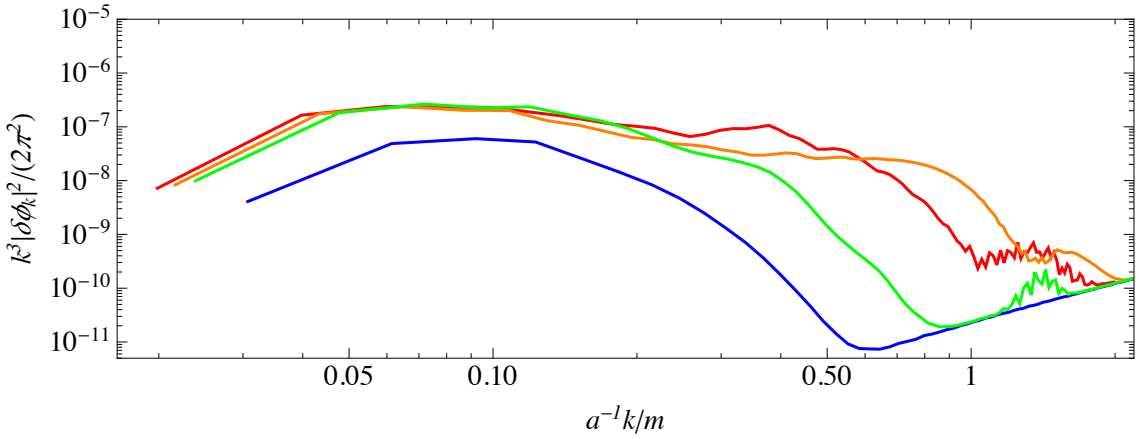

Figure 7.6: Spectrum of field fluctuations as a function of the physical momentum $a^{-1}k/m$. The spectrum is shown at different moments in time corresponding to: shortly after the end of the linear regime $a = 4.98$ (blue), $a = 6.41$ (green), $a = 7.07$ (orange), and at the end of the simulation $a = 8.3$ (red). The peak which initially forms around $a^{-1}k/m \sim 0.1$ eventually stops growing and broadens towards the UV. Towards the end of the simulation, additional structures become visible on scales $1 \lesssim a^{-1}k/m \lesssim 2$ in form of an additional small peak or "bump" in the spectrum. The results originate from a lattice simulation of the KKLT model with $W_0 = 10^{-5}$.

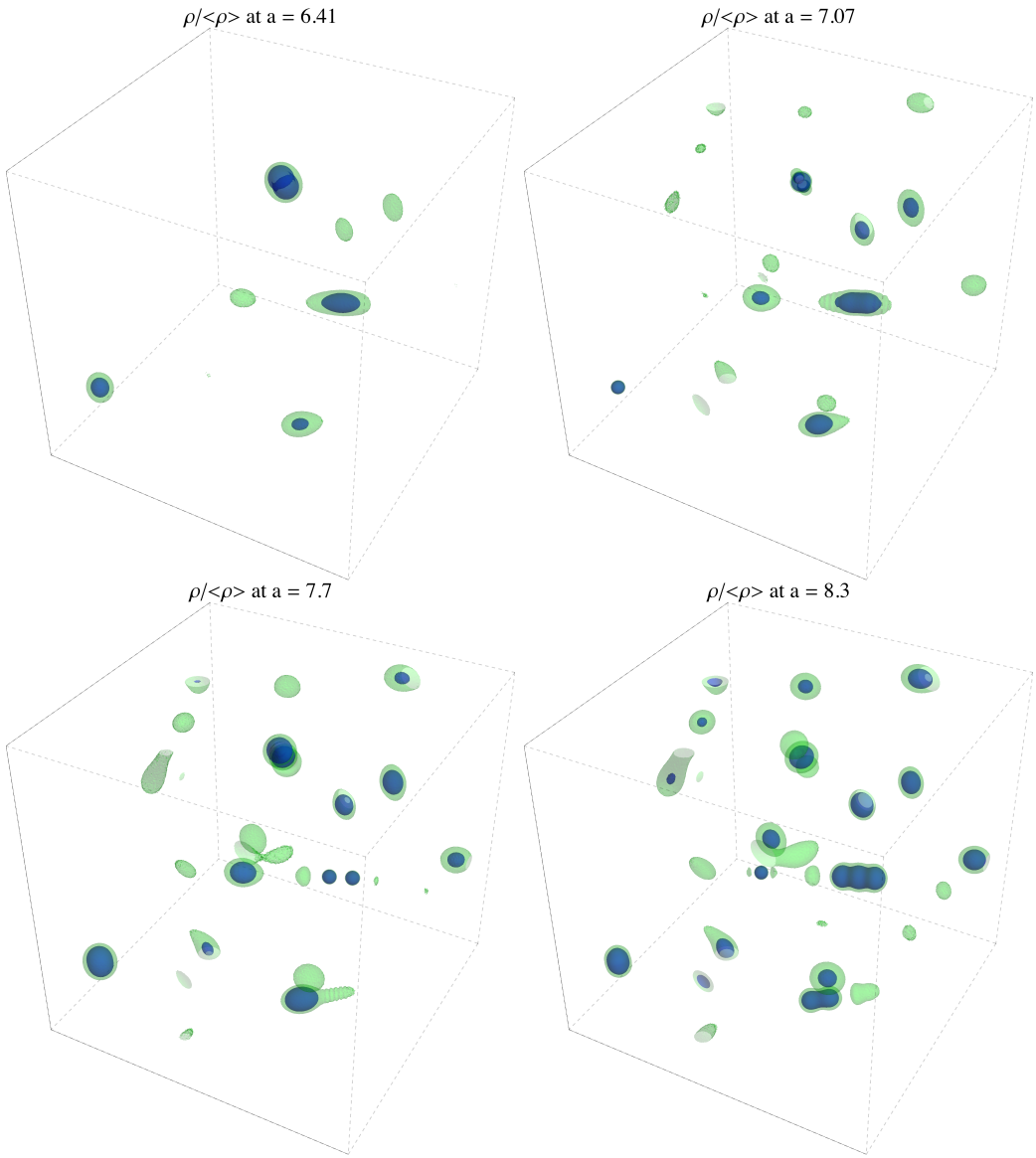

Figure 7.7: Snapshots of the three-dimensional energy density distribution taken at different moments in time. The energy density is represented by constant energy density isosurfaces corresponding to six (green) and twelve (blue) times the average energy density $\langle\rho\rangle$. The bubbly overdensities correspond to localised, large-amplitude oscillations of the field, i.e. to oscillons. For animations see [254].

7.2 Dynamics of blow-up moduli in the Large Volume Scenario

As a second example we want to consider the case of a single blow-up modulus in the LVS [22, 23]. Just as the KKLT scenario, it is a scenario of moduli stabilisation in type IIB string theory.

To be more explicit, in the following we will consider the following effective scalar potential of blow-up Kähler moduli τ_i

$$\begin{aligned}\frac{V}{m_{\rm Pl}^4} &= \frac{3|W_0|^2\hat{\xi}}{4\mathcal{V}^3} + \frac{D}{\mathcal{V}^2} \\ &+ \frac{g_s}{8\pi}\left[\frac{8}{3\mathcal{V}}\left((a_1A_1)^2\, e^{-2a_1\tau_1}\sqrt{\tau_1} + \sum_{i=2}^{n}(a_iA_i)^2 e^{-2\tau_i}\sqrt{\tau_i}\right)\right. \\ &\left. - \frac{4W_0}{\mathcal{V}^2}\left((a_1A_1)\, e^{-a_1\tau_1}\tau_1 + \sum_{i=2}^{n}(a_iA_i)e^{-\tau_i}\tau_i\right)\right]\,, \end{aligned} \tag{7.12}$$

where $\mathcal{V}$ denotes the volume whichis assumed to be constant and W_0 is the VEV of the "flux superpotential". Moreover, we have $\hat{\xi} = \xi g_s^{-3/2}$, where the parameter $g_s = 0.2$ is the so-called string coupling. The coefficitens A_i and a_i originate from non-perturbative effects [3]. The term $V_{\rm up} = D/\mathcal{V}^2$ is responsible for the up-lifting of the Anti-de-Sitter to an approximate Minkowski vacuum. For a more sophisticated and string related motivation of the model we refer to Refs. [22, 23] (or section 3.2 of [3]).

In what follows we are going to consider the situation where a single blow-up modulus τ_1 is displaced from its post-inflationary VEV, while all other τ_i with $i \geq 1$ are assumed to be stabilised at their minima $\langle\tau_i\rangle$. The latter are determined by the following relation

$$a_i\langle\tau_i\rangle = -\log\left(\frac{3\alpha\alpha_i}{a_iA_i\,\mathcal{V}}\frac{(1-a_i\langle\tau_i\rangle)}{(1-4a_i\langle\tau_i\rangle)}\sqrt{\langle\tau_i\rangle}\right), \tag{7.13}$$

where α and the α_i are numerical constants.

The results presented in the following section originate from simulating the evolution of the initially displaced canonically normalised blow-up modulus

$$\sigma = \tau_1^{3/4}\sqrt{\frac{4}{3\mathcal{V}}}\,, \tag{7.14}$$

for a realisation of the potential (7.12) which is fixed by the following choice of parameters:

$$n\,=\,10\,,\quad a_i = \pi\,,\quad \text{and}\quad W_0 = A_i = \xi = a_1 = 1\,. \tag{7.15}$$

The numerical values of the volume modulus $\mathcal{V}$, the uplifting parameter D, as well as the VEVs $\langle\tau_i\rangle$ of the stabilised moduli ($i \geq 1$) were calculated numerically[7] and

[7] We note that this was done by our collaborators Dr. Sven Krippendorf and Dr. Francesco Muia.

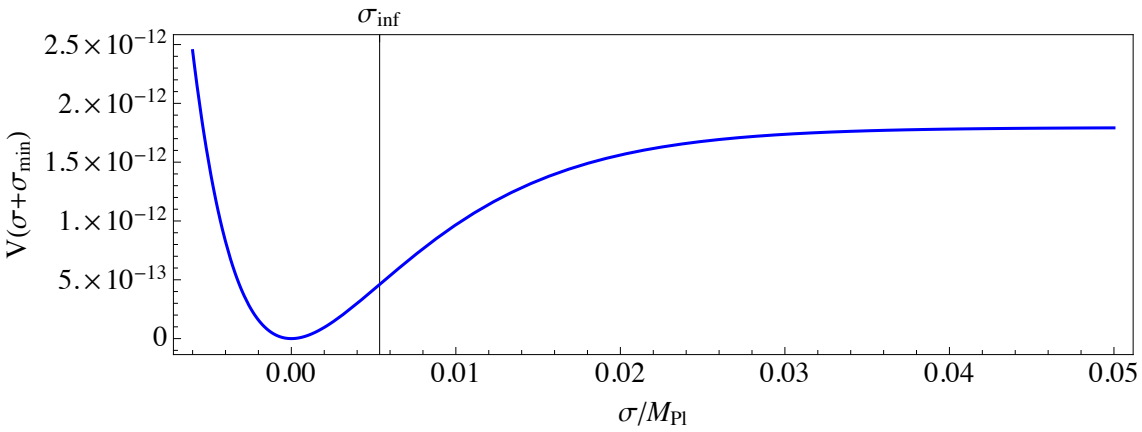

Figure 7.8: Illustration of the blow-up modulus potential in the LVS. The potential is shown in terms of the canonically normalised field $\sigma = \tau_1^{3/4}\sqrt{\frac{4}{3\mathcal{V}}}$. The solid black line denotes the field value $\sigma_{\rm inf}$ at the inflection point. The potential is plotted for $W_0 = A_i = \xi = a_2 = 1$, $g_s = 0.2$, $\gamma = 2$, and $n = 10$.

are

$$\mathcal{V} \,=\, 5278.03\,, \quad D \,=\, 0.0000266545\,, \quad \text{and} \quad \langle\tau_i\rangle \,=\, 3.03443\,. \tag{7.16}$$

An illustration of the potential for the (canonically normalised) modulus σ with the origin shifted to the minimum $\sigma_{\rm min} \simeq 0.075\, m_{\rm Pl}$ is shown in figure 7.8.

7.2.1 Results of lattice simulations in $3+1$ dimensions

In this section we present results of a lattice simulation of the evolution of the canonically normalised blow-up modulus σ. The simulation was performed using a modified version of LatticeEasy (see appendix C.4). The initial conditions for the homogeneous mode and its derivative were chosen as follows:

$$\langle\sigma\rangle_{\rm i} \,=\, \sigma_{\rm min} + 0.025\, m_{\rm Pl} \,\simeq\, 0.1 m_{\rm Pl}, \quad \text{and} \quad \langle\dot{\sigma}\rangle_{\rm i} = 0\,, \tag{7.17}$$

i.e. with an initial displacement from the post-inflationary VEV $\Delta\phi_{\rm i} = 0.025 m_{\rm Pl}$. Also in this scenario we assumed that the entire energy density is dominated by the modulus, such that the initial Hubble parameter is given by

$$H_{\rm i} = \frac{1}{m_{\rm pl}}\sqrt{\frac{V(\sigma_{\rm i})}{3}} = 7.477\times10^{-7} m_{\rm Pl}\,. \tag{7.18}$$

As in our previous lattice simulations, the fluctuations have been initialised as quantum vacuum fluctuations (see appendix C.3) but here with a (comoving) UV cutoff $k_{\rm UV} = m$, where

$$m \,\equiv\, \sqrt{\frac{\partial^2 V}{\partial\sigma^2}}\bigg|_{\sigma=\sigma_{\rm min}} \,=\, 2.46935\times10^{-4} m_{\rm Pl}, \tag{7.19}$$

$\langle\sigma\rangle_\mathrm{i}/m_\mathrm{Pl}$	$\langle\dot{\sigma}\rangle_\mathrm{i}/m_\mathrm{Pl}^2$	$H_\mathrm{i}/m_\mathrm{Pl}$	N	Lm
0.1	0	7.477×10^{-7}	512	15π

Table 7.2: Initial conditions and lattice setup. The initial value of the homogeneous component $\langle\sigma\rangle_\mathrm{i}$ was chosen such that the potential is sufficiently steep, such that the universe does not inflate (i.e. such that $\eta_V > 1$ and $\varepsilon_V > 1$) and the Hubble parameter was again calculated by assuming that the entire energy density is dominated by the modulus.

is the modulus mass at the minimum of the potential. The reason a cutoff was imposed is simply to avoid unphysical contributions to the vacuum energy, while keeping the resolution benefits of a small lattice spacing. The simulation was performed in $3+1$ dimensions and the details regarding the configuration of the lattice box are summarised in table 7.2.

The results of our simulation are presented in figures 7.9 and 7.10. The left part of figure 7.9 shows the evolution of homogeneous modulus component $\langle\sigma\rangle$ as a function of the scale factor a. The solid black line denotes the field value at the inflection point σ_inf. The right part of figure 7.9 shows the evolution of the variance $\langle\delta\sigma^2\rangle^{1/2}$. Within this scenario, the fluctuations are amplified by tachyonic oscillations and the homogeneous mode eventually decays into inhomogeneous fluctuations already after the first 3-4 oscillations. As can be seen from the variance the fluctuations then stop to grow and the dynamics become dominated by non-linear mode-mode interactions. Notice the similar behaviour of the variance compared to the hilltop inflation model (cf. figure 4.5) where tachyonic oscillations are the dominant mechanism for the growth of fluctuations.

The power spectrum of σ is depicted in figure 7.10 as a function of the physical wavenumber $a^{-1}k/m$ and at different moments in time. The blue curve shows the spectrum at the end of the linear regime at $a \simeq 1.16$ (cf. the evolution of the variance in figure 7.9). At that stage, the spectrum is dominated by modes with wavenumbers $k/a \lesssim 0.5m$. The growth of fluctuations due to tachyonic oscillations is eventually terminated by non-linearities after ~ 4 oscillations of the zero-mode. As a consequence, the spectrum widens towards the UV, as can bee seen by comparing the spectrum at $a \simeq 1.16$ with those at later times e.g. already at $a \simeq 1.45$ (green curve). The orange and red curves show the spectrum at $a \simeq 2.1$ and at the end of the simulation $a \simeq 2.5$, respectively.

Finally, in figure 7.11 we show the three-dimensional distribution of the energy density. The coloured surfaces correspond to isosurfaces of constant energy density with $\rho = 6\,\langle\rho\rangle$ (green) and $\rho = 12\,\langle\rho\rangle$ (blue). The fragmentation of the energy density (or equivalently of the field), which happens shortly after the dynamics become non-linear at $a \sim 1.2$, turns out to be much more violent and chaotic than in the previously discussed KKLT scenario. Over time, the large and asymmetric bubbles which form at the very beginning of the non-linear regime, fragment further into smaller and somewhat more spherical bubbles which eventually become stable. These bubbly regions represent localised large amplitude oscillations in field space, i.e. oscillons. Indeed, by comparing the energy density distribution for $a \geq 1.78$

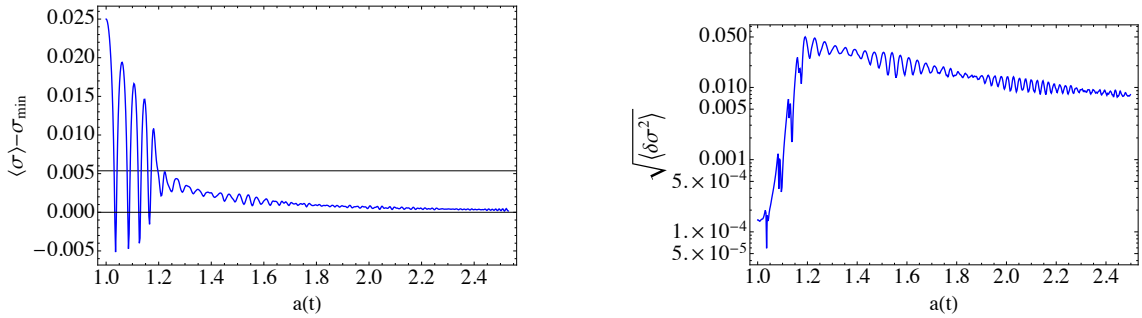

Figure 7.9: Results of a lattice simulation showing the evolution of the homogeneous component of the blow-up modulus $\langle\sigma\rangle$ (left) as a function of the scale factor a. The solid black line denotes the field value at the inflection point of the potential $\sigma_{\rm inf}$. The right part of the figure shows the evolution of the variance $\sqrt{\langle\delta\sigma^2\rangle}$ as a function of a. As one can see, the homogeneous component $\langle\phi\rangle$ decays quickly into inhomogeneous fluctuations within only four homogeneous oscillations. During these oscillations the fluctuations grow by more than three orders of magnitude until non-linearities terminate the growth.

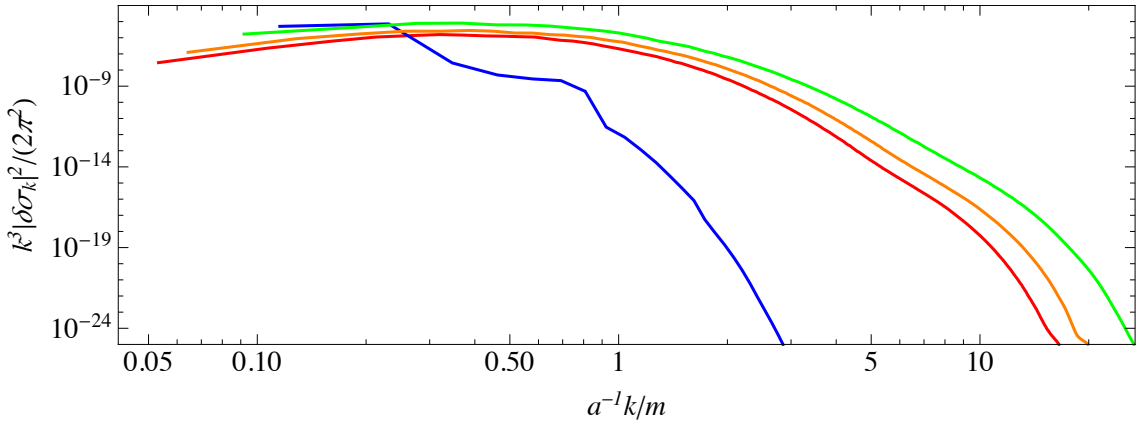

Figure 7.10: Power spectrum of blow-up modulus fluctuations shown as a function of the physical wavenumber $a^{-1}k/m$ and at different moments in time: at the end of the linear regime $a \simeq 1.16$ (blue), shortly after the beginning of the non-linear regime $a \simeq 1.45$ (green), at $a \simeq 2.1$ (orange), and at the end of the simulation $a \simeq 2.5$ (red).

(upper right and lower plots) one may notice that certain bubbles persist until the end of the simulation. This becomes more apparent in figure 7.12 showing the energy density distribution in two spatial dimensions[8].

While in the KKLT scenario (cf. figure 7.7) it looks like bubbly fluctuations already form in form of oscillons, the situation seems to be different in the case of the blow-up modulus in the LVS. In fact, the formation of oscillons seems to happen through an intermediate stage during which previously generated, bubbly inhomogeneities first undergo a rather chaotic and violent behaviour before they eventually relax into quasi-stable oscillons.

7.3 GWs from string inspired models: KKLT scenario vs. blow-up moduli in the LVS

To study the production of GWs associated with the non-linear moduli dynamics we simultaneously solved the field equations and eq. (C.4.29). For the details of the implementation into LatticeEasy we refer to appendix C.3. We would like to mention, that the results presented in this section have been carried out with a different and less accurate version of LatticeEasy than the one that was used for obtaining the results presented in section 6.3. We therefore performed convergence analyses which are presented in appendix D.

In this section we discuss and compare results of the GW spectra originating from the non-linear dynamics experienced in the KKLT and the LVS scenarios. Both scenarios exhibit similarities (such as the formation of oscillons) but also qualitative differences. In what follows we are going to discuss how these differences are manifested in the spectrum of GWs.

Our lattice results of the GW spectra are presented in figure 7.13. The upper plot shows the spectrum $\Omega_{\mathrm{GW,e}}(k)$ obtained from simulating the evolution of the Kähler modulus in the KKLT sceanrio with $W_0 = 10^{-5}$ (cf. table 7.1). The spectrum is shown as a function of the physical wavenumber $a^{-1}k$ and at different moments of emission corresponding to: $a = 5.72$ (blue curve), $a = 6.41$ (green curve), $a = 7.07$ (orange curve), and at the end of the simulation at $a = 8.3$ (red curve). As one can see, the spectrum develops a peak structure consisting of two peaks at $k/a \lesssim m$ and $k/a \lesssim 2m$, as well as a relatively flat plateau towards the IR.

As we shall justify shortly, the spectrum is almost purely attributable to the dynamics of the oscillons. The two peaks are essentially related to the anharmonic oscillations performed by the oscillons. We expect that the dominant peak at $k/a \lesssim m$ is related the fundamental frequency of the oscillon's oscillations, whereas peaks at higher k values are related to higher harmonics (see e.g. the discussion in section 2 and 4 of Ref. [205]).

Let us now consider the spectrum of GWs produced in the LVS (lower plot in figure 7.13). The spectrum is again shown at different moments in time correspond-

[8]The results shown in figure 7.12 originate from a lattice simulation in $2+1$ dimensions carried out assuming the same potential and same initial conditions as for our previously discussed result, but with twice the box size and $N = 1024$.

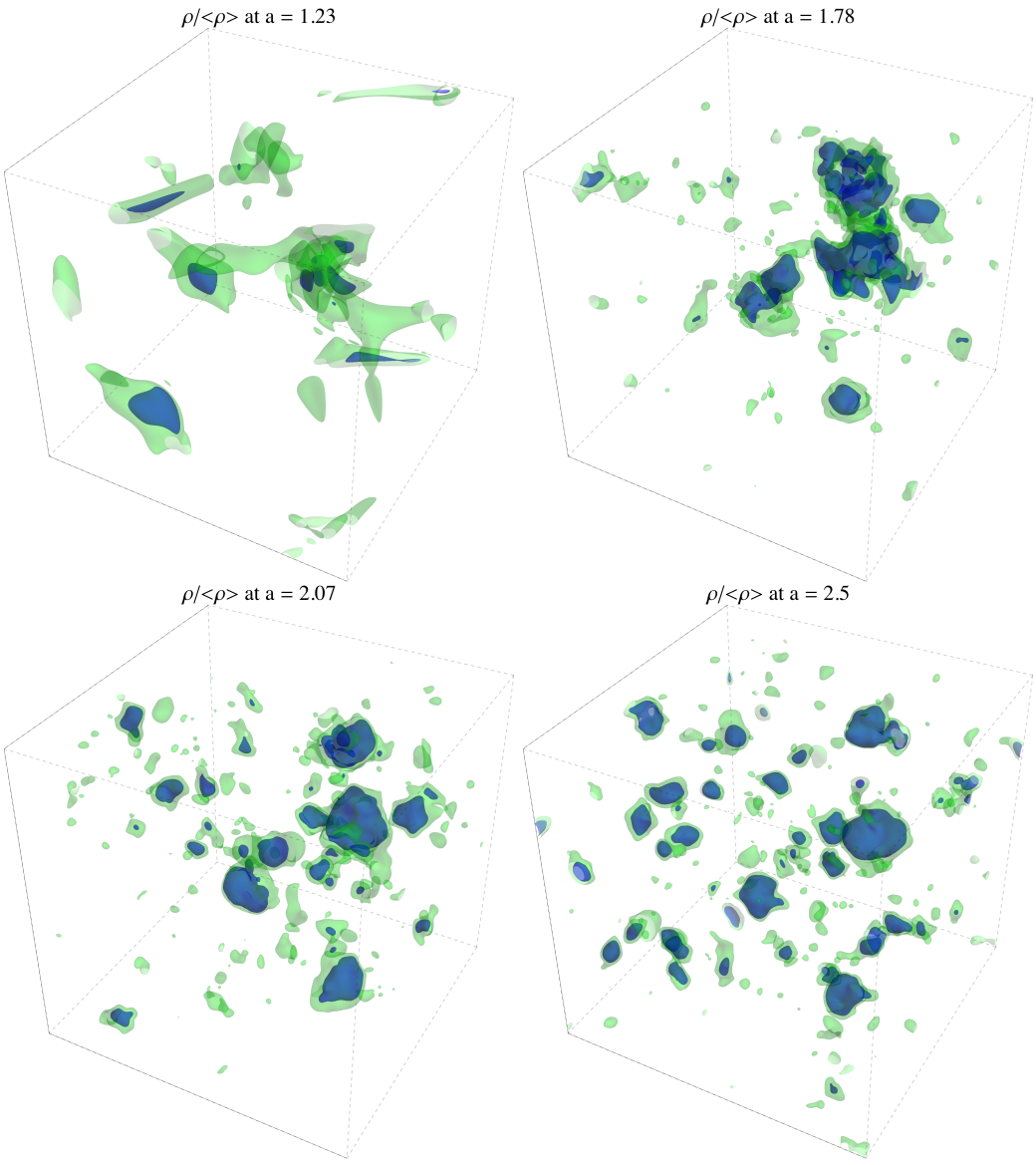

Figure 7.11: Snapshots of the energy density represented by constant energy density isosurfaces shown at different moments in time. The green surfaces correspond to overdensities for which $\rho = 6\langle\rho\rangle$ and the blue surfaces to $\rho = 12\langle\rho\rangle$, respectively.

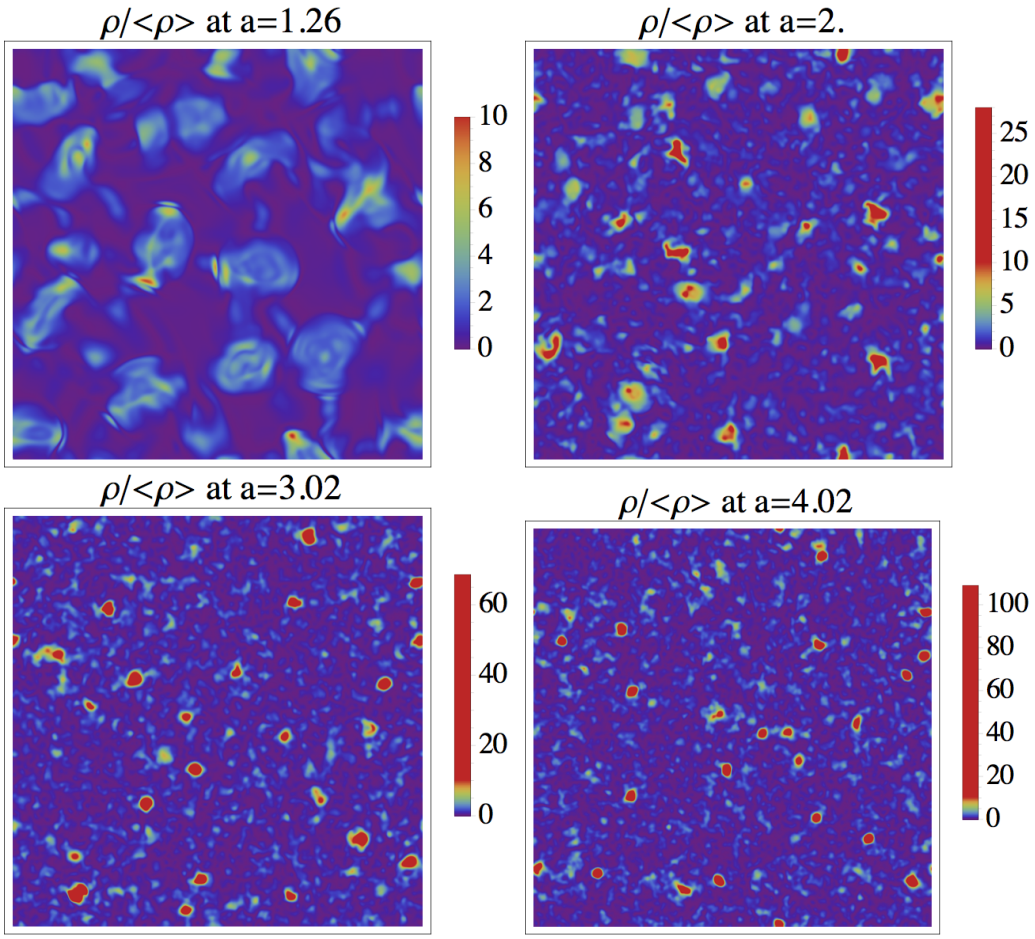

Figure 7.12: Snapshots of the energy density obtained from a two-dimensional lattice simulation of the evolution of the blow-up modulus in the LVS. The energy density is shown at different moments in time: the beginning of the non-linear regime $a = 1.26$ (upper left), $a = 2$ (upper right), $a = 3.02$ (lower left), and $a = 4.02$ (lower right). One can see that around $a \sim 3$ asymmetric bubbles corresponding to oscillons are formed. For an animation of the evolution of both, the field and the energy density see [254].

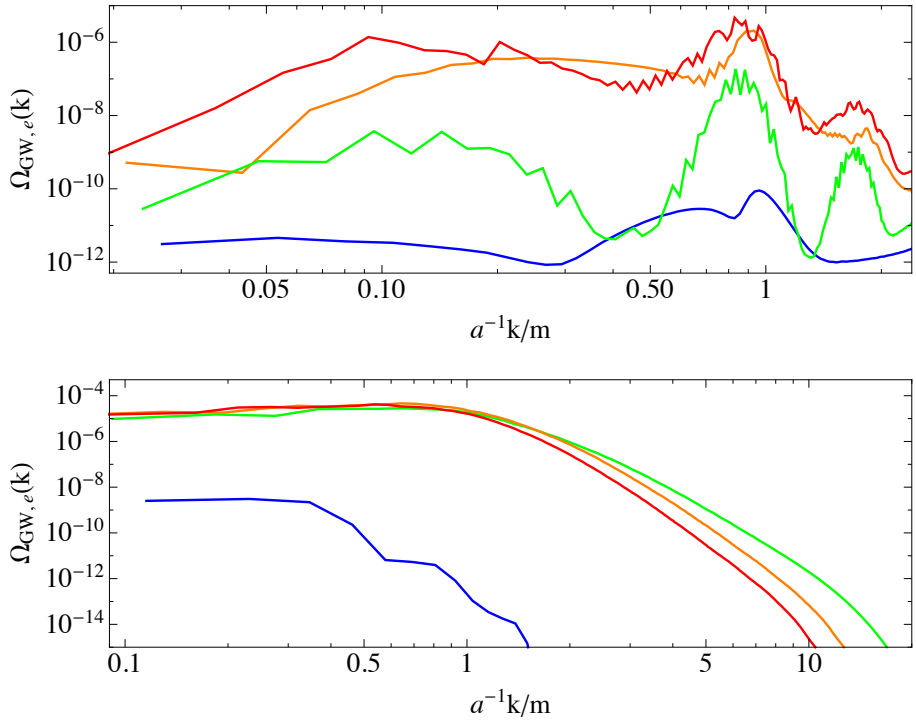

Figure 7.13: *Top:* Spectra of GWs $\Omega_{\mathrm{GW,e}}(k)$ originating from our simulation of the KKLT model with $W_0 = 10^{-5}$. The spectrum is shown as a function of the physical wavenumber $a^{-1}k/m$ and at different moments in time: $a = 5.72$ (blue), $a = 6.41$ (green), $a = 7.07$ (orange) and at the end of the simulation $a = 8.3$ (red). As one can see, a characteristic peak structure consisting of two peaks at $k/a \lesssim m$ and $k/a \lesssim 2m$ develops over time.
Bottom: Spectrum of GWs resulting from the non-linear dynamics of the blow-up modulus in the LVS. The spectra are again shown as a function of the physical wavenumber $a^{-1}\,k/m$. The differently coloured curves represent the spectrum at different moments in time: at the end of linear preheating $a \simeq 1.16$ (blue), shortly after the beginning of the non-linear regime at $a \simeq 1.45$ (green), at $a \simeq 2.1$ (orange), and at the end of the simulation $a \simeq 2.5$ (red). In this scenario, the spectrum clearly exhibits less distinctive features (such as distinct peaks) and, in particular, no characteristic peak structure can be seen.

ing to: the end of the linear stage of preheating $a \gtrsim 1.16$ (blue), shortly after the beginning of the non-linear regime at $a \simeq 1.45$ (green), at $a \simeq 2.1$ (orange), and at the end of the simulation $a \simeq 2.5$ (red). Compared to the spectrum produced in the KKLT scenario, the form and shape is clearly different and exhibits less features. In particular it does not exhibit a characteristic peak structure but rather consists of a flat plateau appearing at wavenumbers $a^{-1}k/m \sim 0.1\text{-}1$. This, however, does not mean that oscillons do not produce GWs, as already emphasised in section 6.3.1. Indeed, the dynamics are very similar to those in the hilltop inflation scenario. We expect that the "oscillon peaks" are most likely hidden somewhere below the spectrum that is produced during the early non-linear stage. Notice that this part of the spectrum is produced once during the early stages and is subsequently redshifted by the universe's expansion. In principle, it may be possible that these peaks eventually show up at later stages, if the oscillons efficiently produce GWs during a sufficiently long period.

7.3.1 GW spectra today

In the results discussed above we showed the spectra at the moment of emission and in terms of the physical wavenumber k/a. As discussed in section 4.4.3, in order to get an estimate of the spectra at present time, we have to take into account the history of the universe since the time of emission until today. Notice, however, that the final spectra shown above (red curves in the plots of figure 7.13) may not necessarily represent a final result. In the KKLT scenario for example, the production of oscillons and thus the production GW may still continue. Another source of GW production might be the decay of the oscillons. However, if these effects are neglected we can make use of (4.84) and (4.85) to account for the cosmological history between the moment of emission and today.

Assuming that the universe's energy density is instantly transferred into a thermal bath of radiation, for the KKLT scenario with $W_0 = 10^{-5}$ we obtain the following estimate for the present amplitude of the GW spectrum at the characteristic peak scale $a^{-1}k/m \simeq 1$

$$\Omega_{\mathrm{GW},0}(f_{0,\mathrm{peak}}) \sim 3 \times 10^{-11}\,, \tag{7.20}$$

with present frequencies

$$f_{0,\mathrm{peak}} \sim 10^{9}\,\mathrm{Hz}\,. \tag{7.21}$$

For the case of the blow-up modulus in the LVS, we consider the frequency range that corresponds to the flat plateau in the final spectrum (i.e. to wavenumbers $a^{-1}k/m \sim 0.1\text{-}1$ in the lower plot of figure 7.13). Based on the assumptions mentioned above we find

$$\Omega_{\mathrm{GW},0} \sim 10^{-10}\text{-}5 \times 10^{-10}\,, \tag{7.22}$$

with frequencies in the following range

$$f_0 \sim 10^{8}\,\mathrm{Hz}\text{-}10^{9}\,\mathrm{Hz}\,. \tag{7.23}$$

Unfortunately, in both scenarios the frequencies are far too high to be observable with present and envisaged GW observatories. Lower frequencies are in principle possible e.g. if the universe does not immediately reheat as we assumed, but rather continues to behave as matter for some extended period of time. Notice, however, that the frequencies scale as a^{-1}, whereas the amplitude of the spectrum scales as radiation (i.e. as a^{-4}). An extended period of matter domination would therefore not only lead to lower frequencies but also to a strong suppression of the signal.

Another effect that could, in principle, lower the frequencies is related to a contribution $K_{\rm cs}$ to the Kähler potential arising from so-called complex structure moduli, which we neglected in our analysis. For the KKLT scenario, for example, a non-vanishing $K_{\rm cs}$ would imply [3]

$$f \propto \frac{m}{\rho_{\rm e}^{1/4}} \propto \frac{(e^{K_{\rm cs}})^{1/2}}{(e^{K_{\rm cs}})^{1/4}} \propto (e^{K_{\rm cs}})^{1/4} \,. \tag{7.24}$$

Hence, $e^{K_{\rm cs}} < 1$ would naturally lower the frequencies. Similar arguments apply to the blow-up modulus in the LVS. On the other hand, let us note that similar to lowering W_0 in the KKLT scenario, lowering $e^{K_{\rm cs}}$ would also imply a smaller amplitude of the initial vacuum fluctuations. Notice, however, that this is counterproductive for the development of large inhomogeneities.

7.3.2 Comparison of the KKLT spectrum to semi-analytical results

To test the reliability of our semi-analytical approach for computing the GW spectrum from oscillons (cf. the discussion in chapter 5) we compared our lattice results of the KKLT scenario with results obtained by numerically integrating eq. (5.15).

In essence, we made the same assumptions as in chapter 5, i.e. we assumed oscillons with Gaussian spatial profile and a time-dependent field value at the center $\Phi_q(t)$ that is given by

$$\Phi_q(t) = A \, \cos(\omega_{\rm osc} t + \varphi^q) \,, \tag{7.25}$$

with randomly chosen phases $\varphi^q \sim U([0, 2\pi])$. For the background cosmology we assumed a matter dominated universe described by (5.30) with $w = 0$.

In order to get a realistic estimate though, we extracted some of the parameters which are required as an input for the integration of (5.15) from our lattice results. These include in particular the following quantities:

- The comoving volume $\mathcal{V}$ appearing in (5.15).
- The value of the scale factor a_0 at which the oscillons start to form, as well as the related Hubble parameter $H_0 \equiv H(a_0)$ used to model the background evolution.
- The amplitude at the center of the oscillons A, and the number of oscillons N per comoving volume $\mathcal{V}$.

- The width of the oscillons R required to model the oscillon's spatial profile (cf. eq. 5.11).

The comoving volume $\mathcal{V}$ was chosen to coincide with the physical volume in our lattice simulation at $a = a_0$, i.e. when quasi-stable oscillons are formed. More explicitly we chose $\mathcal{V} = \mathcal{V}_{\text{lattice}} \cdot a_0^3$, where $\mathcal{V}_{\text{lattice}}$ is the comoving volume of the lattice box. In our lattice simulation we found that $a_0 \simeq 5.8$.

The amplitude at the center of the oscillons A can be extracted from the field histograms. The easiest way to extract the number of oscillons N is to consider the energy density distribution as e.g. in figure 7.7. The positions of the oscillons within the comoving volume $\mathcal{V}$ were chosen randomly, with a minimum distance $d_{\text{min}} \geq 4\,R$. The width R, in turn, was extracted from the lattice by considering the crosssections of different oscillons as demonstrated in figure 7.14. There the blue contours correspond to a factor $e^{-1/2}$ of the (current) maximum amplitude. Then, by definition of the oscillon profile (5.11), the diameter corresponds to $2R$.

As already discussed in chapter 5, the spectrum peaks at the frequency of the source which is proportional to $\Phi_q^2(t)$. Assuming (7.25) this implies that the frequency of the source corresponds to twice the oscillation frequency of the oscillons. In the KKLT scenario, however, the potential is asymmetric around the minimum and leads to a frequency of the source which coincides with the fundamental frequency of the oscillons. Therefore, ω_{osc} was chosen to be half the frequency at which the spectrum obtained from our lattice simulation peaks, i.e. $\omega_{\text{osc}} \lesssim m/2$ (cf. figure 7.13).

In the KKLT scenario we found that the number of oscillons increases with time. Therefore we assumed a time-dependent number of oscillons $N(a)$ to evaluate (5.15) for our artificial KKLT setup. Explicitly, we assumed

$$N(a) = N(a_0) \cdot \left(\frac{a}{a_0}\right)^3 , \quad \text{with} \quad N(a_0) = 4\,, \tag{7.26}$$

or in other words that the number of oscillons per *physical* volume remains constant. The initial number of oscillons was taken at $a_0 \simeq 5.8$. On the other hand, at the end of the simulation at $a_{\text{end}} = 8.3$ we counted $N \simeq 12$, which is consistent with (7.26). We note, however, that we neglected tiny overdensities and counted spatially large overdensities, i.e. double- and triple-oscillons (cf. the upper right plot in figure 7.14) as single oscillons. This in turn may eventually lead to an underestimation of the signal. Finally, the value of the oscillon asymmetry parameter Δ was considered as a free parameter.

The numerical values of all the parameters used to infer the GW spectrum using the semi-analytical method are summarised in table 7.3. Eq. (5.15) was then solved numerically from $a_{\text{i}} = 1$ to $a_{\text{f}} = a_{\text{end}}/a_0 = 1.38$. The result is presented in figure 7.15, together with the final spectrum of our lattice simulation of the KKLT scenario with $W_0 = 10^{-5}$ (solid blue line). The spectrum obtained from integrating (5.15) is denoted by the orange dots. Both spectra are represented as a function of the physical wavenumber $a^{-1}k/m$.

Despite our (extremely) simplified assumptions, we find that the results originating from our semi-analytical method are in good agreement with those from the more realistic lattice simulation for $\Delta = 0.5$. This may initially seem large, however

oscillon amplitude A	oscillon width R	number of oscillons N	comoving volume $\mathcal{V}$
$0.0085\, m_{\rm Pl}$	$99234.9\, m_{\rm Pl}^{-1}$	$N(a) \propto a^3$, $N(a_0) = 4$, $N(a_{\rm end}) = 12$	$2.574 \times 10^{20}\, m_{\rm Pl}^{-3}$

Table 7.3: Parameters extracted from the lattice simulation of the KKLT model that were used for the semi-analytical computation of the GW spectrum.

notice that for certain oscillons (in particular for the douple- and tripple-oscillons which are counted as single oscillons) this assumption is rather underestimating.

The difference between the two approaches can in principle be caused by different effects, such as assuming identical oscillons, which is clearly not the case. The slightly different slope of the peak might be explained by our lack of knowledge regarding the precise time dependence of N. Moreover, note that in our derivation of (5.15) we neglected interference effects between oscillons that are separated by small distances. As clearly visible in figure 7.7, where oscillons apparently interact with each other, assuming that oscillons are separated by large distances certainly not justified throughout the entire evolution.

7.4 Short comment on other string inspired scenarios

Before summarising the results of this chapter we would like to mention that apart from the scenarios considered above, we also considered other string inspired models. In particular, the dynamics of an initially displaced volume modulus in the LVS as well as the post-inflationary dynamics of the inflaton in the simplest realisation of Fibre inflation [255, 256]. We note that we did not find any signs of efficient growth of fluctuations or even of non-linear effects. We therefore skip the discussion of those results and refer to appendix A of Ref. [3].

7.5 Summary

We studied the dynamics of Kähler moduli in type IIB string theory scenarios during moduli preheating. In particular, we focused on cases in which a single modulus is initially displaced from its post-inflationary minimum and around which it starts oscillating as the Hubble parameter becomes comparable to its mass at that time. We thereby assumed that at the moment at which the modulus becomes dynamical, it dominates the energy.

Explicitly we considered two example potentials: that of an overall volume moduls in the KKLT scenario and an example potential of a single blow-up modulus in the LVS. We found that in one of the two considered realisations of the KKLT model, as well as for the considered blow-up modulus potential, the fields experi-

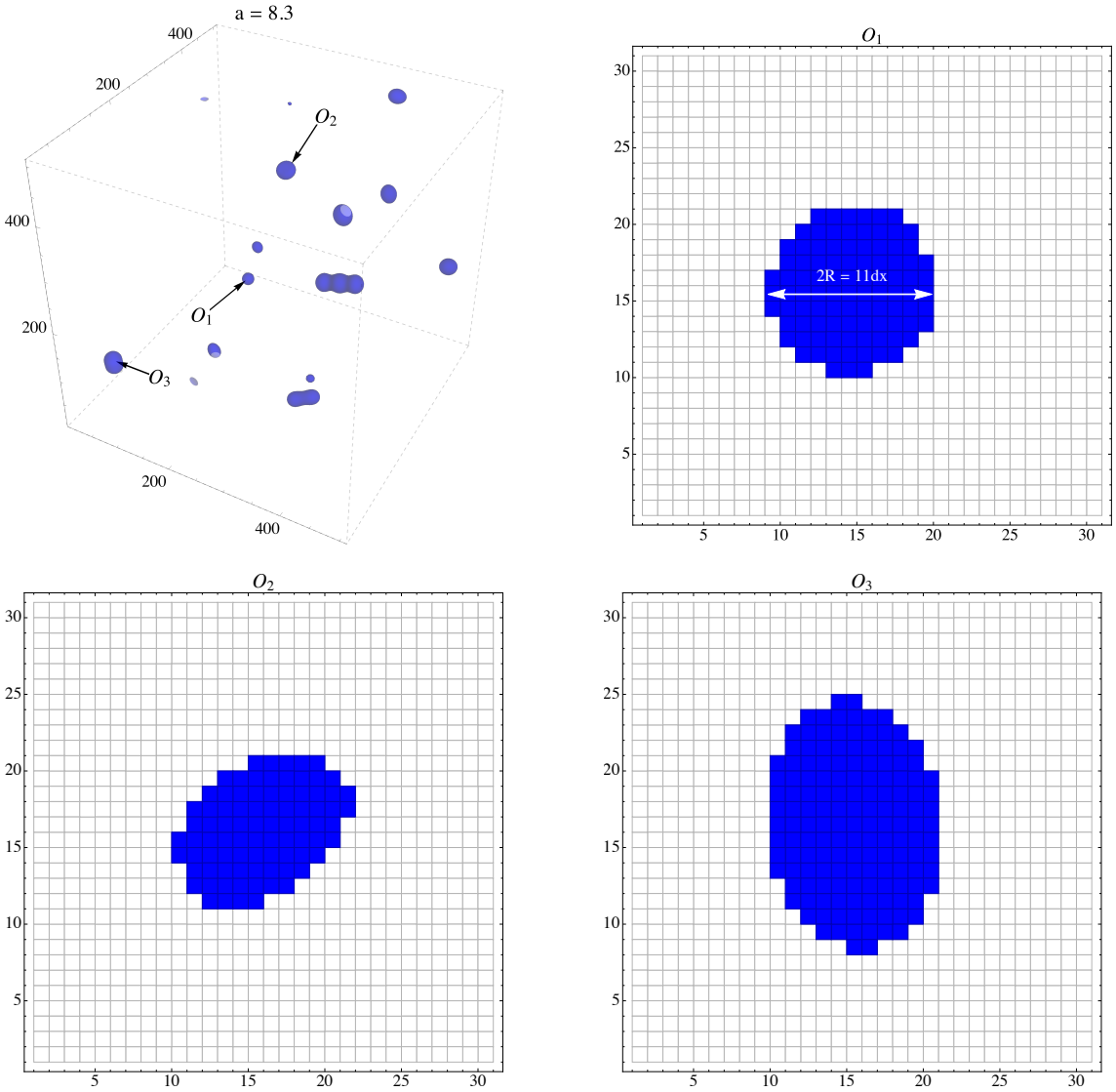

Figure 7.14: Final distribution of oscillons, represented by constant energy density isosurfaces where $\rho = 16\langle\rho\rangle$ (upper left). The remaining figures show the cross sections of selected oscillons in terms of the field at the end of the lattice simulation ($a_{\text{end}} = 8.3$). The blue contour denotes points at which the amplitude takes values above a fraction $1/\sqrt{e}$ of the (current) maximum amplitude of the respective oscillon. In other words, the widths of the oscillons R correspond to about half the diameter of the cross sections. Notice that each pixel corresponds to one lattice point.

ence growth of fluctuations, eventually leading to the non-linear fragmentation of the moduli.

By comparing the results obtained from the different models we found both, similarities as well as qualitative differences. In particular, we found that both scenarios oscillons can form through qualitatively different mechanisms.

In the KKLT scenario the growth of fluctuations happens due to a parametric self-resonance. The latter leads to linear growth of fluctuations which happens over dozens of oscillations of the homogeneous component. In that case, we find that

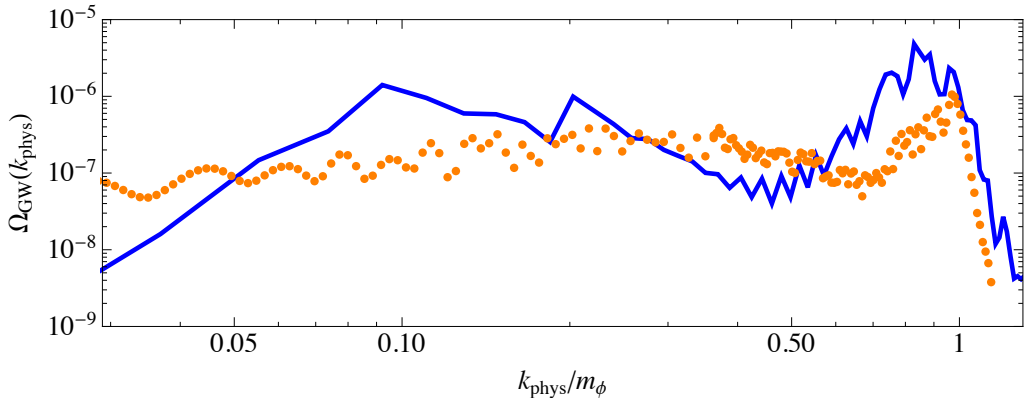

Figure 7.15: Comparison of the final GW spectra obtained from purely numerical lattice simulations (blue) and from the semi-analytical method discussed in chapter 5 (orange dots). Both spectra are shown as a function of the physical wavenumber $k_{\rm phys}/m_\phi = a_{\rm f}^{-1}k/m$, with m defined as in eq. (7.10).

inhomogeneities are "leisurely" formed directly in form of localised, oscillating lumps in field space, i.e. oscillons.

The dynamics of the blow-up modulus in the LVS, in turn, are found to be considerably more violent and very similar to those experienced by the inflaton after hilltop inflation. Indeed, the growth of fluctuations happens due to the mechanism of tachyonic oscillations. The formation of oscillons in this scenario happens through an intermediate, violent, and chaotic stage: initially, a filamentary structure forms. These filaments eventually collapse into large asymmetric and deformed bubbles which then fragment further into smaller lumps. Finally, they eventually relax into quasi-stable oscillons (see figure 7.11).

Another aspect that we studied is the formation of GWs associated with the non-linear dynamics of the moduli. In both, models for which the dynamics exhibits non-linear fragmentation of the fields we found that GWs are produced and that the qualitative features of the dynamics are manifested in the GW spectra. In particular, we found that in the KKLT scenario where the only inhomogeneities are the oscillons, the GW spectrum exhibits a characteristic peak structure (cf. the upper plot in figure 7.13). We also compared the purely numerical results of the GW spectrum from lattice simulations to results obtained using the semi-analytical method discussed in chapter 5 finding good agreement. This, in turn, strengthens the applicability of the semi-analytical approach. On the other hand, for the blow-up modulus in the LVS we found that the spectrum is more similar to that produced during preheating after hilltop inflation (see for instance figure 6.10). We did not find any signs of oscillons (i.e. no peak structure) imprinted in the GW spectrum. For the models considered in this, the present day frequencies of the GW spectra are, however, found to be far too high to be observable with current and planned GW observatories.

Let us finally comment on our choice of initial conditions. As discussed above we assumed that the moduli start oscillating (with zero initial velocity) at a moment at which the entire energy is dominated by the potential energy of the modulus. We would like to note that the results showed above might be sensitive to different

choices of initial conditions. Assuming that parts of the energy density are dominated by a (non-interacting) radiation fluid, for example, would inevitably result in a stronger damping of the modulus oscillations. This, in turn, would most likely lead to milder preheating.

Part VI

Conclusions and outlook

Chapter 8

Conclusions and outlook

On the basis of numerical lattice simulations, we studied the non-linear dynamics of scalar fields and the associated production of GWs in different, particle physics motivated models of the early universe. In particular, we studied the dynamics of preheating in scenarios of hilltop inflation in which the inflaton is coupled to an additional scalar field χ. Furthermore, we have investigated the dynamics of Kähler moduli in scenarios of moduli preheating for two explicit and well motivated string scenarios: the dynamics of the overall volume modulus in the KKLT model as well as the dynamics of a single blow-up modulus in the LVS.

Our study of preheating after hilltop inflation clearly emphasises the importance of studying this regime detail. We focused on realisations of hilltop inflation in which the driving mechanism for the growth of inflaton fluctuations are tachyonic oscillations. We found that fluctuations of the field (χ) that couples to the inflaton (ϕ) can be produced efficiently, even well after the dynamics of ϕ become dominated by inhomogeneous, non-linear fluctuations. Based on our lattice study, we argued that the resonant amplification of χ happens due to a non-standard parametric resonance which is driven by the dynamics of the inhomogeneous inflaton fluctuations. Depending on the coupling between the two fields, we found that strength and rapidity of the χ resonance can vary significantly and lead to qualitatively different dynamics. As was already shown in a previous (two-dimensional) lattice study, we found that in those scenarios in which χ fluctuations get amplified almost immediately after ϕ becomes inhomogeneous, the formation of oscillons is strongly suppressed. On the other hand, for realisations in which the growth of $\delta\chi$ is less efficient, it turns out that oscillons can form in both fields and in the same spatial regions (cf. Figure 6.9).

Why are these results interesting and important? As mentioned in chapter 6, when viewed from a particle physics point of view, χ could for instance play the role of a right-handed sneutrino. It would then provide a decay channel that allows for non-thermal leptogenesis. The predictions for the baryon asymmetry, in turn, can be sensitive to the particle abundances at the moment at which the process is triggered. Indeed, this was explicitly demonstrated in a recent study. Based on partial results of the work presented in this thesis (essentially those of figure 6.3) it was shown that a non-zero abundance of χ particles can significantly change the predictions of leptogenesis. In particular, it was shown that the predicted bayron asymmetry can be enhanced by even more than one order of magnitude, compared to the case where the χ particle abundance by the onset of leptogenesis is vanishingly

small. This study further highlights the importance of our results.

Among all the scenarios considered in this thesis we found similarities but also differences in both, the dynamics and in the resulting spectra of GWs. In particular, we found that all scenarios (depending on the realisation) can lead to the formation of oscillons. The way the formation occurs, in turn, was found to depend on the mechanism that drives the growth of fluctuations.

In the hilltop inflation model and for the blow-up modulus in the LVS, we found that the dynamics are qualitatively very similar: at the end of linear preheating, relatively (spatially) large fluctuations get formed, which first exhibit a rather chaotic dynamical behaviour. They are then found to further fragment into smaller lumps until they eventually relax into quasi-stable oscillons.

Regarding the production of GWs in these scenarios we found that the initial violent and non-linear stage of preheating leads to a broad peak in the spectrum of GWs. We argued that this peak is likely to be the reason for the fact that no clear indications of GW production from oscillons could be found within these scenarios. Indeed, in contrast to what we originally claimed in an earlier study, and apart from some hints of features that might be attributable to the oscillon dynamics in certain realisations of hilltop inflation (cf. the discussion in section 6.3), we did not find any clear signs of oscillon features in the GW spectra obtained from our improved analyses. We found that the preheating dynamics in different realisations of hilltop inflation, can give rise to slight differences in the resulting GW spectra, which could render possible an observational distinction, at least in principle. Unfortunately, the frequencies are found to lie well outside the observable reach of current and proposed GW detectors.

The situation is different for the case of the overall volume modulus in the KKLT scenario. There, the growth of fluctuations is attributable to the mechanism of parametric resonance. In this case, we found that the growth of fluctuations is less violent and that fluctuations are produced rather directly in form of oscillons, i.e. without going through a violent intermediate stage. In particular, this is reflected in the GW spectra resulting from the dynamics of the modulus. The spectrum is found to exhibit a characteristic peak structure which is clearly attributable to the dynamics of oscillons since they are found to be the only potential source of GW production in this scenario.

That stochastic backgrounds of GWs produced from the dynamics of scalar fields can contain valuable information about the underlying cosmological scenario as demonstrated within our semi-analytical analysis where we focused on the GWs produced by asymmetric oscillons. On the basis of simplifying but model-independent assumptions, we showed that information about the properties that characterise a given cosmological scenario (e.g. the background cosmology) might be explicitly manifested in the resulting GW background. This illustrates the depth of potential that the observation of a stochastic GW background could offer for discovering new physics.

Finally, let us comment on the observability of the GW backgrounds resulting from the dynamics of preheating (or moduli preheating) in the models studied in this thesis. We found that none of the considered models predicts a stochastic background of GWs that could be observable with the technologies available today

and in the near future. Essentially, this is due to the fact that the considered models have all been high scale models which generically give rise to high frequency GWs beyond the reach of current and planned GW detectors. On the other hand, similar dynamics may occur in low scale models e.g. along the lines of hybrid (or tribrid) inflation. There the dynamics could, indeed, be very similar while the predicted GWs could exhibit much lower frequencies, in the range of current or future detectors. Similar conclusions may, in turn, apply to moduli potentials for which the energy scale is also allowed to be lower.

It is clear that there are still a lot of open question to be answered: Regarding our semi-analytical estimates of the GW spectrum for example, we considered simplified cases in which most of the oscillon related quantities (i.e. the oscillon amplitude, the oscillon width, and the asymmetry parameter) were assumed to be constant. This is certainly not the case in realistic scenarios. Better estimates could be obtained by allowing these quantities to be time-dependent. A possible method that would allow to estimate (or fit) the evolution of the oscillon amplitude would, for example, be to simulate the evolution of the oscillons in 1D lattice simulations assuming spherical symmetry. Similar studies could be carried out to study the relaxation towards spherical symmetry of asymmetric oscillons.

Regarding the string inspired models we considered cases in which a single modulus is assumed to get displaced from its post-inflationary VEV during inflation. However, many moduli are generically present which could get displaced during inflation and would also become dynamical at later stages. Moreover, we assumed that the axion component of the modulus remains stabilised at the minimum of its potential. In principle, just as the χ field in our hilltop inflation model, the axion could experience resonant growth due to a parametric resonance. Notice that the same could apply to the imaginary comoponents of the fields in our hilltop model, which were not included in our lattice study. It would be interesting to further investigate these possibilities.

Another interesting aspect to study would be the effect of (scalar) metric perturbations on the production of GWs. It would be interesting to see whether these effects could change the qualitative features of the stochastic GW background, in particular, in those models where oscillon features are inapparent.

The recent direct detection of GWs has certainly generated a lot more interest and excitement for the field of GW cosmology. It will be interesting to see in which directions this field of research is going to develop. Definitely, new technologies will be proposed. For the moment, however, probing the universe with high frequency GWs remains a dream of the future. In any case, there are certainly exciting times ahead of us.

Part VII

Appendix

Appendix A

Notation and conventions

In this appendix we clarify the notation and conventions that are used throughout this thesis.

We always work in natural units

$$c = \hbar = m_{\rm pl} = 1/\sqrt{8\pi G} = 1\,, \tag{A.0.1}$$

with c denoting the speed of light in vacuum, $\hbar$ is the reduced Planck constant, G denotes the gravitational constant, and $m_{\rm pl} \simeq 2.436\times10^{18}$ GeV is the reduced Planck mass. To emphasise the mass dimension in we sometimes write $m_{\rm pl}$ explicitly.

Throughout this thesis we adopt the metric signature $(-,+,+,+)$. Four-vector indices are denoted by Greek letters $(\mu,\nu,\rho,\dots)$ running from 0 to 3, where 0 denotes the time coordinate. Spatial coordinates are denoted by Roman letters $(i,j,l,...)$ which run from 1 to 3. Covariant quantities are represented by lowercase indices and contravariant quantities by upper case indices, respectively. Moreover, we adopt the Einstein summation convention, i.e. whenever an index appears as an upper case and a lower case index in the same expression, summation over the respective index is implied.

For the partial derivatives with respect to spacetime coordinates we use the notation

$$\partial_\mu f = \frac{\partial f}{\partial x^\mu}\,, \quad \text{and} \quad \partial^\mu f = \frac{\partial f}{\partial x_\mu}\,. \tag{A.0.2}$$

Derivatives with respect to cosmic time t are abbreviated by an overdot, i.e.

$$\dot f \equiv \frac{df}{dt}\,, \tag{A.0.3}$$

while derivatives with respect to conformal time $d\eta = a^{-1}dt$ are denoted by a prime

$$f' \equiv \frac{df}{d\eta}\,. \tag{A.0.4}$$

Derivatives with respect to quantities other than spacetime coordinates are denoted explicitly.

Finally, for the (three-dimensional) Fourier transform of a function $f(t,\mathbf{x})$ we adopt the convention

$$f(t,\mathbf{x}) = \int \frac{d^3\mathbf{k}}{(2\pi)^3}\, f_{\mathbf{k}}(t)\, e^{i\,\mathbf{k}\cdot\mathbf{x}}\,. \tag{A.0.5}$$

Appendix B

List of abbreviations

BAO	Baryon Acoustic Oscillations
BBN	Big Bang Nucleosynthesis
CDM	Cold Dark Matter
CL	Confidence Level
CMB	Cosmic Microwave Background
DM	Dark Matter
EFE	Einstein Field Equation
EOS	Equation Of State
EOSp	Equation Of State parameter
FLRW	Friedmann-Lemaître-Robertson-Walker
GR	General Relativity
GUT	Grand Unified Theory
GW	Gravitational Wave
IR	Infrared
KKLT	Kachru-Kallosh-Linde-Trivedi
LSS	Large Scale Structure
LVS	Large Volume Scenario
PBH	Primordial Black Hole
PH	Pure Hilltop
SFSR	Single Field Slow-Roll
SM	Standard Model
SUGRA	Supersymmetry
SUSY	Supergravity
TT	Transverse-Traceless
UV	Ultraviolet
VEV	Vacuum Expectation Value

Appendix C

Tools and techniques for studying preheating

In this appendix we discuss common techniques that are used for the study of scalar field preheating.

C.1 Linearised equations

As long as the backraction of the fluctuations on the homogeneous mode as well as mode-mode interactions are negligible, the dynamics during preheating are well-captured by the linearised equations for the perturbations. In the following we consider a multi-field system governed by the action (4.5). The system of equations that captures the dynamics of the fluctuations during the linear regime can be obtained by proceeding as follows: We first expand all fields into a homogenous background $\overline{\phi^\ell}(t)$ and a perturbation $\delta\phi^\ell(t,\mathbf{x})$ as

$$\phi^\ell(t,\mathbf{x}) \,=\, \overline{\phi^\ell}(t) + \delta\phi^\ell(t,\mathbf{x}) \tag{C.1.1}$$

Eq. (4.6) is then linearised to first order in the perturbations and the latter are decomposed into Fourier modes $\delta\phi^\ell_{\mathbf{k}}$ according to (A.0.5). By doing so, one finds the following equation for the Fourier modes

$$\delta\ddot{\phi}^\ell_{\mathbf{k}} + 3H\delta\dot{\phi}^\ell_{\mathbf{k}} + \left(\frac{k^2}{a^2} + \frac{\partial^2 V}{\partial(\overline{\phi^\ell})^2}\right)\delta\phi_{\mathbf{k}} + \sum_{m\neq\ell}\frac{\partial^2 V}{\partial\overline{\phi^\ell}\partial\overline{\phi^m}}\delta\phi^m_{\mathbf{k}} \,=0\,, \tag{C.1.2}$$

The potential and the Hubble parameter

$$H^2 \,=\, \frac{1}{3\,m_{\rm Pl}^2}\left[\frac{1}{2}\sum_\ell \dot{\overline{\phi^\ell}}^2 + V(\overline{\phi^1},\ldots,\overline{\phi^{N_f}})\right]\,, \tag{C.1.3}$$

are both evaluated as a function of the homogeneous background fields obeying

$$\ddot{\overline{\phi^\ell}} + 3H\dot{\overline{\phi^\ell}} + \frac{\partial V}{\partial\overline{\phi^\ell}} \,=\, 0\,, \quad \ell = 1,\ldots,N_f\,. \tag{C.1.4}$$

Given a set of initial conditions, the above equations are typically solved numerically. In scenarios of inflation, the inflaton ($\overline{\phi} \equiv \overline{\phi}^1$) can in principle be initialised shortly before the end of inflation when the slow-roll conditions (3.19) still hold and the field velocity $\dot{\phi}$ is accurately given by (3.16).

Alternatively, one may initialise $\overline{\phi}$ (and $\dot{\overline{\phi}}$) somewhat later, e.g. shortly after the end of the slow-roll regime, but before fluctuations have experienced resonant growth. In such cases, the initial conditions can be extracted by integrating eq. (C.1.4) up to the desired moment in time.

Within this thesis, the initial conditions for the homogeneous inflaton component and the Hubble parameter are generally specified at some moment in time $t = t_\mathrm{i}$

$$\overline{\phi}_\mathrm{i} \equiv \overline{\phi}(t_\mathrm{i})\,, \quad \dot{\overline{\phi}}_\mathrm{i} \equiv \dot{\overline{\phi}}(t_\mathrm{i})\,, \quad H_\mathrm{i} \equiv H_\mathrm{i}(t_\mathrm{i})\,, \tag{C.1.5}$$

at which

$$\varepsilon_V(t_\mathrm{i}) \quad \vee \quad \eta_V(t_\mathrm{i}) \gtrsim 1\,, \quad \text{with} \quad \dot{H} \simeq 0 \quad \text{for} \quad t \leq t_\mathrm{i}\,. \tag{C.1.6}$$

Moreover, we generally assume that inflation happens in the single-field limit and that other fields $\phi^2, \ldots, \phi^{N_f}$, if present, are stabilised at their minimum $\overline{\phi^\ell} = \overline{\phi^\ell}_\mathrm{min}$ during inflation, such that

$$\overline{\phi^\ell}_\mathrm{i} = \overline{\phi^\ell}_\mathrm{min}\,, \quad \text{and} \quad \dot{\overline{\phi^\ell}}_\mathrm{i} = 0\,, \quad \text{for} \quad \ell \geq 2\,. \tag{C.1.7}$$

For the initialisation of the fluctuations we will assume that any possibly preexisting inhomogeneities have been diluted during inflation such that the fluctuations can be considered to be in their quantum vacuum state. At the end of inflation the fluctuations are typically initialised according to the Bunch-Davies vacuum solution

$$\delta\phi^\ell_\mathbf{k}(t) = \frac{e^{i\,k/(aH)} H}{\sqrt{2k^3}} \left(i + \frac{k}{aH}\right)\,. \tag{C.1.8}$$

In practice, eqs. (C.1.2) - (C.1.3) are integrated numerically for a set of discrete k values that cover the range of dynamically relevant scales.

C.2 Floquet theory

The dynamics of scalar fields are determined by the shape of the scalar potential, i.e. essentially by the choice of parameters (such as couplings, powers of fields, etc.) that define a specific model realisation. Changes of parameter values that do not change the qualitative shape of the potential can in principle have a significant impact on the evolution of fluctuations.

A first insight into the dynamics of preheating during the oscillatory regime, might be gained through the application of Floquet theory. It allows to determine whether, and at which scales the fluctuations are expected to experience a strong amplification by performing a so-called Floquet stability analysis.

Notice, however, that the applicability of Floquet theory is limited to the linear regime and even then, only if the homogeneous background motion is periodic.

The latter is certainly not the case if the universe expands. Moreover, even if the expansion is neglected, periodicity is generally not guaranteed in the presence of multiple dynamical fields that couple to each other [139].

Nevertheless, for scenarios in which the perturbation equations of different fields decouple, Floquet theory may be used to estimate the growth rate of the fluctuations in Minkowski spacetime[1]. On the other hand, if the growth rates are found to be much larger than the Hubble parameter, this is typically a reliable indicator for the resonance to be efficient, also in an expanding universe [139].

Let us now come back to the multi-field system discussed above in appendix C.1. If we neglect the expansion and further assume that the linearised equations (C.1.2) decouple from each other (i.e. that the mixed derivatives of the potential vanish) we obtain the following equation for each of the fields

$$\delta\ddot{\phi}^{\ell}_{\mathbf{k}}(t) + [\omega^{\ell}_{k}(t)]^2 \delta\phi^{\ell}_{\mathbf{k}}(t) \;=\; 0\,, \tag{C.2.9}$$

with ω_k as in (4.13). If ω_k is periodic in t, the Floquet theorem applies, and the above equation takes the form of Hill's equation [170]. Then the Floquet theorem states that the solutions to eq. (C.2.9) can be written as

$$\delta\phi^{\ell}_{k}(t) = P_{+}(t)\, e^{\mu_k\, t} + P_{-}(t)\, e^{-\mu_k\, t}\,. \tag{C.2.10}$$

The functions $P_{\pm}$ are periodic and have the same periodicity as $\omega^2_k(t)$. The constant quantity μ_k is generally complex-valued and is referred to as *Floquet exponent*. Solutions for which μ_k exhibits a non-vanishing real part ($|\Re[\mu_k]| > 0$) grow exponentially. The growing modes are those which are of major interest for the study of preheating.

For the specific case in which $\omega_k(t)$ is harmonic, eq. (C.2.9) is referred to as Mathieu equation [257, 258]. The latter can be written in the following form

$$\frac{d^2\delta\phi^{\ell}_{\mathbf{k}}(\tau)}{d\tau^2} + [A_k + 2q\cos(2\tau)]\,\delta\phi^{\ell}_{\mathbf{k}}(\tau) \;=\; 0\,, \tag{C.2.11}$$

where the modes are now expressed in terms of a dimensionless time variable τ, and A_k contains the k dependent part of the mode equation.

The goal of a Floquet analysis is to compute the Floquet exponents μ_k as a function of the wavenumber k, and typically also as a function of the amplitude of the oscillating background. Depending on the model it might be also interesting to consider different model realisations (i.e. perform Floquet analyses with different values of model parameters).

For a system with N_f real scalar fields $\phi^1, \ldots, \phi^{N_f}$, we now discuss how a Floquet analysis can be carried out in practice. The following discussion is based on Ref. [139], to which we refer for further details.

After neglecting the expansion and assuming that the perturbation equations decouple, we may rewrite the system of equations (C.1.2) as a system of linear

[1]Notice, that if the oscillation frequency of the homogeneous background is large compared to the Hubble parameter, neglecting the expansion may even be justified during a single (or a few) oscillation(s), but certainly not over many oscillations.

first-order differential equations as follows

$$\dot{\mathbf{v}}(t) = A(t)\mathbf{v}(t)\,. \tag{C.2.12}$$

Here $\mathbf{v}(t)$ is a column vector defined as

$$\mathbf{v}(t) \equiv (\delta\phi^1_{\mathbf{k}}, \ldots, \delta\phi^{N_f}_{\mathbf{k}}, \pi^1_{\mathbf{k}}, \ldots, \pi^{N_f}_{\mathbf{k}})^T\,, \tag{C.2.13}$$

with

$$\pi^\ell_k \equiv \delta\dot{\phi}^\ell_{\mathbf{k}}\,. \tag{C.2.14}$$

The matrix A is given by

$$A(t) = \left(\begin{array}{c|c} \mathbb{0}_{N_f\times N_f} & \mathbb{1}_{N_f\times N_f} \\ \hline \mathcal{F}(k,t) & \mathbb{0}_{N_f\times N_f} \end{array}\right)\,,$$

where $\mathbb{1}_{N_f\times N_f}$ and $\mathbb{0}_{N_f\times N_f}$ are an $N_f\times N_f$ unit matrix, and a null matrix, respectively. The $N_f\times N_f$ matrix $\mathcal{F}(k,t)$ is diagonal and given by

$$-\mathcal{F}(k,t) \equiv \mathrm{diag}\left(k^2 + \frac{\partial^2 V}{\partial(\overline{\phi^1})^2}\,, \ldots, k^2 + \frac{\partial^2 V}{\partial(\overline{\phi^{N_f}})^2}\right)\,. \tag{C.2.15}$$

The solution to eq. (C.2.12) can be expressed in terms of the fundamental matirx $\mathcal{O}(t,t_0)$ according to (see e.g. Ref. [259])

$$\mathbf{v}(t) = \mathcal{O}(t,t_0)\mathbf{v}(t_0)\,, \tag{C.2.16}$$

with t_0 being some arbitrary initial time (i.e. $\mathbf{v}(t_0)$ are the initial conditions) and $\mathcal{O}(t,t_0)$ satisfies

$$\dot{\mathcal{O}}(t,t_0) = A(t)\,\mathcal{O}(t,t_0)\,, \quad \text{with} \quad \mathcal{O}(t_0,t_0) = \mathbb{1}_{4\times 4}\,. \tag{C.2.17}$$

If $\mathcal{F}(k,t)$ is periodic, the Floquet theorem states that the fundamental solutions can be expressed as

$$\mathcal{O}(t,t_0) = P(t,t_0)\,e^{-(t-t_0)\Lambda(t_0)}\,. \tag{C.2.18}$$

where P shares the same periodicity as $\mathcal{F}$, while the Floquet exponents μ^m_k ($m = 1,\ldots,2N_f$) are now encoded in the $2N_f\times 2N_f$ matrix Λ and essentially correspond to its eigenvalues.

For different values of k the Floquet exponents μ^m_k can be computed by iteratively carrying out the following steps:

1. Compute the period of the system (i.e. the period of $\mathcal{F}(k,t)$) T.

2. Solve

$$\dot{\mathcal{O}}(t,t_0) = A(t)\,\mathcal{O}(t,t_0)\,, \tag{C.2.19}$$

from $t = t_0$ to $t = t_0 + T$, with initial conditions $\mathcal{O}(t_0,t_0) = \mathbb{1}_{2N_f\times 2N_f}$.

3. Diagonalise $\mathcal{O}(t_0 + T, t_0)$, compute its eigenvalues $\sigma_k^m = |\sigma_k^m|\, e^{i\,\theta_k^m}$. The real part of the Floquet exponents is then given by

$$\Re[\mu_k^m] = \frac{1}{T} \ln |\sigma_k^m| \,. \tag{C.2.20}$$

The procedure above is usually repeated for many different values of k. In addition it is often also interesting to vary the model parameters or the amplitude of the oscillating background. The results of the Floquet analysis are then typically presented in form of a *Floquet stability chart*, in which the growing solutions appear in form of instability "bands" or "tongues" (see figure 4.2 for an example).

C.3 Non-linear preheating & lattice simulations

The amplification of scalar field fluctuations may be so efficient that non-linear effects, such as the backreaction on the zero-mode, as well as interactions between different modes become important. In such a case, the linear theory is no more applicable and the dynamics must be followed by solving the fully non-linear equations (4.6). This is typically done by performing lattice simulations in which the relevant equations are solved numerically on a discretised version of spacetime

A substantial part of the results presented in this thesis has been obtained from lattice simulations that were performed with a program called LatticeEasy [260]. The latter has been released almost two decades ago by G. Felder and I. Tkachev and is only one of several possible options for simulating the non-linear dynamics during preheating. In fact, various publicly available programs exist that account for this task. A list of the most common lattice codes is given below in appendix C.5.

C.3.1 LatticeEasy

LatticeEasy [260] is a publicly available code for simulating the evolution of scalar fields in an expanding universe. It is written in C++ language and is actually relatively Easy to use. This is first and foremost thanks to the efforts of the developers who provide a detailed documentation, which does not only simplify the usage and the modification of the program. Both, the source code and the documentation can be downloaded at http://www.felderbooks.com/latticeeasy/index.html.

Given some model $V(\phi^\ell, \ldots, \phi^{N_f})$, the program solves the field equations of motion eqs. (4.6) on a $N_{\rm dim}$ dimensional lattice in a box of finite size L, volume $L^{N_{\rm dim}}$, and assuming periodic boundary conditions. The user has the option to choose between $N_{\rm dim} = 1$, 2, or 3 spatial dimensions. The spacing between neighboring lattice points in position space is $\Delta x = L/N$, with N being the number of points per spatial dimensions. The latter must be chosen as an integer power of two[2].

The time evolution of the scalar fields is performed using a so-called staggered Leapfrog method [262]. In three spatial dimensions, the time evolution of a scalar

[2]This is basically in order to be consistent with the Fourier transform routine used by the program [261].

field ϕ is computed at each spatial grid point in discrete time steps Δt according to the following routine:

$$\begin{aligned} \phi^{t}_{i,j,k} &= \phi^{t-\Delta t}_{i,j,k} + \Delta t \cdot \left[\dot{\phi}^{\,t-\Delta t/2}_{i,j,k}\right] , \\ \dot{\phi}^{\,t+\Delta t/2}_{i,j,k} &= \dot{\phi}^{\,t-\Delta t/2}_{i,j,k} + \Delta t \cdot \left[\ddot{\phi}^{\,t-\Delta t/2}_{i,j,k}(\phi^{t}_{i,j,k})\right] , \\ \phi^{t+\Delta t}_{i,j,k} &= \phi^{t}_{i,j,k} + \Delta t \cdot \left[\dot{\phi}^{\,t+\Delta t/2}_{i,j,k}\right] , \\ &\vdots \quad , \end{aligned} \tag{C.3.21}$$

where the subscripts i, j, k label the spatial position assuming a three-dimensional lattice, i.e.

$$\phi^{t}_{i,j,k} \equiv \phi(t, i \cdot \Delta x, j \cdot \Delta y, k \cdot \Delta z) . \tag{C.3.22}$$

A schematic illustration of a portion of a two-dimensional lattice is depicted in figure C.1.

Notice that the above method requires that $\ddot{\phi}$ is solely a function of ϕ (not of $\dot{\phi}$). This is not the case in an expanding universe due to the Hubble damping term in the field equation of motion. For the Leapfrog method to be applicable, time-dependent rescalings for the scalar fields and the time coordinate are introduced. In essence, the program works with the following rescaled quantities (denoted by the subscript "pr")

$$\phi_{\mathrm{pr}} \equiv A a^{r} \phi , \quad \mathbf{x}_{\mathrm{pr}} \equiv B\mathbf{x} \quad \Delta t_{\mathrm{pr}} \equiv B a^{s} \Delta t . \tag{C.3.23}$$

If r and s are chosen such that $s - 2r + 3 = 0$, the term that is proportional to the field velocity is eliminated. The rescalings A and B can in principle be chosen as the user prefers. Typically, they are chosen such that in program units both, the field and the box size are of $\mathcal{O}(1)$. This renders the numerical computation more stable, since it avoids the appearance of very small numbers which, in terms of floating-point numbers, can only be represented to a certain accuracy.

In order to evaluate the field acceleration $\ddot{\phi}$ the program has to compute the spatial Laplacian. In the original version of LatticeEasy this is done using a centered difference scheme that is second-order accurate in space (i.e. the error is of the order of Δx^2). To give an example, in two spatial dimensions the Laplacian at a grid point (i, j) is given by

$$\nabla^2 \phi^{t}_{i,j} = \frac{\phi^{t}_{i+1,j} + \phi^{t}_{i-1,j} + \phi^{t}_{i,j+1} + \phi^{t}_{i,j-1} - 4\,\phi^{t}_{i,j}}{\Delta x^2} + \mathcal{O}(\Delta x^2) . \tag{C.3.24}$$

The Leapfrog routine is also used to evolve the scale factor. In contrast to the field, the scale factor is not computed at each spatial grid point but rather as an averaged quantity over the entire grid. For the time evolution one faces a similar issue as for the field evolution, namely that $\ddot{a}$ effectively depends on $\dot{a}$. In this case, however, the dependence cannot be eliminated. The error in computing $\ddot{a}$ that is invoked by using the Leapfrog algorithm is though subsequently minimised by introducing additional correction terms (cf. section 6.2.2 of the documentation [261] for further details).

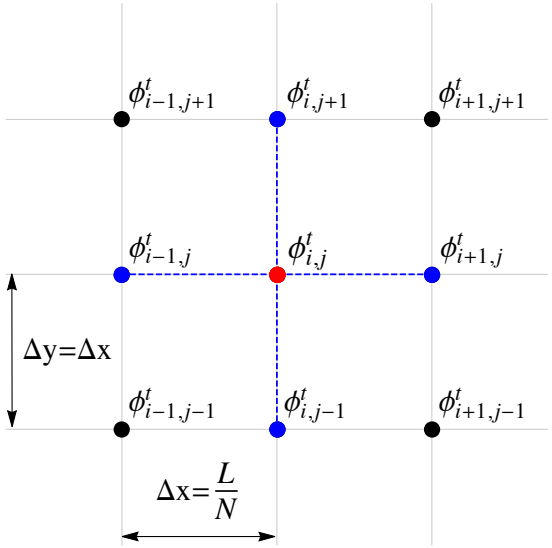

Figure C.1: Schematic illustration of a two-dimensional lattice. At a fixed moment in time t the field value is defined at each lattice point. In the original version of LatticeEasy the two-dimensional Laplacian of the field, at a given lattice point (i, j) (red), is computed using the field value at five different grid points corresponding to (i, j) and its four nearest neighbors (blue).

To simulate the evolution of a specific model with LatticeEasy, the program needs the information about the potential, its first derivative with respect to each field, and finally the effective mass squared of each field. The latter is required to set the initial conditions of the field fluctuations, as well as to compute the number density and energy density spectra (see [261]). All these quantities have to be implemented in terms of the rescaled quantities used by the program, i.e.

$$V_{\rm pr}(\phi^\ell_{\rm pr},\ldots,\phi^{N_f}_{\rm pr}) \equiv \frac{A^2}{B^2}a^{-2s+2r}\,V(\phi^\ell_{\rm pr},\ldots,\phi^{N_f}_{\rm pr})\,, \quad \frac{\partial V_{\rm pr}}{\partial\phi^\ell_{\rm pr}}\,, \tag{C.3.25}$$

and

$$m^2_{\ell,{\rm pr}} \equiv a^{2s+2}\frac{\partial^2 V_{\rm pr}}{\partial(\phi^\ell)^2_{\rm pr}}\,. \tag{C.3.26}$$

Once a specific model has been implemented one has to specify the initial conditions for the zero-modes of the present scalar fields. Ideally, the fields are initialised such that the amount of expansion, before growth of fluctuations occurs, is minimised. In other words, one wants to intialise the fields as late as possible but without omitting essential parts of the preheating regime. In principle, the initialisation can be done as discussed in section C.1, i.e. in accordance with (C.1.5) and (C.1.6).

The initial conditions of the field fluctuations are automatically set by LatticeEasy. The field fluctuations $\delta\phi^\ell_{\mathbf{k}}$ (and their derivatives $\delta\dot{\phi}^\ell_{\mathbf{k}}$) are initialised[3] as

[3]See e.g. sections 6.3.2 and 6.3.3 of [261].

stochastic random variables with a variance reproducing the two-point function of the quantum vacuum fluctuations [171, 263]

$$\langle|\delta\phi_{\mathbf{k}}^{\ell}|^2\rangle \simeq \frac{1}{2\omega_k}, \quad \text{with} \quad \omega_k^2 = k^2 + \frac{\partial^2 V}{\partial(\phi^{\ell})^2}\,. \tag{C.3.27}$$

Before letting the program do the hard work, one has to properly set the time step Δt used for the Leapfrog integration, the box size L, as well as the number of grid points N. By "properly" we mean the time step must be chosen in accordance with the Courant stability condition [262]

$$\Delta t \;<\; \frac{\Delta x}{\sqrt{N_{\rm dim}}}\,, \tag{C.3.28}$$

in order to ensure the stability of the numerical algorithm. The box size L, on the other hand, must be chosen large enough to include all the scales which are dynamically relevant during preheating. In turn, to find those scales one can e.g. perform a Floquet analysis or solve the linearised equations (cf. section C.1).

In order to avoid unphysical effects, such as numerical artifacts related to a poor resolution, it is advisable to perform convergence tests, i.e. to perform multiple simulations with different number of lattice points N and different box sizes L. Results that represent physical effects should not change significantly, if the box size and the resolution have been chosen adequately.

LatticeEasy provides the user with the possibility to freely decide which of the numerous quantities[4] which can be computed by the program, should be saved in output files. This decision should be taken before a simulation is launched.

An output one should be careful with are, for example, the field slices (i.e. the spatial field distribution). Particularly when simulations are performed in three spatial dimensions, they can consume a huge amount of disc space and significantly increase the run time. At the beginning of a run, when the field is still homogeneous, it does not even make sense to save the spatial distribution of any quantity. Instead, one could minimise the amount of "unnecessary" output while following the evolution of the system until non-linear effects start to become important, save a grid image, and then continue the run with as much output as desired.

C.4 Modifications to LatticeEasy

The results presented in this thesis have been carried out using a modified version of the original code. In addition to the default outputs our version can generate output of the energy density distribution, as well as the spectrum of GWs. The former has been implemented by Dr. Stefano Orani. Our code is, moreover, OpenMP parallelised i.e. the equations can be evolved in parallel on a multi-core processor, which significantly reduces the computation time[5]. To increase the numerical accuracy and reduce the error related to the discretisation of the spatial derivatives,

[4] For a list of all the quantities we refer to the LatticeEasy documentation [261].

[5] As an example, for a lattice simulation performed in $2+1$ dimensions with 1024^2 grid points performed on a MacBook Pro with 2,8 GHz Intel Core i7 Processor the computation time was reduced by more than a factor of six.

we replaced the second-order finite difference scheme by one that is fourth-order accurate in space.

C.4.1 Implementation of GWs in LatticeEasy

LatticeEasy is designed to solve for the non-linear scalar field evolution in an expanding universe. To investigate the production of GWs during preheating we extended the LatticeEasy source code to simultaneously solve (cf. the discussion in section 4.4.3)

$$\ddot{h}_{ij} + 3H\dot{h}_{ij} - \frac{1}{a^2}\nabla^2 h_{ij} = \frac{2}{m_{\rm Pl}^2}\Pi_{ij}^{\rm TT}\,. \tag{C.4.29}$$

with

$$\Pi_{ij}^{\rm TT} = \frac{1}{a^2}\sum_{\ell}\left[\partial_i\phi^\ell\partial_j\phi^\ell\right]^{\rm TT}\,, \tag{C.4.30}$$

Notice that if one would directly solve eq. (C.4.29) in configuration space, one would have to perform a Fourier transform at each time step in order to project out the TT part of the anisotropic stress. This is due to the fact that the projection operator P_{ij} defined in eq. (4.69) is non-local. Following the procedure proposed in [224] our code rather computes the evolution of the non-TT tensor u_{ij} which obeys the equation

$$\ddot{u}_{ij} + 3H\dot{u}_{ij} - \frac{1}{a^2}\nabla^2 u_{ij} = \frac{2}{m_{\rm Pl}^2}\frac{1}{a^2}\partial_i\phi\partial_j\phi\,. \tag{C.4.31}$$

with zero initial conditions for the components u_{ij} i.e.

$$u_{ij} = \dot{u}_{ij} = 0 \quad \text{at} \quad t = 0\,. \tag{C.4.32}$$

Then, instead of performing a Fourier transform at each time step, our code simply performs the TT projection

$$h_{ij}(\mathbf{k},t) = \left(P_{il}(\hat{\mathbf{k}})P_{jm}(\hat{\mathbf{k}}) - \frac{1}{2}P_{ij}(\hat{\mathbf{k}})P_{lm}(\hat{\mathbf{k}})\right)u_{lm}(\mathbf{k},t)\,, \tag{C.4.33}$$

only when GW output is desired. Notice that this procedure is mathematically equivalent to directly solving (C.4.29) but is by far more economical from the computational point of view [224].

The spectrum of GWs can then be computed as the energy density in GWs per logarithmic momentum interval. In principle, this can be done in similar way as in eqs. (4.79) and (4.80). The only difference is that one has to account for the fact that the lattice is finite and discrete and not an infinite continuum. On the lattice, the spectrum becomes [264]

$$\Omega_{\rm GW}(k,t) = \frac{1}{\rho_{\rm c}}\frac{d\rho_{\rm GW}}{d\ln k} = \frac{m_{\rm Pl}^2 k^3}{\rho_{\rm c}}\frac{\Delta x^6}{(4\pi)^3 L^3}\langle\dot{h}_{ij}(\mathbf{k},t)\dot{h}_{ij}^*(\mathbf{k},t)\rangle\,, \tag{C.4.34}$$

where L^3 is the volume of the three-dimensional box, Δx is the lattice spacing and $\langle\ldots\rangle$ denotes an average over lattice momenta $\mathbf{k}$ with $|\mathbf{k}| = k$.

C.4.2 Fourth-order accurate Laplacian

The numerical computation of the stochastic GW background, when performed on a discrete lattice, can be very sensitive to the numerical accuracy of the spatial derivatives (see e.g. the discussion in section 6.3.1). A reduction of the numerical errors can, in principle, be achieved in two different ways by[6]

1. increasing the resolution by increasing the number of lattice points N while keeping the box size L fixed

2. improving the numerical accuracy of the finite difference scheme

The first is clearly the easier solution but not necessarily the best. In fact, when performing simulations in three spatial dimensions, doubling the number of points essentially means that the computation time is increased by a factor of eight. Moreover, notice that if one decreases the grid spacing Δx one necessarily has to decrease the time step Δt in order to ensure the stability of the numerical algorithm (cf. eq. (C.3.28)). The latter gives an additional factor of two. Thus, doubling the number of points per dimension inevitably leads to a computation time that is increased by a factor of 16.

Alternatively, one can reduce the error in the finite difference approximation of the spatial derivatives. We did this by replacing the second-order finite difference scheme eq. (C.3.24) with a fourth-order accurate Laplacian which (in three spatial dimensions) reads [265]

$$\begin{aligned}\nabla^2\phi^t_{i,j,k} &= \Big[16\left(\phi^t_{i+1,j,k}+\phi^t_{i,j+1,k}+\phi^t_{i,j,k+1}+\phi^t_{i-1,j,k}+\phi^t_{i,j-1,k}+\phi^t_{i,j,k-1}\right)\\ &- \left(\phi^t_{i+2,j,k}+\phi^t_{i,j+2,k}+\phi^t_{i,j,k+2}+\phi^t_{i-2,j,k}+\phi^t_{i,j-2,k}+\phi^t_{i,j,k-2}\right)\\ &- 90\,\phi^t_{i,j,k}\Big]\frac{1}{12\Delta x^2}+\mathcal{O}(\Delta x^4)\,. \end{aligned} \tag{C.4.35}$$

Notice, that in addition we also had to modify the Laplacian at the boundaries of the box, since the Laplacian evaluated at a lattice point (i,j,k) now depends on the next-to-nearest neighboring points. As explained and demonstrated in section 6.3.1 using the (C.4.35) instead of (C.3.24) for the discrete Laplacian noticeably improved our numerical results for the GW spectra, particularly in that part of the GW spectrum that is related to the oscillon dynamics in the hilltop inflation model. This finally allowed us to perform a *successful* convergence analysis.

C.5 Codes for studying the non-linear dynamics of scalar fields in an expanding universe

All the codes listed below have been developed to study the non-linear dynamics of preheating. Each of these programs has its own advantages and disadvantages

[6] A third method would be to use a pseudo-spectral code which computes the spatial derivatives in Fourier space. As shown in [248] this can significantly reduce the numerical errors related to the discretisation of space. Notice, however, that this method requires to Fourier transform the scalar fields at each time step which is computational very expensive.

and not all of them may be equally suited for certain problems. Studying non-Gaussian curvature fluctuations originating from preheating, for example, requires a high degree of accuracy in computing the energy of the system [266]. We note that this is not necessarily provided by all of the publicly available codes listed below. Hence, depending on the problem that one wants to tackle one may choose an appropriate program, or develop one's own code, if necessary.

- ClusterEasy by Gary Felder [267]: it is an MPI parallelised version of LatticeEasy, i.e. it allows to run a simulation in parallel on different processors. The program and its documentation can be downloaded at http://www.felderbooks.com/latticeeasy/index.html.

- DEFROST by Andrei Frolov [268]: is a fast and accurate finite difference code written in Fortran. According to the developer, the program is easy to use and instrumented for 3D visualisation. In contrast to LatticeEasy it does not evolve the scale factor but rather the Hubble length H^{-1} which results in "a disproportionately huge gain in numerical accuracy" [268]. For the time integration the current version of the program (v2.0) uses a symplectic integrator. More details as well as the source code can be found at http://www.sfu.ca/physics/cosmology/defrost/.

- CudaEasy by Jani Sainio [269]: works in the same way as LatticeEasy, with the difference that the scalar field evolution is performed in parallel on graphics processing units (GPUs) resulting in an accelerated computation.

- PSpectRe by Richard Easther, Hal Finkel, and Nathaniel Roth [270]: is written in C++ and uses a pseudo-spectral method, i.e. the time integration is basically performed in Fourier space. To handle non-linearities in the scalar potential, the latter are computed in position space and then transformed back to Fourier space. This allows to bypass computationally expensive convolutions in Fourier space. Moreover, the user has the possibility to choose between two different integrators: a fourth-order Runge-Kutta, and a second-order Velocity Verlet (see e.g. the appendix of [271]).

- HLattice by Zhiqi Huang [272]: it provides the user with the possibility to choose between a second-, forth- and sixth-order symplectic integrator, as well as three different discretisation schemes. The code includes scalar, vector, and tensor perturbations, and also their backreaction on the fields. The program can be downloaded at http://www.cita.utoronto.ca/~zqhuang/hlat/.

- PyCOOL by Jani Sainio [273]: is written in Python where "COOL" stands for "Cosmological Object-Oriented Lattice code". Just as CudaEasy, PyCOOL is also GPU accelerated and uses a symplectic method for the time integration.

- GABE by H. Child *et al.* Giblin [274,275]: is written in C++ language and the numerical integration is performed with a second-order Runge-Kutta method. GABE which stands for "Grid And Bubble Evolver" allows to simulate the evolution of scalar fields with non-canonical kinetic terms. It can be downloaded at http://cosmo.kenyon.edu/gabe.html.

Appendix D

Convergence analyses

Here we present convergence analyses of the GW spectra obtained within our study of moduli preheating in the KKLT scenario, as well as for the blow-up modulus in the LVS. The results are presented and discussed in figures D.1 and D.2.

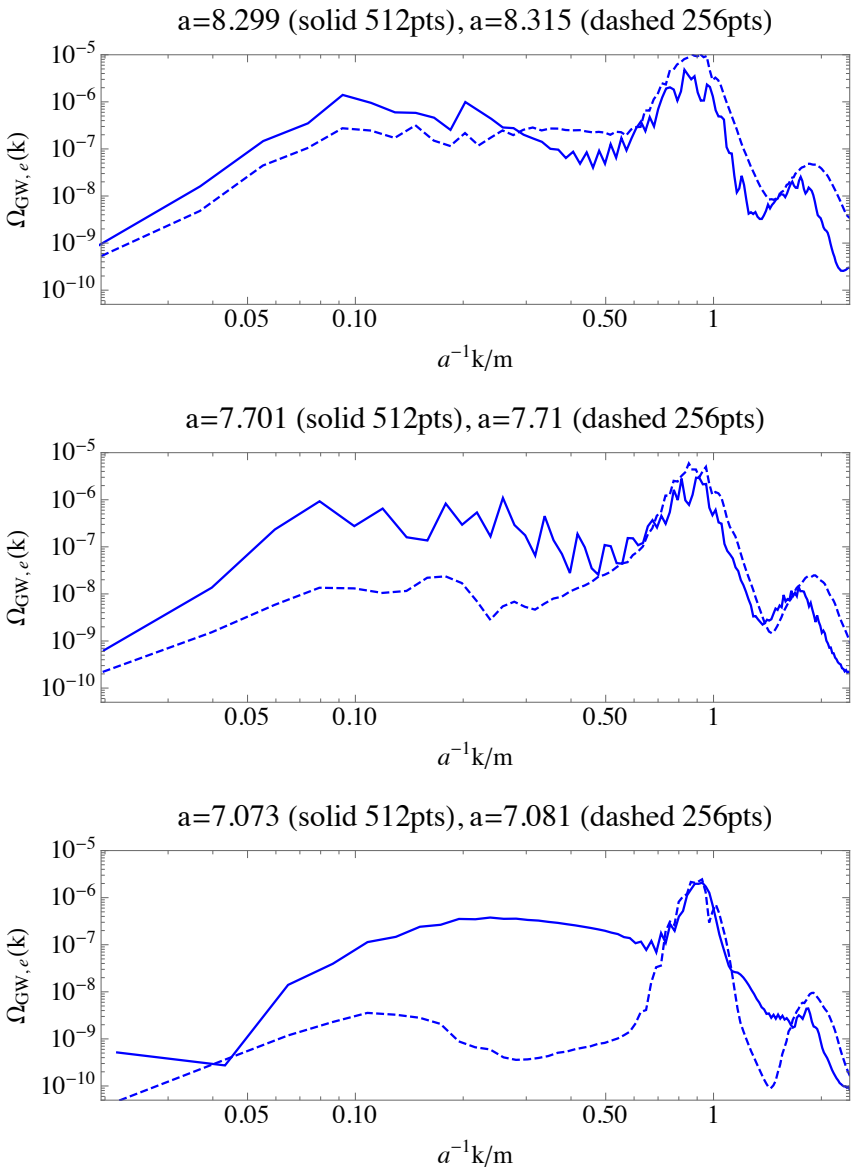

Figure D.1: Convergence analysis of the GW spectrum produced during moduli preheating in the KKLT model (7.5). The figures compare results of simulations carried out with 512 (solid), and 256 (dashed) lattice points per spatial dimension but same box size. The model parameters and initial conditions have been chosen as discussed in section 7.1.2 (cf. the second row of table 7.1). The spectra are shown at different moments in time (cf. the figure labels). At early times (lower two figures) the spectra are noticeably different. In this scenario, we expect that the differences are most likely attributable to the different (random) vacuum fluctuations, rather than to resolution issues. Different random seeds may in this case lead to quantitatively different oscillon formation stages (i.e. slightly different number of oscillons, forming at different positions and times with slightly different sizes/assymetry). Since in this scenario, the oscillons are essentially the only significant inhomogeneities (cf. the discussion in section 7.1.2) this may have a considerable effect on the early evolution of the spectrum. At the end of the simulation (upper plot), the spectra are in good agreement up to factors of $\mathcal{O}(1)$.

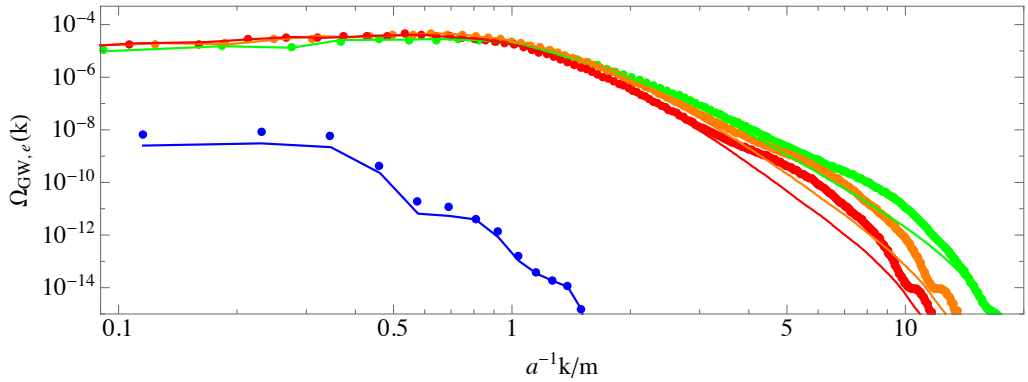

Figure D.2: Results of a convergence analysis of the GW spectra produced during preheating of the blow-up modulus in the LVS. The modulus potential is that of eq. (7.12) and the simulations were performed with parameters as discussed in section 7.2 with initial conditions as in table 7.2. The solid line corresponds to the same results shown in the lower plot of figure 7.13 and originate from a simulation carried out with 512 per spatial dimension. The dotted spectra represent results of a simulation carried out with 256 points per dimension. Both simulations were performed with the same box size and the spectra are shown at the sime times: at $a \simeq 1.16$ (blue), $a \simeq 1.45$ (green), $a \simeq 2.1$ (orange), and at the end of the simulation $a \simeq 2.5$ (red). The results are in good agreement, particularly in the IR where the amplitude of the spectrum Ω_{GW} dominates the spectrum. In the UV for $a^{-1}k/m \gtrsim 4$ the spectra start differing from each other. This is likely related to the resolution. Notice, however, that there the amplitude of the spectrum is orders of magnitudes below that in the dominant part of the spectrum for $a^{-1}k/m \lesssim 1$, where the results are in excellent agreement.

Bibliography

[1] S. Antusch, F. Cefala, D. Nolde, and S. Orani, *Parametric resonance after hilltop inflation caused by an inhomogeneous inflaton field*, *JCAP* **1602** (2016), no. 02 044, [arXiv:1510.0485].

[2] S. Antusch, F. Cefala, and S. Orani, *Gravitational waves from oscillons after inflation*, *Phys. Rev. Lett.* **118** (2017), no. 1 011303, [arXiv:1607.0131]. [Erratum: Phys. Rev. Lett.120,no.21,219901(2018)].

[3] S. Antusch, F. Cefala, S. Krippendorf, F. Muia, S. Orani, and F. Quevedo, *Oscillons from String Moduli*, *JHEP* **01** (2018) 083, [arXiv:1708.0892].

[4] S. Antusch, F. Cefala, and S. Orani, *What can we learn from the stochastic gravitational wave background produced by oscillons?*, *JCAP* **1803** (2018), no. 03 032, [arXiv:1712.0323].

[5] **Planck** , P. A. R. Ade et al., *Planck 2015 results. XIII. Cosmological parameters*, *Astron. Astrophys.* **594** (2016) A13, [arXiv:1502.0158].

[6] M. Green, M. Green, J. Schwarz, and E. Witten, *Superstring Theory: Volume 1, Introduction*. Cambridge Monographs on Mathematical Physics. Cambridge University Press, 1988.

[7] M. Gleiser, *Pseudostable bubbles*, *Phys. Rev.* **D49** (1994) 2978–2981, [hep-ph/9308279].

[8] E. J. Copeland, M. Gleiser, and H. R. Muller, *Oscillons: Resonant configurations during bubble collapse*, *Phys. Rev.* **D52** (1995) 1920–1933, [hep-ph/9503217].

[9] M. Gleiser and A. Sornborger, *Longlived localized field configurations in small lattices: Application to oscillons*, *Phys. Rev.* **E62** (2000) 1368–1374, [patt-sol/9909002].

[10] A. B. Adib, M. Gleiser, and C. A. S. Almeida, *Long lived oscillons from asymmetric bubbles: Existence and stability*, *Phys. Rev.* **D66** (2002) 085011, [hep-th/0203072].

[11] N. Graham and N. Stamatopoulos, *Unnatural Oscillon Lifetimes in an Expanding Background*, *Phys. Lett.* **B639** (2006) 541–545, [hep-th/0604134].

[12] E. Farhi, N. Graham, A. H. Guth, N. Iqbal, R. R. Rosales, and N. Stamatopoulos, *Emergence of Oscillons in an Expanding Background*, *Phys. Rev.* **D77** (2008) 085019, [arXiv:0712.3034].

[13] M. A. Amin, R. Easther, H. Finkel, R. Flauger, and M. P. Hertzberg, *Oscillons After Inflation*, *Phys. Rev. Lett.* **108** (2012) 241302, [arXiv:1106.3335].

[14] M. Gleiser and N. Graham, *Transition To Order After Hilltop Inflation*, *Phys. Rev.* **D89** (2014), no. 8 083502, [arXiv:1401.6225].

[15] G. D. Coughlan, W. Fischler, E. W. Kolb, S. Raby, and G. G. Ross, *Cosmological Problems for the Polonyi Potential*, *Phys. Lett.* **131B** (1983) 59–64.

[16] T. Banks, D. B. Kaplan, and A. E. Nelson, *Cosmological implications of dynamical supersymmetry breaking*, *Phys. Rev.* **D49** (1994) 779–787, [hep-ph/9308292].

[17] B. de Carlos, J. A. Casas, F. Quevedo, and E. Roulet, *Model independent properties and cosmological implications of the dilaton and moduli sectors of 4-d strings*, *Phys. Lett.* **B318** (1993) 447–456, [hep-ph/9308325].

[18] F. Quevedo, *Lectures on string/brane cosmology*, *Class. Quant. Grav.* **19** (2002) 5721–5779, [hep-th/0210292].

[19] **Virgo, LIGO Scientific** , B. P. Abbott et al., *Observation of Gravitational Waves from a Binary Black Hole Merger*, *Phys. Rev. Lett.* **116** (2016), no. 6 061102, [arXiv:1602.0383].

[20] S. Antusch and S. Orani, *Impact of other scalar fields on oscillons after hilltop inflation*, *JCAP* **1603** (2016), no. 03 026, [arXiv:1511.0233].

[21] S. Kachru, R. Kallosh, A. D. Linde, and S. P. Trivedi, *De Sitter vacua in string theory*, *Phys. Rev.* **D68** (2003) 046005, [hep-th/0301240].

[22] V. Balasubramanian, P. Berglund, J. P. Conlon, and F. Quevedo, *Systematics of moduli stabilisation in Calabi-Yau flux compactifications*, *JHEP* **03** (2005) 007, [hep-th/0502058].

[23] J. P. Conlon, F. Quevedo, and K. Suruliz, *Large-volume flux compactifications: Moduli spectrum and D3/D7 soft supersymmetry breaking*, *JHEP* **08** (2005) 007, [hep-th/0505076].

[24] V. Mukhanov, *Physical Foundations of Cosmology*. Cambridge University Press, Oxford, 2005.

[25] S. Weinberg, *Cosmology*. Oxford Univ. Press, Oxford, 2008.

[26] S. M. Carroll, *Spacetime and geometry: An introduction to general relativity*. 2004.

[27] C. W. Misner, K. S. Thorne, and J. A. Wheeler, *Gravitation*. W. H. Freeman, San Francisco, 1973.

[28] L. Lehner, *Numerical relativity: A Review*, *Class. Quant. Grav.* **18** (2001) R25–R86, [gr-qc/0106072].

[29] H. Stephani, D. Krämer, M. MacCallum, C. Hoenselaers, and E. Herlt, *Exact solutions of Einstein's field equations; 2nd ed.* Cambridge Univ. Press, Cambridge, 2003.

[30] D. W. Hogg, D. J. Eisenstein, M. R. Blanton, N. A. Bahcall, J. Brinkmann, J. E. Gunn, and D. P. Schneider, *Cosmic homogeneity demonstrated with luminous red galaxies*, *Astrophys. J.* **624** (2005) 54–58, [astro-ph/0411197].

[31] M. Scrimgeour et al., *The WiggleZ Dark Energy Survey: the transition to large-scale cosmic homogeneity*, *Mon. Not. Roy. Astron. Soc.* **425** (2012) 116–134, [arXiv:1205.6812].

[32] C. Marinoni, J. Bel, and A. Buzzi, *The Scale of Cosmic Isotropy*, *JCAP* **1210** (2012) 036, [arXiv:1205.3309].

[33] D. Alonso, A. I. Salvador, F. J. Sánchez, M. Bilicki, J. García-Bellido, and E. Sánchez, *Homogeneity and isotropy in the Two Micron All Sky Survey Photometric Redshift catalogue*, *Mon. Not. Roy. Astron. Soc.* **449** (2015), no. 1 670–684, [arXiv:1412.5151].

[34] K. K. S. Wu, O. Lahav, and M. J. Rees, *The large-scale smoothness of the Universe*, *Nature* **397** (1999) 225–230, [astro-ph/9804062]. [,19(1998)].

[35] C. A. Scharf, K. Jahoda, M. Treyer, O. Lahav, E. Boldt, and T. Piran, *The 2-10 kev xrb dipole and its cosmological implications*, *Astrophys. J.* **544** (2000) 49, [astro-ph/9908187].

[36] S. Gupta and T. D. Saini, *Direction Dependence in Supernova Data: Constraining Isotropy*, *Mon. Not. Roy. Astron. Soc.* **407** (2010) 651, [arXiv:1005.2868].

[37] H.-N. Lin, S. Wang, Z. Chang, and X. Li, *Testing the isotropy of the Universe by using the JLA compilation of type-Ia supernovae*, *Mon. Not. Roy. Astron. Soc.* **456** (2016), no. 2 1881–1885, [arXiv:1504.0342].

[38] **Planck** , P. A. R. Ade et al., *Planck 2015 results. XVI. Isotropy and statistics of the CMB*, *Astron. Astrophys.* **594** (2016) A16, [arXiv:1506.0713].

[39] R. Maartens, *Is the Universe homogeneous?*, *Phil. Trans. Roy. Soc. Lond.* **A369** (2011) 5115–5137, [arXiv:1104.1300].

[40] S. Weinberg, *Gravitation and Cosmology: Principles and Applications of the General Theory of Relativity*. Wiley, New York, NY, 1972.

[41] A. Friedman, *Über die krümmung des raumes*, *Zeitschrift für Physik* **10** (Dec, 1922) 377–386.

[42] A. Friedmann, *Über die möglichkeit einer welt mit konstanter negativer krümmung des raumes*, *Zeitschrift für Physik* **21** (Dec, 1924) 326–332.

[43] G. Lemaître, *Un Univers homogène de masse constante et de rayon croissant rendant compte de la vitesse radiale des nébuleuses extra-galactiques*, *Annales de la Société Scientifique de Bruxelles* **47** (1927) 49–59.

[44] H. P. Robertson, *Kinematics and World-Structure*, *Astrophys.J.* **82** (Nov., 1935) 284.

[45] H. P. Robertson, *Kinematics and World-Structure II.*, *Astrophys.J.* **83** (Apr., 1936) 187.

[46] H. P. Robertson, *Kinematics and World-Structure III.*, *Astrophys.J.* **83** (May, 1936) 257.

[47] A. G. Walker, *On Milne's Theory of World-Structure*, *Proceedings of the London Mathematical Society, (Series 2) volume 42, p. 90-127* **42** (1937) 90–127.

[48] A. Lewis and S. Bridle, *Cosmological parameters from CMB and other data: A Monte Carlo approach*, *Phys. Rev.* **D66** (2002) 103511, [astro-ph/0205436].

[49] A. Lewis, *Efficient sampling of fast and slow cosmological parameters*, *Phys. Rev.* **D87** (2013), no. 10 103529, [arXiv:1304.4473].

[50] B. Audren, J. Lesgourgues, K. Benabed, and S. Prunet, *Conservative Constraints on Early Cosmology: an illustration of the Monte Python cosmological parameter inference code*, *JCAP* **1302** (2013) 001, [arXiv:1210.7183].

[51] T. Brinckmann and J. Lesgourgues, *MontePython 3: boosted MCMC sampler and other features*, arXiv:1804.0726.

[52] A. Lewis, A. Challinor, and A. Lasenby, *Efficient computation of CMB anisotropies in closed FRW models*, *Astrophys. J.* **538** (2000) 473–476, [astro-ph/9911177].

[53] C. Howlett, A. Lewis, A. Hall, and A. Challinor, *CMB power spectrum parameter degeneracies in the era of precision cosmology*, *JCAP* **1204** (2012) 027, [arXiv:1201.3654].

[54] J. Lesgourgues, *The Cosmic Linear Anisotropy Solving System (CLASS) I: Overview*, arXiv:1104.2932.

[55] D. H. Lyth and A. R. Liddle, *The primordial density perturbation: Cosmology, inflation and the origin of structure*. 2009.

[56] J. Lesgourgues, *Cosmological Perturbations*, in *Proceedings, Theoretical Advanced Study Institute in Elementary Particle Physics: Searching for New Physics at Small and Large Scales (TASI 2012): Boulder, Colorado, June 4-29, 2012*, pp. 29–97, 2013. arXiv:1302.4640.

[57] F. Bernardeau, S. Colombi, E. Gaztanaga, and R. Scoccimarro, *Large scale structure of the universe and cosmological perturbation theory*, *Phys. Rept.* **367** (2002) 1–248, [astro-ph/0112551].

[58] J. Carlson, M. White, and N. Padmanabhan, *A critical look at cosmological perturbation theory techniques*, *Phys. Rev.* **D80** (2009) 043531, [arXiv:0905.0479].

[59] **Planck** , N. Aghanim et al., *Planck 2018 results. VI. Cosmological parameters*, arXiv:1807.0620.

[60] R. Barkana and A. Loeb, *In the beginning: The First sources of light and the reionization of the Universe*, *Phys. Rept.* **349** (2001) 125–238, [astro-ph/0010468].

[61] C. Heymans et al., *CFHTLenS: The Canada-France-Hawaii Telescope Lensing Survey*, *Mon. Not. Roy. Astron. Soc.* **427** (2012) 146, [arXiv:1210.0032].

[62] R. Mandelbaum, A. Slosar, T. Baldauf, U. Seljak, C. M. Hirata, R. Nakajima, R. Reyes, and R. E. Smith, *Cosmological parameter constraints from galaxy-galaxy lensing and galaxy clustering with the SDSS DR7*, *Mon. Not. Roy. Astron. Soc.* **432** (2013) 1544, [arXiv:1207.1120].

[63] B. A. Benson et al., *Cosmological Constraints from Sunyaev-Zel'dovich-Selected Clusters with X-ray Observations in the First 178 Square Degrees of the South Pole Telescope Survey*, *Astrophys. J.* **763** (2013) 147, [arXiv:1112.5435].

[64] M. Hasselfield et al., *The Atacama Cosmology Telescope: Sunyaev-Zel'dovich selected galaxyclusters at 148 GHz from three seasons of data*, *JCAP* **1307** (2013) 008, [arXiv:1301.0816].

[65] **Planck** , P. A. R. Ade et al., *Planck 2013 results. XX. Cosmology from Sunyaev?Zeldovich cluster counts*, *Astron. Astrophys.* **571** (2014) A20, [arXiv:1303.5080].

[66] **SDSS** , D. J. Eisenstein et al., *Detection of the Baryon Acoustic Peak in the Large-Scale Correlation Function of SDSS Luminous Red Galaxies*, *Astrophys. J.* **633** (2005) 560–574, [astro-ph/0501171].

[67] F. Beutler, C. Blake, M. Colless, D. H. Jones, L. Staveley-Smith, L. Campbell, Q. Parker, W. Saunders, and F. Watson, *The 6dF Galaxy Survey: Baryon Acoustic Oscillations and the Local Hubble Constant*, *Mon. Not. Roy. Astron. Soc.* **416** (2011) 3017–3032, [arXiv:1106.3366].

[68] **BOSS** , L. Anderson et al., *The clustering of galaxies in the SDSS-III Baryon Oscillation Spectroscopic Survey: baryon acoustic oscillations in the Data Releases 10 and 11 Galaxy samples*, *Mon. Not. Roy. Astron. Soc.* **441** (2014), no. 1 24–62, [arXiv:1312.4877].

[69] A. J. Ross, L. Samushia, C. Howlett, W. J. Percival, A. Burden, and M. Manera, *The clustering of the SDSS DR7 main Galaxy sample ? I. A 4 per cent distance measure at $z = 0.15$*, *Mon. Not. Roy. Astron. Soc.* **449** (2015), no. 1 835–847, [arXiv:1409.3242].

[70] **Supernova Cosmology Project** , M. Kowalski et al., *Improved Cosmological Constraints from New, Old and Combined Supernova Datasets*, *Astrophys. J.* **686** (2008) 749–778, [arXiv:0804.4142].

[71] **SNLS** , A. Conley et al., *Supernova Constraints and Systematic Uncertainties from the First 3 Years of the Supernova Legacy Survey*, *Astrophys. J. Suppl.* **192** (2011) 1, [arXiv:1104.1443].

[72] A. Rest et al., *Cosmological Constraints from Measurements of Type Ia Supernovae discovered during the first 1.5 yr of the Pan-STARRS1 Survey*, *Astrophys. J.* **795** (2014), no. 1 44, [arXiv:1310.3828].

[73] **SDSS** , M. Betoule et al., *Improved cosmological constraints from a joint analysis of the SDSS-II and SNLS supernova samples*, *Astron. Astrophys.* **568** (2014) A22, [arXiv:1401.4064].

[74] R. A. Alpher, H. Bethe, and G. Gamow, *The origin of chemical elements*, *Phys. Rev.* **73** (Apr, 1948) 803–804.

[75] D. N. Schramm and M. S. Turner, *Big-bang nucleosynthesis enters the precision era*, *Rev. Mod. Phys.* **70** (Jan, 1998) 303–318.

[76] B. D. Fields, *The primordial lithium problem*, *Ann. Rev. Nucl. Part. Sci.* **61** (2011) 47–68, [arXiv:1203.3551].

[77] B. D. Fields, P. Molaro, and S. Sarkar, *Big-Bang Nucleosynthesis*, *Chin. Phys.* **C38** (2014) 339–344, [arXiv:1412.1408].

[78] A. H. Guth, *The Inflationary Universe: A Possible Solution to the Horizon and Flatness Problems*, *Phys. Rev.* **D23** (1981) 347–356.

[79] A. D. Linde, *A New Inflationary Universe Scenario: A Possible Solution of the Horizon, Flatness, Homogeneity, Isotropy and Primordial Monopole Problems*, *Phys. Lett.* **108B** (1982) 389–393.

[80] A. Albrecht and P. J. Steinhardt, *Cosmology for Grand Unified Theories with Radiatively Induced Symmetry Breaking*, *Phys. Rev. Lett.* **48** (1982) 1220–1223.

[81] A. D. Linde, *Particle physics and inflationary cosmology*, vol. 5 of *Contemporary concepts in physics*. Harwood, Chur, Mar, 2005. Transl. from the Russian.

[82] A. R. Liddle and D. H. Lyth, *Cosmological Inflation and Large-Scale Structure*. Cambridge Univ. Press, Cambridge, 2000.

[83] D. Baumann, *Inflation*, in *Physics of the large and the small, TASI 09, proceedings of the Theoretical Advanced Study Institute in Elementary Particle Physics, Boulder, Colorado, USA, 1-26 June 2009*, pp. 523–686, 2011. arXiv:0907.5424.

[84] D. Bailin and A. Love, *Supersymmetric gauge field theory and string theory*. Graduate student series in physics. IOP, Bristol, 1994.

[85] M. Yu. Khlopov and A. D. Linde, *Is It Easy to Save the Gravitino?*, *Phys. Lett.* **138B** (1984) 265–268.

[86] J. R. Ellis, D. V. Nanopoulos, and S. Sarkar, *The Cosmology of Decaying Gravitinos*, *Nucl. Phys.* **B259** (1985) 175–188.

[87] M. Kawasaki and T. Moroi, *Gravitino production in the inflationary universe and the effects on big bang nucleosynthesis*, *Prog. Theor. Phys.* **93** (1995) 879–900, [hep-ph/9403364].

[88] A. Vilenkin and E. P. S. Shellard, *Cosmic Strings and Other Topological Defects*. Cambridge University Press, 2000.

[89] G. 't Hooft, *Magnetic Monopoles in Unified Gauge Theories*, *Nucl. Phys.* **B79** (1974) 276–284. [,291(1974)].

[90] T. W. B. Kibble, *Topology of Cosmic Domains and Strings*, *J. Phys.* **A9** (1976) 1387–1398.

[91] Ya. B. Zeldovich and M. Yu. Khlopov, *On the Concentration of Relic Magnetic Monopoles in the Universe*, *Phys. Lett.* **79B** (1978) 239–241.

[92] J. Preskill, *Cosmological Production of Superheavy Magnetic Monopoles*, *Phys. Rev. Lett.* **43** (1979) 1365.

[93] J. R. Ellis, D. V. Nanopoulos, and M. Quiros, *On the Axion, Dilaton, Polonyi, Gravitino and Shadow Matter Problems in Supergravity and Superstring Models*, *Phys. Lett.* **B174** (1986) 176–182.

[94] D. Lindley, *Cosmological Constraints on the Lifetime of Massive Particles*, *Astrophys. J.* **294** (1985) 1–8.

[95] S. Dimopoulos, R. Esmailzadeh, L. J. Hall, and G. D. Starkman, *Limits on Late Decaying Particles From Nucleosynthesis*, *Nucl. Phys.* **B311** (1989) 699–718.

[96] J. R. Ellis, G. B. Gelmini, J. L. Lopez, D. V. Nanopoulos, and S. Sarkar, *Astrophysical constraints on massive unstable neutral relic particles*, *Nucl. Phys.* **B373** (1992) 399–437.

[97] **Planck** , P. A. R. Ade et al., *Planck 2015 results. XX. Constraints on inflation*, *Astron. Astrophys.* **594** (2016) A20, [arXiv:1502.0211].

[98] P. J. Steinhardt and M. S. Turner, *A Prescription for Successful New Inflation*, *Phys. Rev.* **D29** (1984) 2162–2171.

[99] A. R. Liddle, P. Parsons, and J. D. Barrow, *Formalizing the slow roll approximation in inflation*, *Phys. Rev.* **D50** (1994) 7222–7232, [astro-ph/9408015].

[100] A. A. Starobinsky, *A New Type of Isotropic Cosmological Models Without Singularity*, *Phys. Lett.* **B91** (1980) 99–102. [,771(1980)].

[101] A. D. Sakharov, *The Initial Stage of an Expanding Universe and the Appearance of a Nonuniform Distribution of Matter*, *Soviet Journal of Experimental and Theoretical Physics* **22** (Jan., 1966) 241.

[102] V. F. Mukhanov and G. V. Chibisov, *Quantum Fluctuations and a Nonsingular Universe*, *JETP Lett.* **33** (1981) 532–535. [Pisma Zh. Eksp. Teor. Fiz.33,549(1981)].

[103] A. H. Guth and S. Y. Pi, *Fluctuations in the New Inflationary Universe*, *Phys. Rev. Lett.* **49** (1982) 1110–1113.

[104] A. A. Starobinsky, *Dynamics of Phase Transition in the New Inflationary Universe Scenario and Generation of Perturbations*, *Phys. Lett.* **117B** (1982) 175–178.

[105] S. W. Hawking, *The Development of Irregularities in a Single Bubble Inflationary Universe*, *Phys. Lett.* **115B** (1982) 295.

[106] J. M. Bardeen, P. J. Steinhardt, and M. S. Turner, *Spontaneous Creation of Almost Scale - Free Density Perturbations in an Inflationary Universe*, *Phys. Rev.* **D28** (1983) 679.

[107] V. F. Mukhanov, *Gravitational Instability of the Universe Filled with a Scalar Field*, *JETP Lett.* **41** (1985) 493–496. [Pisma Zh. Eksp. Teor. Fiz.41,402(1985)].

[108] V. F. Mukhanov, *Quantum Theory of Gauge Invariant Cosmological Perturbations*, *Sov. Phys. JETP* **67** (1988) 1297–1302. [Zh. Eksp. Teor. Fiz.94N7,1(1988)].

[109] V. F. Mukhanov, H. A. Feldman, and R. H. Brandenberger, *Theory of cosmological perturbations. Part 1. Classical perturbations. Part 2. Quantum theory of perturbations. Part 3. Extensions*, *Phys. Rept.* **215** (1992) 203–333.

[110] A. Riotto, *Inflation and the theory of cosmological perturbations*, *ICTP Lect. Notes Ser.* **14** (2003) 317–413, [hep-ph/0210162].

[111] D. Langlois, *Lectures on inflation and cosmological perturbations*, *Lect. Notes Phys.* **800** (2010) 1–57, [arXiv:1001.5259].

[112] N. D. Birrell and P. C. W. Davies, *Quantum Fields in Curved Space*. Cambridge Monographs on Mathematical Physics. Cambridge Univ. Press, Cambridge, UK, 1984.

[113] V. Mukhanov and S. Winitzki, *Introduction to quantum effects in gravity*. Cambridge University Press, 2007.

[114] T. S. Bunch and P. C. W. Davies, *Quantum Field Theory in de Sitter Space: Renormalization by Point Splitting*, *Proc. Roy. Soc. Lond.* **A360** (1978) 117–134.

[115] R. H. Brandenberger, *Lectures on the theory of cosmological perturbations*, *Lect. Notes Phys.* **646** (2004) 127–167, [hep-th/0306071].

[116] R. Durrer, *The Cosmic Microwave Background*. Cambridge University Press, Cambridge, 2008.

[117] E. Lifshitz, *Republication of: On the gravitational stability of the expanding universe*, *J. Phys.(USSR)* **10** (1946) 116. [Gen. Rel. Grav.49,no.2,18(2017)].

[118] E. M. Lifshitz and I. M. Khalatnikov, *Investigations in relativistic cosmology*, *Adv. Phys.* **12** (1963) 185–249.

[119] J. M. Bardeen, *Gauge Invariant Cosmological Perturbations*, *Phys. Rev.* **D22** (1980) 1882–1905.

[120] H. Kodama and M. Sasaki, *Cosmological Perturbation Theory*, *Prog. Theor. Phys. Suppl.* **78** (1984) 1–166.

[121] V. Acquaviva, N. Bartolo, S. Matarrese, and A. Riotto, *Second order cosmological perturbations from inflation*, *Nucl. Phys.* **B667** (2003) 119–148, [astro-ph/0209156].

[122] J. M. Maldacena, *Non-Gaussian features of primordial fluctuations in single field inflationary models*, *JHEP* **05** (2003) 013, [astro-ph/0210603].

[123] S. Dodelson and E. Stewart, *Scale dependent spectral index in slow roll inflation*, *Phys. Rev.* **D65** (2002) 101301, [astro-ph/0109354].

[124] E. D. Stewart, *The Spectrum of density perturbations produced during inflation to leading order in a general slow roll approximation*, *Phys. Rev.* **D65** (2002) 103508, [astro-ph/0110322].

[125] D. H. Lyth, *What would we learn by detecting a gravitational wave signal in the cosmic microwave background anisotropy?*, *Phys. Rev. Lett.* **78** (1997) 1861–1863, [hep-ph/9606387].

[126] **BICEP2, Keck Array** , P. A. R. Ade et al., *Improved Constraints on Cosmology and Foregrounds from BICEP2 and Keck Array Cosmic Microwave Background Data with Inclusion of 95 GHz Band*, *Phys. Rev. Lett.* **116** (2016) 031302, [arXiv:1510.0921].

[127] S. Antusch and D. Nolde, *BICEP2 implications for single-field slow-roll inflation revisited*, *JCAP* **1405** (2014) 035, [arXiv:1404.1821].

[128] D. H. Lyth and A. Riotto, *Particle physics models of inflation and the cosmological density perturbation*, *Phys. Rept.* **314** (1999) 1–146, [hep-ph/9807278].

[129] A. Mazumdar and J. Rocher, *Particle physics models of inflation and curvaton scenarios*, *Phys. Rept.* **497** (2011) 85–215, [arXiv:1001.0993].

[130] J. Martin, C. Ringeval, and V. Vennin, *Encyclopædia Inflationaris*, *Phys. Dark Univ.* **5-6** (2014) 75–235, [arXiv:1303.3787].

[131] A. D. Linde, *Chaotic Inflation*, *Phys. Lett.* **129B** (1983) 177–181.

[132] K. I. Izawa and T. Yanagida, *Natural new inflation in broken supergravity*, *Phys. Lett.* **B393** (1997) 331–336, [hep-ph/9608359].

[133] K. I. Izawa, M. Kawasaki, and T. Yanagida, *Dynamical tuning of the initial condition for new inflation in supergravity*, *Phys. Lett.* **B411** (1997) 249–255, [hep-ph/9707201].

[134] V. N. Senoguz and Q. Shafi, *New inflation, preinflation, and leptogenesis*, *Phys. Lett.* **B596** (2004) 8–15, [hep-ph/0403294].

[135] S. Antusch, D. Nolde, and S. Orani, *Hilltop inflation with preinflation from coupling to matter fields*, *JCAP* **1405** (2014) 034, [arXiv:1402.5328].

[136] **Planck** , Y. Akrami et al., *Planck 2018 results. X. Constraints on inflation*, arXiv:1807.0621.

[137] P. Creminelli, D. L. López Nacir, M. Simonovi?, G. Trevisan, and M. Zaldarriaga, *Detecting Primordial B-Modes after Planck*, *JCAP* **1511** (2015), no. 11 031, [arXiv:1502.0198].

[138] R. Allahverdi, R. Brandenberger, F.-Y. Cyr-Racine, and A. Mazumdar, *Reheating in Inflationary Cosmology: Theory and Applications*, *Ann. Rev. Nucl. Part. Sci.* **60** (2010) 27–51, [arXiv:1001.2600].

[139] M. A. Amin, M. P. Hertzberg, D. I. Kaiser, and J. Karouby, *Nonperturbative Dynamics Of Reheating After Inflation: A Review*, *Int. J. Mod. Phys.* **D24** (2014) 1530003, [arXiv:1410.3808].

[140] M. E. Peskin and D. V. Schroeder, *An Introduction to quantum field theory*. Addison-Wesley, Reading, USA, 1995.

[141] M. Kawasaki, K. Kohri, and T. Moroi, *Big-Bang nucleosynthesis and hadronic decay of long-lived massive particles*, *Phys. Rev.* **D71** (2005) 083502, [astro-ph/0408426].

[142] M. Gleiser and R. O. Ramos, *Microphysical approach to nonequilibrium dynamics of quantum fields*, *Phys. Rev.* **D50** (1994) 2441–2455, [hep-ph/9311278].

[143] L. Kofman, A. D. Linde, and A. A. Starobinsky, *Reheating after inflation*, *Phys. Rev. Lett.* **73** (1994) 3195–3198, [hep-th/9405187].

[144] J. H. Traschen and R. H. Brandenberger, *Particle Production During Out-of-equilibrium Phase Transitions*, *Phys. Rev.* **D42** (1990) 2491–2504.

[145] A. D. Dolgov and D. P. Kirilova, *ON PARTICLE CREATION BY A TIME DEPENDENT SCALAR FIELD*, *Sov. J. Nucl. Phys.* **51** (1990) 172–177. [Yad. Fiz.51,273(1990)].

[146] Y. Shtanov, J. H. Traschen, and R. H. Brandenberger, *Universe reheating after inflation*, *Phys. Rev.* **D51** (1995) 5438–5455, [hep-ph/9407247].

[147] L. Kofman, A. D. Linde, and A. A. Starobinsky, *Towards the theory of reheating after inflation*, *Phys. Rev.* **D56** (1997) 3258–3295, [hep-ph/9704452].

[148] G. N. Felder, J. Garcia-Bellido, P. B. Greene, L. Kofman, A. D. Linde, and I. Tkachev, *Dynamics of symmetry breaking and tachyonic preheating*, *Phys. Rev. Lett.* **87** (2001) 011601, [hep-ph/0012142].

[149] G. N. Felder, L. Kofman, and A. D. Linde, *Tachyonic instability and dynamics of spontaneous symmetry breaking*, *Phys. Rev.* **D64** (2001) 123517, [hep-th/0106179].

[150] P. Brax, J.-F. Dufaux, and S. Mariadassou, *Preheating after Small-Field Inflation*, *Phys. Rev.* **D83** (2011) 103510, [arXiv:1012.4656].

[151] S. Yu. Khlebnikov and I. I. Tkachev, *Resonant decay of Bose condensates*, *Phys. Rev. Lett.* **79** (1997) 1607–1610, [hep-ph/9610477].

[152] G. N. Felder and L. Kofman, *The Development of equilibrium after preheating*, *Phys. Rev.* **D63** (2001) 103503, [hep-ph/0011160].

[153] L. Kofman, *Preheating after inflation*, in *Particle physics and the early universe. Proceedings, 1st International Workshop, COSMO-97, Ambleside, UK, September 15-19, 1997*, pp. 312–321, 1997. astro-ph/9802221.

[154] M. Desroche, G. N. Felder, J. M. Kratochvil, and A. D. Linde, *Preheating in new inflation*, *Phys. Rev.* **D71** (2005) 103516, [hep-th/0501080].

[155] S. R. Coleman, *Q Balls*, *Nucl. Phys.* **B262** (1985) 263. [Erratum: Nucl. Phys.B269,744(1986)].

[156] T. D. Lee and Y. Pang, *Nontopological solitons*, *Phys. Rept.* **221** (1992) 251–350. [,169(1991)].

[157] S. Khlebnikov, L. Kofman, A. D. Linde, and I. Tkachev, *First order nonthermal phase transition after preheating*, *Phys. Rev. Lett.* **81** (1998) 2012–2015, [hep-ph/9804425].

[158] J. Garcia-Bellido, A. D. Linde, and D. Wands, *Density perturbations and black hole formation in hybrid inflation*, *Phys. Rev.* **D54** (1996) 6040–6058, [astro-ph/9605094].

[159] A. M. Green and K. A. Malik, *Primordial black hole production due to preheating*, *Phys. Rev.* **D64** (2001) 021301, [hep-ph/0008113].

[160] B. A. Bassett and S. Tsujikawa, *Inflationary preheating and primordial black holes*, *Phys. Rev.* **D63** (2001) 123503, [hep-ph/0008328].

[161] M. Khlopov, B. A. Malomed, and I. B. Zeldovich, *Gravitational instability of scalar fields and formation of primordial black holes*, *Mon. Not. Roy. Astron. Soc.* **215** (1985) 575–589.

[162] S. Y. Khlebnikov and I. I. Tkachev, *Relic gravitational waves produced after preheating*, *Phys. Rev.* **D56** (1997) 653–660, [hep-ph/9701423].

[163] J. R. Ellis, K. Enqvist, D. V. Nanopoulos, and K. A. Olive, *Inflationary Fluctuations, Entropy Generation and Baryogenesis*, *Phys. Lett.* **B191** (1987) 343–348.

[164] S. Dodelson, *The Postinflationary Era and Baryogenesis*, *Phys. Rev.* **D37** (1988) 2059.

[165] K. Enqvist and K. J. Eskola, *Thermalization in the Early Universe*, *Mod. Phys. Lett.* **A5** (1990) 1919–1926.

[166] R. Allahverdi, *Thermalization after inflation and reheating temperature*, *Phys. Rev.* **D62** (2000) 063509, [hep-ph/0004035].

[167] A. Mazumdar and B. Zaldivar, *Quantifying the reheating temperature of the universe*, *Nucl. Phys.* **B886** (2014) 312–327, [arXiv:1310.5143].

[168] R. Micha and I. I. Tkachev, *Relativistic turbulence: A Long way from preheating to equilibrium*, *Phys. Rev. Lett.* **90** (2003) 121301, [hep-ph/0210202].

[169] R. Micha and I. I. Tkachev, *Turbulent thermalization*, *Phys. Rev.* **D70** (2004) 043538, [hep-ph/0403101].

[170] W. Magnus and S. Winkler, *Hill's equation*. Dover books on advanced mathematics. Dover Publications, 1979.

[171] S. Yu. Khlebnikov and I. I. Tkachev, *Classical decay of inflaton*, *Phys. Rev. Lett.* **77** (1996) 219–222, [hep-ph/9603378].

[172] A. D. Linde, *Hybrid inflation*, *Phys. Rev.* **D49** (1994) 748–754, [astro-ph/9307002].

[173] J. F. Dufaux, G. N. Felder, L. Kofman, M. Peloso, and D. Podolsky, *Preheating with trilinear interactions: Tachyonic resonance*, *JCAP* **0607** (2006) 006, [hep-ph/0602144].

[174] A. A. Abolhasani, H. Firouzjahi, and M. M. Sheikh-Jabbari, *Tachyonic Resonance Preheating in Expanding Universe*, *Phys. Rev.* **D81** (2010) 043524, [arXiv:0912.1021].

[175] M. Cicoli and F. Quevedo, *String moduli inflation: An overview*, *Class. Quant. Grav.* **28** (2011) 204001, [arXiv:1108.2659].

[176] C. P. Burgess, M. Cicoli, and F. Quevedo, *String Inflation After Planck 2013*, *JCAP* **1311** (2013) 003, [arXiv:1306.3512].

[177] D. Baumann and L. McAllister, *Inflation and String Theory*. Cambridge Monographs on Mathematical Physics. Cambridge University Press, 2015.

[178] M. Dine, W. Fischler, and D. Nemeschansky, *Solution of the Entropy Crisis of Supersymmetric Theories*, *Phys. Lett.* **136B** (1984) 169–174.

[179] A. S. Goncharov, A. D. Linde, and M. I. Vysotsky, *COSMOLOGICAL PROBLEMS FOR SPONTANEOUSLY BROKEN SUPERGRAVITY*, *Phys. Lett.* **147B** (1984) 279–283.

[180] G. D. Coughlan, R. Holman, P. Ramond, and G. G. Ross, *Supersymmetry and the Entropy Crisis*, *Phys. Lett.* **140B** (1984) 44–48.

[181] M. Dine, L. Randall, and S. D. Thomas, *Supersymmetry breaking in the early universe*, *Phys. Rev. Lett.* **75** (1995) 398–401, [hep-ph/9503303].

[182] M. Dine, L. Randall, and S. D. Thomas, *Baryogenesis from flat directions of the supersymmetric standard model*, *Nucl. Phys.* **B458** (1996) 291–326, [hep-ph/9507453].

[183] K. Das, K. Dutta, and A. Maharana, *Inflationary Predictions and Moduli Masses*, *Phys. Lett.* **B751** (2015) 195–200, [arXiv:1506.0574].

[184] N. Barnaby, J. R. Bond, Z. Huang, and L. Kofman, *Preheating After Modular Inflation*, *JCAP* **0912** (2009) 021, [arXiv:0909.0503].

[185] M. P. Hertzberg, *Quantum Radiation of Oscillons*, *Phys. Rev.* **D82** (2010) 045022, [arXiv:1003.3459].

[186] H. Segur and M. D. Kruskal, *Nonexistence of Small Amplitude Breather Solutions in ϕ^4 Theory*, *Phys. Rev. Lett.* **58** (1987) 747–750.

[187] G. Fodor, P. Forgacs, Z. Horvath, and M. Mezei, *Radiation of scalar oscillons in 2 and 3 dimensions*, *Phys. Lett.* **B674** (2009) 319–324, [arXiv:0903.0953].

[188] M. Gleiser and D. Sicilia, *A General Theory of Oscillon Dynamics*, *Phys. Rev.* **D80** (2009) 125037, [arXiv:0910.5922].

[189] M. A. Amin and D. Shirokoff, *Flat-top oscillons in an expanding universe*, *Phys. Rev.* **D81** (2010) 085045, [arXiv:1002.3380].

[190] P. M. Saffin, P. Tognarelli, and A. Tranberg, *Oscillon Lifetime in the Presence of Quantum Fluctuations*, *JHEP* **08** (2014) 125, [arXiv:1401.6168].

[191] K. Mukaida, M. Takimoto, and M. Yamada, *On Longevity of I-ball/Oscillon*, *JHEP* **03** (2017) 122, [arXiv:1612.0775].

[192] E. J. Copeland, S. Pascoli, and A. Rajantie, *Dynamics of tachyonic preheating after hybrid inflation*, *Phys. Rev.* **D65** (2002) 103517, [hep-ph/0202031].

[193] M. Broadhead and J. McDonald, *Simulations of the end of supersymmetric hybrid inflation and non-topological soliton formation*, *Phys. Rev.* **D72** (2005) 043519, [hep-ph/0503081].

[194] S. Antusch, D. Nolde, and S. Orani, *Hill crossing during preheating after hilltop inflation*, *JCAP* **1506** (2015), no. 06 009, [arXiv:1503.0607].

[195] K. D. Lozanov and M. A. Amin, *Self-resonance after inflation: oscillons, transients and radiation domination*, *Phys. Rev.* **D97** (2018), no. 2 023533, [arXiv:1710.0685].

[196] F. Hasegawa and J.-P. Hong, *Inflaton fragmentation in E-models of cosmological α-attractors*, *Phys. Rev.* **D97** (2018), no. 8 083514, [arXiv:1710.0748].

[197] E. Farhi, N. Graham, V. Khemani, R. Markov, and R. Rosales, *An Oscillon in the SU(2) gauged Higgs model*, *Phys. Rev.* **D72** (2005) 101701, [hep-th/0505273].

[198] G. Fodor, P. Forgacs, P. Grandclement, and I. Racz, *Oscillons and Quasi-breathers in the phi**4 Klein-Gordon model*, *Phys. Rev.* **D74** (2006) 124003, [hep-th/0609023].

[199] M. Gleiser and J. Thorarinson, *A Phase transition in U(1) configuration space: Oscillons as remnants of vortex-antivortex annihilation*, *Phys. Rev.* **D76** (2007) 041701, [hep-th/0701294].

[200] V. Achilleos, F. K. Diakonos, D. J. Frantzeskakis, G. C. Katsimiga, X. N. Maintas, E. Manousakis, C. E. Tsagkarakis, and A. Tsapalis, *Oscillons and oscillating kinks in the Abelian-Higgs model*, *Phys. Rev.* **D88** (2013) 045015, [arXiv:1306.3868].

[201] M. A. Amin, R. Easther, and H. Finkel, *Inflaton Fragmentation and Oscillon Formation in Three Dimensions*, *JCAP* **1012** (2010) 001, [arXiv:1009.2505].

[202] M. A. Amin, *K-oscillons: Oscillons with noncanonical kinetic terms*, *Phys. Rev.* **D87** (2013), no. 12 123505, [arXiv:1303.1102].

[203] S. Kasuya and M. Kawasaki, *Q ball formation: Obstacle to Affleck-Dine baryogenesis in the gauge mediated SUSY breaking?*, *Phys. Rev.* **D64** (2001) 123515, [hep-ph/0106119].

[204] K. D. Lozanov and M. A. Amin, *End of inflation, oscillons, and matter-antimatter asymmetry*, *Phys. Rev.* **D90** (2014), no. 8 083528, [arXiv:1408.1811].

[205] S.-Y. Zhou, E. J. Copeland, R. Easther, H. Finkel, Z.-G. Mou, and P. M. Saffin, *Gravitational Waves from Oscillon Preheating*, *JHEP* **10** (2013) 026, [arXiv:1304.6094].

[206] E. Silverstein and A. Westphal, *Monodromy in the CMB: Gravity Waves and String Inflation*, *Phys. Rev.* **D78** (2008) 106003, [arXiv:0803.3085].

[207] L. McAllister, E. Silverstein, and A. Westphal, *Gravity Waves and Linear Inflation from Axion Monodromy*, *Phys. Rev.* **D82** (2010) 046003, [arXiv:0808.0706].

[208] J. Liu, Z.-K. Guo, R.-G. Cai, and G. Shiu, *Gravitational Waves from Oscillons with Cuspy Potentials*, *Phys. Rev. Lett.* **120** (2018), no. 3 031301, [arXiv:1707.0984].

[209] A. R. Liddle and S. M. Leach, *How long before the end of inflation were observable perturbations produced?*, *Phys. Rev.* **D68** (2003) 103503, [astro-ph/0305263].

[210] J. Martin and C. Ringeval, *First CMB Constraints on the Inflationary Reheating Temperature*, *Phys. Rev.* **D82** (2010) 023511, [arXiv:1004.5525].

[211] R. Easther and E. A. Lim, *Stochastic gravitational wave production after inflation*, *JCAP* **0604** (2006) 010, [astro-ph/0601617].

[212] R. Easther, J. T. Giblin, Jr., and E. A. Lim, *Gravitational Wave Production At The End Of Inflation*, *Phys. Rev. Lett.* **99** (2007) 221301, [astro-ph/0612294].

[213] J. Garcia-Bellido and D. G. Figueroa, *A stochastic background of gravitational waves from hybrid preheating*, *Phys. Rev. Lett.* **98** (2007) 061302, [astro-ph/0701014].

[214] J. F. Dufaux, A. Bergman, G. N. Felder, L. Kofman, and J.-P. Uzan, *Theory and Numerics of Gravitational Waves from Preheating after Inflation*, *Phys. Rev.* **D76** (2007) 123517, [arXiv:0707.0875].

[215] D. G. Figueroa and T. Meriniemi, *Stochastic Background of Gravitational Waves from Fermions – Theory and Applications*, *JHEP* **10** (2013) 101, [arXiv:1306.6911].

[216] D. G. Figueroa, *A gravitational wave background from the decay of the standard model Higgs after inflation*, *JHEP* **11** (2014) 145, [arXiv:1402.1345].

[217] D. G. Figueroa, J. García-Bellido, and F. Torrentí, *Gravitational wave production from the decay of the standard model Higgs field after inflation*, *Phys. Rev.* **D93** (2016), no. 10 103521, [arXiv:1602.0308].

[218] D. G. Figueroa and F. Torrenti, *Gravitational wave production from preheating: parameter dependence*, *JCAP* **1710** (2017), no. 10 057, [arXiv:1707.0453].

[219] **LIGO Scientific** , B. P. Abbott et al., *LIGO: The Laser interferometer gravitational-wave observatory*, *Rept. Prog. Phys.* **72** (2009) 076901, [arXiv:0711.3041].

[220] M. Punturo et al., *The Einstein Telescope: A third-generation gravitational wave observatory*, *Class. Quant. Grav.* **27** (2010) 194002.

[221] S. Kawamura et al., *The Japanese space gravitational wave antenna: DECIGO*, *Class. Quant. Grav.* **28** (2011) 094011.

[222] P. Amaro-Seoane et al., *eLISA/NGO: Astrophysics and cosmology in the gravitational-wave millihertz regime*, *GW Notes* **6** (2013) 4–110, [arXiv:1201.3621].

[223] **VIRGO** , F. Acernese et al., *Advanced Virgo: a second-generation interferometric gravitational wave detector*, *Class. Quant. Grav.* **32** (2015), no. 2 024001, [arXiv:1408.3978].

[224] J. Garcia-Bellido, D. G. Figueroa, and A. Sastre, *A Gravitational Wave Background from Reheating after Hybrid Inflation*, *Phys. Rev.* **D77** (2008) 043517, [arXiv:0707.0839].

[225] J.-F. Dufaux, D. G. Figueroa, and J. Garcia-Bellido, *Gravitational Waves from Abelian Gauge Fields and Cosmic Strings at Preheating*, *Phys. Rev.* **D82** (2010) 083518, [arXiv:1006.0217].

[226] M. Bastero-Gil, J. Macias-Perez, and D. Santos, *Non-linear metric perturbation enhancement of primordial gravitational waves*, *Phys. Rev. Lett.* **105** (2010) 081301, [arXiv:1005.4054].

[227] E. E. Flanagan and S. A. Hughes, *The Basics of gravitational wave theory*, *New J. Phys.* **7** (2005) 204, [gr-qc/0501041].

[228] R. A. Isaacson, *Gravitational Radiation in the Limit of High Frequency. I. The Linear Approximation and Geometrical Optics*, *Phys. Rev.* **166** (1967) 1263–1271.

[229] R. A. Isaacson, *Gravitational Radiation in the Limit of High Frequency. II. Nonlinear Terms and the Ef fective Stress Tensor*, *Phys. Rev.* **166** (1968) 1272–1279.

[230] G. D. Birkhoff and R. E. Langer, *Relativity and modern physics*. 1923.

[231] M. Fukugita and T. Yanagida, *Baryogenesis Without Grand Unification*, *Phys. Lett.* **B174** (1986) 45–47.

[232] V. A. Kuzmin, V. A. Rubakov, and M. E. Shaposhnikov, *On the Anomalous Electroweak Baryon Number Nonconservation in the Early Universe*, *Phys. Lett.* **155B** (1985) 36.

[233] M. A. Luty, *Baryogenesis via leptogenesis*, *Phys. Rev.* **D45** (1992) 455–465.

[234] T. Asaka, K. Hamaguchi, M. Kawasaki, and T. Yanagida, *Leptogenesis in inflaton decay*, *Phys. Lett.* **B464** (1999) 12–18, [hep-ph/9906366].

[235] S. P. Martin, *A Supersymmetry primer*, hep-ph/9709356. [Adv. Ser. Direct. High Energy Phys.18,1(1998)].

[236] S. Antusch, M. Bastero-Gil, K. Dutta, S. F. King, and P. M. Kostka, *Solving the eta-Problem in Hybrid Inflation with Heisenberg Symmetry and Stabilized Modulus*, *JCAP* **0901** (2009) 040, [arXiv:0808.2425].

[237] D. Nolde, *Effects of the imaginary inflaton component in supergravity new inflation*, *JCAP* **1311** (2013) 028, [arXiv:1310.0820].

[238] E. J. Copeland, A. R. Liddle, D. H. Lyth, E. D. Stewart, and D. Wands, *False vacuum inflation with Einstein gravity*, *Phys. Rev.* **D49** (1994) 6410–6433, [astro-ph/9401011].

[239] E. D. Stewart, *Inflation, supergravity and superstrings*, *Phys. Rev.* **D51** (1995) 6847–6853, [hep-ph/9405389].

[240] M. K. Gaillard, H. Murayama, and K. A. Olive, *Preserving flat directions during inflation*, *Phys. Lett.* **B355** (1995) 71–77, [hep-ph/9504307].

[241] S. Antusch, M. Bastero-Gil, K. Dutta, S. F. King, and P. M. Kostka, *Chaotic Inflation in Supergravity with Heisenberg Symmetry*, *Phys. Lett.* **B679** (2009) 428–432, [arXiv:0905.0905].

[242] S. Antusch, M. Bastero-Gil, J. P. Baumann, K. Dutta, S. F. King, and P. M. Kostka, *Gauge Non-Singlet Inflation in SUSY GUTs*, *JHEP* **08** (2010) 100, [arXiv:1003.3233].

[243] S. Antusch, K. Dutta, J. Erdmenger, and S. Halter, *Towards Matter Inflation in Heterotic String Theory*, *JHEP* **04** (2011) 065, [arXiv:1102.0093].

[244] M. Kawasaki, M. Yamaguchi, and T. Yanagida, *Natural chaotic inflation in supergravity*, *Phys. Rev. Lett.* **85** (2000) 3572–3575, [hep-ph/0004243].

[245] S. Antusch and F. Cefalà, *SUGRA New Inflation with Heisenberg Symmetry*, *JCAP* **1310** (2013) 055, [arXiv:1306.6825].

[246] S. Antusch, S. F. King, M. Malinsky, L. Velasco-Sevilla, and I. Zavala, *Flavon Inflation*, *Phys. Lett.* **B666** (2008) 176–180, [arXiv:0805.0325].

[247] M. Yamaguchi and J. Yokoyama, *Smooth hybrid inflation in supergravity with a running spectral index and early star formation*, *Phys. Rev.* **D70** (2004) 023513, [hep-ph/0402282].

[248] M. A. Amin, J. Braden, E. J. Copeland, J. T. Giblin, C. Solorio, Z. J. Weiner, and S.-Y. Zhou, *Gravitational waves from asymmetric oscillon dynamics?*, arXiv:1803.0804.

[249] S. Antusch and K. Marschall, *Non-thermal Leptogenesis after Majoron Hilltop Inflation*, *JCAP* **1805** (2018), no. 05 015, [arXiv:1802.0564].

[250] M. Cicoli, K. Dutta, A. Maharana, and F. Quevedo, *Moduli Vacuum Misalignment and Precise Predictions in String Inflation*, *JCAP* **1608** (2016), no. 08 006, [arXiv:1604.0851].

[251] N. Shuhmaher and R. Brandenberger, *Non-perturbative instabilities as a solution of the cosmological moduli problem*, *Phys. Rev.* **D73** (2006) 043519, [hep-th/0507103].

[252] M. R. Douglas and S. Kachru, *Flux compactification*, *Rev. Mod. Phys.* **79** (2007) 733–796, [hep-th/0610102].

[253] S. B. Giddings, S. Kachru, and J. Polchinski, *Hierarchies from fluxes in string compactifications*, *Phys. Rev.* **D66** (2002) 106006, [hep-th/0105097].

[254] S. Antusch and F. Cefala, "Animations of oscillons from string moduli." https://particlesandcosmology.unibas.ch/en/downloads/oscillons-from-string-moduli-movies.html, 2017.

[255] M. Cicoli, C. P. Burgess, and F. Quevedo, *Fibre Inflation: Observable Gravity Waves from IIB String Compactifications*, *JCAP* **0903** (2009) 013, [arXiv:0808.0691].

[256] C. P. Burgess, M. Cicoli, S. de Alwis, and F. Quevedo, *Robust Inflation from Fibrous Strings*, *JCAP* **1605** (2016), no. 05 032, [arXiv:1603.0678].

[257] É. Mathieu, *Mémoire sur le mouvement vibratoire d'une membrane de forme elliptique.*, *Journal de Mathématiques Pures et Appliquées* **13** (1868) 137–203.

[258] N. McLachlan, *Theory and application of Mathieu functions*. Clarendon Press, 1947.

[259] C.-T. Chen, *Linear System Theory and Design*. Oxford University Press, Inc., New York, NY, USA, 3rd ed., 1998.

[260] G. N. Felder and I. Tkachev, *LATTICEEASY: A Program for lattice simulations of scalar fields in an expanding universe*, *Comput. Phys. Commun.* **178** (2008) 929–932, [hep-ph/0011159].

[261] G. N. Felder and I. Tkachev, "LatticeEasy documentation." http://www.felderbooks.com/latticeeasy/download/latticeeasydocs.pdf, 2008.

[262] W. H. Press, S. A. Teukolsky, W. T. Vetterling, and B. P. Flannery, *Numerical Recipes 3rd Edition: The Art of Scientific Computing*. Cambridge University Press, New York, NY, USA, 3 ed., 2007.

[263] D. Polarski and A. A. Starobinsky, *Semiclassicality and decoherence of cosmological perturbations*, *Class. Quant. Grav.* **13** (1996) 377–392, [gr-qc/9504030].

[264] D. G. Figueroa, J. Garcia-Bellido, and A. Rajantie, *On the Transverse-Traceless Projection in Lattice Simulations of Gravitational Wave Production*, *JCAP* **1111** (2011) 015, [arXiv:1110.0337].

[265] B. Fornberg, *Generation of finite difference formulas on arbitrarily spaced grids*, *Mathematics of Computation* **51** (1988), no. 184 699–699.

[266] J. R. Bond, A. V. Frolov, Z. Huang, and L. Kofman, *Non-Gaussian Spikes from Chaotic Billiards in Inflation Preheating*, *Phys. Rev. Lett.* **103** (2009) 071301, [arXiv:0903.3407].

[267] G. N. Felder, *CLUSTEREASY: A program for lattice simulations of scalar fields in an expanding universe on parallel computing clusters*, *Comput. Phys. Commun.* **179** (2008) 604–606, [arXiv:0712.0813].

[268] A. V. Frolov, *DEFROST: A New Code for Simulating Preheating after Inflation*, *JCAP* **0811** (2008) 009, [arXiv:0809.4904].

[269] J. Sainio, *CUDAEASY - a GPU Accelerated Cosmological Lattice Program*, *Comput. Phys. Commun.* **181** (2010) 906–912, [arXiv:0911.5692].

[270] R. Easther, H. Finkel, and N. Roth, *PSpectRe: A Pseudo-Spectral Code for (P)reheating*, *JCAP* **1010** (2010) 025, [arXiv:1005.1921].

[271] W. C. Swope, H. C. Andersen, P. H. Berens, and K. R. Wilson, *A computer simulation method for the calculation of equilibrium constants for the formation of physical clusters of molecules: Application to small water clusters*, *The Journal of Chemical Physics* **76** (1982), no. 1 637–649.

[272] Z. Huang, *The Art of Lattice and Gravity Waves from Preheating*, *Phys. Rev.* **D83** (2011) 123509, [arXiv:1102.0227].

[273] J. Sainio, *PyCOOL - a Cosmological Object-Oriented Lattice code written in Python*, *JCAP* **1204** (2012) 038, [arXiv:1201.5029].

[274] H. L. Child, J. T. Giblin, Jr, R. H. Ribeiro, and D. Seery, *Preheating with Non-Minimal Kinetic Terms*, *Phys. Rev. Lett.* **111** (2013) 051301, [arXiv:1305.0561].

[275] J. T. Giblin, T. Deskins, and H. Child, "GABE: Grid And Bubble Evolver." Astrophysics Source Code Library, Jan., 2018.